Habilitation à diriger des recherches

La plasmonique non-linéaire: un monde à découvrir.

Guillaume Bachelier

Laboratoire de Spectrométrie Ionique et Moléculaire,
Université Claude Bernard Lyon 1 – CNRS (UMR 5579)

Soutenue le 15 juin 2011 devant le Jury composé de:

Alexandre Bouhelier
Sophie Brasselet
Michel Broyer
Christophe Dujardin
Jean-Jacques Greffet
Serge Huant

Table des matières

Guillaume Bachelier

Maître de conférences agrégé

Né le 14 octobre 1976 à Auxerre (89)
Nationalité: Française
Situation familiale: marié, 2 enfants

Adresse:
Laboratoire de Spectrométrie Ionique et Moléculaire (LASIM)
Université Claude Bernard - Lyon 1
Bât. A. Kastler
43 bd du 11 Novembre 1918
69622 Villeurbanne Cedex (France)
E-mail: guillaume.bachelier@lasim.univ-lyon1.fr
Page web: http://bachelier.guillaume.free.fr

FORMATION

2004-2005: Stage post-doctoral à l'Institut d'Optique de Madrid (Espagne).
2000-2004: DEA de Physique de la Matière, mention Bien, Monitorat et Doctorat de l'Université Paul Sabatier (Toulouse), Spécialité Physique de la Matière, mention très honorable.
1998-2000: CAPES, puis Agrégation de Sciences Physiques option Physique, rang 15ème sur 150 admis (Université P. Sabatier, Toulouse).
1996-1998: Licence, Maîtrise es Sciences Physiques, mention Bien (Université P. Sabatier, Toulouse).
1994-1996: Maths sup., Maths spé. (Lycée Bellevue, Toulouse).
Juin 1994: Bac C, mention Bien (Lycée Bellevue, Toulouse).

ACTIVITE DE RECHERCHE

2005: Maître de Conférences à l'Université Claude Bernard (Lyon).

- **Théorie**: Etude des processus non-linéaires (SHG) dans les nanostructures métalliques. Etude de l'interaction électron-phonon dans les nanostructures semi-conductrices et les nanoparticules métalliques (proposition d'un nouveau mécanisme de couplage).
- **Simulations**: Calcul des propriétés optiques de nanostructures par éléments finis (propriétés optiques linéaires et SHG) et de manière analytique (diffusion Raman); Comparaison quantitative avec l'expérience; Développement d'outils de caractérisation (nano-structuration, tailles, distribution de tailles).
- **Développements expérimentaux**: Réalisation d'un ampli femtoseconde au kHz; Mise en place d'un dispositif de spectrométrie et d'imagerie femtoseconde (expériences pompe-sonde, streak camera, interférométrie); Développement d'un SNOM dédié à la spectrométrie au centre NanOpTec; Proposition d'une technique interférentielle (démodulation poly-harmonique) pour mesurer l'amplitude d'oscillation de la pointe d'un SNOM; Adaptation d'un microscope à champ sombre sur un spectromètre optique de très haute résolution (gain en résolution spatiale, en réjection et en sensibilité).

- **Techniques spectrométriques**: Champ proche optique (SNOM), expériences pompe-sonde et spectrométrie femtosecondes, diffusion non linéaire (SHG), diffusion Raman, photoluminescence, réflectivité, réflectivité modulée.
- **Mobilité**: Séjour de trois mois chez P. Gucciardi, à l'Istituto per i Processi Chimico-Fisici (Sicile, 2003) pour le développement d'un SNOM; Séjour d'un mois aux Etats-Unis chez P. Yu, au Department of Physics (Berkeley, 2004) pour apprendre les techniques de mesure sous hautes pressions; Stage post-doctoral sous la direction de Javier Solis à l'Institut d'Optique de Madrid (Espagne, 2005) pour me former aux spectrométies et imageries résolues en temps.
- **Collaborations**: France et étranger pour les développements expérimentaux, la synthèse et la caractérisation des nanostructures.
- **Communications**: 40 publications dans des revues internationales (31 depuis 2007), présentations orales à des conférences nationales et internationales, séminaires invités dans des laboratoires étrangers, rapporteur pour Physical Review B et Physical Review Letters.

ENSEIGNEMENT ET ENCADREMENT

2009-2011: Demi-délégations CNRS.
2005-...: Maître de Conférences à l'Université Claude Bernard (Lyon).
2001-2004: Moniteur de l'Université Paul Sabatier (Toulouse).

- **Cours** de plasmonique (Master Nanoscale Engineering).
- **Cours/TP** de simulations part éléments finis en physique (Ecole doctorale PHAST, Masters de physique) ouvert aux enseignants-chercheurs.
- **Cours** d'électrocinétique et d'optique (CAPES puis Master EDSE), forte implication dans la mise en place du master.
- **Séances de montages** d'optique (Préparation à l'Agrégation de l'ENS Lyon), optique, mécanique, électricité (CAPES puis Master EDSE).
- **Responsable des travaux pratiques** d'électromagnétisme, rédaction d'un polycopié de TP, rénovation du matériel (Licence 2ème année).
- **Séances de travaux pratiques:** Optique, mécanique, électricité, électromagnétisme (Licence 1ère, 2ème et 3ème année).
- **Cours-TP**: Physique statistique (Licence 1ère année) avec rédaction d'un polycopié de cours (2002-2004).
- **Correction d'épreuves écrites:** épreuves de physique du Concours Commun Polytechnique MP (2001 et 2002).
- **Interrogations orales:** Khôlles en classes préparatoires PC* au lycée Bellevue de Toulouse (2000-2001).

RESPONSABILITES ADMINISTRATIVES

- **Membre du conseil scientifique** du centre NanOpTec (2007-...).
- **Représentant élu du collège B** au conseil du laboratoire du LASIM (2006-...).
- **Réalisation d'un site web** pour gérer le matériel optique du centre NanOpTec, et des laboratoires lyonnais partenaires (2005).
- **Représentant du personnel** non permanent au conseil de l'institut de recherche IRSAMC (2002-2004).
- **Rédaction des comptes-rendus du conseil** de l'institut de recherche IRSAMC (2003-2004).

Introduction

Les propriétés optiques des nanoparticules de métaux nobles occupent une position singulière dans les nanosciences, de par la présence d'oscillations collectives des électrons: les plasmons. Pourtant, ces résonances n'ont à première vue pas que des qualités: 1) elles sont plutôt larges comparées à des transitions électroniques, aux excitons, aux polaritons, 2) elles ne se couplent pas à la lumière dans le cas d'une surface plane, 3) elles sont dominées par l'absorption lorsque les particules sont petites. Qu'est-ce qui rend donc si attrayantes ces excitations collectives apparemment mal nées? C'est qu'elles ont aussi beaucoup d'avantages comme nous le verrons tout au long de se manuscrit et que, malgré les dizaines (ou centaines?) de milliers d'articles qui leurs ont été dévolus, elles ont encore beaucoup de chose à nous apprendre...

Les nanoparticules m'ont accompagné tout au long de mon parcours en recherche. Et pas n'importe lesquelles: les nanoparticules d'or et d'argent. Je ne saurais expliquer cette attirance toute particulière pour ces deux métaux. Peut-être parce que je les trouve simplement beaux à l'état massif. Et pourtant, comme nous le verrons, rien ne ressemble moins à de l'or et de l'argent que ces nanoparticules dont elles sont constituées. Et c'est probablement cette propriété qui me fascine le plus: on peut contrôler par des effets de forme, de taille ou d'interaction la réponse spectrale des plasmons. Bref, voici donc un système extrêmement versatile... Mais comme le disent les chimistes, il est également extrêmement difficile à reproduire! Ceci a largement motivé le développement de dispositifs sensibles à des particules uniques pour s'affranchir des effets de distribution de morphologie et donc d'élargissement hétérogènes des spectres. Mais quels progrès tout de même en une dizaine d'année sur les formes que ces artistes arrivent à fabriquer: des sphères, des bâtonnets, des triangles, des cubes, des décaèdres... Une profusion de formes permises par une croissance sélective de faces cristallines. La physique n'est pas en reste grâce aux propriétés singulières des nanoparticules qui reposent essentiellement sur une caractéristique fondamentale des structures plasmoniques. Par nature, les oscillations collectives des électrons sont accompagnées par un champ électrique fortement évanescent, localisé au voisinage de la

surface métallique: le champ proche. Ainsi, bien que les résonances plasmons aient un facteur de qualité plutôt modeste, elles compensent très largement par cet effet de localisation qui "piège" les photons comme dans un puits de potentiel. Il est ainsi possible de confiner sur des échelles extrêmement courtes (très largement sub-longueur d'onde) des champs gigantesques au niveau de gaps entre particules notamment. La conséquence la plus spectaculaire se traduit par des facteurs d'exaltations allant jusqu'à plus de 14 ordres de grandeurs dans le cas de la diffusion Raman! Mais là encore, la reproductibilité de tels facteurs d'exaltation est on ne peut plus délicate. On ne sait d'ailleurs pas encore à l'heure actuelle contrôler la position de ces "hots-spots" qui semblent largement liés au désordre et donc pour le moment au hasard.

Comment s'inscrit mon travail dans cette thématique extrêmement prolifique? La spécificité de mon activité de recherche est de mener conjointement:

- le développement d'une approche expérimentale et théorique (analytique et numérique).
- l'étude de propriétés optiques complémentaires: linéaires (diffusion, absorption, champ proche), non-linéaires (SHG, HRS, pompe-sonde) et inélastiques (Raman).
- la combinaison de résolution spatiale (nm), temporelle (fs) et spectrale (cm-1).

Ce qui est passionnant de mon point de vue en physique ce n'est pas tant l'expérience ou la théorie prises séparément, c'est la confrontation permanente entre théorie et expérience, l'une venant parfois conforter l'autre, ce qui est rassurant, ou au contraire l'une venant défier l'autre, ce qui est nettement plus stimulant. C'est ce va et vient qui fait la richesse de la démarche scientifique et auquel j'attache beaucoup d'importance. Il s'en suit une démarche invariable depuis mon début en recherche: partir de résultats expérimentaux, comprendre et modéliser la physique de ces systèmes pour ensuite pouvoir proposer de nouvelles idées d'expériences. Cette démarche s'est notamment traduit par des avancées scientifiques significatives avec la proposition d'un nouveau mécanisme de couplage pour expliquer la diffusion Raman basse fréquence dans les nanoparticules métalliques, la découverte des profils Fano dans des structures purement plasmoniques composées d'un dimère or-argent et la compréhension de l'origine des sources non-linéaires dans les nanoparticules métalliques et leur mise en évidence expérimentale.

La deuxième caractéristique de ma démarche est la pluralité des techniques utilisées pour comprendre la physique des objets que j'étudie. Cela se traduit par l'utilisation d'outils analytiques comme numériques pour les simulations, ou encore de techniques résolues temporellement, spectralement et spatialement pour la partie expérimentale ayant trait aux propriétés optiques linéaires (diffusion, absorption), non-linéaires (génération de second

harmonique) et inélastiques (Raman). C'est cette "pluridisciplinarité" (purement physicienne) qui m'a notamment permis d'identifier les profils Fano, bien connus en diffusion Raman, lors de l'étude théorique des dimères or-argent. Il y a cependant une grande constance dans les techniques abordées: la notion d'onde. Les états électroniques, les plasmons, les phonons, les modes de vibrations, la génération de second harmonique, tout est décrit par des ondes, ce qui facilite grandement leur compréhension et leur manipulation.

Enfin, mon activité de recherche se caractérise par le développement de nouvelles thématiques dans les laboratoires que j'ai fréquenté: les particules métalliques au cours de ma thèse, un dispositif d'imagerie et d'interférométrie femtoseconde pendant mon post-doc, les simulations par éléments finis au LASIM et enfin le développement d'un dispositif de champ proche. Il y a donc eu tout à mettre en place, à construire, à comprendre pour développer de nouvelles compétences. Mon travail s'inscrit donc généralement dans la durée et demande un très fort investissement initial, mais c'est aussi ce qui le rend passionnant.

Je vous invite donc au cours de ce manuscrit à suivre le cheminement des idées, des concepts qui ont guidé ma recherche depuis mon recrutement en tant que maître de conférences dans l'équipe de Pierre-François Brevet. De nombreux aspects liés à ma thèse et à mon post-doc et qui se sont poursuivis au cours de ces années seront donc volontairement mis de côté au profit du coeur de mon travail: la compréhension des propriétés optiques linéaires et non-linéaires de nanoparticules métalliques. Dans une première partie "Plasmonique", je présenterai la démarche scientifique qui, depuis l'étude de la diffusion de Mie dans les particules métalliques sphériques, m'a conduit à découvrir les profils Fano dans les dimères or-argent. Dans une seconde partie, j'exposerai les grandes questions qui se sont posées dans l'étude de la réponse non-linéaire des particules métalliques: rôle de la rupture de symétrie de la forme des particules, dépendance en taille du signal de second harmonique, rôles des différents courants non-linéaires. Nous verrons comment ce travail pionnier par de nombreux aspects et assidu pendant quatre ans a permis de déterminer quantitativement les différentes contributions non-linéaires dans les nanoparticules. Ce sera aussi l'occasion de présenter les dernières avancées du point de vue expérimental ayant ouvert la voie vers l'étude de la génération de second harmonique de nanoparticules uniques dans une matrice homogène. La dernière partie de ce manuscrit sera quant-à elle résolument tournée vers l'avenir en présentant mon projet de recherche autour du champ proche optique et les questionnements, laissés jusque là de côté, mais qui seront dorénavant le centre de toute mon attention...

La plasmonique

1- Interaction lumière matière dans les métaux nobles

1.1- Les plasmons de surface

Pour peu que l'on ne rentre pas dans des régimes "quantiques" où la taille de la particule devient comparable au libre parcours moyen des électrons ou que le nombre de photons ne soit pas trop faible pour qu'une statistique quantique fasse jour, la plupart des résultats obtenus sur la plasmonique s'expliquent dans le cadre de l'électromagnétisme standard. La réponse du milieu est ainsi entièrement contenue dans sa constante diélectrique $\varepsilon(\omega)$ mais aussi dans sa morphologie. En effet, contrairement à des excitations localisées autour de lacunes du réseau cristallin ou de défauts de surface, l'oscillation collective des électrons, qui donne naissance aux plasmons, est essentiellement délocalisée et donc fortement dépendante des conditions aux limites qui lui sont appliquées. Ainsi, la réponse d'une surface plane est très différente de celle d'une sphère, d'un bâtonnet ou de toute autre géométrie. Mais commençons par voir la spécificité et l'originalité des structures métalliques, comparées à d'autres types de matériaux, venant de la constante diélectrique uniquement. Dans le cas de métaux nobles, cette constante diélectrique peut s'écrire

$$\varepsilon(\omega) = 1 - \frac{\omega_p^2}{\omega^2 + i\gamma\omega} + \varepsilon^{ib}(\omega).$$

Le premier terme traduit la réponse des électrons de conductions dans le cadre du modèle de Drude (ω_p est la pulsation plasma et γ traduit l'amortissement des oscillations). La partie interbande est donnée par le terme $\varepsilon^{ib}(\omega)$. Suivant le métal considéré le seuil des transitions varie de 2.1 eV et 2.4 eV pour le cuire et l'or respectivement à 3.9 eV pour l'argent, expliquant notamment la différence de couleur entre les métaux. Le fait remarquable est que la constante diélectrique est négative en dessous du seuil de transition interbande. Pour entrevoir les conséquences sur la nature des ondes électromagnétiques, il suffit d'écrire la relation de dispersion pour une onde plane:

$$k_{//}^2 + k_{\perp}^2 = \varepsilon(\omega)\frac{\omega^2}{c^2} < 0$$

où ω est la pulsation, $k_{//}$ et $k_{\perp}$ les composantes du vecteur d'onde parallèle et perpendiculaire à l'interface. Ainsi, l'une au moins des composante est imaginaire, donnant aux ondes un comportement évanescent dans au moins une des directions de l'espace. Le champ est donc au moins partiellement localisé. Le calcul complet montre en fait que le champ électrique est évanescent de part et d'autre de l'interface, d'où le nom de plasmons de surface par opposition aux plasmons de volume correspondant à une onde longitudinale de charge dans le matériau massif, caractérisée par $\varepsilon(\omega)=0$ et $\mathrm{div}\vec{E} = \rho/\varepsilon_0 \neq 0$. Le schéma ci-dessous résume ainsi les propriétés essentielles des plasmons qui vont êtres utilisées tout au long de ce manuscrit:

- les photons sont "piégés" au voisinage de l'interface donnant naissance à la notion de champ proche. Ainsi non seulement une partie de l'information est inaccessible en champ lointain mais les nanostructures plasmoniques ne vont interagir fortement entre elles que si elles sont proches à l'échelle de la décroissance de l'onde évanescente.
- le champ est exalté au voisinage de la surface, ce qui aura des conséquences importantes sur les propriétés non-linéaires des nanoparticules qui dépendent quadratiquement de l'amplitude du champ dans le cas de la génération de second harmonique.

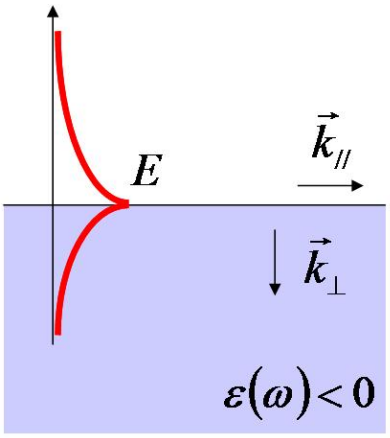

$$\vec{E}_p = \vec{E}_{p0} e^{i\vec{k}_{\perp}\cdot\vec{r}} e^{i\vec{k}_{//}\cdot\vec{r}}$$

Il y a en revanche une propriété qui n'est pas directement accessible par la relation de dispersion, mais qui s'obtient aisément en traçant la composante du vecteur d'onde parallèle à la surface en fonction de l'énergie

$$k_{//}(\omega) = \frac{\omega}{c}\sqrt{\frac{\varepsilon(\omega)\varepsilon_m}{\varepsilon(\omega)+\varepsilon_m}}$$

où ε_m correspond à la constante diélectrique du milieu extérieur (voir Figure 1). La partie réelle de $k_{//}(\omega)$ traduit la propagation du plasmon le long de l'interface tandis que sa partie imaginaire est associée à l'absorption du plasmon, ou en d'autres termes à sa longueur de

propagation. On voit ainsi apparaître très clairement un comportement d'anti-croisement entre les photons et les plasmons de volume (en pointillés) donnant naissance à la branche des plasmons de surface pour une énergie inférieure au seuil des transitions interbandes (3.9 eV dans le cas de l'argent). Cet anti-croisement impose de fait que la composante du vecteur d'onde des plasmons le long de l'interface est au-delà du cône de lumière et que, par conséquent, ces plasmons ne sont pas directement excitables par des photons.

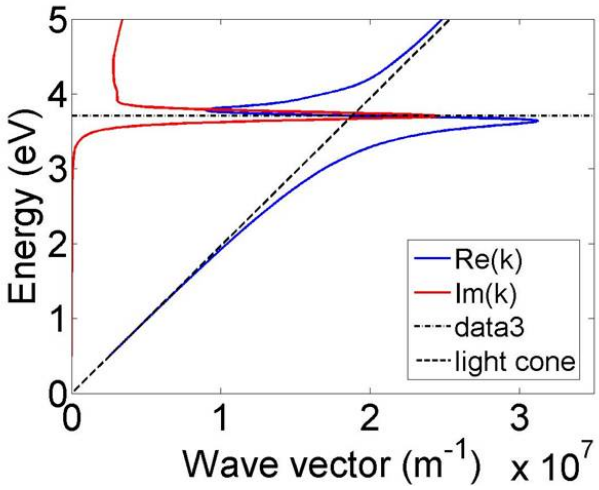

Figure 1: *Tracé de la partie réelle et imaginaire de la composante du vecteur d'onde parallèle à la surface en fonction de l'énergie du plasmon de surface dans le cas de l'argent. Les pointillés correspondent respectivement à la ligne de lumière (droite passant par l'origine) et aux plasmons de volume (trait horizontal).*

Différentes stratégies ont été utilisées pour exciter ces plasmons: utiliser la réflexion totale à la surface d'un prisme (configuration Otto) afin de créer une onde évanescente présentant des caractéristiques similaires aux plasmons ($k_{//}$) et autorisant de fait leur excitation; introduire un réseau de stries à la surface du métal et bénéficier de l'échange Δk de vecteur d'onde avec le réseau: $k_{//}(\omega) = \omega / c + \Delta k$. La dernière solution est de rompre toute invariance par translation de sorte que le vecteur d'onde n'ait plus à être conservé. Ceci peut être réalisé en excitant les plasmons de surface avec une sonde de champ proche (type fibre étirée par exemple) ou plus simplement en utilisant des nanoparticules métalliques. C'est précisément ce que nous allons faire dans l'ensemble de ce manuscrit, bénéficiant ainsi des avantages des plasmons de surfaces (localisation et exaltation du champ) sans en avoir l'un de ses inconvénients, à savoir la difficulté de les exciter optiquement.

1.2- Résonances plasmons dans les nanoparticules sphériques

Ayant rompu toute invariance par translation, les résonances ne sont plus associées à un vecteur d'onde donné mais, dans le cas de particules sphériques, à un moment angulaire. On observe ainsi lorsque la taille des particules devient de plus en plus grande des résonances dipolaires (l=1), quadripolaires (l=2), etc... Pour les petites particules, l'essentiel de la physique est contenue dans la polarisabilité de la nanoparticule:

$$\alpha = 3V \frac{\varepsilon(\omega) - \varepsilon_m}{\varepsilon(\omega) + 2\varepsilon_m}.$$

Tout d'abord, cette dernière fait intervenir un dénominateur résonant pour $\mathrm{Re}\{\varepsilon(\omega) + 2\varepsilon_m\} = 0$: c'est la résonance plasmon de surface. A la différence des excitons dans les semi-conducteurs, il s'agit ici d'une réponse collective des électrons. La polarisabilité est ainsi proportionnelle au nombre d'électrons excités et donc, classiquement, au volume de la particule. C'est tout l'intérêt de ces résonances: une force d'oscillateur extrêmement importante. Le prix à payer en revanche est d'avoir une résonance assez large due à l'absorption. Cette largeur est donnée par la partie imaginaire du dénominateur. On comprend ainsi aisément pourquoi la résonance plasmon dans les particules d'argent, qui a lieu au dessous du seuil des transitions interbandes ($\mathrm{Im}\{\varepsilon(\omega)\}$ faible), est nettement plus étroite que celles des particules d'or qui se produisent au dessus du seuil. Ou encore qu'un changement de milieu extérieur (ε_m) modifie la position de la résonance.

Toutes ces propriétés se retrouvent naturellement dans les sections efficaces de diffusion

$$C_{sca} = V^2 \frac{24\pi^3 \varepsilon_m^2}{\lambda^4} \left| \frac{\varepsilon(\omega) - \varepsilon_m}{\varepsilon(\omega) + 2\varepsilon_m} \right|^2$$

et d'absorption

$$C_{abs} = V \frac{18\pi \varepsilon_m^{3/2}}{\lambda} \frac{\mathrm{Im}\{\varepsilon(\omega)\}}{\left|\varepsilon(\omega) + 2\varepsilon_m\right|^2}$$

avec une information supplémentaire, à savoir que la diffusion et l'absorption ne présentent pas la même dépendance en taille. Pour les petites particules, l'absorption, proportionnelle au volume de la particule, domine la diffusion. C'est l'un des grands défauts des nanoparticules de métaux nobles, comme nous l'avons déjà vu: elles absorbent. Donc, s'il est possible d'exalter un signal grâce à la résonance plasmon, il ne faut pas oublier qu'une grande partie de l'énergie sert à chauffer les particules, le bilan énergétique complet est donc à regarder de

près. C'est d'ailleurs l'une de leurs applications dans le traitement des tumeurs cancéreuse où l'énergie déposées dans les particules sert à tuer les tumeurs par transfert thermique.

A partir d'une certaine taille, où les effets retards commencent à prendre de l'importance, l'approche précédente n'est plus valable. Il faut alors utiliser la théorie de Mie pour quantifier l'absorption et la diffusion par les particules. S'il n'est pas question ici de dériver cette théorie, notons simplement qu'elle permet de rendre compte de nombreux phénomènes comme l'élargissement et le décalage vers les grandes longueurs d'ondes de la résonance lorsque la taille de la particule augmente. Ceci peut se comprendre par le fait que la taille de la particule devenant importante, le couplage avec la lumière devient plus efficace, ce qui se traduit, comme en mécanique quantique, par un "décalage radiatif" et un élargissement de la transition. Si l'on considère des particules toujours plus grosses, de nouvelles résonances apparaissent, s'élargissent et se décalent à leur tour: ce sont les résonances quadripolaires, octupolaires, etc... Une autre caractéristique importante des résonances plasmons vient de la section efficace d'extinction (somme de la diffusion et de l'absorption) qui peut devenir bien plus grande que la section de la particule elle-même. Tout se passe comme si la particule était plus grosse qu'elle ne l'est réellement, jouant ainsi le rôle d'entonnoir à photon. C'est cette particularité qui a donné naissance au concept de nano-antenne avec comme ambition de faire le lien entre l'échelle mésoscopique, où la particule interagit fortement avec la lumière, et le monde nanométrique (particules et molécules de petites tailles) grâce à la localisation du champ.

Je voudrais, pour conclure cette partie, attirer votre attention sur une bizarrerie de la théorie de Mie qui a longtemps heurté ma compréhension: le paradoxe de l'extinction. Que dit ce paradoxe? Lorsque la longueur d'onde devient très petite devant la taille de la particule, on s'attend à retrouver les règles de l'optique géométrique et que la section efficace d'extinction devienne simplement égale à la section de la particule. Il n'en est rien dans la théorie de Mie. Plus précisément, cette section efficace tend vers le double de la section de la particule. Pourquoi le double? Voilà une question qui m'a longtemps intrigué et a focalisé mon attention. La réponse se trouve dans la figure suivante qui trace le champ électrique autour d'un cylindre (le phénomène dont je veux discuter est plus visible que dans le cas d'une sphère, d'où ce choix de géométrie). La partie du haut montre le champ diffusé autour de la particule tandis que la partie du bas montre le champ total (incident plus diffusé). Si l'allure du champ total se comprend aisément (onde partiellement stationnaire en amont de la particule provenant de la réflexion et absence de lumière derrière), un détail choque dans le cas du champ diffusé: pourquoi a-t-on un maximum de signal derrière la particule? C'est

contraire à toute intuition. L'explication vient de la formulation même de la théorie de Mie qui impose dans tout l'espace (en dehors de la particule) un champ incident $\vec{E}_i$ auquel vient se superposer un champ diffusé $\vec{E}_s$, de sorte que le champ total vaut $\vec{E}_t = \vec{E}_i + \vec{E}_s$. Derrière la particule, de grande taille comparée à la longueur d'onde, le champ total est pratiquement nul comme attendu. Ceci impose que $\vec{E}_i + \vec{E}_s = \vec{0}$ soit $\vec{E}_s = -\vec{E}_i$. Par construction le champ diffusé doit donc compenser exactement le champ incident qui a été arbitrairement imposé derrière la particule! Ainsi la particule doit non seulement réfléchir ou absorber le champ incident, mais elle doit aussi, dans la théorie de Mie, compenser le champ incident imposé derrière la particule alors qu'il n'y a pas de source. Voici donc pourquoi la section efficace d'extinction est deux fois plus grande que la section de la particule. Ceci n'est pas sans conséquences: si le champ total est à priori bien calculé, son "découpage" en terme de champ incident et champ diffusé demande, lui, quelques précautions dans son interprétation. Le corolaire est que la section efficace d'absorption est bien calculée, puisqu'elle ne fait intervenir que le champ total, tandis que la section efficace de diffusion peut-être surestimée.

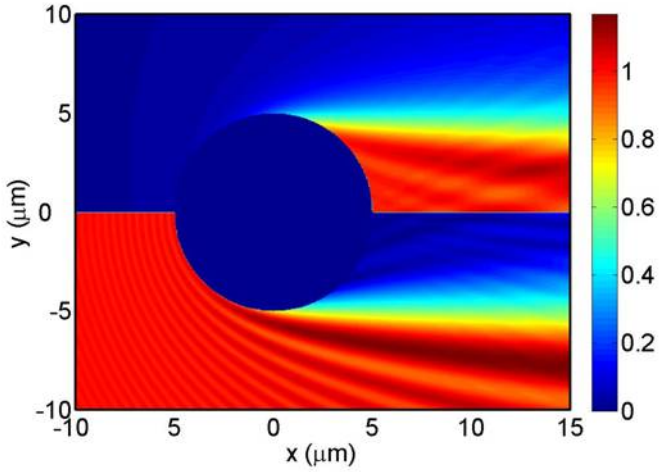

Figure 2: *Calcul du champ électrique autour d'un cylindre de rayon 5 μm et de constante diélectrique égale à 1+0,1i. La partie supérieure correspond au champ diffusé, la partie inférieure au champ total (incident + diffusé) pour une longueur d'onde de 800 nm.*

2- Comparaison expériences/simulations sur des particules uniques

2.1- Effet de forme: les nano-bâtonnets

L'un des grands succès de la plasmonique vient de la capacité qu'ont les particules d'or ou d'argent à modifier leurs spectres en fonction de leur forme. C'est une propriété précieuse puisqu'elle permet d'adapter la réponse optique des particules à l'application désirée, ou à l'énergie de transition que l'on veut exciter. Les techniques de synthèse ont ainsi connu des progrès spectaculaires depuis une dizaine d'années offrant une large gamme de formes présentant une forte symétrie (bâtonnets, triangles, cubes...) ou pas (étoiles). Conjointement, les méthodes de caractérisation et les simulations ont dû emboiter le pas afin d'établir la relation forme-réponse spectrale.

Dans cette quête, l'une des principales difficultés vient du fait que, aussi rigoureuses soient-elles, ces synthèses chimiques mènent toujours à une certaine distribution de forme ou de taille faisant que les mesures d'ensemble sont toujours entachées d'un élargissement hétérogène des spectres. Quand bien même les particules seraient toutes identiques, leurs orientations aléatoires brouilleraient une partie de l'information recueillie par des mesures de diffusion ou d'absorption. Afin de palier à cet obstacle, la sensibilité des dispositifs expérimentaux a été considérablement améliorée et des techniques spécifiques ont vu le jour pour atteindre le seuil de la particule unique. C'est le cas de la spectrométrie par modulation spatiale développée conjointement par les équipes "Agrégat et Nanostructure" et "FemtoNanoOptics" du LASIM. Le principe de base est de faire osciller la position d'une particule sous un faisceau fortement focalisé afin de moduler la transmission de l'échantillon. La section efficace absolue d'extinction est alors extraite du signal démodulé à la fréquence d'oscillation de l'échantillon.

L'autre aspect du problème est d'être capable de simuler les propriétés optiques de nanoparticules de formes de plus en plus exotiques. Ayant passé une partie de ma thèse à développer une approche analytique pour calculer les spectres Raman de nanoparticules métalliques sphériques, je connaissais bien les qualités et les limites d'une telle démarche. D'un côté on contrôle tous les ingrédients de la simulation et l'on peut aisément isoler la contribution de tel effet ou de tel mode. Mais on est extrêmement contraint par la géométrie du système ce qui n'allait vraiment pas dans la bonne direction étant donnée l'évolution de la plasmonique. C'est pourquoi je me suis attelé peu après mon arrivée au LASIM au

développement de simulations par éléments finis à l'aide du logiciel COMSOL. Ce travail pionnier au laboratoire était aussi un passage obligatoire avant de m'attaquer à ce qui est le coeur du travail de mon équipe, à savoir l'optique non-linéaire. En effet, avant d'essayer de simuler la réponse optique non-linéaire de nano-objets, il fallait s'assurer que mes simulations rendaient bien compte des propriétés optiques linéaires.

L'une des premières études a été menée avec l'équipe "FemtoNanoOptics" sur des nano-bâtonnets d'or de taille comprise entre 40 et 60 nm (voir figure 3). Les bâtonnets présentant une forme anisotrope, contrairement aux particules sphériques, deux résonances sont observées: la plus intense et décalée vers le rouge est obtenue pour une excitation le long du bâtonnet, i.e. selon la direction de plus forte polarisabilité; l'autre, moins intense et autour 530nm, correspond à une excitation perpendiculaire au bâtonnet. La levée de dégénérescence étant partielle (selon un seul axe), il est naturel de retrouver l'une des résonances au niveau de celle obtenue pour une particule sphérique de même diamètre. L'autre dépend quant à elle du rapport d'aspect de la particule, c'est à dire du rapport entre sa longueur et son diamètre. Comme le montre la figure 3, les mesures d'ensemble aboutissent à une réponse spectrale très large (une centaine de nanomètres pour la courbe noire) bien au-delà des résultats attendus et effectivement obtenus pour différents bâtonnets uniques repérés par les triangles, carrés et cercles. Cet élargissement est donc de type hétérogène et provient directement de la distribution morphologique des bâtonnets (voir image TEM).

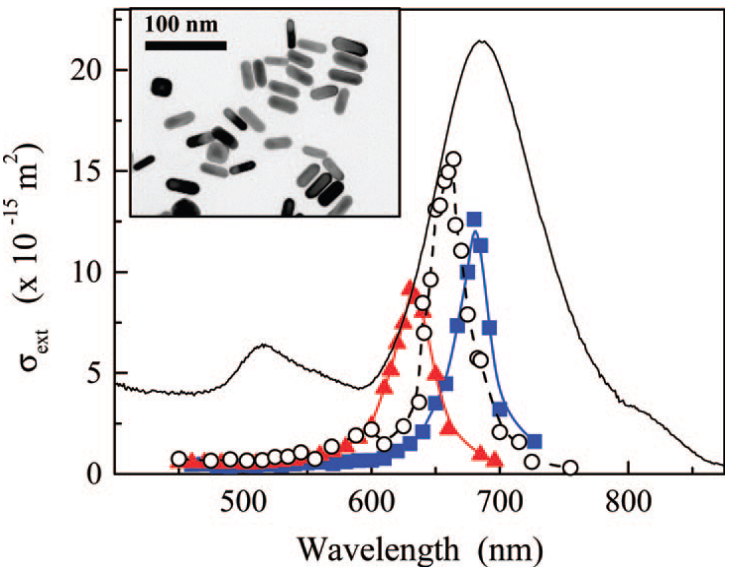

Figure 3: *Section efficace absolue d'extinction pour trois nano-bâtonnets d'or uniques (triangles, cubes, sphères) obtenue pour une excitation le long des bâtonnets. La courbe noire correspond à une mesure d'ensemble de la solution colloïdale (longueur des bâtonnets de 40 à 60 nm). En insert une image TEM de l'échantillon.*

La question qui se posait à nous était de savoir s'il était possible d'aller plus loin et de déterminer, à partir des spectres, la forme exacte du bâtonnet. De manière subjacente, se pose un problème de fond: y a-t-il une sorte de bijection entre la forme et le spectre? Ma contribution à ce travail a donc été de simuler la réponse des particules pour différents rapports d'aspects et pour différentes formes des extrémités du bâtonnet. En effet, si le rôle du rapport d'aspect sur la longueur d'onde de résonance est bien connu, le caractère plus ou moins arrondi des extrémités joue également un rôle déterminant: plus l'apex est pointu, plus la longueur d'onde de résonance est faible.

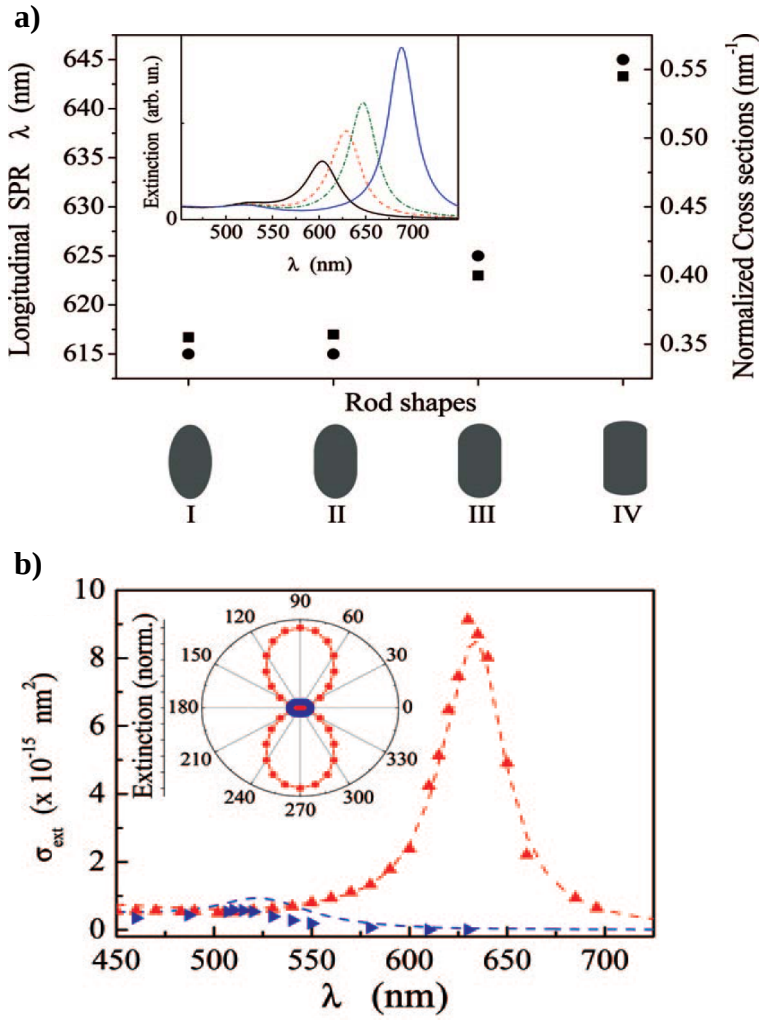

Figure 4: *a) dépendance de la longueur d'onde de résonance longitudinale (points) et de la section efficace d'extinction (carrés) en fonction de la forme des extrémités d'un nano-bâtonnet de longueur 30 nm et de 15 nm de diamètre. En insert, les spectres calculés pour des rapports d'aspect de 1.75, 2, 2.15 et 2.5 de gauche à droite pour la forme III. b) Comparaison entre les spectres expérimentaux (triangles) et simulés (pointillés) pour un bâtonnet de forme III, de diamètre 25.5 nm et de longueur 50 nm et une polarisation parallèle ou perpendiculaire à l'axe du bâtonnet. En insert, les spectres d'extinction simulés en fonction de la polarisation incidente pour une excitation aux longueurs d'onde des résonances longitudinales (640 nm) et transverse (525 nm).*

Dès lors, comment parvenir à remonter à la morphologie de la particule à partir de sa réponse spectrale? Dans le cas des bâtonnets, nous avons trois paramètres ajustables: la longueur, le diamètre et la forme des extrémités, les deux premiers pouvant être ramenés au volume et au rapport d'aspect du bâtonnet. Cette dernière description est en fait plus avantageuse pour plusieurs raisons:

- au-dessus du seuil des transitions interbandes, l'absorption de la particule est pratiquement insensible à la forme de la particule. Elle est donc directement proportionnelle au volume de celle-ci comme c'est le cas pour une particule sphérique. Ainsi, l'ajustement de la partie du spectre correspondant aux transitions interbandes fixe le volume de la particule.
- pour des particules de petite taille, la longueur d'onde de la résonance longitudinale est largement indépendante du volume de la particule (pas d'effet retard) mais dépend fortement du rapport d'aspect et de la forme des extrémités (cf. figure 4). Ces deux paramètres peuvent donc être ajustés indépendamment du volume mais sont interdépendants.
- le rapport d'intensité entre la résonance longitudinale et la résonance transverse dépend de également du rapport d'aspect et de la forme des extrémités. Ceci nous fournit une deuxième contrainte qui fixe donc ces deux paramètres.

Ainsi, nous avons pu extraire pour la première fois la morphologie d'un bâtonnet unique, à savoir son volume, son rapport d'aspect et la courbure de ses extrémités, en comparant quantitativement les spectres expérimentaux et simulés obtenus pour deux polarisations orthogonales (cf. figure 4). Si ce résultat est un fait marquant en soit, il faut bien garder en tête qu'une petite plage de valeur donnait un accord acceptable entre expérience et simulation et qu'il apparaît donc illusoire de parler d'unicité de la solution si on ne connait rien de la forme. D'autre part les simulations ne sont jamais qu'un modèle simplifié où différents aspects ne sont pas nécessairement bien pris en compte (homogénéité du milieu extérieur, forme exacte du faisceau, etc...) et où l'on suppose que la constante diélectrique de la particule est bien connue (or on sait qu'il y a différentes tables comme celles de Palik ou de Johnson et Christy qui ne donnent pas le même résultat). Il faut donc toujours considérer avec recul un très bon accord entre les simulations et les expériences.

Je voudrais pour conclure cette partie souligner l'extraordinaire liberté qu'offrent les simulations numériques tant elles permettent de varier les morphologies et les tailles des nano-objets étudiés (dans la limite des ressources informatiques disponibles...). L'une des conséquences que l'on peut regretter est qu'elles ont eu tendance à encourager une certaine

"zoologie" de formes où il est parfois difficile de voir quelle nouvelle physique est abordée. Elles présentent en revanche un réel danger de part le fait qu'elles s'apparentent bien plus à une boite noire que les simulations analytiques, qu'elles durent suffisamment longtemps pour refreiner la multiplication de tests de validité, et finalement qu'elles fournissent de trop belles images qui hypnotisent notre vigilance. La comparaison avec un modèle analytique, quand cela est possible, est donc un point de départ plus que souhaitable.

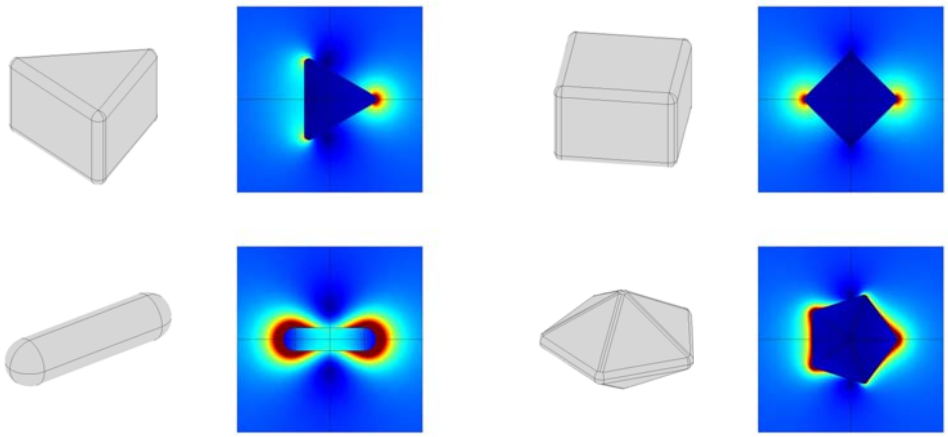

Figure 5: *Cartographie du champ autour de diverses particules pour une excitation horizontale à 800 nm. Les différentes figurent sont à la même échelle, donnée par la taille du bâtonnet: 100 nm.*

Quantitative Absorption Spectroscopy of a Single Gold Nanorod

Otto L. Muskens,† Guillaume Bachelier, Natalia Del Fatti,* and Fabrice Vallée

Université Lyon 1, Centre National de la Recherche Scientifique (CNRS), Laboratoire de Spectrométrie Ionique et Moléculaire (LASIM), 43 bd du 11 novembre, 69622 Villeurbanne cedex, France

Arnaud Brioude, Xuchuan Jiang, and Marie-Paule Pileni

Université Paris 6, CNRS, LM2N, 4 Place Jussieu, 75252 Paris cedex 05, France

Received: February 13, 2008; Revised Manuscript Received: March 19, 2008

The spectrally- and polarization-resolved absorption cross-sections of a single gold nanorod have been investigated using the spatial modulation spectroscopy technique. The ensemble of its optical features, that is, longitudinal and transverse surface plasmon resonances and interband absorption, has been quantitatively characterized. The results are compared with numerical simulations using the discrete dipole approximation and the finite element method, yielding information on the investigated nanorod size and shape.

Reduction of the size of a metal particle down to a nanometric scale is accompanied by large modifications of its optical properties, with apparition of new resonances. These features, the surface plasmon resonances (SPR), and the possibility of adjusting them by modifying the size, shape, structure, and environment of the nanoparticles are at the origin of the interest they have attracted during the past decade. Among the different synthesized nanoobjects, nanorods are of special interest because of the large amplitude and the tunability of their SPR, whose spectral position can be adjusted from the visible to the near-infrared by adapting their aspect ratio.[1] This opens up many possibilities for applications such as enhanced Raman scattering,[2] sensing or imaging,[3] or local heating for medical applications.[4,5] Furthermore, the large sensitivity of the SPR characteristics on the nanorod shape makes it an efficient tool for monitoring the rod-growing mechanism itself.[6] Actually, slight modifications of the fabrication procedure can lead to large changes of the nanorod morphology and size.[7] Key structural parameters, such as aspect ratio, cap-end shape, and volume of the particles, are frequently polydispersed, resulting in a strongly inhomogeneous optical response. This dispersion is preventing not only precise comparison of the experimental and computed spectra but also quantitative analysis of nanorod efficiency in applications such as those based on field enhancement effect. This limitation can be overcome by investigating a single nanorod. Scattering-based techniques have yielded precise spectral information on the main SPR of a nanorod, that is, corresponding to light polarized along its long axis.[6,8,9] However, full analysis of the optical response of a single gold nanorod, including quantitative investigation of its transverse SPR and interband absorption cross-sections, has not yet been performed. Furthermore, quantitative measurements yield important information for most applications, providing insight in the amount of absorbed light energy per nanorod or the amplitude of the field enhancement effect, for instance. Actually, for the usually investigated sizes (nanorod diameter in the 15−20 nm range), the optical response, especially around the transverse SPR, is dominated by absorption, making difficult a full characterization in scattering experiments.

Absorption-based methods for optical detection and spectroscopy of single metal nanoparticles have been recently demonstrated, thereby enabling, in particular, quantitative determination of the extinction cross-section of a nanoobject down to a few nanometers.[10,11] This opens up the possibility of detailed determination of the optical response of a single nano-object over a large spectral range. Using the spatial modulation spectroscopy (SMS) technique,[10,11] we have performed the first quantitative absorption spectroscopy of a single gold nanorod. Light-polarization dependent measurements allow us to identify the origin of the absorption features and to identify longitudinal and transverse SPR and interband absorption. The measured spectrally resolved extinction cross-sections have been quantitatively compared to numerical calculations based on the discrete dipole approximation (DDA) and finite element method (FEM), yielding information on the volume, aspect ratio, and shape of the investigated nanorod.

The gold nanorods are synthesized using a revisited procedure of that described in ref 2.[7,13] Briefly, Au seeds are produced by mixing 1.25 mL of 0.002 M aqueous $HAuCl_4$ solution and 2.74 mL of 18 MΩ water in a test tube and then adding 3.76 mL of 0.20 M aqueous cetyl trimethylammonium bromide (CTAB) solution with further mixing. Finally, 0.9 mL of an aqueous 0.01 M $NaBH_4$ solution at 0 °C is added to the mixture, followed by vigorously shaking the solution. The growth solution (total volume of 8 mL) contains $HAuCl_4 \cdot 3H_2O$ (4.0×10^{-4} M), CTAB (0.095 M), and Ag^+ (6.0×10^{-5} M), and the molar ratio of reducing agent (6.4×10^{-4} M) to $[AuCl_4^-]$ is kept at 1.6:1; they are added in a test tube one by one in that order. In the final step, the 2 h aged seed solution is added into the growth solution, and the final seed concentration [Au] seed is 5.0×10^{-7} M. The mixed solution is vigorously stirred for 20 s and then left undisturbed overnight.

The synthesized gold nanoparticles were characterized by transmission electron microscopy (TEM). A large majority of nanorods were observed, with only few particles with other shapes, mostly nanocubes (inset of Figure 1). Their length (L) is in the 40−60 nm range with a width (D) between 15 and 20 nm, corresponding to aspect ratios (η) ranging from 2 to 4. As

* Corresponding author e-mail: delfatti@lasim.univ-lyon1.fr.
† Present address: FOM-Institute AMOLF, Kruislaan 407, 1098SJ, Amsterdam, The Netherlands.

10.1021/jp8012865 CCC: $40.75
Published on Web 05/21/2008

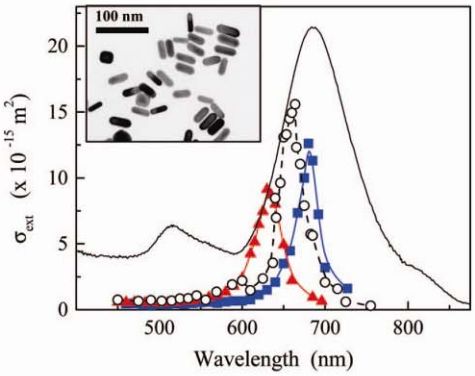

Figure 1. Absolute cross sections spectra measured for three different single gold nanorods, for a light polarization direction maximizing the amplitude of their main resonance (triangles, dots, and squares). The full line is the ensemble spectrum of the colloidal solution on an arbitrary scale. The inset shows a TEM image of the nanorods.

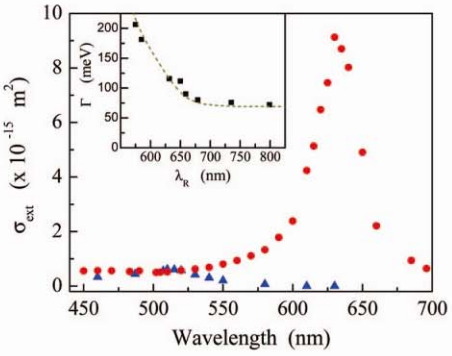

Figure 2. Absolute extinction cross-section of a single gold nanorod measured using the SMS technique. The two spectra (dots and triangles) have been obtained for two orthogonal linear polarizations (α = 87° and 177°). Insert: Full width half-maximum (fwhm) of the main resonance as a function of its wavelength measured in different single nanorods. The dotted line is the computed width using eq 2 with the dielectric function of gold reported by Johnson and Christy.[17]

expected for nanorods, the ensemble absorption spectrum of the aqueous solution (Figure 1) exhibits two main resonances. The red-shifted peak at 680 nm corresponds to the longitudinal surface plasmon resonance. It is associated to the dipolar response of each nanorod polarized along its long axis (i.e., to electron oscillation along this direction induced by the incoming electromagnetic field). Its peak wavelength is known to strongly depend on the nanorod aspect ratio (η).[14–16] The spectral position of the second resonance at 515 nm is consistent with the estimated wavelength of the transverse SPR of an ellipsoid (i.e., its dipolar response polarized along its short axis). In addition to transverse SPR of the nanorods, the resonance at 515 nm also contains contributions from other nanoparticles present in the solution.

The extinction spectra of individual gold nanorods are measured using the spatial modulation technique.[10,11] This method is based on modulating, at a frequency (f) in the kHz range, the position of the studied nanoparticle in the focal plane of a tightly focused light beam. For this purpose, we use a transmission microscope consisting of two 100×, N.A. = 0.8 microscope objectives. The transmitted intensity is detected by a Si-photodiode and demodulated at the fundamental (f) or harmonic ($2f$) of the modulation frequency using a lock-in amplifier. The demodulated signal amplitude gives direct access to the nanoparticle extinction cross-section (σ_{ext}).[11] Because of the limited spatial resolution of this far-field technique, dilute samples have to be prepared (with a surface density of typically less than one particle per square micrometer). This is done by spincoating onto a glass substrate a drop of the gold nanorod solution after addition of a polymer (PVOH). Nanoparticles embedded in a thin layer of polymer are thus obtained, providing them with a relatively homogeneous environment. The sample is mounted on the piezoelectric shaker, and the ensemble is displaced in the focal plane by a $X-Y$ piezo-stage for two-dimensional (2D) imaging of the sample surface. For σ_{ext} spectrum measurements, this system is associated to a broadly tunable source.[11] This is based on supercontinuum generation in a photonic crystal fiber injected by a femtosecond pulse train delivered by a homemade 20 fs Ti/sapphire oscillator working at 780 nm. A spectral bandwidth of about 3 nm is filtered out of the generated unpolarized white-light continuum using a grating pair system. After selection of a linear polarization direction, it is used as the light source for the spatial modulation microscope. In these studies, both absorption and scattering contribute to the measured extinction cross-section. However, for a small particle the latter yield a small contribution, and absorption dominates the observed extinction. This is the case for the single nanorods investigated here (see below).

Polarized extinction spectra measured for different single gold nanorods are shown in Figure 1. For these spectra, the polarization of the incident light was rotated to maximize the amplitude of extinction in the 600−700 nm range. The shape and strong dependence of the resonances on the linear polarization of the incident light is characteristic of a nanorod-like object. Most of the investigated nanoparticles show this spectral signature, with only few particles exhibiting different wavelength and polarization responses. These deviating spectra have been attributed to the presence of nano-objects with different shapes, in agreement with TEM measurements (Figure 1, inset), and will not be discussed here.

The extinction around the long wavelength resonance at about 630 nm is strongly polarization dependent (Figure 2). This is better shown by plotting the measured extinction cross section as a function of the polarization direction (α) of the incident light defined in the laboratory frame (Figure 3). As expected for the longitudinal surface plasmon resonance of a small nanorod, a purely dipolar behavior is observed with a very high polarization contrast ratio exceeding 10^2 (ratio between the maximum and minimum extinction cross sections, Figure 3a). This polarization dependence is lost by orientational averaging in ensemble measurements. In single particle experiments, the maximum amplitude corresponds to the nanorod long axis whose orientation on the substrate can thus be precisely determined. Defining it by the angle α_L relative to the laboratory frame and fitting the data using eq 1,

$$\sigma_{ext}(\alpha;\lambda) = \sigma_{||}(\lambda)\cos^2(\alpha - \alpha_L) + \sigma_{\perp}(\lambda)\sin^2(\alpha - \alpha_L) \quad (1)$$

$\alpha_L = 87 \pm 1°$ is obtained for the nanorod displayed in Figure 2. The extinction cross-section at the longitudinal SPR wavelength is precisely determined; $\sigma_{ext}(\alpha_L) = \sigma_{||} = 9.2 \times 10^3$ nm^2(with $\sigma_{\perp} \approx 0$). Note that σ_{ext} can be crudely estimated from the ensemble spectrum by assuming that all the gold ions are reduced and using the nanorod mean size. The obtained value of $2.5 \times 10^3 nm^2$ at the mean SPR wavelength is of the same order of magnitude but is considerably smaller than the one measured for individual nanorods, because of the SPR inhomogeneous broadening.

Actually, spectra recorded for different single nanorods show a large dispersion of the SPR wavelength (Figure 2 inset), ascribed to fluctuations in the nanoparticle aspect ratio and/or

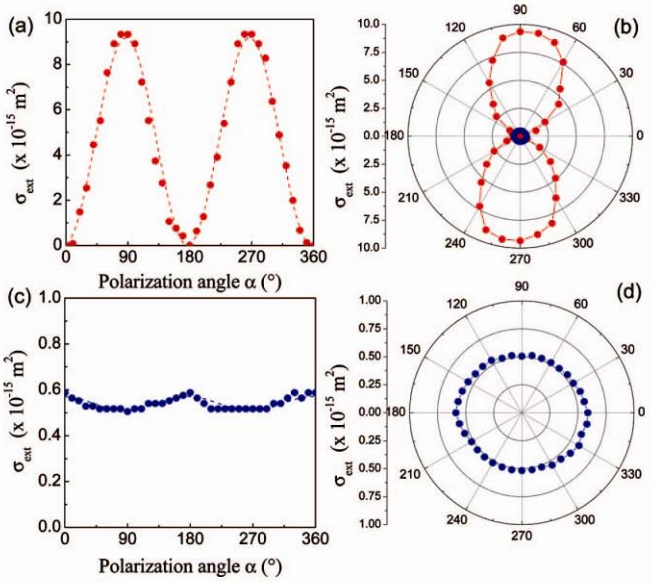

Figure 3. Linear and polar plot of the polarization dependence of the extinction cross section measured for the gold nanorod of Figure 2 at the longitudinal (panels a and b, $\lambda \approx 630$ nm) and transverse (panels c and d, $\lambda = 515$ nm) SPR (the latter data are also shown in panel b). The dashed lines in panels a and b are fit of the experimental data using eq 1, with $\alpha_L = 87°$, $\sigma_{\parallel}(630\text{ nm}) = 9.2 \times 10^3$ nm^2, and $\sigma_{\perp}(630$ nm$) = 0$; $\sigma_{\parallel}(515\text{ nm}) = 510$ nm^2 and $\sigma_{\perp}(515\text{ nm}) = 570$ nm^2.

environment. This translates into a large inhomogeneous broadening of the SPR feature measured in ensemble, which exhibits a much larger width than for a single nanorod (Figure 2). For the latter, the measured full width half-maximum (fwhm) Γ corresponds to the intrinsic one due to SPR damping. Its increase with decreasing the SPR wavelength λ_{ext} and its absolute value are consistent but slightly smaller than previous dark-field scattering measurements (about 75 meV as compared to 80 meV for $\lambda_{ext} \approx 730$ nm).[8,9] As a first approximation, the theoretical longitudinal SPR width can be estimated from the extinction cross-section of a spheroid in the quasistatic approximation, which has the advantage of taking a simple analytic form.[18] A quasi-Lorentzian profile for the SPR is obtained if the imaginary part (ε_2) and interband contribution to the real part of the metal dielectric function are weakly dispersed around the SPR frequency (ω_R).[19,20] Its width (Γ) can then be properly defined and takes the same form as in a nanosphere under the same approximations,

$$\Gamma = \frac{\omega_R^3}{\omega_p^2}\varepsilon_2(\omega_R) \approx \gamma + \frac{\omega_R^3}{\omega_p^2}\varepsilon_2^{ib}(\omega_R) \qquad (2)$$

where ω_p is the plasma frequency, γ is the mean conduction electron scattering rate, and ε_2^{ib} is the interband contribution to ε_2. These approximations are valid when the SPR is away from the metal interband transitions, as in the case of gold nanorods or silver nanospheres.[19,20] For scattering cross-sections, the same width is computed, under the same approximations. The measured data are in excellent agreement with the estimated Γ, using the bulk ε_2 values reported by Johnson and Christy,[17] without introducing additional broadening effects such as electron−surface scattering or radiative damping. This confirms that they play minor roles and that Γ is dominated by bulk-like electron interaction effects for the investigated sizes.[9] In the long wavelength range, Γ is set by the electron scattering rate (γ) and is thus almost constant. In the short wavelength range, ε_2^{ib} increases, reflecting the rise of the interband absorption. SPR damping due to interband electron excitation becomes significant, leading to the observed increase of Γ (Figure 2, inset).[8] Our data are also consistent with the values of Γ reported by Palik,[21] with the main difference being the prediction of a larger long wavelength Γ value: about 85 meV instead of 69 meV, the experimental value being 72 meV (detailed comparison is, however, difficult because of the large energy step of the ε data in the wavelength range of interest).

In the small wavelength range, below 550 nm, a weak resonance is observed around 510 nm for light polarization perpendicular to that maximizing the 630 nm SPR. This is better observed by plotting the measured extinction cross-section as a function of the light polarization direction. A maximum amplitude is observed for light polarization directions $\alpha_T \approx 357$ or 177° with, conversely to the long wavelength resonance, only a weak contrast of about 1.1 (Figure 3). In this spectral range, absorption is dominated by the polarization independent interband transitions in gold. The observed weak polarization effect is ascribed to enhancement of this absorption by the transverse surface plasmon resonance that is observed for the first time on a single nanoparticle here. Its amplitude is strongly reduced by its large broadening, a consequence of its overlap with the interband transitions.

The large sensitivity of the optical response of a nanorod on its geometry (volume, aspect ratio, and tip shape) reflects in the uncorrelated rod-to-rod variation of its SPR wavelength and amplitude (Figure 1). In particular, for an ellipsoid of fixed volume, σ_{ext} is expected to increase with λ_R,[22] in contrast to the experimental observation (Figure 1), probably because of volume fluctuations. This is an important parameter for application, absorption, or field enhancement effects strongly depending not only on the nanoparticle aspect ratio but also on its full size. It can be addressed here since the absolute σ_{ext} value is determined. To more precisely analyze the impact of the nanorod shape and size, we have quantitatively compared our experimental data with that of numerical modeling. Discrete dipole approximation (DDA) or finite element method (FEM) were used, both approaches permitting description of an arbitrary shape nano-object.[23–26]

In the DDA method the studied nano-object is represented as a cubic lattice of N polarizable point dipoles subject to a monochromatic plane wave.[23] The obtained complex linear equations were solved with the code adapted by Draine and Flatau.[27] An important parameter is the number of dipoles mimicking the homogeneous particle to converge the computed physical quantities.[28] As cross-sections are accurate to a few percent for typically $N \approx 10^4$ dipoles, about 4×10^4 dipoles were used here. FEM simulations were performed with the COMSOL Multiphysics software. The electric field around the nanorod was computed using both the weak form and the scattered field formulation.[26] To avoid spurious reflection effects at the simulation zone boundaries, perfectly matched layers (PML) were used as an anisotropic absorber coating the matrix in which the nanorod is embedded.[26] Absorption and scattering cross-sections were computed by integrating the absorbed power over the nanorod volume and the Pointing vector flux over the matrix boundary, respectively. Both mesh and PML parameters were optimized to give excellent agreement with the Mie theory for spherical particles.

In both calculations, the gold nanoparticles were described using the bulk dielectric function (ε) measured by Johnson and Christy,[17] as they yield the best agreement with the measured longitudinal SPR width (Figure 2). Furthermore, using the ε data reported by Palik leads to additional structures that only

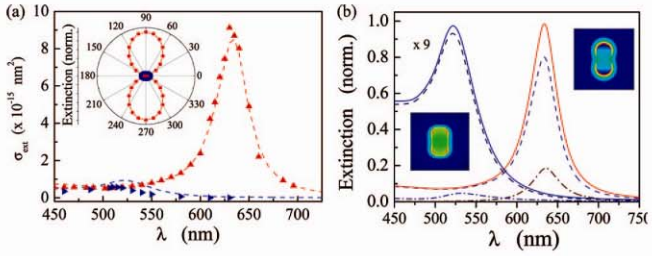

Figure 4. (a) Computed (dashed lines) and measured (triangles) absolute values of the extinction cross section of a single nanorod for two linear polarizations parallel or perpendicular to the main rod axis. A cigar-like shape with an aspect ratio of $\eta \approx 2$ is assumed in the calculation. Inset: polar plot of the computed extinction polarization dependence close to the longitudinal $\lambda = 640$ nm (red dots) and transverse $\lambda = 525$ nm (blue thick line) SPRs. (b) Computed absorption (dashed lines) and scattering (dash-dotted lines) contributions to the optical extinction (full lines) for light polarized perpendicular (blue-shifted resonance, with amplitude multiplied by 9) or along (red-shifted resonance) the main rod axis. The images show the electric field amplitude around the particle for light polarized along the long (short) axis at 640 (525) nm.

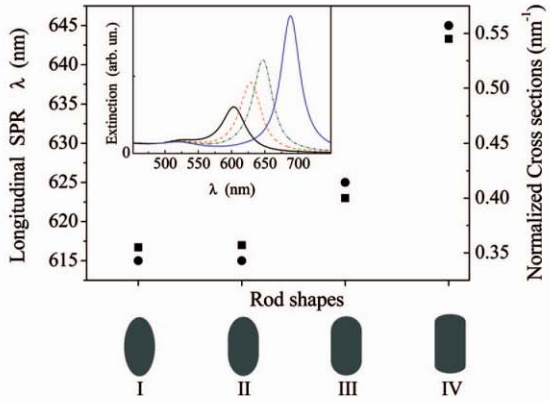

Figure 5. Longitudinal surface plasmon resonance wavelength (dots) and peak extinction cross section per unit nanorod volume (squares) computed for four different gold nanorod shapes. They all correspond to a total rod length of 30 nm and a diameter of 15 nm ($\eta = 2$). Inset: calculated dependence of the extinction spectrum on the nanorod aspect ratio $\eta = 1.75$ (solid, black), 2 (dashed, red), 2.15 (dash-dotted, green), and 2.5 (solid, blue), for a cigar-like shape (III).

reflect the unsmoothness of the measured ε_1 in this range.[29] These new resonances, predicted in the 500−600 nm wavelength range (particularly visible for small aspect ratio nanorods []), are neither observed experimentally nor obtained by using the Johnson and Christy data. Following previous results performed in similar conditions for nanospheres,[10] the dielectric constant of the polymer environment was assumed to be homogeneous with $\varepsilon_m = 2.1$. Because the optical response depends on the nanoparticle shape, and to mimic the actual one observed with TEM (Figure 1), simulations were performed for cigar-like shaped particles formed by a cylinder of length l, diameter D, and capped by hemispheres of radius $D/2$ (Figure 4b and shape III in Figure 5). The remaining parameters in comparing the experimental and simulated extinction cross-sections (σ_{ext}) are thus only l and D, which translate into the particle volume (V) and aspect ratio, $\Gamma = 1 + l/D$. The former essentially sets the amplitude of σ_{ext} and is actually the only parameter in the interband transition region ($\lambda \leq 500$ nm). In contrast, as for a prolate ellipsoid, the latter determines the wavelength and amplitude of the SPRs with a much larger sensitivity for the longitudinal one (Figure 5, inset).

A good reproduction of the measured extinction spectra for different single nanorods is obtained with a cigar-like shape (shape III in Figure 5) as illustrated in Figure 4. The DDA and FEM models yield similar results, with deviation of the computed peak wavelength of less than 5 nm. Both the amplitude and the shape of the polarization-dependent spectra are well-reproduced assuming $D = 25.5$ nm and a full length $L = l + D = 50$ nm (the incident light polarization is polarized either along the short or long axis of the rod, the latter being identified with the 90° direction). In both cases, as expected for relatively small rods, absorption strongly dominates over scattering, with the latter contributing less than 20% and 5% of the extinction at the longitudinal and transverse SPR wavelength, respectively (Figure 4b). For light polarized along the rod axis, excellent reproduction of the spectral position, width, and amplitude of the main resonance is obtained. In particular, the computed fwhm of about 115 meV is in excellent agreement with the estimated one using eq 2 (Figure 2, inset). Furthermore, as observed experimentally (Figure 3), a dipolar type of dependence of σ_{ext} on light polarization is computed at the longitudinal SPR wavelength with a much smaller variation than that of the transverse SPR (Figure 4). Actually, although the amplitude of the interband transition is also well-reproduced away from the SPR, the computed properties of the latter significantly differ from the experimental one; its calculated spectral position is slightly red-shifted and, concomitantly, its amplitude is larger (its broadening due to overlap with the interband transitions being reduced).

This discrepancy can probably be ascribed to the nanorod geometry chosen for the calculation. Although the used shape seems more realistic than the pure cylinder[16,30] or the ellipsoidal model, it contains a degree of arbitrariness. Actually, the shape of the end caps has an important impact on the calculated position and amplitude of the SPR.[31,32] This is illustrated in Figure 5, showing the red-shift and peak amplitude increase of the longitudinal SPR when flattening the nanorod caps, that is, evolving from a prolate ellipsoid (I) to a quasicylinder (IV), keeping the same aspect ratio (the extinction cross-section is normalized to the nanorod volume to show only its shape dependence). This evolution is similar to that induced by an increase of the nanorod aspect ratio (inset of Figure 5 for a cigar-like rod). Actually, as the cap shape differently influence the longitudinal and transverse SPR, it constitutes an additional parameter to better reproduced the experimental data.[31,32] Using the relative extinction cross-section of the two SPR as the relevant criterion, a very good reproduction of the data is obtained, sharpening the nanorod shape. However, although this shape modification yields excellent results, it might compensate for other effects such as slight nanorod asymmetry or local variation of the dielectric constant of the surrounding matrix. More detailed experimental−theoretical comparison requires limiting the number of involved parameters, for instance, by performing electron microscopy and optical measurements on the same nanoparticle.[33,34]

In conclusion, the extinction spectra of single nanorods have been investigated using the spatial modulation technique. In contrast to previous scattering based studies of single nanorods,[8,9] the measured signal yields access to the absorption of a single nanorod. This permits observation of both its longitudinal and transverse surface plasmon resonances. The additional information brought by determination of the absolute value of the extinction cross-section and measurement of the transverse SPR permit detailed comparison with theoretical models. Quantitative agreement with the results of DDA and FEM simulations is obtained by assuming a nanorod with a cigar-like shape. These results open up many possibilities for precise investigation of

detailed shape effects on the optical properties of metal nanoparticles and for their in situ characterization before nonlinear optical studies.[35] Such precise quantitative investigation is also a prerequisite for using single nanoparticle as a calibrated local absorber or local field enhancer.

Acknowledgment. The authors would like to thank Institut Universitaire de France (IUF).

References and Notes

(1) Murphy, C. J.; Sau, T. K.; Gole, A. M.; Orendorff, C. J.; Gao, J.; Gou, L.; Hunyadi, S. E.; Li, T. *J. Phys. Chem. B.* **2005**, *109*, 13857.

(2) Nikoobakht, B.; Wang, Z.; El-Sayed, M. A. *Chem. Phys. Lett.* **2002**, *366*, 17.

(3) Mohamed, M. B.; Volkov, V.; Link, S.; El-Sayed, M. A. *Chem. Phys. Lett.* **2000**, *317*, 51.

(4) McFarland, A. D.; van Duyne, R. P. *Nano Lett.* **2003**, *3*, 1057.

(5) (a) Huang, X; El-Sayed, I. H.; Qian, W.; El-Sayed, M. A. *J. Am. Chem. Soc* **2006**, *128*, 2115. (b) Huff, T. B.; Tong, L.; Zhao, Y.; Hansen, M. H.; Cheng, J.-X.; Wei, A. *Nanomedicine* **2007**, *2*, 125.

(6) Boleininger, J.; Kurz, A.; Reuss, V.; Sönnichsen, C. *Phys. Chem. Chem. Phys.* **2006**, *8*, 3824.

(7) Jiang, X C.; Pileni, M. P *Colloids Surf. A* **2007**, *295* (1−3), 228–232.

(8) Sönnichsen, C.; Franzl, T.; Wilk, T.; von Plessen, G.; Feldmann, J.; Wilson, O.; Mulvaney, P. *Phys. Rev. Lett.* **2002**, *88*, 077402.

(9) Novo, C.; Gomez, D.; Perez-Juste, J.; Zhang, Z.; Petrova, H.; Reismann, M.; Mulvaney, P.; Hartland, G. V. *Phys. Chem. Chem. Phys.* **2006**, *8*, 3540.

(10) Arbouet, A.; Christofilos, D.; Del Fatti, N.; Vallée, F.; Huntzinger, J-R.; Arnaud, L.; Billaud, P.; Broyer, M. *Phys. Rev. Lett.* **2004**, *93*, 127401.

(11) Muskens, O.; Del Fatti, N.; Vallée, F.; Huntzinger, J-R.; Billaud, P.; Broyer, M. *Appl. Phys. Lett.* **2006**, *88*, 063109.

(12) Murphy, C. J.; Jana, N. R. *Adv. Mater.* **2002**, *14*, 80.

(13) Jiang, X. C.; Brioude, A.; Pileni, M. P. *Colloids Surf. A* **2006**, *277*, 201.

(14) El-Sayed, A.-M.; Majied, A.-S. *Colloids Surf. A* **2004**, *246*, 61.

(15) Pérez-Juste, J.; Liz-Marzan, L. M.; Carnie, S.; Chan, D. Y. C.; Mulvanay, P. *Adv. Funct. Mater.* **2004**, *14*, 571.

(16) Brioude, A.; Jiang, X. C.; Pileni, M. P. *J. Phys. Chem B* **2005**, *109*, 13138.

(17) Johnson, P. B.; Christy, R. W. *Phys. Rev. B* **1972**, *6*, 4370.

(18) Kreibig, U.; Vollmer, M.; , *Optical Properties of Metal Clusters*; Springer: Berlin, 1995.

(19) Del Fatti, N.; Vallée, F.; Flytzanis, C.; Hamanaka, Y.; Nakamura, A. *Chem. Phys.* **2000**, *251*, 215.

(20) Voisin, C.; Del Fatti, N.; Christofilos, D.; Vallée, F. *J. Phys. Chem. B* **2001**, *105*, 2264.

(21) *Handbook of Optical Constants of Solids*, Palik, E.D, Ed.;Academic Press: New York, 1985.

(22) Muskens, O.; Christofilos, D.; Del Fatti, N.; Vallée, F. *J. Opt. A* **2006**, *8*, 264.

(23) Purcell, E. M.; Pennypacker, C. R. *Astrophys. J.* **1973**, *186*, 705.

(24) Salzemann, C; Lisiecki, I; Brioude, A; Urban, J; Pileni, M. P. *J. Phys. Chem. B* **2004**, *108* (35), 13242–13248.

(25) Kelly, K. L.; Coronado, E.; Zhao, L. L.; Schatz, G. C. *J. Phys. Chem. B* **2003**, *107*, 668.

(26) Jin, J.; *The Finite Elements Method in Electrodynamics*; Wiley Interscience: New York, 2002.

(27) Draine, B. T.; Flatau, P. J. *J. Opt. Soc. Am. A* **1994**, *11*, 1491.

(28) Sosa, I. O.; Noguez, C.; Barrera, R. G. *J. Phys. Chem. B* **2003**, *107*, 6269.

(29) Blanchard, N. P.; Smith, C.; Martin, D. S.; Hayton, D. J.; Jenkins, T. E.; Weightman, P. *Phys. Status Solidi C* **2003**, *8*, 2931.

(30) Brioude, A.; Pileni, M. P. *J. Phys. Chem B* **2005**, *109*, 23371.

(31) Prescott, S. W.; Mulvanay, P. *J. Appl. Phys.* **2006**, *99*, 123504.

(32) Lee, K-S.; El-Sayed, M. A. *J. Phys. Chem B* **2005**, *109*, 20331.

(33) Hu, M; Chen, J; Marquez, M; Xia, Y; Hartland, G. V *J. Phys. Chem. C* **2007**, *111*, 12558.

(34) Billaud, P.; Marhaba, S.; Cottancin, E.; Arnaud, L.; Bachelier, G.; Bonnet, C.; Del Fatti, N.; Lermé, J.; Vallée, F.; Vialle, J.-L; Broyer, M.; Pellarin, M. J. *Phys. Chem. C* **2008**, *112*, 978.

(35) Muskens, O. L.; Del Fatti, N.; Vallée, F. *Nano Letters* **2006**, *6*, 552.

JP8012865

2.2- Effet de couplage en champ proche dans les dimères

Les effets de forme que nous venons de voir offrent une grande versatilité dans la résonance plasmon, mais une versatilité statique: à chaque particule sa résonance plasmon. Il faut donc changer de particule pour ajuster la réponse à l'application désirée, ce qui, vous en conviendrez, est assez peu pratique. Il existe cependant une deuxième façon de modifier drastiquement les propriétés optiques d'un système: les interactions. Comme nous l'avons discuté précédemment, le champ électrique est fortement localisé au voisinage des particules sur des distances comparables au rayon de courbure de leur surface. Ces effets d'interaction ont donc une très courte portée mais présentent l'immense avantage d'être contrôlables pour peu que l'on maitrise la distance inter-particule. Cette possibilité n'est pas purement théorique même si elle demeure pour le moins ardue. Plusieurs méthodes ont ainsi été proposées comme le collage d'une particule sur une sonde de champ proche, le déplacement des particules à la surface d'un substrat à l'aide d'une pointe AFM ou encore l'utilisation de polymères extensibles sur lesquels reposent les particules. La connaissance précise de l'arrangement des particules devient alors d'une importance capitale pour pouvoir interpréter la réponse optique des systèmes. Dans ce sens, l'équipe "Agrégats et Nanostructures" du LASIM a fait un pas décisif en développant une technique de corrélation entre les mesures sur une particule unique (spectrométrie par modulation spatiale) et la microscopie électronique (TEM). Il est ainsi possible de connaître, pour le même nano-système, la réponse spectrale et la morphologie (2D) ouvrant de nouvelles perspectives sur la compréhension des effets d'interactions.

L'étude que dont je vais discuter ici porte sur des dimères de particules d'or de 100 nm de diamètre. Comme dans le cas des bâtonnets, le système n'est plus isotrope ce qui amène à des réponses très différentes selon que le champ incident est parallèle ou perpendiculaire à l'axe du dimère. La résonance transverse est ici encore assez peu affectée par rapport au cas d'une particule isolée et dépend donc peu de la distance interparticule. Il en est tout autrement pour une excitation le long de l'axe du dimère. Dans ce cas, la résonance (notée "D") se décale vers les grandes longueurs d'ondes et une nouvelle résonance apparaît ("q"). Ce comportement n'est pas sans rappeler les effets retards que l'on peut observer lorsque l'on augmente la taille d'une particule sphérique unique (décalage de la résonance dipolaire vers les grandes longueurs d'onde, apparition de la résonance quadripolaire, et ainsi de suite). Pourtant, son origine est ici bien différente. Tout d'abord, on peut constater que la résonance dipolaire ne s'élargit pas lorsqu'elle se décale et que son amplitude n'est que peu modifiée. Ainsi, contrairement aux effets retards, la résonance dipolaire du dimère ne se couple pas mieux à la

lumière lorsque la distance interparticule diminue: il n'y a pas d'élargissement radiatif. Ensuite, l'apparition de la résonance quadripolaire n'est pas due au fait que la particule devient de plus en plus grosse et que donc les variations du champ se font sur des échelles comparables à la longueur d'onde. C'est tout l'inverse: plus les particules sont proches, plus le champ se localise dans le gap entre les particules créant ce que l'on appelle souvent un point chaud. Ainsi, l'apparition des contributions multipolaires vient de la très forte variation spatiale du champ lorsque l'on fait le tour de la particule. Dans le cas limite juste avant le contact, le champ est tellement localisé qu'il se comporte comme une source ponctuelle excitant de ce fait toutes les harmoniques sphériques, de la même manière qu'une impulsion temporelle excite toutes les fréquences. Selon les distances interparticules, les multipoles excités peuvent entrer en résonance et se coupler efficacement à la lumière, comme c'est le cas de la figure ci-dessous où les pics notés "q" et "q'" correspondent aux résonances quadripolaires.

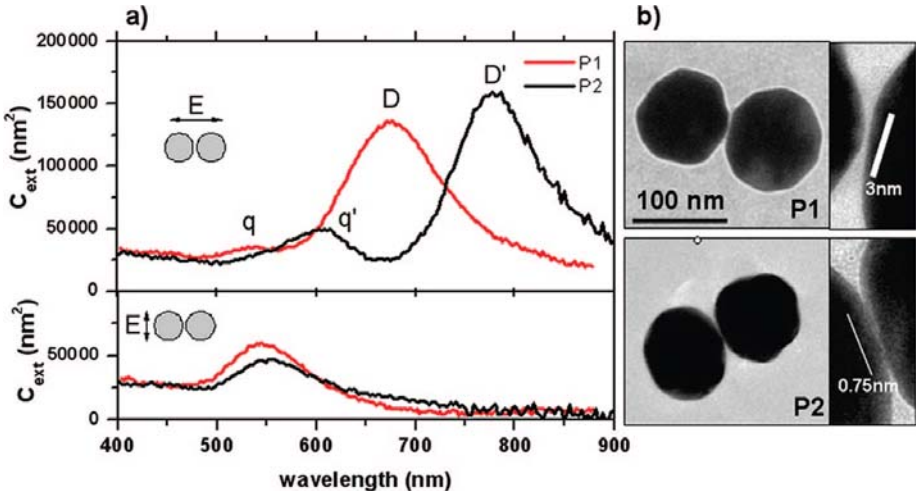

Figure 6: *Spectres d'extinctions obtenus par la méthode de spectrométrie par modulation spatiale sur les deux dimères dont les images TEM sont présentées à droite. Les deux graphes ont étés obtenus pour une excitation le long du dimère (partie supérieure) et perpendiculaire à l'axe du dimère (partie inférieure).*

Ma contribution "directe" à ce travail n'a pas été, soyons honnêtes, déterminante dans la mesure où la plupart des résultats ont put être comparés de manière tout à fait satisfaisante avec des calculs analytiques (théorie de Mie généralisée) développés par Jean Lermé. Cela dit, autant pour lui que pour moi, ce fut l'occasion de comparer, valider et peaufiner nos armes respectives (simulations analytiques d'une part contre simulations numériques avec Comsol d'autre part). Et tant qu'à être totalement honnête, autant dire que pour des systèmes simples

comme des dimères, j'ai fait un peu pâle figure: plusieurs ordres de grandeurs séparent les ressources en mémoire et en temps nécessaire pour faire des simulations numériques!

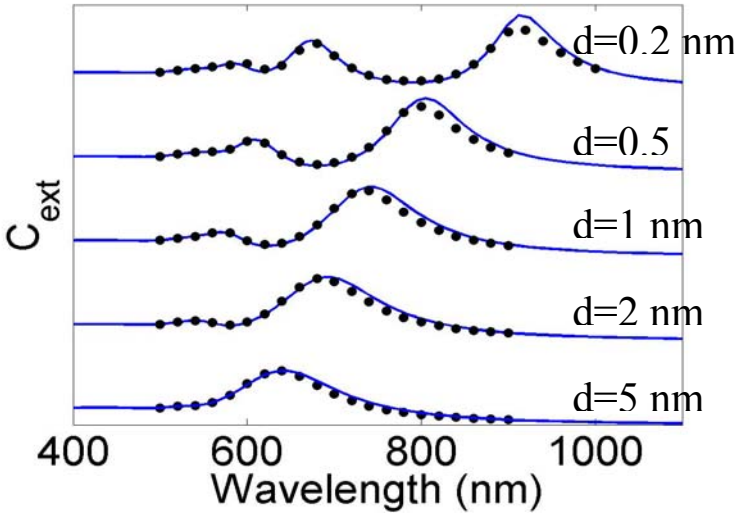

Figure 7: *Comparaison entre les spectres d'extinction obtenus par la théorie de Mie généralisée (analytique) et par simulations par éléments finis (numérique) dans le cas d'un dimère de particules d'or 100 nm de diamètre et dont la distance interparticules est d.*

Là où les choses deviennent souvent passionnantes, c'est quand les résultats expérimentaux ne collent plus à la théorie. C'est précisément le cas pour le dimère "P6" présenté dans la figure 8. A première vue, rien ne le distingue vraiment de son alter égo "P2". Et pourtant il présente des résonances plus étroites et plus nombreuses. Il y a donc là derrière une nouvelle physique qu'il convient d'appréhender: non-localité de la réponse diélectrique? effet tunnel permettant un contact électrique entre les particules? rôle de la géométrie exacte du contact? Beaucoup de questions qu'il faudrait tester plus en détails. Je me suis attelé à étudier l'effet du facétage des particules au voisinage du point de contact avec comme objectif d'évaluer l'influence de la taille des facettes, de leurs orientations et de leur distance. Si un accord qualitatif a été obtenu grâce à la rupture de symétrie induite par la géométrie du contact, le nombre de paramètres ajustables rend à première vue suspicieux tout accord entre les simulations numériques réalisées et les expériences, la physique mise en jeu pouvant être particulièrement riche et le système assez loin d'un modèle idéal... Quoi qu'il en soit, la corrélation à des images de microscopie électronique apporte ainsi une information extrêmement précieuse permettant de contraindre le domaine accessible de l'espace des configurations, point particulièrement critique quand un spectre calculé numériquement pour une géométrie donnée peut prendre plusieurs jours...

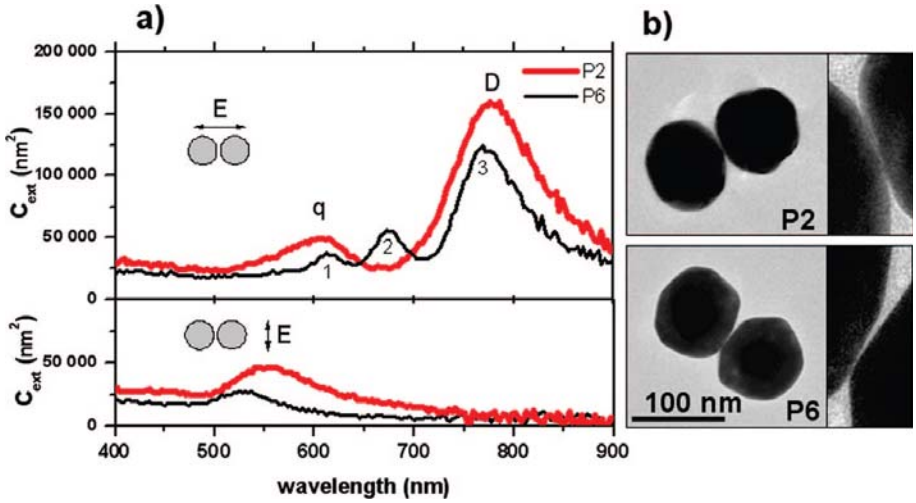

Figure 8: *Spectres d'extinctions obtenus par la méthode de spectrométrie par modulation spatiale sur les deux dimères dont les images TEM sont présentées à droite. Les deux graphes ont étés obtenus pour une excitation le long du dimère (partie supérieure) et perpendiculaire à l'axe du dimère (partie inférieure).*

Surface Plasmon Resonance of Single Gold Nanodimers near the Conductive Contact Limit

Salem Marhaba, Guillaume Bachelier, Christophe Bonnet, Michel Broyer, Emmanuel Cottancin, Nadia Grillet, Jean Lermé, Jean-Louis Vialle, and Michel Pellarin*

Université de Lyon, Université Lyon 1, CNRS, Laboratoire de Spectrométrie Ionique et Moléculaire (UMR 5579) 43, Bld du 11 Novembre 1918, 69622 Villeurbanne Cedex, France

Received: November 26, 2008; Revised Manuscript Received: January 21, 2009

We have studied the spectral response of individual pairs of gold nanoparticles chemically synthesized and stabilized on a transparent thin film. Very thin interspacing distances are explored by taking advantage of a residual layer of surfactant molecules at the metal surface. Absolute extinction cross section measurements by the spatial modulation spectroscopy technique are correlated to the corresponding high magnification images independently obtained from transmission electron microscopy. The signature of a transition from isolated to conductively coupled particles is evidenced in the optical spectra and is discussed in relation with their morphology. The strength of the electromagnetic coupling is controlled not only by their spacing but also by the shape of their opposite surfaces in the gap region.

1. Introduction

Noble metal nanoparticles have been intensively studied for their unique optical properties from both experimental and theoretical points of view.[1] The excitation of their localized surface plasmon (LSP) resonance by incident electromagnetic radiation is responsible for a very large field enhancement at their surface.[2,3] This singular and spatially localized optical response has proven to be of main interest for specific applications such as high sensitivity detection and spectroscopy of molecules suitably attached to the nanoparticle surface (fluorescence,[4] Raman scattering,[5] biochemical sensing, etc.[6,7]).

For a single nanoparticle, the spectral features of the LSP are known to closely depend on its size, shape, and dielectric environment.[1,8] More recent studies have shown that interparticle coupling effects can be used for tailoring LSP resonances with even more flexibility. This was clearly evidenced for nanoparticle pairs which are the most basic systems of such interacting objects. In this field, most of the experimental studies consisted of measuring the scattering spectra from periodic gratings of identical nanoparticle pairs (mainly disks) designed by electron beam lithography.[9−12] This technique ensures a good control of the lattice constant, the particle size, and the interparticle distance. For reasons of symmetry, a pair of isotropic particles will experience two different excitation schemes depending on whether the incident radiation is linearly polarized along (longitudinal excitation) or perpendicular (transverse excitation) to the interparticle axis.

Roughly, the optical response of a pair deviates from the mere sum of the individual particle contributions as soon as the surface-to-surface distance (d) becomes of the order of their lateral size (radius R). For a transverse excitation, the optical spectrum is not very sensitive to d (weak blue-shift[10,11]) and the plasmon resonance of the pair remains close to the LSP of each particle. On the contrary, in the case of a longitudinal excitation, the LSP resonance is strongly shifted toward long wavelengths as d is reduced. This shift discloses a universal scaling as a function of the dimensionless parameter d/R and increases almost exponentially when the latter decreases.[13] For very small values of d/R, the red-shifted resonance is attenuated to the benefit of a second one at higher energies which is assigned to the hybridization of the main dipole mode with a higher-order multipole mode.[9,12] Whatever the experimental context, these observations are quite general and are corroborated by several theoretical studies considering the ideal case of spherical particle dimers,[14−17] or even more complex geometries.[3,18−22]

On the other hand, the regime where the particles are no longer separated but conductively coupled has also been investigated. The particle pairs then adopt a "dumbbell" shape with various degrees of overlap ($d' < 0$) and consequently various transversal sizes of the neck region (contact area). For an incident polarization along the pair axis, the optical spectrum is dominated by a long wavelength resonance associated with the dipolar nature of the electronic excitation across the pair as a whole.[9,12] It is blue-shifted with increasing overlap, as the pair is more and more compact and the "peanutlike" shape becomes spherical. This is consistent with the expected behavior of the longitudinal LSP resonance when the aspect ratio of elongated and axially symmetric particles is increasing (ellipsoidal particles, for instance).[1] When the overlap is reduced and the neck region around the contact zone (antiwedge) is more clearly outlined, this resonance is repelled in the infrared, and a second resonance grows at smaller wavelengths. As in the case of nearly touching particles, the latter is attributed to the development of a higher-order plasmon mode in relation with the complex spatial distribution of local electric field in the confined interparticle region.

The transition at the touching limit, when the conductive contact becomes effective, is an interesting and still unsolved issue. This transition is highly singular and difficult to explore in both experiment and theory. Various numerical procedures for determining the electromagnetic field distribution (discrete dipole approximation,[23] boundary element method,[24] multiple scattering approach in the Mie Theory, etc.[25,26]) come up against convergence problems as the free space between particles is vanishing. On the other hand, experiments on particle pairs designed by electron lithography give a great deal of latitude

* To whom correspondence should be addressed. E-mail: pellarin@lasim.univ-lyon1.fr.

10.1021/jp810405y CCC: $40.75
Published on Web 02/25/2009

for defining the center-to-center distance of paired particles. This technique is quite useful to investigate the contact and noncontact regimes on a large scale, but it is not the best suited to achieve very small interparticle spacings (less than a few nanometers), not only because of the limited engraving resolution but also because of a possible and spontaneous bridging driven by dispersion forces combined with surface atomic diffusion. Nevertheless, it is possible to get over this difficulty by passivating the particle surface with a thin insulating layer that will act as a mechanical spacer. This is illustrated in the study of Tamaru et al.[27] on pairs of silver particles extracted from a colloidal suspension and protected by organic surfactants.

In any case, a control of the pair morphology and an accurate measurement of the interparticle spacing are both necessary. In most of the previous experiments, this is achieved by means of scanning electron microscopy, for which resolution is not always sufficient to investigate details on the nanometer scale. In this study, we have tried to overcome some of these limitations by combining high sensitivity extinction spectroscopy and imaging with transmission electron microscopy (TEM) in order to investigate the regime of near contact between gold nanoparticles. The absolute far field extinction is measured on individual and isolated nanoparticle pairs. Their geometrical structure can be inferred from TEM images that are helpful inputs for appropriate numerical calculations and a further comparison with experiment.

2. Experimental Methods

Gold nanoparticles from an aqueous colloidal suspension (100 nm mean diameter, British Biocell International) are dispersed on suitable substrates by means of the spin coating technique. The samples are designed for a combined study by optical spectroscopy and TEM. They consist of nickel TEM grids coated with a thin film (30 nm) made of a Formvar resin. The latter is transparent in the visible range (refractive index of about 1.5) and is resistant to electron irradiation in TEM.

The absolute extinction cross section of single gold nanoparticle pairs is measured by the spatial modulation spectroscopy (SMS) technique which was described in detail in previous papers.[28−30] Its basic principle consists of irradiating a supported particle by the light beam provided by a quartz tungsten halogen (QTH) lamp which is focused at the diffraction limit by a high aperture reflecting objective. The transmitted light is dispersed via a monochromator and measured by using a photomultiplier device. The sample is mounted on a high resolution *XY* piezoelectric stage. A sine displacement is applied to one axis of the stage so as a given particle periodically enters in and out the light beam (frequency *f*). The subsequent modulation of the transmitted light is detected by using a lock-in amplifier at frequency *f* (or 2*f*) which greatly improves the signal-to-noise ratio. The knowledge of the spatial oscillation amplitude and a previous characterization of the beam spot profile in the focal plane allow us to convert the ratio of the lock-in signal to the DC transmitted light signal into an absolute extinction cross section (absorption and scattering). The small fraction (5−10%) of the scattered light directed in the acceptance angle of the collecting objective does not blur this measurement significantly. The solution is diluted so that the average particle density on the substrate is less than 1 μm^{-2} and only one particle is irradiated by the focused light beam at any time. Transmission electron microscopy shows that most of the supported objects are single nanoparticles but a small fraction of them can be made of several agglomerated nanoparticles, essentially in the form of pairs.

Experiments are carried out in two successive stages: optical spectroscopy and TEM observation. The nanoparticles are first detected and localized on a 100 × 100 μm^2 area by recording a map of the SMS signal at a fixed wavelength chosen to coincide with the LSP of isolated gold nanoparticles (about 530 nm). When the second harmonic (2*f*) of the modulated signal is recorded by the lock-in amplifier, which will be the choice made in the following, it reaches a relative maximum (bright spot) when the average position of a particle on the oscillating sample coincides with the center of the focused light beam. For some selected bright spots, the extinction spectrum is recorded from 400 to 900 nm. Measurements are performed with linearly polarized light with the help of a rotating polarizing prism. In conventional experiments of this kind, the natural choice consists of selecting the polarization of the incident beam by placing the polarizing device upstream from the sample. Unfortunately, in this configuration and because of a residual refraction effect induced by the polarizer, a weak angular deviation of the collimated beam will result in an appreciable shift of the focused spot on the sample surface. Since the SMS technique requires a perfect superimposition of the nanoparticle with the center of the light spot (detection at frequency 2*f*, for instance), the sample position has to be carefully adjusted so as to offset the spot shifts for each selected angular position of the polarizing prism. For experimental convenience and to ensure that the nanoparticles were subjected to accurate and reproducible illumination conditions for any light polarization direction, we preferred placing the polarizing prism downstream from the sample, at the entrance of the spectrometer. It must be remarked that both configurations are not rigorously equivalent with regard to optical measurements. Nevertheless, because the white light delivered by our QTH lamp is basically temporally incoherent and integration times are quite large (typically 300 ms), it can be theoretically shown that the total extinction cross section measurements are independent of the exact location of the polarizer. Possible differences may come from scattering cross section measurements. More precisely, these differences are only expected when (i) the polarization distribution of the incident beam is not homogeneous and (ii) the nanoparticle is not symmetric with respect to the light propagation axis. Since only a weak part of the scattered light is recollected in our experiment as evoked before, this effect can be neglected here. This was actually verified in additional experiments where extinction spectra recorded on the whole spectral range do not disclose significant differences depending on whether the polarizer is located before or after the sample.

After optical studies, the samples are analyzed by TEM, and particles previously studied with the SMS technique are imaged at magnifications up to ×110 000. Locating particles with TEM is made easier by the use of 300 nm polystyrene balls that are added to the colloidal solution before deposition and that act as markers for both experiments.[30] The TEM analysis gives access not only to the shape of the particle, projected in the *XY* plane, but also to the orientation of the dimer axis relative to the direction of light polarization in SMS measurements. The optical spectrum of a given nano-object may be significantly different depending on whether it is recorded before or after TEM observations. The supporting film is strongly heated by the electron beam and may be altered in the close vicinity of the nanoparticle. This may induce a drastic modification of the extinction spectrum, since the dielectric properties of the local environment are known to be of main importance in this respect.[1] As a consequence, TEM measurements have been systematically performed after optical studies.

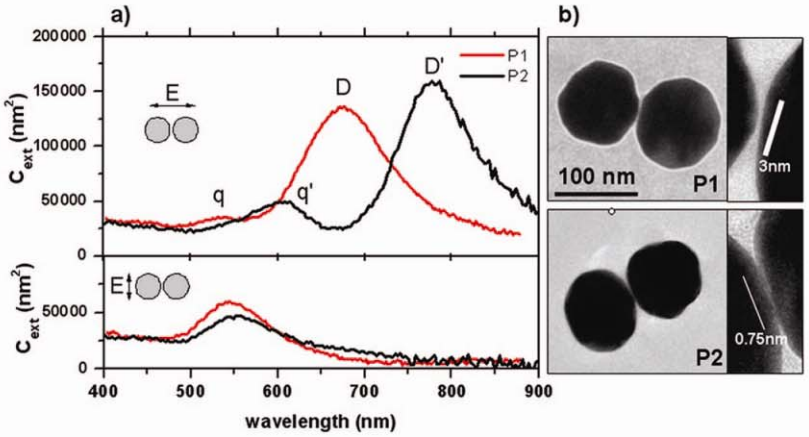

Figure 1. (a) Absolute extinction cross sections measured on gold nanoparticle pairs (red lines, P1; black lines, P2). The upper spectra correspond to a longitudinal excitation (light linearly polarized along the interparticle axis), and the lower spectra to a transverse excitation. The resonances of "dipolar" and "quadrupolar" characters are labeled by letters D (D′) and q (q′), respectively. (b) TEM images of particle pairs P1 and P2. White bars with thicknesses 3 and 0.75 nm for P1 and P2, respectively, are drawn at the scale of enlarged views of the interparticle regions.

3. Results and Discussion

3.1. Interparticle Distance Effects on the Optical Response: Experimental Observations. Figure 1 shows the absolute extinction spectra of two gold nanoparticle pairs (P1 and P2) with their corresponding TEM images. The spectra are recorded for two orthogonal directions of the linearly polarized light, adjusted so as to obtain a maximum difference in the spectral location of the LSP resonances. In view of the TEM images oriented relative to the frame of the optical setup, both directions are proven to correspond to the long and short symmetry axes of each pair, with an accuracy of ±3°. The extinction spectra obtained for an electric field along the interparticle axis (longitudinal excitation) are reported at the top of the figure and those for the direction normal to this axis (transverse excitation) at the bottom. For the transverse excitation, the extinction spectra of P1 and P2 pairs are almost proportional to the extinction spectrum of a single isolated gold nanoparticle, with comparable position and width of the resonance. However, it should be remarked that the optical response of a pair is not exactly the mere superimposition of the optical responses of two noninteracting particles, since the overall signal is less than twice as large. Relative to a single particle spectrum, the enhancement is only of the order of 1.2−1.4 here. On the other hand, the spectra corresponding to a longitudinal excitation exhibit both a very strong enhancement and a red-shift of the plasmon resonance as compared to the single particle case. A small additional peak (q,q′) is also detected in the shorter wavelength side of the spectral range. It is all the more pronounced and red-shifted that the shift of the main peak (D, D′) itself is large.

It is well-known that an excitation along the long axis of elongated single particles also induces a red-shift of the plasmon resonance.[2] For instance, Figure 2 gives a comparison between the extinction spectrum of the P2 pair and the calculated spectrum of a cylinder with hemispherical end caps having a lateral size 100 nm and an aspect ratio of 2, in the case of a longitudinal excitation. Finite element method (FEM) calculations are performed with the COMSOL Multiphysics package. The effective index of the surrounding medium is chosen to be $n = 1.15$, and the gold dielectric function is taken from Palik.[31] Quite similar results would be obtained with dielectric function data from Johnson and Christy.[32]

Clearly, the nanoparticle pair discloses a specific optical response as compared to a single object with a similar

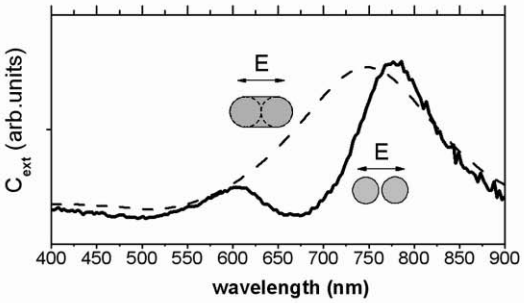

Figure 2. Experimental extinction spectrum (full line) of the nanoparticle pair P2 and calculated extinction spectrum (dotted line) of a hemispherical end-capped rod (100 nm wide, 200 nm long). The spectra are not drawn on the same vertical scale.

deformation. The spectra are quite different even though the aspect ratios are the same. The extinction spectrum of the nanorod discloses only one resonance. It is centered about 750 nm and is above all much wider than the resonance of the particle pair. Therefore, the details of the extinction spectra in Figure 1 require an alternative explanation.

3.2. Interparticle Distance Effects on the Optical Response: Qualitative Description. The red-shift of the LSP resonance of close but nontouching supported nanoparticle pairs (spheres or parallel cylinders) was previously observed and discussed in the literature.[9−13,27,33−35] The well-known "dipolar coupling" model can give a first and intuitive description of this effect.[1,10,13] In the quasi-static limit, the particle radius is assumed to be small compared with the wavelength (λ) of the incident electromagnetic (EM) field. The LSP resonance is related to the collective oscillation of the conduction electrons and is then of dipolar nature. Each particle is not merely polarized by the electric field of the incident light but also feels the field from the oscillating dipole induced on the other particle. Because of this feedback coupling, the particles no longer respond as individual independent harmonic oscillators and the LSP frequency is modified. It is found red-shifted in the case of a longitudinal excitation where both dipoles oscillate in phase along the interparticle axis. As observed experimentally, this shift is all the more pronounced that the interparticle spacing (d) is small, since the dipolar coupling scales as D^{-3}, where D is the center-to-center distance ($D = 2R + d \cong d$ when $d \gg R$). In the case of a transverse excitation, the LSP resonance will shift in the opposite direction and with a lower magnitude because the dipoles are now oriented perpendicularly to the

interparticle axis. This dipolar coupling model is valid for interparticle distances sufficiently large to assume that the dipolar field created by a particle is spatially uniform on its neighbor ($d \gg R$). If it is not the case, the particles cannot be considered as pointlike dipoles. Highly nonsymmetric surface charge distributions will actually develop in each of them, in response to the incident excitation and to their mutual electrostatic interaction.

The birth of new collective excitation modes for the entire system underlies the excitation of higher multipolar modes in the optical response as it can be guessed in the optical spectra shown in Figure 1. To investigate this strong coupling regime, Prodan et al. have proposed a general formalism devoted to complex metallic nanostructures and based on the concept of an "hybridization" of the free plasmons of their elementary subunits.[36] It was later applied to describe, within a simple "molecular picture," the collective modes of excitation in small coupled nanoparticle dimers.[37] Although it is suitable only for systems small compared with the wavelengths of interest (quasi-static limit), it seems worthwhile discussing our experimental results in the frame of this approach that will be outlined in the following.

Generally speaking, when a homogeneous conducting sphere is excited by any external EM wave, its surface charge density discloses a complex spatial structure at any time and can always be expressed in the form of a multipolar expansion over spherical harmonics $Y_{l,m}$. Each individual term of this expansion (with dipolar, quadrupolar, hexapolar symmetry) is associated with a specific eigen mode of electron oscillation (i.e., plasmon) and a corresponding value of the surface plasmon energy that scales as $\omega_l = \omega_B[l/(2l + 1]^{1/2}$, where ω_B is the bulk plasmon energy and l (=1, 2,...) is the order of the l-pole term. A single sphere embedded in the EM field can then be considered as a giant atom with discrete energy levels. Their selective excitation (or population) is closely related to the multipolar expansion of the EM field itself. For instance, in the quasi-static limit ($R \ll \lambda$), only the dipolar plasmon ($l = 1$) will be populated. In the case of a pair of close particles and because of the mutual electrostatic interaction between their respective surface charge densities, the whole energy diagram will be formally modified in a very similar way as for the bonding and antibonding states of a diatomic molecule. For reasons of symmetry, the "molecular level spectrum" will be decoupled with respect to the azimuthal quantum number m (the polar axis is chosen as the interparticle axis). Assuming in the following that the incident EM field is a linearly polarized plane wave, only $m = 0$ or $m = \pm 1$ values should be considered in the respective cases of a longitudinal or a transverse electric field excitation. It must be noted that if the plane wave structure is only approached in the present study, owing to the very specific geometry of the strongly focused light beam in the SMS setup, it can be however considered as a reliable approximation.[38,39]

Let us first consider a longitudinal excitation ($m = 0$). If we ignore higher plasmon modes for simplicity, the electrostatic coupling between the dipolar plasmon charge distributions ($l = 1$, $m = 0$) of each sphere will lift the degeneracy, giving rise to two new "dipolar" plasmon modes for the pair, one of lower energy (bonding level) and the second of higher energy (antibonding level). Furthermore, the bonding level corresponds to two parallel dipoles oscillating in phase along the interparticle axis (referred as the symmetric field configuration by Nordlander et al.[37]), and the antibonding level corresponds to two antiparallel dipoles oscillating out of phase (antisymmetric field configuration). For identical spheres, the latter cannot be directly excited by the electric field of a long-wavelength EM plane wave because of a net zero dipole. The level splitting and therefore the energy downshift of the only "active" dipolar bonding mode (symmetric fields and large net dipole) will be all the more important that the interparticle distance is small and the coupling is strong. This picture accounts for the main experimental feature (peaks D and D′ in Figure 1).

Similar analyses and conclusions apply to the interaction between higher plasmon modes of the same order ($l \geq 2$, $m = 0$). In the quasi-static limit, these modes can hardly be excited if the particles are far apart and almost isolated. In this case, the dipolar mode ($l = 1$) is the only populated and the corresponding dipolar LSP resonance dominates the extinction spectrum.[2] When the interparticle distance is much more reduced, the strong mutual electrostatic interaction will be responsible for a coupling between modes with different orders l. Through this hybridization scheme, the oscillator strength of the bonding dipolar mode ($l = 1$) is transferred to higher-order bonding modes in the coupled system, authorizing the emergence of "hybrid" resonances connected to charge distributions of different symmetries. The number of l-terms contributing to each of these resonances is all the larger, as the coupling is strong. Because of the dilution of the dipole plasmon oscillator strength, further reduction of the interparticle gap will result in the sequential birth of resonances of increasing order to the detriment of low-order ones and in their progressive red-shift (referring to the "molecular diagram" picture). The first hybridization step involves the dipolar and quadrupolar modes and explains the presence of the high energy peaks q and q′ in Figure 1. As expected from the relative particle spacings, q′ is red-shifted as compared to q and is also more intense. The red-shift of the "dipolar" plasmon energy discussed before (D and D′ peaks) is certainly also enhanced through hybridization, since the low lying bonding level ($l = 1$, $m = 0$) is repelled by the higher energy bonding levels ($l \geq 2$, $m = 0$).

Finally, considering a transverse excitation ($|m| = 1$), it can be shown that the energy diagrams and their dependence with the interparticle distance are very similar to those corresponding to a longitudinal excitation. The mere difference is that the only states that can be efficiently excited by a structureless EM field (plane wave) are now the antibonding ones (symmetric modes relative to the in-phase oscillation of the surface charges perpendicularly to the interparticle axis). Within the present "hybridization" formalism, they are found to be only weakly shifted to high energies when the gap is decreasing. This smooth evolution of the optical response for the $|m| = 1$ symmetry is related to the absence of a significant accumulation of surface charges in the interparticle region. However, we experimentally observe a slight red-shift instead (see Figure 1). This discrepancy may be explained by a quantitative breakdown of the "hybridization approach" predictions (the quasi-static regime is assumed) when dealing with large particles. A non-negligible shift of the LSP resonances induced by slight differences in the particle sizes and shapes may also mask the weak predicted effects.

3.3. Generalized Mie Theory Calculations and Quantitative Trends. Despite that the incident EM field (plane wave) is quasi homogeneous over the whole system, the "plasmon-hybridization" model clearly points out that, in strongly coupled systems, the complex near field created by each polarized particle is strongly inhomogeneous and contributes noticeably to the effective near field experienced by the other one (birth of high-order plasmon resonances for instance). A complex optical response is thus expected for nearly touching particle

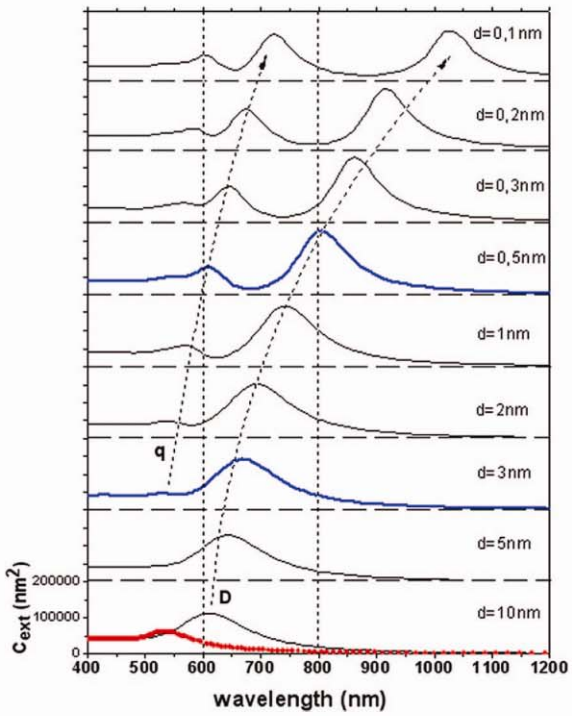

Figure 3. Extinction spectra (longitudinal excitation) calculated in the generalized Mie theory for a pair of gold spheres ($R = 50$ nm) as a function of the surface-to-surface distance d (the refractive index of the surrounding medium is $n = 1.15$). The absolute scale and a spectrum calculated for a transverse excitation are given in the bottom (red dotted line). For guiding the eye, the curved arrows show the red-shift of resonances with dipolar (D) and quadrupolar (q) character. Spectra for $d = 0.5$ and 3 nm are drawn with thicker blue lines.

pairs. The previous description is useful to account for plasmon energy shifts, but more information can be gained from a simulation of the full optical spectra, considering the interparticle distance d as an adjustable parameter. In the case of spherical particles, detailed calculations using the boundary elements method have been performed by Romero et al.[14] in the case of identical gold spheres (R=60 nm) embedded in vacuum and for interparticle distances in the range $5 \times 10^{-4} < d/R < 1$. For a direct comparison with our experimental results, absolute extinction cross sections are calculated here for gold spheres of lower radius ($R = 50$ nm) embedded in an effective medium of refractive index $n = 1.15$ chosen to mimic the presence of the supporting film.[30] We use a multiple scattering approach based on the generalized Mie theory, [25,26,40] and the gold dielectric function is taken from Johnson and Christy.[32] The results are displayed in Figure 3 for interparticle distances $d =$ 10 nm down to 0.1 nm, the smallest value for which convergence can be reached in the calculations. The spectra are quite similar to those presented in Figure 1a from Romero et al.[14] for comparable d/R ratios. In agreement with the preceding discussion based on the "plasmon hybridization" approach, the spectra obtained for a transverse excitation are found to be almost independent of the interparticle spacing d. One of them is shown as a reference in the bottom of Figure 3 for $d = 10$ nm. A comparison with the extinction spectrum of a single nanoparticle ($R = 50$ nm) would show that the spectra of particle pairs only differ in their overall intensity. The corresponding cross sections are about 1.4−1.5 times larger, while a factor 2 would be expected if the spheres were not interacting. This is in line with the experimental results discussed from Figure 1a in the case of a transverse excitation, indicating that the particle coupling mainly results in a decrease in the net oscillator strength. Focusing now on the case of a longitudinal excitation, the extinction cross section for $d = 10$ nm (bottom of Figure 3) is larger than that of the reference spectrum (transverse excitation) and the dipolar mode is clearly shifted to longer wavelengths. This shift is increasing with decreasing distance d. On the other hand, an extra peak (q) appears on the short wavelength side from $d \cong 3$ nm, red-shifts, and grows steadily as d is reduced. This is exactly what is predicted from the "hybridization" scheme, with this resonance being of "quadrupolar" character. For smaller interparticle distances ($d < 0.5$ nm), the same behavior can be noticed for a third resonance that develops at an even higher energy. As discussed previously, the "l-polar" character of these resonances is all the more approximate that the hybridization is strong (small d values). The intensity of the D peak begins to decrease below $d = 0.3$ nm, which is actually the signature of a redistribution of its oscillator strength into higher plasmon modes.

The experimental spectra in Figure 1a can be fully understood from a comparison with the calculations displayed in Figure 3. The extinction spectrum of the P1 pair is nicely reproduced for an interparticle spacing of 3 nm, regarding the position, the absolute intensity, as well as the width of the resonance. In the case of the P2 pair, similar conclusions can be drawn with an intermediate spacing, between 0.5 and 1 nm (about 0.75 nm). To check this correlation, we have indicated spacing marks of 3 and 0.75 nm wide at the scale of the enlarged TEM views of the interparticle regions for each pair (see Figure 1b). There is a good agreement for P1. It is also correct for P2 despite the poor contrast of the TEM image for such a small spacing which is certainly weakened by the presence of surfactant molecules at the particle surface.

3.4. Nearly Touching Particles: The Role of Surfactants. At this point, one may discuss the possibility of detecting pairs where the gold nanoparticles may be in a closer proximity than those labeled P1 and P2. In general, the probed particle pairs have very similar extinction spectra. As an illustration, Figure 4 presents extinction spectra for four selected dimers including P2 as a reference.

Surprisingly, for all the particle pairs under consideration, the red-shifted dipolar plasmon is located at about 800 nm and the quadrupolar resonance is close to 600 nm. Regarding the deviation of the particle pair morphologies from the ideal case assumed in numerical calculations (two identical spheres), the differences that can be noticed in the peak positions, intensities, and widths are actually not very significant. It is worthwhile emphasizing that Transmission electron microscopy gives only access to the projected shape of the particles. Most of them are more or less faceted and clearly deviate from perfect spheres. Moreover, the projected diameter distribution of the particles presents a slight dispersion about the average value of 100 nm. For instance, P3 consists of a quasi-spherical particle and a second one shaped in the form of a truncated prism. This singularity explains why the "transverse" plasmon for P3 is broader than that for the other particle pairs, with the LSP of such an object being known to be shifted to longer wavelengths as compared to a sphere with the same volume.[8,41] It is also expected that, for nonspherical particles, the optical spectrum will be sensitive not only to the shortest distance between both surfaces but also to the shape (curvature) of the latter. This point will be discussed below.

Owing to the strong dependence of the LSP shift on the interparticle gap d, obtaining a large number of similar spectra is an indication that d should be almost the same in every case. This can be explained by the presence of a mechanical and

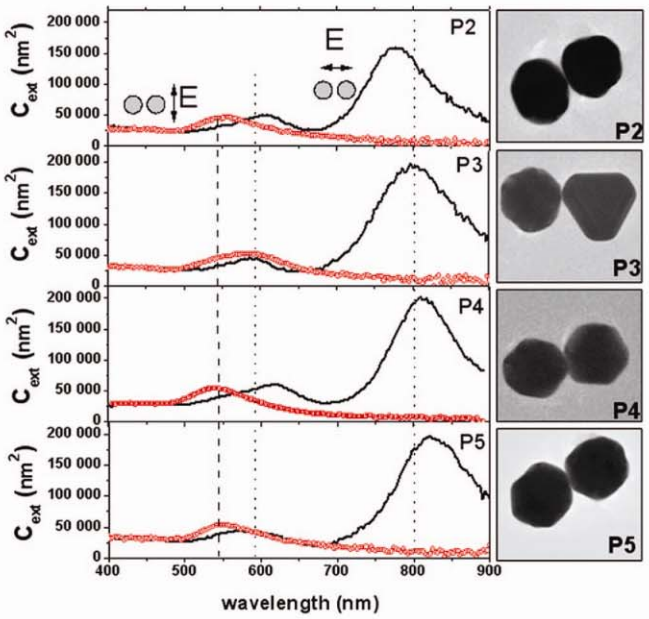

Figure 4. Extinction spectra of four gold nanoparticle pairs recorded with linearly polarized light and their corresponding TEM images (black solid lines, longitudinal excitation; red circles, transverse excitation). The vertical lines are drawn for guiding the eye and correspond to the maximum of the LSP resonance of a single particle (dashed) and the average locations of the dipolar and "quadrupolar-like" modes for a longitudinal excitation (dotted).

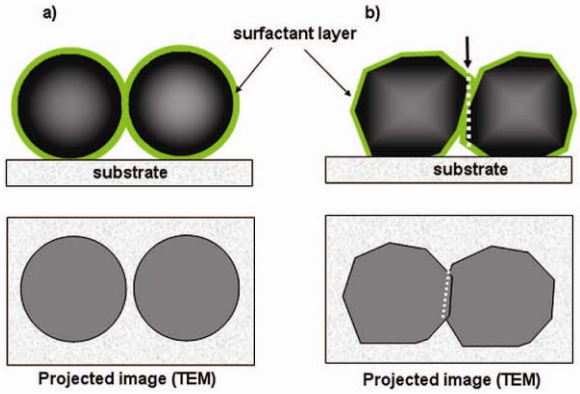

Figure 5. (a) Schematic view of a pair of spherical nanoparticles supported on a substrate and covered with a shell of surfactant molecules (not to scale). The bottom picture shows the projected TEM image of such a pair (the low density molecular shell is not detected). (b) Schematic view of a pair of faceted and deformed nanoparticles supported on a substrate. Just as in (a), they are not in metallic contact but their projected images can overlap because of the shape and orientation of their facing surfaces.

electrically insulating barrier of fixed width that prevents a further approach of the particles. In our experiments, a molecular layer of surfactant molecules used in the chemical synthesis may actually wet the particle surface (see Figure 5a). The width of this layer is probably governed by the size of the molecular species. In the absence of information about the nature of surfactants or stabilizing molecules in the commercial colloidal solution used in this work, the hypothesis of a minimum layer thickness of the order of 0.4 nm (≅0.75/2 nm) is reasonable. Moreover, numerical simulations based on classical electromagnetism assume perfectly metallic spheres and a sharp metal−air interface. The conduction electrons are thus supposed to be strictly confined within the geometric volume, while more elaborated modeling near the surface should take into account the spill-out of the electron cloud. It is known to be about 0.5−1 Å from the sharp geometrical interface, at half-maximum of the electron density.[42] As a consequence, the effective interparticle spacing deduced from a comparison between theory and experiment (≅7.5 Å) may be somewhat underestimated and the thickness of the surfactant layer slightly larger than 4 Å. For P2 and P3 pairs, high magnification TEM images are consistent with the presence of an interparticle spacing of the order of 0.5−1 nm. On the other hand, although it is hardly detected in the TEM images of P4 and P5 pairs, a free space between the particles cannot be totally ruled out. The particles are clearly faceted, which may authorize, even in the absence of contact, a slight overlap of their TEM images projected on the substrate plane as it is illustrated in Figure 5b. Moreover, a neat metallic contact and the onset of particle sintering would result in a vanishing contrast of the TEM images in the neck region which is unlikely, since the particle contours can be still distinguished (see P4 in Figure 4, for instance).

3.5. The Special Case of Nearly Contacting Particles. From the previous discussion, it seems that most of the gold particles are paired without contact and with a minimum value of the surface-to-surface distance d, even if some of them can be more widely separated as P1 in Figure 1. Their extinction spectra are actually consistent with theoretical predictions introducing a positive d value (i.e., nonoverlapping particles). However, we have detected a particle pair (P6) with a totally different extinction spectrum while its TEM image does not show, at first glance, any clear differences with the other ones. This specific spectrum is compared to the reference spectrum of the P2 pair in Figure 6. For the transverse excitation, the resonance is weaker and blue-shifted. The major differences between P6 and P2 appear in the case of the longitudinal excitation. Three resonances are now detected in the 400−900 nm range. The more intense resonance (3) is located in the vicinity of the "dipole" resonance of the P2 pair but is weaker and less broad. Resonances (1) and (2) at higher energies are particularly narrow.

If one refers to the calculations of Romero et al.[14] for nontouching particles, such a spectral pattern (relative peak positions and peak widths) can first be reproduced theoretically, at least on qualitative grounds, for a very small interparticle distance which can be estimated to be of the order of 0.25 Å ($d/R \cong 0.0005$ in Figure 1a from Romero et al.[14]). In this case, the resonances (1), (2), and (3) would originate from the hybridization of high-order plasmon modes with the dipolar one as explained before. For such a small interparticle distance, the major contribution with a "dipolar" character would be almost rubbed out and repelled farther in the long wavelength range (infrared), outside the experimental window. Even if the insulating molecular shell around both particles in the P6 pair is partially missing or thinner than in other pairs (P2−P5), the hypothesis of such a close proximity is physically unrealistic since the necessary interparticle spacing would be found smaller than the electron spill-out tail and much smaller than the atomic interplane distances in bulk gold.[43]

The second configuration explored by Romero et al.[14] corresponds to the case where the spheres are in metallic contact or even overlap over a small distance $d' < 0$. It is a well established fact that the possibility of electron sharing and transfer from one particle to the other drastically changes the physical nature of the collective excitations induced by an incident radiation. In the case where particles are separated, electron oscillations are confined into each of them because charge neutrality has to be fulfilled in each particle independently. When the particles are in electric contact, a new mode

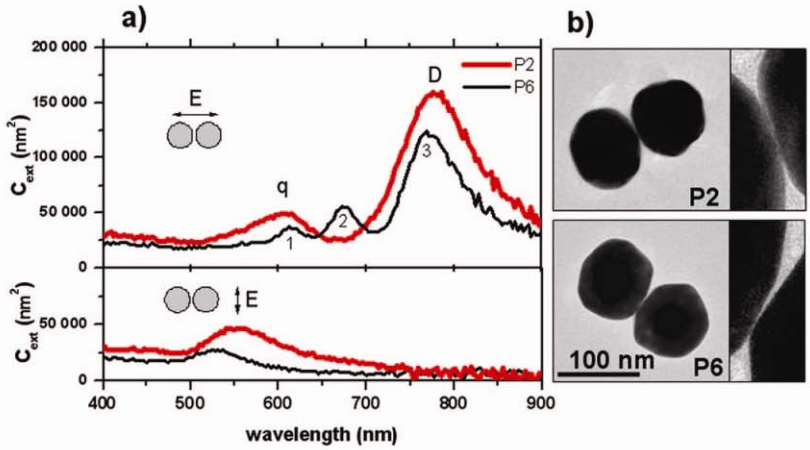

Figure 6. (a) Absolute extinction cross sections measured on two gold nanoparticle pairs (red lines, P2; black lines, P6). The top spectra correspond to a longitudinal excitation, and the bottom spectra to a transverse excitation. The resonances of "dipolar" and "quadrupolar" character are labeled by letters D and q, respectively, for P2. The three resonances observed for P6 are labeled 1, 2, and 3. (b) TEM images of P2 and P6 pairs and enlarged views of the interparticle regions.

of electron oscillation associated with the charge displacement over the pair as a whole is now physically allowed. It is responsible for a dipolar resonance that starts to grow and blue-shift for large enough sphere overlaps, as the antiwedge at the contact region widens and the dimer becomes more compact by adopting a "peanutlike" shape. At the nearly touching limit ($d = |d'| = \varepsilon \ll R$), the spectral features are very similar, either in the presence or in the absence of contact, because the optical response is ruled by the contributions of the highest-order plasmon modes (see Figure 1a and b in Romero et al.[14]). Those are related to the complex structure of the surface charge pile-up in the region surrounding the geometrical contact point which is of similar shape in both cases. A comparison with the spectra calculated by Romero et al.[14] for $|d'|/R \cong 0.001$ or 0.0005 indicates that a fourth resonance should be detected on the long wavelength side of the resonance labeled (3) in Figure 6. Unfortunately, it lies outside the experimental spectral window, but its presence may be guessed since a part of the integrated oscillator strength is missing in the spectrum of the P6 pair as compared to the spectrum of the P2 pair.

If a very close proximity without contact ($d = \varepsilon \ll R$) is physically unrealistic, the inspection of TEM images (P6 in Figure 6) is not in favor of a clear metallic connection either. Nevertheless, the singularity of the P6 pair spectra is consistent with a situation of quasi contact, with regard not only to the longitudinal excitation but also to the transverse one, as suggested by the weakening of the "transverse" LSP band in the bottom of Figure 6. This effect has been qualitatively reproduced in preliminary calculations with the COMSOL package by comparing the transverse extinction spectra of separated and overlapping spheres. A lowering of about 10% in the extinction signal is observed when changing from $d/R = 0.5$ to $d'/R = -0.5$ (d/R and $|d'|/R$ values were taken large enough to ensure calculation convergence). Even in the absence of metallic contact, a conducting path in the region of maximum proximity could be induced by an electric breakdown in the dielectric spacer (air, surfactants, etc.) because of the huge and localized electromagnetic field enhancement when surface plasmons are excited.

An alternative explanation could be found in the geometry of the interparticle region. Gold nanoparticles are far from being perfectly spherical and are often irregularly faceted as in the P6 pair (Figure 6). Numerical calculations are mainly performed in assuming spherical particles, and effects of a deviation from

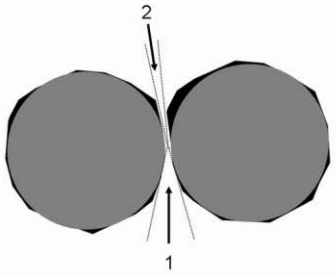

Figure 7. Schematic representation of a pair made of faceted particles. The inscribed perfect spheres are filled in gray. Regions 1 and 2 are delimited by the tangent to the particle surfaces drawn from the geometrical center of symmetry. Region 1 is the same as that for perfect spheres.

this ideal case (for very small d) are not discussed in the literature. For very close objects, it has been demonstrated that the rich structure made of multipolar plasmon resonances is underlain by the strong surface charge oscillations near the interparticle spacing. The shape of the gap region is of main importance, since it defines the capacitance of the facing "electrodes" formed by the particle surfaces. The capacitance may be very different depending on the local curvature of each particle as schematized in Figure 7. For instance, the region above the quasi contact point in the P6 pair (see enlarged view in Figure 6b) is much narrower than it would be for perfectly spherical particles. The overall effect of this locally faceted geometry might be equivalent to a decrease of the effective spacing between ideal spherical particles. This hypothesis would benefit to be checked on numerical grounds in the future. Whatever the best explanation (electric breakdown through the dielectric spacer or shape of the quasi contact zone), it must be remarked that optical spectra are very sensitive to fine details of the nanoparticle pair morphology that are not necessarily apparent from a mere inspection of TEM images in spite of their resolution.

4. Conclusion

In this work, the extinction spectra of individual pairs of gold nanoparticles have been recorded on an absolute scale thanks to the spatial modulation spectroscopy technique. Because of their chemical synthesis, colloidal gold particles dispersed on a transparent substrate by spin-coating are protected by a dielectric layer made of surfactant molecules. This layer prevents an easy

contact between them and limits the distance of closest approach in particle aggregates. As compared to the particle radii (about 50 nm in this work), the resulting interparticle spacings (d) are rather small (less than a few nm). It has been then possible to prepare nanoparticle pairs in the quasi touching limit in order to measure their individual optical response.

The electrostatic coupling between close but not touching particles induces a red-shift of the dipolar surface plasmon resonance and the birth of higher-order plasmon modes. These effects have been discussed on the basis of numerical simulations and a correlation has been established between the main spectral features and the interparticle distance d independently measured by TEM. The correlation is unambiguous for interparticle distances of the order of a few nanometers and only qualitative for smaller ones because of the irregular particle shape in the interparticle region and of the limited contrast of TEM images in the conventional operation mode, in the presence of an amorphous shell at the particle surface. We have shown that, in most cases, the interparticle distance reaches a limiting value which can be ascribed to the presence of a surfactant layer of fixed thickness. Deviations from this general trend are illustrated through two examples. The first concerns a pair of more distant particles. The second is more interesting and corresponds to a pair of particles exhibiting an optical signature consistent with theoretical predictions in the case of metallic contact. Although the contact is not obvious in view of TEM images, the latter are informative enough to show that the particles are faceted and deviate from ideal spheres. The particular geometry of the interparticle region may be invoked to explain the spectral features observed, even in the absence of a conductive contact. The specific optical response observed for small spacings is intimately related to the highly complicated spatial structure of the near field generated by both particles in the interparticle region. This emphasizes the strong influence of the local geometry in the quasi contact regime.

The extreme situations of a large particle separation or a neat overlap are now well understood from theory and experiment. However, the transition from isolated to conductively coupled particles in the strong coupling regime remains a very interesting issue that should benefit from the richness of single particle absolute extinction spectroscopy. In the future, the high sensitivity of optical spectra in this regime will enable us to more precisely correlate the optical properties with the local particle shape. Experiments on particles functionalized with molecular chains of controlled length are now in progress.

References and Notes

(1) Kreibig, U.; Vollmer, M. *Optical properties of Metal Clusters*; Springer: Berlin, 1995.

(2) Bohren, C. F.; Huffman, D. P. *Absorption and scattering of light by small particles*; Wiley: New York, 1983.

(3) Hao, E.; Schatz, G. C. *J. Chem. Phys.* **2004**, *120*, 357.

(4) Ringler, M.; Schwemer, A.; Wunderlich, M.; Nichtl, A.; Kürzinger, K.; Klar, T. A.; Feldman, J. *Phys. Rev. Lett.* **2008**, *100*, 203002.

(5) Talley, C. E.; Jackson, J. B.; Oubre, C.; Grady, N. K.; Hollars, C. W.; Lane, S. M.; Huser, T. R.; Nordlander, P.; Halas, N. J. *Nano Lett.* **2005**, *5*, 1569.

(6) Baciu, C. L.; Becker, J.; Janshoff, A.; Sönnichsen, C. *Nano Lett.* **2008**, *8*, 1724.

(7) Stewart, M. E.; Anderton, C. R.; Thompson, L. B.; Maria, J.; Gray, S. K.; Rogers, J. A.; Nuzzo, R. G. *Chem. Rev.* **2008**, *108*, 494.

(8) Kelly, K. L.; Coronado, E.; Zhao, L. L.; Schatz, G. C. *J. Phys. Chem. B* **2003**, *107*, 668.

(9) Atay, T.; Song, J.-H.; Nurmikko, A. V. *Nano Lett.* **2004**, *4*, 1627.

(10) Rechberger, W.; Hohenau, A.; Leitner, A.; Krenn, J. R.; Lamprecht, B.; Aussenegg, F. R. *Opt. Commun.* **2003**, *220*, 137.

(11) Su, K. H.; Wei, G. H.; Zhang, X.; Mock, J. J.; Smith, D. R.; Schultz, S. *Nano Lett.* **2003**, *3*, 1087.

(12) Gunnarsson, L.; Rindzevivius, T.; Prikulis, J.; Kasemo, B.; Käll, M.; Zou, S.; Schatz, G. C. *J. Phys. Chem. B* **2005**, *109*, 1079.

(13) Jain, P. K.; Huang, W.; Sayed, M. A. E. *Nano Lett.* **2007**, *7*, 2080.

(14) Romero, I.; Aizpurua, J.; Bryant, G. W.; Abajo, J. G. d. *Opt. Express* **2006**, *14*, 9988.

(15) Enoch, S.; Quidant, R.; Badenes, G. *Opt. Express* **2004**, *12*, 3422.

(16) Chu, P.; Mills, D. L. *Phys. Rev. B* **2008**, *77*, 045416.

(17) Hohenester, U.; Krenn, J. *Phys. Rev. B* **2005**, *72*, 195429.

(18) Jain, P.; El-Sayed, M. A. *J. Phys. Chem. C* **2008**, *112*, 4954.

(19) Gluodenis, M.; Foss, C. A., Jr *J. Phys. Chem. B* **2002**, *106*, 9484.

(20) Jensen, T.; Kelly, L.; Lazarides, A.; Schatz, G. C. *J. Cluster Sci.* **1999**, *10*, 295.

(21) Aizpurua, J.; Bryant, G. W.; Richter, L. J.; Abajo, F. J. G. d.; Kelley, B. K.; Mallouk, T. *Phys. Rev. B* **2005**, *71*, 235420.

(22) Jain, P. K.; Eustis, S.; El-Sayed, M. A. *J. Phys. Chem. B* **2006**, *110*, 18243.

(23) Yang, W. H.; Schatz, G. C.; Duyne, R. P. V. *J. Chem. Phys.* **1995**, *103*, 869.

(24) Abajo, F.J. G. d.; Howie, A. *Phys. Rev. Lett.* **1998**, *80*, 5180.

(25) Xu, Y. L. *Appl. Opt.* **1997**, *36*, 9496.

(26) Gerardy, J. M.; Ausloos, M. *Phys. Rev. B* **1981**, *25*, 4204.

(27) Tamaru, H.; Kuwata, H.; Miyazaki, H. T.; Miyano, K. *Appl. Phys. Lett.* **2002**, *80*, 1826.

(28) Arbouet, A.; Christofilos, D.; Fatti, N. D.; Vallée, F.; Huntzinger, J. R.; Arnaud, L.; Billaud, P.; Broyer, M. *Phys. Rev. Lett.* **2004**, *93*, 127401.

(29) Billaud, P.; Huntzinger, J.-R.; Cottancin, E.; Lermé, J.; Pellarin, M.; Arnaud, L.; Broyer, M.; Fatti, N. D.; Vallée, F. *Eur. Phys. J. D* **2007**, *43*, 271.

(30) Billaud, P.; Marhaba, S.; Cottancin, E.; Arnaud, L.; Bachelier, G.; Bonnet, C.; Fatti, N. D.; Lermé, J.; Vallée, F.; Vialle, J.-L.; Broyer, M.; Pellarin, M. *J. Phys. Chem. C* **2007**, *112*, 978.

(31) Palik, E. D. *Handbook of optical constants of solids*; Academic Press Inc.: New York, 1985−1991; Vols. *I* and *II*.

(32) Johnson, P. B.; Christy, R. W. *Phys. Rev. B* **1972**, *6*, 4370.

(33) Sönnichsen, C.; Reinhard, B. M.; Liphardt, J.; Alivisatos, A. P. *Nat. Biotechnol.* **2005**, *23*, 741.

(34) Muskens, O. L.; Giannini, V.; Sanchez-Gil, J. A.; Rivas, J. G. *Opt. Express* **2007**, *15*, 17736.

(35) Kottmann, J. P.; Martin, O. J. F. *Opt. Lett.* **2001**, *26*, 1096.

(36) Prodan, E.; Radloff, C.; Halas, N. J.; Nordlander, P. *Science* **2003**, *302*, 419.

(37) Nordlander, P.; Oubre, C.; Prodan, E.; Li, K.; Stockman, M. I. *Nano Lett.* **2004**, *4*, 899.

(38) Lermé, J.; Bonnet, C.; Broyer, M.; Cottancin, E.; Marhaba, S.; Pellarin, M. *Phys. Rev. B* **2008**, *77*, 245406.

(39) Lermé, J.; Bachelier, G.; Billaud, P.; Bonnet, C.; Broyer, M.; Cottancin, E.; Marhaba, S.; Pellarin, M. *J. Opt. Soc. Am. A* **2008**, *25*, 493.

(40) Chern, R. L.; Liu, X. X.; Chang, C. C. *Phys. Rev. E* **2007**, *76*, 016609.

(41) Mock, J. J.; Barbic, M.; Smith, D. R.; Schultz, D. A.; Schultz, S. *J. Chem. Phys.* **2002**, *116*, 6755.

(42) Brack, M. *Rev. Mod. Phys.* **1993**, *65*, 677.

(43) Akita, T.; Okumara, M.; Tanaka, K.; Kohyama, M.; Haruta, M. *J. Mater. Sci.* **2005**, *40*, 3101.

JP810405Y

3- Contrôler la forme spectrale des résonances: les profils Fano

Il est des rencontres en recherche qui demandent un travail assidu, une persévérance hors norme, à la limite de l'obsession, jusqu'à ce qu'un jour le déclic survienne, la clé de tout finisse par apparaître naturelle, du moins à postériori. Nous en verrons un exemple avec l'étude de la réponse non-linéaire des particules métalliques. Il est d'autres au contraire qui sont presque fortuites. Presque. L'intuition et la curiosité sont d'excellents guides pour peu qu'on les y ait préparés.

L'étude des dimères Or-Or nous a montré une facette du contrôle des résonances plasmons en jouant sur la distance inter-particule. Cependant, quand bien même de nouvelles résonances apparaissent, elles ont invariablement la même forme... lorentzienne. Comme nous l'avons vu précédemment, même en changeant la forme des particules, les résonances demeurent lorentzienne. Est-ce une malédiction? Peut-on aller au-delà? Comment modifier l'allure spectrale des résonances plasmons? Il faut pour cela dissymétriser le système. On est finalement assez peu habitué à cette démarche, la physique (le physicien théoricien?) poussant souvent à la recherche de symétries, d'invariances. Rompez la symétrie et une "nouvelle" physique apparaît! C'est précisément le cas dans les dimères Or-Argent que j'ai étudié dans le cadre de l'ANR Opthermal, coordonnée par Pierre-François Brevet, visant à analyser le transfert thermique entre une particule d'or et une particule d'argent.

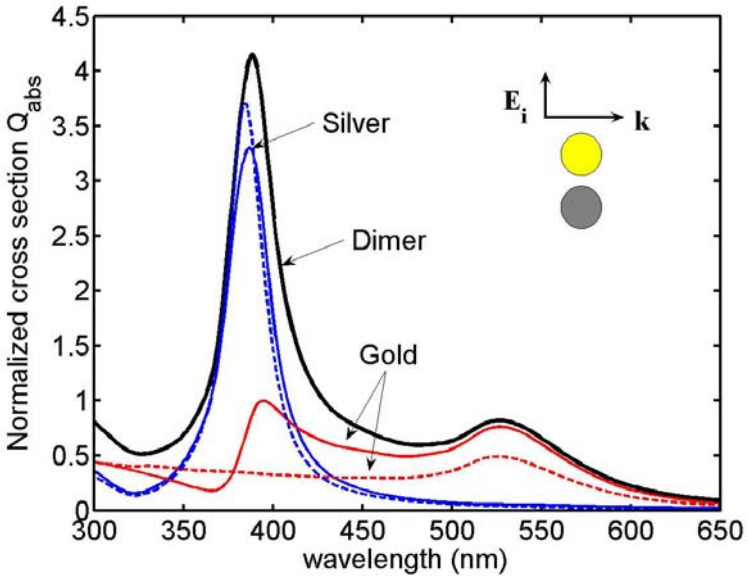

Figure 9: *Sections efficaces d'absorption d'une particule d'argent (bleu) et d'or (rouge) dans le cas de particules isolées (pointillés) et dans le cas du dimère (traits pleins). Les spectres sont calculés pour un rayon de 5 nm et un indice de 1.33 pour la matrice.*

Si l'on regarde les propriétés des particules isolées, on voit apparaître la résonance "aigue" de la particule d'argent au dessous de 400 nm et celle de la particule d'Or vers 530 nm (cf. courbes en pointillés de la figure 9). Mais plus intéressant encore, le plasmon de la particule d'argent vient se superposer spectralement avec le continuum de transition interbande de la particule d'or. Que se passe-t-il dans le cas où les particules entrent en interaction, et plus précisément lorsque l'on atteint le régime de couplage fort en champ proche optique? A examiner la réponse du dimère, pas grand chose. C'est plutôt décevant. Le but de l'ANR Opthermal étant d'évaluer par des techniques de pompe-sonde le transfert thermique entre les deux particules (expériences réalisées par l'équipe de Nathalia Del Fatti et Fabrice Vallée), il apparaissait important d'évaluer la quantité d'énergie absorbée par chacune des particules en fonction de la longueur d'onde. Le profil obtenu pour la particule d'or (cf. courbe en trait plain de la figure 9) était caractéristique: un profil Fano! Le moyen de déformer les résonances plasmons venait tout juste de se révéler...

Les profils Fano apparaissent dans de nombreux domaines de la physique: en acoustique, en mécanique quantique, en électromagnétisme et que sais-je encore. J'affectionne tout particulièrement le point de vue de la mécanique quantique par lequel j'ai fait la connaissance des profils Fano la première fois (voir figure 10). L'idée est la suivante. Lorsque l'on couple un état discret $|\varphi\rangle$ à un continuum $|k\rangle$, l'état du nouveau système se décrit par un nouveau continuum où l'état discret semble s'être dissout. Pourtant, lorsque l'on excite le système avec un photon par exemple $|\chi\rangle$, la réponse du système dépend très fortement de l'énergie du photon autour de l'énergie de l'état discret $|\varphi\rangle$. Ainsi, le nouveau continuum a gardé une trace, une mémoire de l'état discret. Suivant le facteur de couplage $q = {}^{w}\!/_{v.w'}$ faisant intervenir les différents potentiels d'interaction, le profil Fano peut présenter des allures très différentes comme le montre la figure 10. C'est là toute leur richesse et leur intérêt. Leur origine est en fait associée à des interférences entre les différents canaux d'excitation (amplitudes de probabilité), le continuum $|k\rangle$ pouvant être excités soit directement par les photons $|\chi\rangle$, soit indirectement par l'intermédiaire de l'état discret $|\varphi\rangle$. La phase relative entre ces deux processus dépend donc des différentes interactions mises en jeu.

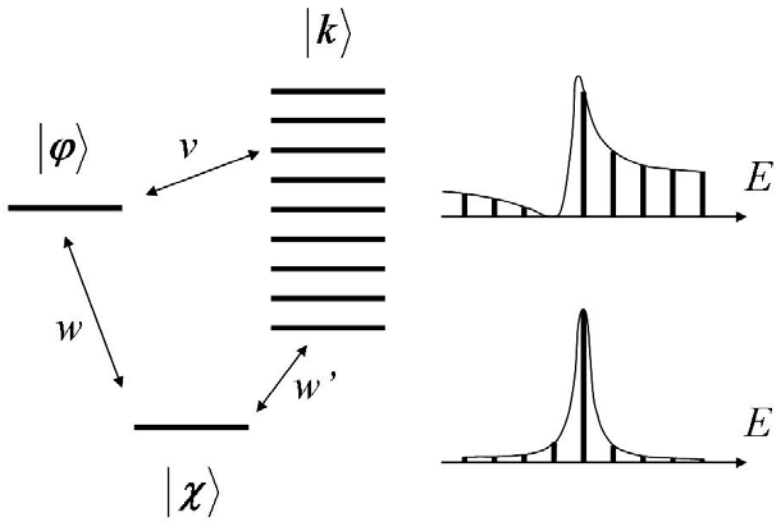

Figure 10: *Schéma du couplage entre un état discret* $|\varphi\rangle$ *et un continuum d'états* $|k\rangle$ *excités tous deux par un photon* $|\chi\rangle$*. Les différents potentiels de couplage sont données par* v, w *et* w'*. Les profils Fano en fonction de l'énergie E du photon correspondent à un facteur de couplage* $q = w/v.w'$*, égal à 2 (haut) et très grand devant 1 (bas).*

L'observation ou la prédiction de ces profils Fano dans des structures purement plamoniques ont eu lieu presque simultanément dans deux système assez différents: un disque d'or entouré par une couronne également en or mais décentrée, pour l'équipe de P. Nordlander, et un dimère or-argent dans le cas de l'étude que je vais présenter. Pourquoi de tels systèmes présentent le même type de comportement physique? Qui joue le rôle d'état discret et celui de continuum? Très clairement, la rupture de symétrie joue un rôle capital dans le système proposé par P. Nordlander. En effet, la relaxation des règles de sélection qui en découle permet de faire interagir des modes quadripolaires de la couronne avec les modes dipolaires du disque. Les premiers sont dits sombres car ils interagissent peu avec la lumière et présentent donc des résonances étroites (état "discret"). Les seconds sont optiquement actifs et présentent donc une résonance large pour peu que la particule soit assez grande (intervention des effets retards) ou que le matériau soit absorbant (damping). Ils jouent donc le rôle de continuum. Dans le cas des dimères or-argent, les choses sont assez différentes puisque l'état discret est joué par la résonance de la particule d'argent, qui est naturellement étroite pour des particules de petite taille (peu d'absorption en dessous des transitions interbandes). Le continuum est celui des transitions interbandes de l'or (hors résonance plasmon). Ainsi, bien que ces systèmes soient intrinsèquement très différents, on retrouve dans les deux cas les ingrédients de bases indispensables à l'existence des profils Fano.

Notons que le dénominateur commun est aussi la rupture de symétrie qui joue un rôle capital et qui est devenu un sujet très à la mode.

Ces deux travaux pionniers et quasi simultanés n'ont pourtant pas eu le même écho dans la communauté plasmonique. Pour s'en convaincre, il suffit de faire une petite recherche biblio sur P. Nordlander tant du point de vue de la production scientifique que du nombre de citations associées aux profils Fano. Le constat est clair et sans appel: la force de frappe de certains groupes rend la concurrence pour le moins déséquilibrée dans le cadre d'une compétition internationale... Il faut tout de même reconnaître que l'une des particularités du système que j'ai proposé est que les profils Fano interviennent dans l'absorption de la particule d'or et ne se voient pas directement dans l'absorption du dimère complet. Il faut donc venir adresser spécifiquement ce qui se produit dans la particule d'or, ce qui ajoute un degré de complexité non-négligeable. Nous en discuterons plus loin. Quoiqu'il en soit, le dimère or-argent présente tout de même de nombreux avantages!

Tout d'abord, le dimère or argent est un système modèle pour comprendre l'origine des profils Fano, si la vision offerte par la mécanique quantique ne vous a pas convaincue. En effet, les profils Fano ont pour origine l'interférence entre plusieurs canaux d'excitation. Dans le cas présent, la particule d'or peut être excitée soit directement par l'onde incidente, soit indirectement par l'onde diffusée par la particule d'argent. Tout dépend donc de la phase relative entre ces deux champs et donc de la réponse fréquentielle de la particule d'argent. Bien que les calculs aient été réalisés numériquement, on peut très bien rendre compte des principaux effets avec un simple modèle dipolaire (et donc intuitif) dans lequel la particule d'argent est décrite par un dipôle de polarisabilité

$$\alpha = 3V \frac{\varepsilon(\omega) - \varepsilon_m}{\varepsilon(\omega) + 2\varepsilon_m}$$

Le point important ici est que, lorsque l'on balaye spectralement la résonance plasmon, le dénominateur change de signe. C'est une propriété extrêmement générale en physique dès que l'on excite un oscillateur (qu'il soit mécanique, électrique, etc...): pour des fréquences faibles par rapport à la fréquence propre d'oscillation, le système réagit "instantanément" et est donc en phase avec l'excitation; plus la fréquence augmente et plus il est difficile pour le système de suivre l'excitation (le système est en retard), ce qui se traduit par une augmentation du déphasage entre l'amplitude d'oscillation et l'excitation jusqu'à atteindre un déphasage maximal de $-\pi$. Quelle conséquence dans le cas présent? Si le champ incident et le camp diffusé par la particule d'argent sont en phase, il y a interférences constructives et donc une exaltation de l'absorption induite dans la particule d'or. Si au contraire ces champs sont en

opposition de phase, il y a interférences destructives conduisant à une réduction de l'absorption. Ceci explique le profil dissymétrique observé dans la particule d'or, au voisinage de la résonance plasmon de la particule d'argent (figure 9).

Deuxième point important, le couplage entre les particules se fait par l'intermédiaire du champ proche optique, c'est à dire de la partie évanescente du champ (photons "piégés" par la particule) correspondant aux termes en $1/r^2$ et $1/r^3$ dans le développement dipolaire. Le couplage dépend donc très fortement de la distance inter-particule. On dispose ainsi d'un moyen de contrôler dynamiquement la forme des profils en jouant sur la distance. Pas besoin pour cela de lithographier une nouvelle structure: une particule d'or greffée sur une pointe AFM ou une fibre étirée et que l'on approche d'une particule d'argent déposée sur le substrat peut parfaitement faire l'affaire. Certes on s'écarte du système modèle de part la modification de l'environnement des particules mais le gain est plus que significatif: on peut faire varier sur le même dimère et de manière contrôlée la distance interparticule. Comme nous l'avons montré, il est ainsi possible de passer d'un régime de couplage faible à ce lui d'un couplage fort, balayant ainsi toute la palette de profils Fano accessibles et modifiant à souhait la forme de la résonance plasmon de la particule d'or (cf. figure 10). Mais il y a plus intéressant encore.

Le terme de couplage ou d'interférence fait intervenir des grandeurs vectorielles (les champs) dépendant de la position relative des deux particules. On peut s'en convaincre à l'aide de l'expression du champ rayonné par un dipôle ou, plus simplement, à l'aide des schémas de la figure 11. Lorsque le champ incident est parallèle à l'axe du dimère on retrouve le résultat discuté précédemment: exaltation de l'absorption aux grandes longueurs d'ondes et inhibition dans le domaine des courtes longueurs d'onde (courbe bleue). En effet, les dipôles créés dans la particule d'or par l'onde incidente (symbolisé par la flèche épaisse) et par l'onde diffusée par la particule d'argent (selon les lignes de champ) sont toujours parallèles. Il en va tout autrement lorsque l'on tourne la polarisation du champ incident par rapport à l'axe du dimère, comme le montrent les différents spectres de la figure 11. Pour bien comprendre l'origine de cette modification drastique de la réponse spectrale, plaçons-nous autour de 400 nm et faisons tourner le champ. Au départ, le champ incident et celui induit par la particule d'argent sont parallèles, induisant un contraste d'interférence maximal. Pour une certaine orientation du champ incident (dépendant de la distance interparticule), le champ incident et le champ diffusé par la particule d'argent sont orthogonaux (courbe verte). Il n'y a donc plus d'interférences! L'absorption dans la particule d'or se réduit donc la somme des absorptions induites par l'onde incidente et le champ diffusé par la particule d'argent pris séparément. Ainsi l'absorption dans la particule d'or est toujours supérieure à celle que l'on aurait eue pour

une particule isolée (somme incohérente des contributions). Si l'on continue à tourner le champ incident, de sorte qu'il soit perpendiculaire à l'axe du dimère, le champ incident et le champ diffusé par la particule d'argent sont alors opposés conduisant cette fois à des interférences destructive. Il est ainsi possible d'allumer, d'éteindre et d'inverser à distance le couplage entre les particules offrant une occasion unique de contrôler à souhait et macroscopiquement la forme de la résonance plasmon dans la particule d'or.

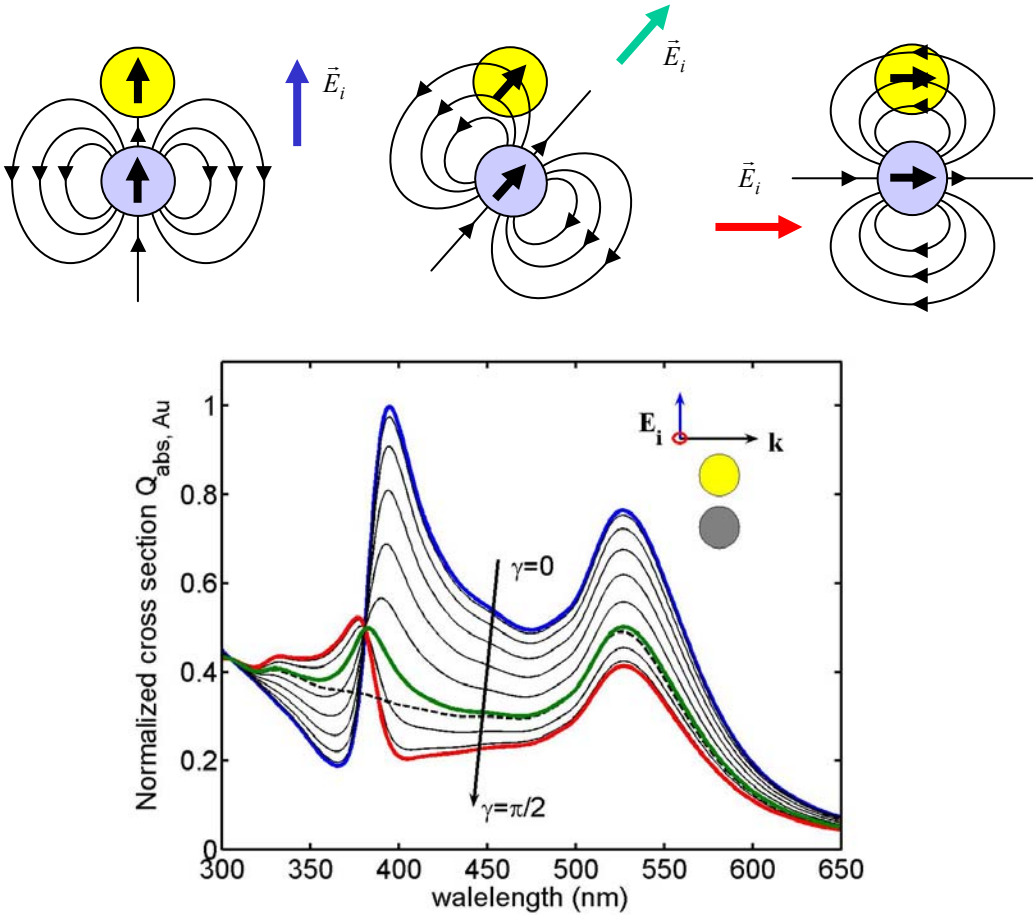

Figure 11: *Spectre d'absorption de la particule d'or au sein du dimère en fonction de la polarisation de l'onde incidente repérée par l'angle γ entre le champ et l'axe du dimère. Les courbes bleues, verte et rouge correspondent au configurations ci-dessus. La courbe en pointillés correspond à l'absorption d'une particule isolée d'or isolée.*

Il y a bien des curiosités que je pourrais discuter ici comme l'apparition de points isobestiques (indépendants de la polarisation incidente), dus au fait qu'il n'y a que deux états de plasmons longitudinaux et transverses, ou le fait que l'exaltation induite par la particule d'argent se fait sentir à des longueurs d'ondes bien plus grandes que celle de la résonance plasmon associée, ce qui est contre-intuitif, ou enfin l'effet d'ombrage lorsque l'on modifie l'orientation du dimère par rapport au vecteur d'onde incident... Je préfère vous renvoyer pour

cela à l'article joint ci-après et discuter ici plus en détail des stratégies permettant de passer du monde virtuel des simulations et de la théorie au monde réel de l'expérience.

Comme anticipé plus haut, il faut venir adresser spécifiquement ce qu'il se passe dans la particule d'or. Pour peu que l'on baigne un peu dans la communauté, on pense directement à des expériences de champ proche, l'idée serait alors de venir sonder le champ au dessus de la particule d'or. Mais pour cela, il faudrait arriver à une résolution spatiale inférieure à la taille des particules. C'est pour le moins "challenging" vu que les particules doivent idéalement rester de taille modeste (inférieure à 60 nm de diamètre) si l'on veut pouvoir rester dans l'approximation dipolaire et éviter un élargissement et un décalage radiatif très important de la résonance plasmon de l'argent (plus sensible que celle de l'or "engluée" dans les transitions interbandes). Cela dit, rien n'empêche d'aller voir ce qui se passe aux plus grandes tailles pour mettre en évidence des interactions plus exotiques entre multipôles. Cette piste ainsi que celle de venir coller la particule d'or directement sur la pointe sont en projet...

Reste une troisième option tirant directement profit du savoir faire de l'équipe FemtoNanoOptics de Natalia Del Fatti et de Fabrice Vallée: le pompe-sonde! Comme je le disais précédemment, c'est de la nécessité de savoir ce qui était absorbé spécifiquement dans les deux particules lors d'expériences pompe-sonde que sont apparus les profils Fano. C'est donc en utilisant cette technique pompe sonde qu'il doit être possible de les révéler. Pour cela, j'ai simulé la modification de l'absorption du dimère (vue par la sonde) due à une modification de la constante diélectrique des particules (induite par la pompe). Les résultats sont présentés dans la figure 12. Comme la constante diélectrique possède une partie réelle et une partie imaginaire il y a deux courbes à chaque fois. Le fait marquant et quelque peu inattendu, soyons honnête, est qu'une variation de la constante diélectrique de l'argent ne modifie significativement l'absorption du dimère qu'au voisinage de la résonance plasmons de la particule d'argent, alors qu'une modification de la constante diélectrique de la particule d'or induit une forte évolution de l'absorption au niveau des deux résonances plasmons. Cette dissymétrie offre une porte d'entrée élégante pour mettre en évidence les profils Fano dans les dimères or-argent: si l'on vient sonder la modulation de l'absorption du dimère au voisinage de la résonance de la particule d'or, on n'est sensible qu'à la modulation de la constante diélectrique de la particule d'or. Celle de l'argent n'intervient pratiquement pas. En excitant avec la pompe le dimère au voisinage de la résonance plasmon de l'argent, on dépose ainsi de l'énergie dans les deux particules, et ce proportionnellement aux sections efficaces d'absorption de celles-ci (cf figures 9 et 11). Ainsi, on obtient une image des profils Fano en

scannant la longueur d'onde de la pompe au voisinage de la résonance plasmon de l'argent et en sondant à la résonance plasmon de l'or.

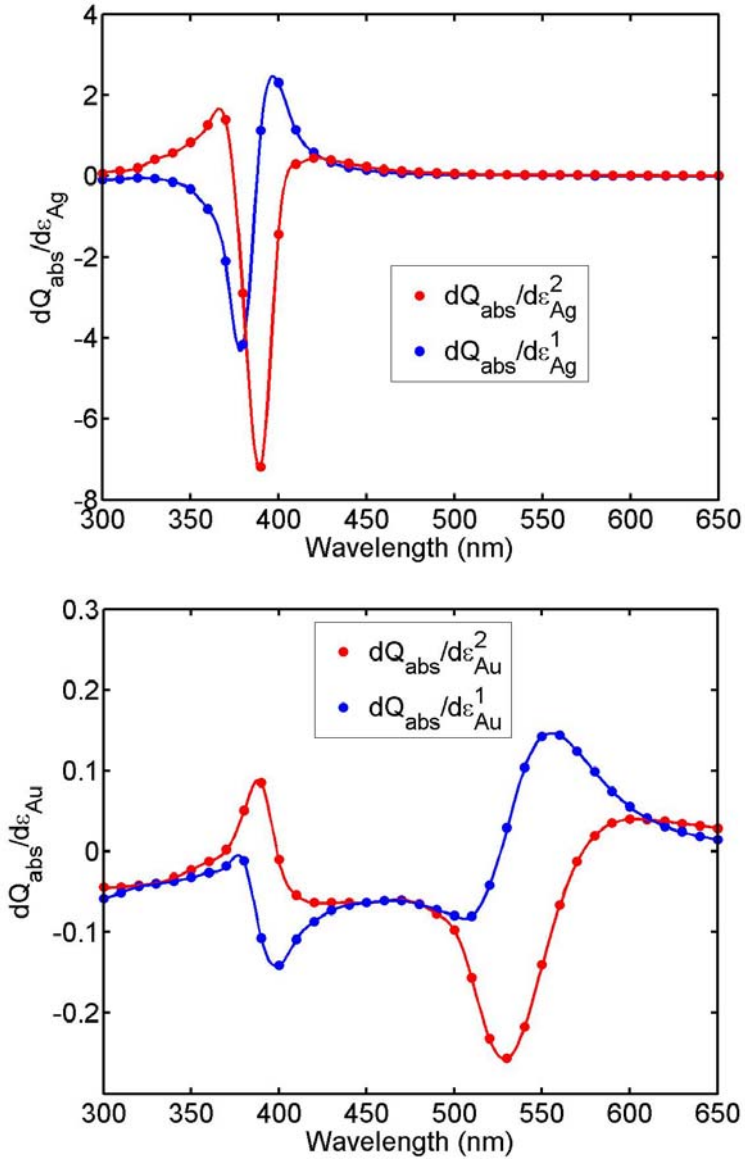

Figure 12: *Modulation des spectres d'absorption du dimère induits par une modulation de la constante diélectrique dans la particule d'argent (haut) ou dans la particule d'or (bas).*

La mise en évidence des profils Fano dans les dimères or-argent serait déjà en soit une première. Mais l'utilisation des techniques pompes-sondes donnerait de mon point de vue une saveur particulière! Ce serait aussi la consécration d'un travail théorique ayant non seulement révélé l'existence d'un "nouveau" phénomène physique dans ces structures plasmoniques mais aussi tracé la voie vers leur démonstration expérimentale. La route est cependant encore longue...

Fano Profiles Induced by Near-Field Coupling in Heterogeneous Dimers of Gold and Silver Nanoparticles

G. Bachelier, I. Russier-Antoine, E. Benichou, C. Jonin, N. Del Fatti, F. Vallée, and P.-F. Brevet

Laboratoire de Spectrométrie Ionique et Moléculaire, Université Lyon 1-CNRS (UMR 5579), 43 Boulevard du 11 Novembre 1918, 69622 Villeurbanne Cedex, France

(Received 28 April 2008; published 4 November 2008)

The near-field coupling between a gold and a silver spherical nanoparticle is investigated theoretically. Fano profiles are observed in the absorption cross section of the gold nanoparticle due to the coupling between the spectrally localized surface plasmon resonance of the silver nanoparticle and the continuum of interband transitions of the gold one. The effect of dimer internal characteristics (particle sizes and distance), surrounding medium (through the refractive index), and external excitation (polarization and propagation directions) are addressed. In particular, it is shown that the near-field coupling can be tuned from the weak to the strong regime by rotating the polarization direction, and that the Fano profiles are sensitive to the shadowing effect even for small particle sizes.

DOI: 10.1103/PhysRevLett.101.197401 PACS numbers: 78.67.Bf, 42.25.Fx, 73.20.Mf, 73.22.−f

Scaling down the size of noble metal structures has opened an extensively productive road to manipulate light at a subwavelength scale. The shape-driven frequency of the surface plasmon resonances (SPR) allows the tailoring of almost any desired spectral response in the visible and the near infrared domains, depending on the targeted applications [1]. Another powerful strategy, the focus of a large and increasing interest in plasmonics, lies in the interparticle near-field coupling through the evanescent waves surrounding the metal nanostructures. Bonding and antibonding plasmon modes, in a hybridization picture [2], strongly depend on the particle distance [3–5] and eventually lead to a singular response in the limit of contacting dimers [6]. Controlling the nanoparticle spacing is therefore a major challenge achieved using either physical or chemical techniques [3,7–10]. The large electric field localized in the dimer gap is indeed a key ingredient used to induce surface enhanced Raman scattering [11], single molecule fluorescence [12], or frequency mixing [10] with a single homogeneous dimer. Additional effects such as radiation damping modification [13] and enhanced optical forces [14] have also been predicted, underlying the wide interest in coupled metal structures.

Fano profiles are typical spectral features arising from the coupling of a discrete state with a continuum [15]. They have been reported in the past for J-aggregated Dye or semiconductor quantum dots (discrete exciton) coupled with gold nanoparticles (continuum) [16,17]. In these systems, the SPR of the noble metal particles was used to enhance the response of the coupled system, but does not play any key role in the observation of the Fano profiles. Fano-like line shapes were also reported recently in reflection spectra of interacting metal nanowires made of the same metal, but their origin was assigned to the interference between the light scattered by (noninteracting) subradiant and superradiant plasmon modes [18]. In this Letter we investigate theoretically the optical properties of heterogeneous dimers composed of a gold and a silver nanoparticle. We demonstrate for the first time the presence of Fano profiles in a purely plasmonic system, where the spectrally localized SPR of the silver nanoparticle (the "discrete" level) is coupled to the gold interband transitions (the continuum). These characteristic spectral features are revealed in the absorption spectrum of the gold nanoparticle, and their sensitivity on the dimer structure, the surrounding medium, and the excitation configuration is addressed.

When the excitation wavelength largely exceeds the particle size, the optical properties of noble metal nanoparticles are dominated by absorption [1]. The latter is quantified by a normalized cross section $Q_{\mathrm{abs}} = \sigma_{\mathrm{abs}}/S$ weighting the Joule dissipation inside the particle with respect to the incident power intercepted by the particle:

$$Q_{\mathrm{abs}} = \frac{\int \mathbf{j}\mathbf{E}\,dV}{\int \mathbf{E}_i \times \mathbf{H}_i\,dS}. \quad (1)$$

$\mathbf{E}$ and $\mathbf{j}$ are the total electric field and charge currents inside the particle, and $\mathbf{E}_i$ and $\mathbf{H}_i$ account for the incident electric and magnetic fields. V and S are the particle volume and the particle section normal to the incident wave, respectively. In this work, the adimensional quantity Q_{abs} was computed for the gold and silver particles in the heterogeneous dimer using finite element method (FEM) simulations performed in the framework of the scattered field formulation. Perfectly matched layers were used to avoid spurious reflections at the surrounding medium boundaries [19]. The dielectric constants of the metal particles ϵ_p were taken from Ref. [20], and corrected, for small particle sizes, to account for the Landau damping of the SPR [21]. The results are shown in Fig. 1 for particle radii R and a distance d (surface to surface) of 5 and 3 nm, respectively. The refractive index of the surrounding me-

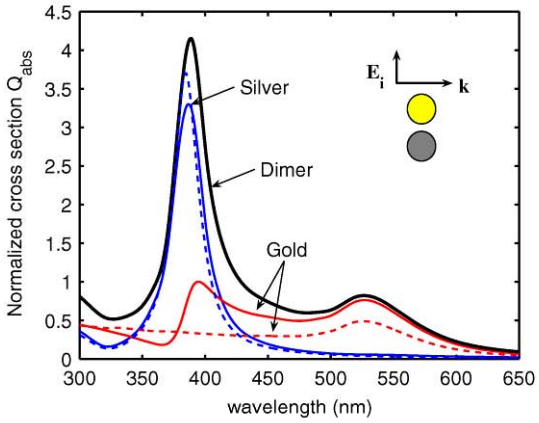

FIG. 1 (color online). Normalized absorption cross sections of the silver and gold nanoparticles. The dashed and full lines correspond to the case of isolated particles or particles within the dimer, respectively. The overall absorption cross section of the coupled particles is given by the bold line. The radius of both particles is 5 nm and the interparticle distance 3 nm. The incoming light is polarized parallel to the dimer axis. The gold and the silver particles are represented by the light gray and the gray disks, respectively.

dium ($\sqrt{\epsilon_m}$) is fixed at 1.33. As observed in Fig. 1, the SPR of the silver nanoparticle is only slightly damped and shifted in the heterogeneous dimer (the increase of the width and the resonance wavelength shift are smaller than 3 nm). On the opposite, the absorption in the gold particle is highly modified in the overall spectral range covered by the simulations. In particular, a clear Fano profile is observed in the gold particle around 378 nm induced by the near-field coupling between the continuum of interband transitions in the gold material and the discrete SPR of the silver particle. More precisely, the interband transitions of the gold particle can be excited either directly by the light source or indirectly through the locally enhanced electric field associated with the SPR of the silver particle. The relative phase between the incident field and that scattered by the silver particle therefore plays a major role. The origin of this phase shift can be qualitatively understood using the particle polarizability α in the Rayleigh approximation [1]

$$\alpha = 4\pi R^3 \frac{\epsilon_p - \epsilon_m}{\epsilon_p + 2\epsilon_m}. \quad (2)$$

The real part of ϵ_p being negative around the SPR, observed for $\mathrm{Re}(\epsilon_p + 2\epsilon_m) = 0$, the dipole induced in the silver particle is in phase with the incident electric field below the SPR (longer wavelengths) and out of phase above the SPR, as given by the sign of the real part of the denominator.

The intrinsic near-field origin of the particle coupling leads to a strong dependence of the Fano profile with the particle distance d as shown in Fig. 2(a). For large distances (greater than the particle diameter), the profiles are almost antisymmetric with respect to the crossing point of

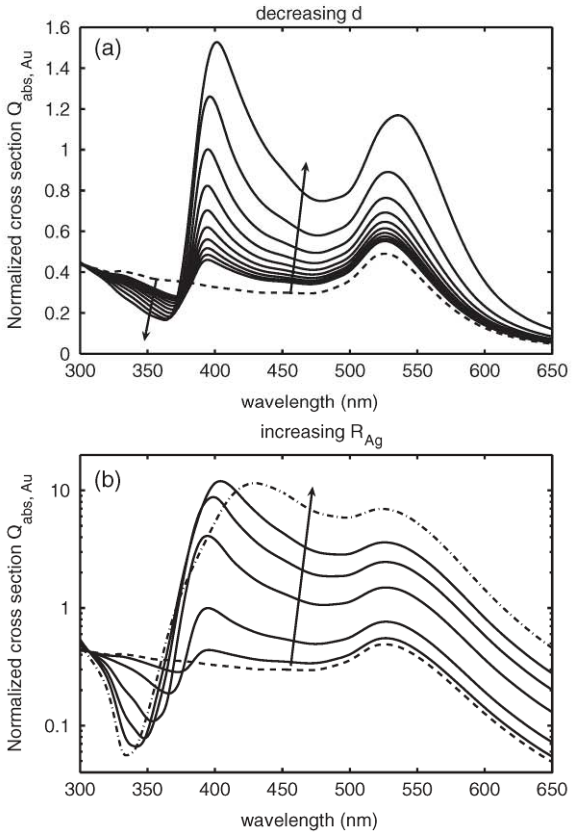

FIG. 2. Normalized absorption cross section of a $R_{Au} = 5$ nm gold nanoparticle (a) as a function of the interparticle distance d (from top to bottom d ranges from 1 to 10 nm by steps of 1 nm) for a fixed silver size ($R_{Ag} = 5$ nm) and (b) as a function of silver particle size (from the bottom to the top $R_{Ag} = 2.5$, 5, 10, 15, 20, and 30 nm) for a fixed interparticle distance $d = 3$ nm. The dash-dotted line is used for $R_{Ag} = 30$ nm. The dashed curves correspond to the absorption cross section of an isolated gold particle. The field configuration is the same as in Fig. 1.

the normalized cross section $Q^{\infty}_{\mathrm{abs,Au}}$ calculated for an isolated particle and $Q_{\mathrm{abs,Au}}$ for the gold particle in the heterogeneous dimer. For shorter distances, the Fano profiles are highly distorted showing the continuous transition from the weak to the strong coupling regime [15]. The same behavior is observed in Fig. 2(b) while increasing the silver particle radius. Indeed, for noble metal nanospheres, the near-field region typically extends over one particle radius [1]. Increasing the silver particle radius R_{Ag} allows us, therefore, to adjust the region of localized and enhanced electric field to the gold nanoparticle size. As a matter of fact, with $R_{Au} = 5$ nm, an optimum was found for $R_{Ag} \approx 2R_{Au} + d$. For larger R_{Ag}, the enhancement of the normalized cross section $Q_{\mathrm{abs,Au}}$ saturates due to the retardation effects on the silver particle, leading to a shift and a radiative broadening of its SPR [see the dash-dotted curve of Fig. 2(b)].

If the gold absorption cross section is spectrally highly affected by the presence of the silver SPR, an almost

constant and comparable enhancement is found for longer wavelengths, as shown in Figs. 2(a) and 2(b). This unusual behavior is at variance with the common picture of local field enhancement used in surface enhanced Raman scattering, for example [11], where a significant enhancement is expected only close to the SPR. For weakly interacting particles [$d > \max(R_{Au}, R_{Ag})$], the field enhancement deduced from the FEM simulations is in good agreement with that calculated analytically, using the dipolar approximation for the field scattered by the silver particle

$$\mathbf{E}_{s,Ag} = \frac{1}{4\pi\epsilon_0\epsilon_m r^3}[3(\mathbf{p}_{Ag}\cdot\mathbf{e}_r)\mathbf{e}_r - \mathbf{p}_{Ag}]. \quad (3)$$

r and $\mathbf{e}_r$ are the distance and the direction from the localized dipole, $\mathbf{p}_{Ag} = \epsilon_0\epsilon_m\alpha_{Ag}\mathbf{E}_i$, to the point where the field is evaluated. The relatively weak enhancement at the silver SPR is indeed due to the large distance between the particle center ($r = d + R_{Au} + R_{Ag}$), and the constant value of the enhancement below the silver SPR (longer wavelengths) simply arises from the polarizability α, which is almost independent of the wavelength ($|\epsilon_p| \gg |\epsilon_m|$). In the strong coupling regime [$d < \max(R_{Au}, R_{Ag})$], the optical properties of the silver particle are significantly modified, so that the previous approach is no longer valid and leads to a largely overestimated enhancements around the silver SPR.

The effects of the surrounding medium, through its dielectric constant ϵ_m, on the Fano profiles were also studied (data not shown here). Since the normalized cross section for an isolated particle

$$Q^{\infty}_{abs,Au} = \frac{k}{\pi R^2_{Au}}\,\mathrm{Im}(\alpha_{Au}) \quad (4)$$

already depends on ϵ_m through both the wave vector k in the surrounding medium and the polarizability α_{Au} [1], the obtained results for the heterogeneous dimer $Q_{abs,Au}$ were normalized by $Q^{\infty}_{abs,Au}$. Doing so, $Q_{abs,Au}/Q^{\infty}_{abs,Au}$ was found to be almost independent of ϵ_m (and approx. equal to 1.5) below the silver SPR (longer wavelengths) for $R =$ 5 nm, $d = 3$ nm, and ϵ_m ranging from 1 to 2. In contrast, the Fano profiles in $Q_{abs,Au}/Q^{\infty}_{abs,Au}$ are frequency shifted, following the SPR of the silver particle, and enhanced as ϵ_m is increased. Those observations can be explained by the ϵ_m dependence of the field scattered by the silver nanoparticle $\mathbf{E}_{s,Ag}$ [cf. Eq. (3)]. The latter is directly proportional to the polarizability α_{Ag} (through $\mathbf{p}_{Ag}$), which is almost independent of ϵ_m for long wavelengths and strongly depends on ϵ_m close to the silver SPR, as expected.

As shown by Eq. (3), the dephasing between the incident and the scattered field, responsible for the observed Fano profiles, not only depends on the polarizability of the silver particle (included in $\mathbf{p}_{Ag}$). It also depends on the relative orientation of the dimer axis (along $\mathbf{e}_r$) with respect to the incident field (parallel to $\mathbf{p}_{Ag}$). The results obtained by the FEM simulations are shown in Fig. 3 where the angle γ between the incident field $\mathbf{E}_i$ and the dimer axis is varied from 0 to $\pi/2$. A clear phase shift is observed together with a reduction of the Fano profile amplitude, as expected from Eq. (3). Hence, in a hybridization picture [2], the coupling parameter between the two particles can be easily adjusted by rotating the polarization angle, allowing us to externally control the coupling regime from the weak to the strong limit.

Interestingly, all curves of Fig. 3 cross in a single point around 381 nm. This can be understood if one keeps in mind that only two eigenmodes of the heterogeneous dimer can be excited (at $\gamma = 0$ and $\gamma = \pi/2$) in the configuration of Fig. 3. Hence, the dimer response is a linear combination of the two eigenmode responses, leading to an isobestic point (independent of γ) where the two curves corresponding to $\gamma = 0$ and $\gamma = \pi/2$ crosses. A striking consequence is that $Q_{abs,Au}$ is larger than $Q^{\infty}_{abs,Au}$ whatever (i) the incident polarization at the isobestic point and (ii) the incident wavelength for a particular value of γ (here $\gamma = \pi/3$), as shown by the intermediate bold curve of Fig. 3. The latter case can be surprising at first glance from Eq. (3), owing to the phase shift of α_{Ag}, and hence of $\mathbf{p}_{Ag}$, while going from one side to the other of the silver SPR spectrum. This singular behavior arises when the scattered field $\mathbf{E}_{s,Ag}$ experienced by the gold particle is perpendicular to the incident field $\mathbf{E}_i$ [the corresponding value of γ can be obtained by setting $\mathbf{E}_{s,Ag}.\mathbf{E}_i = 0$ in Eq. (3)]. In that case, the rms amplitude of the electric field experienced by the gold particle, $\propto(|E_{s,Ag}|^2 + |E_i|^2)^{1/2}$, is always larger than that of the incident field, $\propto|E_i|$, whatever the phase of α_{Ag}.

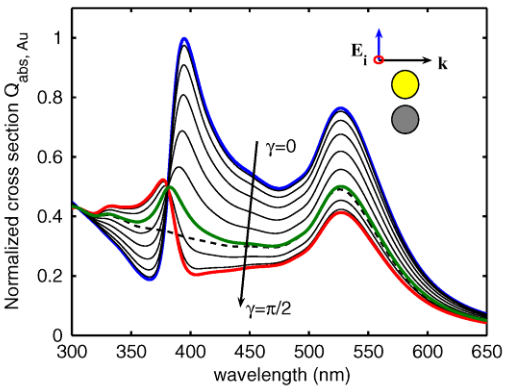

FIG. 3 (color online). Normalized absorption cross section of a $R = 5$ nm gold nanoparticle as a function of the angle γ between the incoming electric field and the dimer axis (the wave vector is perpendicular to the dimer axis). The bold lines from top to bottom (as indicated by the arrow) correspond to $\gamma = 0$, $\pi/3$, and $\pi/2$, respectively. For the thin lines, γ increases by steps of 10 degrees. The dashed curves correspond to the absorption cross section of an isolated gold particle. The radius of the silver nanoparticle is 5 nm and the interparticle distance 3 nm.

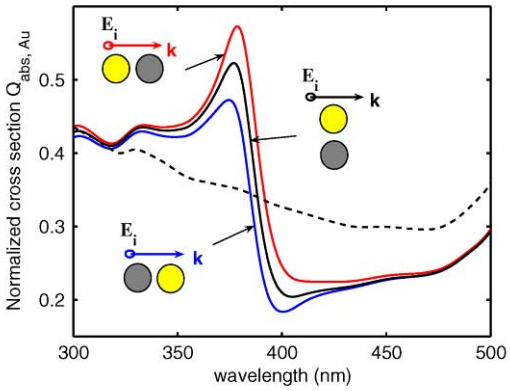

FIG. 4 (color online). Normalized absorption cross section of a $R = 5$ nm gold nanoparticle as a function of the orientation of the dimer with respect to the incoming wave vector. The light gray and gray disks correspond to the gold and silver particles, respectively. The incoming electric field is always perpendicular to the dimer axis ($\gamma = \pi/2$) and the dashed curves correspond to the absorption cross section of an isolated gold particle.

Finally, we would like to discuss the influence of the incidence angle with respect to the dimer axis. In order to decouple this effect from that of the polarization angle γ, the dimer axis $\mathbf{e}_r$was chosen perpendicular to $\mathbf{E}_i$ in all cases. Following Eq. (3), the electric field $\mathbf{E}_{s,\mathrm{Ag}}$ scattered by the silver particle in the dipolar approximation is therefore parallel to $\mathbf{E}_i$ and of constant amplitude whatever the dimer orientation [the first term in brackets of Eq. (3) cancels out]. Hence, in this simple model, no particular effect is expected while rotating the heterogeneous dimer. This is at variance with the results of the FEM simulations reported in Fig. 4. The dependence of the absorption in the gold particle on the orientation of the dimer is a signature of the "shadowing" effect, observed here despite the small nanoparticles size with respect to the wavelength ($R = 5$ nm). This shadowing effect, not present in Eq. (3), is sensitive only close to the silver SPR. It is therefore a direct consequence of the strong coupling regime due to the large field enhancement associated with the silver SPR. Note that the dimer orientation leads to a global increase or decrease of the normalized absorption cross section $Q_{\mathrm{abs,Au}}$, in contrast with the effect of polarization shown in Fig. 3. Therefore, a precise investigation of the absorption in the gold nanoparticle allows in principle to determine the 3D orientation of the heterogeneous dimer, owing to its noncentrosymmetry.

In conclusion, we have explored theoretically the linear optical properties of a heterogeneous dimer composed of a gold and a silver nanoparticle. Fano profiles in the absorption of the gold nanoparticle have been evidenced due to the near-field coupling between the silver SPR and the gold interband transitions. It is shown that (i) the Fano profiles are strongly enhanced while decreasing the gap between the particles and the ratio $R_{\mathrm{Au}}/R_{\mathrm{Ag}}$ until the gold nanoparticle is fully included in the near-field region of the silver particle, (ii) the enhancement of the gold nanoparticle absorption is large not only close to the silver SPR but also for longer wavelengths where it is found to be constant, (iii) it is possible to externally control the coupling regime by rotating the incident polarization, and (iv) the orientation of the heterogeneous dimer can be determined using the shadowing effect, even for particles small compared to the wavelength. The experimental observation of the Fano profiles in heterogeneous dimers is challenging using linear spectroscopy since they are hardly visible on the absorption spectra of the dimers. However, they could be easily observable by nonlinear spectroscopy, using for instance two-color femtosecond pump-probe approach to excite the dimer and selectively probe its gold component.

[1] C. F. Bohren and D. R. Huffman, *Absorption and Scattering of Light by Small Particles* (Wiley Interscience, New York, 1983); U. Kreibig and M. Vollmer, *Optical Properties of Metal Clusters* (Springer, Berlin, 1995).
[2] P. Nordlander, C. Oubre, E. Prodan, K. Li, and M. I. Stockman, Nano Lett. **4**, 899 (2004).
[3] L. Gunnarsson, T. Rindzevicius, J. Prikulis, B. Kasemo, M. Kall, S. L. Zou, and G. C. Schatz, J. Phys. Chem. B **109**, 1079 (2005).
[4] O. L. Muskens, V. Giannini, J. A. Sanchez-Gil, and J. G. Rivas, Opt. Express **15**, 17 736 (2007).
[5] P. Billaud *et al.*, J. Phys. Chem. C **112**, 978 (2008).
[6] I. Romero, J. Aizpurua, G. W. Bryant, and F. J. G. de Abajo, Opt. Express **14**, 9988 (2006).
[7] R. Sardar, T. B. Heap, and J. S. Shumaker-Parry, J. Am. Chem. Soc. **129**, 5356 (2007).
[8] P. Ahonen, D. J. Schiffrin, J. Paprotny, and K. Kontturi, Phys. Chem. Chem. Phys. **9**, 651 (2007).
[9] M. Ringler *et al.*, Nano Lett. **7**, 2753 (2007).
[10] M. Danckwerts and L. Novotny, Phys. Rev. Lett. **98**, 026104 (2007).
[11] C. E. Talley, J. B. Jackson, C. Oubre, N. K. Grady, C. W. Hollars, S. M. Lane, T. R. Huser, P. Nordlander, and N. J. Halas, Nano Lett. **5**, 1569 (2005).
[12] J. Zhang, Y. Fu, M. H. Chowdhury, and J. R. Lakowicz, Nano Lett. **7**, 2101 (2007).
[13] C. Dahmen, B. Schmidt, and G. von Plessen, Nano Lett. **7**, 318 (2007).
[14] A. S. Zelenina, R. Quidant, and M. Nieto-Vesperinas, Opt. Lett. **32**, 1156 (2007).
[15] U. Fano, Phys. Rev. **124**, 1866 (1961).
[16] A. M. Kelley, Nano Lett. **7**, 3235 (2007).
[17] W. Zhang, A. O. Govorov, and G. W. Bryant, Phys. Rev. Lett. **97**, 146804 (2006).
[18] A. Christ, Y. Ekinci, H. H. Solak, N. A. Gippius, S. G. Tikhodeev, and O. J. F. Martin, Phys. Rev. B **76**, 201405 (R) (2007).
[19] J. Jin, *The Finite Elements Method in Electrodynamics* (Wiley Interscience, New York, 2002).
[20] P. B. Johnson and R. W. Christy, Phys. Rev. B **6**, 4370 (1972).
[21] R. A. Molina, D. Weinmann, and R. A. Jalabert, Phys. Rev. B **65**, 155427 (2002).

La plasmonique non-linéaire

1- Génération de second harmonique dans les métaux nobles

L'optique non-linéaire et plus particulièrement la génération de second harmonique (SHG), processus du second ordre où deux photons à la fréquence fondamentale sont convertis en un photon à la fréquence harmonique, constitue le cœur du travail de l'équipe de Pierre-François Brevet, avec deux orientations principales: l'étude des nanoparticules de métaux nobles, qui est l'activité "historique" de l'équipe, et plus récemment l'application aux molécules organiques ayant des implications dans des systèmes biologiques. Ici encore, les métaux nobles jouent un rôle singulier de part la présence des résonances plasmons, qui vont exalter la réponse non-linéaire, mais aussi et surtout à cause de la centrosymétrie de la maille cristalline de ces métaux (cubique face centrée). Pourquoi cette dernière joue-t-elle un rôle déterminant dans la génération de photons harmoniques alors que n'avons pas eu besoin de l'évoquer dans le cas des propriétés optiques linéaires? Revenons quelques instants sur le fait que la SHG est un processus non linéaire d'ordre 2. Lorsque l'on excite fortement un système, sa polarisation ne dépend plus linéairement du champ électrique et des termes supplémentaires, proportionnels aux des puissances successives du champ, apparaissent:

$$\vec{P}(\vec{r},t) = \varepsilon_0 \chi^{(1)} \vec{E}(\vec{r},t) + \varepsilon_0 \vec{\vec{\chi}}^{(2)} : \vec{E}(\vec{r},t)\vec{E}(\vec{r},t) + ...$$

où $\chi^{(1)}$ et $\vec{\vec{\chi}}^{(2)}$ sont les tenseurs de susceptibilité d'ordre 1 et 2. Intéressons nous par exemple à la composante radiale E_r du champ dans le cas d'une excitation d'un milieu centrosymétrique par une onde plane. On considèrera le champ comme localement uniforme. Lorsque l'on passe du point de coordonnée $\vec{r}$ au point de coordonnée $-\vec{r}$ cette composante E_r change de signe, tout comme la polarisation linéaire associée (les susceptibilités sont invariante dans le milieu centrosymétrique). C'est ce qui donne naissance à la réponse dipolaire du matériau. Dans le cas non-linéaire, les choses sont bien différentes: le changement $E_r \rightarrow -E_r$ laisse la polarisation invariante. Le matériau va donc créer en $\vec{r}$ et $-\vec{r}$ des polarisations non-linéaires

qui vont se compenser, ne permettant pas d'exciter de photons harmoniques dans l'approximation dipolaire: le processus SHG est interdit.

Quelle sont alors les sources des courants non-linéaires dans les métaux nobles? Elles sont de deux types. La première, intrinsèque au matériau massif, peut se comprendre aisément en considérant les forces de Lorentz qui s'appliquent sur les électrons du métal considérés comme libres:

$$\vec{F} = q\vec{E} + q\vec{v} \times \vec{B}$$

Dans le cas d'une onde plane, l'amplitude du champ magnétique vaut $B=E/c$. Pour des électrons non relativistes, le mouvement dominant est donc donné par le premier terme, conformément au modèle de Drude, induisant une oscillation collective des électrons dans le sens du champ électrique (perpendiculairement au vecteur d'onde incident). Le second terme apparait quant-à lui comme un terme correctif. Il a pour effet de dévier légèrement les électrons. Ces derniers se déplacent alors selon des arcs de cercle, créant une polarisation supplémentaire parallèle à la direction de propagation de l'onde fondamentale et oscillant à la pulsation 2ω: de part la géométrie de l'arc de cercle, la position de l'électron selon le vecteur d'onde oscille deux fois plus vite que celle parallèle au champ électrique. Voilà donc bien un effet non-linéaire d'ordre 2. Une autre manière de s'en convaincre est de considérer que la vitesse des électrons est proportionnelle au champ électrique en première approximation (cf. modèle de Drude), de sorte que le second terme de la force de Lorentz fait intervenir le produit E^2/c. Plus intéressant encore, le champ magnétique est relié au champ électrique via la relation de Maxwell-Faraday (induction):

$$-\frac{\partial \vec{B}}{\partial t} = \vec{\nabla} \times \vec{E}$$

Ainsi, en régime harmonique, la polarisation non-linéaire du matériau est directement reliée à la variation spatiale du champ électrique dans la direction du vecteur d'onde incident et donc aux effets retards (prise en compte des termes quadrupolaire, octupolaires, etc.). On comprend ainsi aisément pourquoi il a fallu dépasser l'approximation dipolaire pour faire apparaître cette contribution. D'autre part, la polarisation non-linéaire induite ne dépend plus de la valeur du champ électrique en un point donné mais de sa variation spatiale. Elle peut donc être vue comme une contribution volumique non-locale. De manière générale, la polarisation volumique s'écrit, après réorganisation des termes:

$$\vec{P}_{bulk}(\vec{r},2\omega) = \gamma_{bulk}\vec{\nabla}\left[\vec{E}(\vec{r},\omega)^2\right] + \delta_{bulk}\left[\vec{E}(\vec{r},\omega).\vec{\nabla}\right]\vec{E}(\vec{r},\omega)$$

où γ_{bulk} et δ_{bulk} sont les susceptibilités non locales de volume. Il est à noter que dans le cas des métaux nobles et de l'utilisation d'un seul faisceau, le second terme s'annule.

La deuxième contribution non-linéaire dans les métaux nobles vient de l'existence de l'interface entre le matériau et le milieu extérieur. Cette interface rompt localement la centrosymétrie de la maille cristalline, dont nous avons discuté précédemment, autorisant de fait une génération locale, surfacique, de photons harmoniques. Pour un milieux isotrope et centrosymétrique, la susceptibilité surfacique correspondante se réduit drastiquement à seulement trois composantes indépendantes $\chi_{s,\perp\perp\perp}$, $\chi_{s,//\perp}$ et $\chi_{s,\perp//}$ où $//$ et $\perp$ correspondent aux directions parallèles et perpendiculaires à l'interface. Cependant, tant du point de vue théorique qu'expérimental il a été montré que la composante $\chi_{s,\perp//}$ ne contribuait que faiblement à la SHG. Ainsi, les deux composantes dominantes de la polarisation surfacique s'écrivent

$$\vec{P}_{surf,\perp}(\vec{r},2\omega) = \chi_{s,\perp\perp\perp}\vec{E}_{\perp}(\vec{r},\omega)\vec{E}_{\perp}(\vec{r},\omega)$$

$$\vec{P}_{surf,//}(\vec{r},2\omega) = \chi_{s,//\perp}\vec{E}_{//}(\vec{r},\omega)\vec{E}_{\perp}(\vec{r},\omega)$$

La connaissance de $\chi_{s,\perp\perp\perp}$, $\chi_{s,//\perp}$ et γ_{bulk} permet donc de déterminer complètement la réponse non-linéaire des métaux nobles. Ces susceptibilités s'expriment généralement en fonction des paramètres adimensionnels *a*, *b* et *d* introduits par Rüdnick et Stern

$$\chi_{s,\perp\perp\perp} = -\frac{a}{4}\left[\varepsilon_r(\omega)-1\right]\frac{e\varepsilon_0}{m\omega^2}$$

$$\chi_{s,//\perp} = -\frac{b}{2}\left[\varepsilon_r(\omega)-1\right]\frac{e\varepsilon_0}{m\omega^2}$$

$$\gamma_{bulk} = -\frac{d}{8}\left[\varepsilon_r(\omega)-1\right]\frac{e\varepsilon_0}{m\omega^2}$$

où *e* et *m* sont la charge et la masse de l'électron. Tout l'intérêt de cette notation est que dans le cadre du modèle hydrodynamique utilisé pour décrire les électrons de conduction, les paramètres de Rüdnick et Stern se réduisent à $a = 1$, $b = -1$ et $d = 1$. Si les valeurs de *b* et *d* sont assez robustes en fonction des modèles utilisés, il en va tout autrement pour le paramètre *a* traduisant un courant non-linéaire perpendiculaire à la surface. Ceci se comprend aisément de part la discontinuité du matériau au niveau de l'interface: la conservation de la charge induit des variations de la densité électronique sur des échelles très petites (comparables à la longueur de Fermi) qui ne peuvent pas être prises en compte dans un modèle purement macroscopique. Des travaux utilisant la fonctionnelle de la densité ont notamment montré que

ce paramètre peut être résonant, donc complexe, et très largement supérieur à l'unité en module... L'étude tant théorique qu'expérimentale de ces paramètres a longtemps agité la communauté scientifique (pendant plus de trois décennies avec de multiples rebondissements et quelques centaines d'articles passionnants au demeurant) sans pour autant trouver de réponse définitive, les calculs quantiques prenant en compte la structure cristalline étant trop complexes pour être menés jusqu'au bout et comparés aux expériences... La question est donc encore largement ouverte.

2- Origine de la SHG dans les nanoparticules

A quelle nouvelle physique peut-on s'attendre dans les nanoparticules de métaux nobles? De la même manière que les résonances plasmons de surface jouent un rôle déterminant en optique linéaire avec, comme nous l'avons vu, des modifications drastiques de la réponse spectrale en fonction de la taille mais surtout de la forme des particules et de possibles effets d'interaction, ces résonances vont induire un comportement singulier dans la génération de second harmonique. L'amplification des champs est bien sûr un ingrédient clé qui va donner à ces particules une efficacité non-linéaire très importante comparée à d'autres systèmes comme des molécules par exemple. Mais il y a plus intéressant encore puisque ces particules ont pour effet de structurer le champ, induisant des effets de localisation très importants notamment dans des gaps entre particules. Un corolaire est que le poids respectif des sources non-linéaires peut être fortement affecté dans les nanostructures métalliques puisque, comme nous l'avons vu, les courants non-locaux de volumes sont proportionnels au gradient de l'intensité du champ fondamental. Je vous propose ainsi dans cette partie de retracer ma quête de l'origine de la SHG dans les particules métalliques, quête qui a focalisé mon attention depuis mon arrivée au sein de l'équipe de Pierre-François Brevet. Il s'agit là, incontestablement du plus beau travail scientifique que j'ai réalisé à ce jour, mais aussi du plus long à arriver à maturité, tant les difficultés à franchir et les pistes théoriques et expérimentales à explorer étaient nombreuses. Mon but était donc de comprendre et d'expliquer quantitativement l'origine du phénomène physique. Pour ce faire, pas moins de cinq années de travail ont été nécessaires avant de pouvoir, enfin, proposer une configuration expérimentale permettant de quantifier les différentes sources non-linéaires.

2.1- Effet de taille sur l'excitation des multipôles

L'un des résultats marquants obtenus avant mon arrivée dans l'équipe concernait la dépendance en taille de la génération de second harmonique et plus précisément de la diffusion hyper Rayleigh (HRS) de nanoparticules en solution, thématique portée par Isabelle Russier-Antoine. Dans cette technique, les particules étant réparties aléatoirement et évoluant sans aucune corrélation dans le temps, leurs contributions s'ajoutent de manière incohérente et se trouvent être moyennées sur toutes les orientations possibles des particules. Dans le dispositif construit au sein de l'équipe, les photons harmoniques sont collectés à 90 degrés par rapport au faisceau incident et l'intensité est enregistrée en fonction de la polarisation du champ électrique fondamental caractérisée par l'angle γ (cf. figure 13). Les photons harmoniques sont quant à eux sélectionnés avec une polarisation dans le plan de diffusion (polarisation horizontale H) ou perpendiculairement à ce plan (polarisation verticale V).

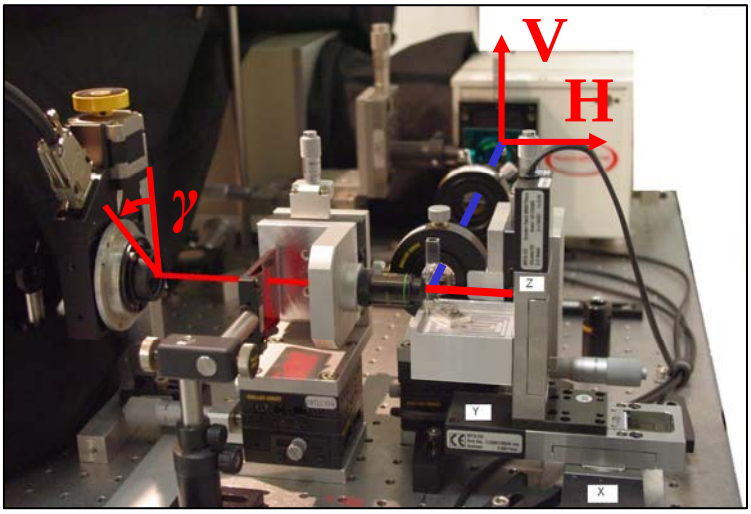

Figure 13: *Dispositif permettant la cartographie 3D du signal SHG d'une particule unique dans une cellule de gélatine. Le faisceau incident (en rouge) est focalisé par l'objectif de microscope et le signal harmonique collecté à 90° (faisceau bleu) par un système de deux lentilles. La polarisation du faisceau incident (angle γ) et celle du signal diffusé (V et H) sont ajustées à l'aide de lames λ/2 (et d'un cube polariseur pour le signal diffusé). Le filtre rouge bloque tout signal de second harmonique généré avant l'échantillon et le filtre rouge supprime la partie du faisceau à la fréquence fondamentale pouvant être diffusée vers le photomultiplicateur.*

L'acquisition du signal se fait par l'intermédiaire d'un monochromateur qui permet de réaliser un spectre autour de la fréquence harmonique et de discriminer la contribution de la fluorescence multiphotonique (au moins trois photons) présentant un spectre large de celle de la génération de second harmonique. Ces deux processus étant incohérents entre eux, un simple fit permet se soustraire la contribution de la fluorescence et de ne conserver que la partie du signal SHG. Comme nous le verrons par la suite, et tout particulièrement dans l'étude d'une particule unique, le nombre de photons est souvent faible. Pour améliorer autant que possible le rapport signal sur bruit, le comptage de photon est synchronisé avec un hacheur optique réalisant sur deux voies indépendantes l'acquisition du signal recueilli avec (porte ouverte) et sans (porte fermée) l'excitation de l'échantillon par le laser. Julien Duboisset, alors en thèse dans l'équipe, avait également porté une attention toute particulière à l'optimisation du discriminent pour optimiser la réjection des coups de bruit.

La figure 14 présente des courbes typiques obtenues pour une polarisation verticale des photons harmoniques avec des particules d'or de 20 et 150 nm de diamètre. La représentation sous forme de diagramme polaire en fonction de la polarisation incidente est particulièrement intéressante ici car elle permet une lecture directe de l'origine de la réponse en terme de multipôles (au sens de la théorie de Mie): la génération de second harmonique est ainsi dominée, à l'émission et pour les petites tailles, par une réponse dipolaire (moment cinétique $l = 1$) tandis que celles des plus grosses particules tend fortement vers une réponse quadripolaire ($l = 2$).

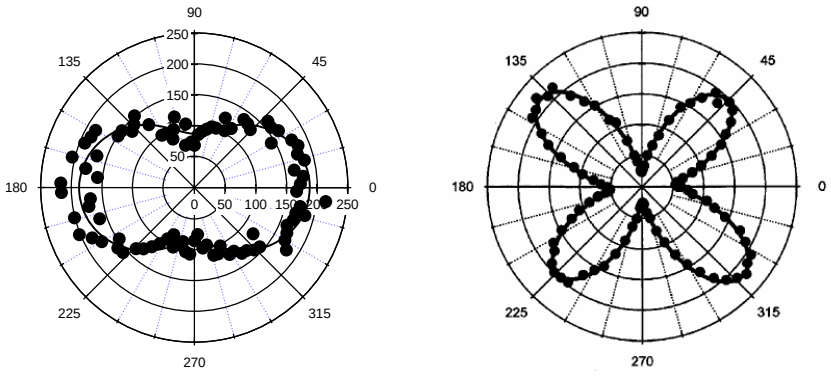

Figure 14: *Intensité HRS collectée perpendiculairement au faisceau incident en fonction de la polarisation du champ (0 correspond à un champ perpendiculaire au plan de diffusion, c'est-à-dire une polarisation verticale). Le signal est analysé verticalement pour une particule d'or de diamètre 20 nm (diagramme polaire de gauche) et 150 nm (droite) et une longueur d'excitation voisine de 800 nm.*

Cette évolution pourrait paraître naturelle, avec l'intervention progressive des effets retard, si nous n'avions pas vu dans la partie précédente que la génération de second harmonique est précisément interdite dans l'approximation dipolaire. Il faut toute fois être prudent. En effet, et c'est peut être passé inaperçu en première lecture, ces graphiques polaires ne nous renseignent que sur le multipôle mis en jeu à l'émission mais ne disent finalement rien sur les multipôles intervenant à l'excitation, les effets retard pouvant intervenir à cette étape du processus. Néanmoins, on peut monter par des arguments de symétrie (nous y reviendrons plus tard dans la partie 2.3) que seuls les modes possédant une valeur de *l* paire peuvent être observés dans cette configuration pour des particules sphériques (les modes impairs sont vus pour une polarisation H). Les diagrammes polaires obtenus pour des particules de petites tailles violent donc les règles de sélection. L'explication avancée était que les particules produites par synthèse chimique ne sont pas parfaitement sphériques, de sorte que les courants nonlinéaires de surface ne se compensent plus exactement, autorisant de fait une réponse dipolaire de type surfacique. Pour des particules de plus grande taille, les effets retards prennent le dessus, conduisant à une réponse majoritairement quadripolaire, comme attendu pour des particules parfaitement sphériques. Cette transition dipôle - quadripôle s'est par la suite vue confirmée avec des particules d'argent.

Dans ce scénario parfaitement huilé, l'étude de la dépendance en taille de l'intensité HRS va quelque peu brouiller les pistes. Si l'on considère des particules d'or, l'intensité semble, à première vue, varier comme le carré de la surface *S* pour des tailles allant de 20nm à 150nm de diamètre. L'interprétation proposée était donc que l'origine de la génération de second harmonique était de type surfacique, en accord avec l'évolution en S^2. Pourtant, si l'on tient compte des effets retard, responsables de l'observation des modes quadripolaires dans les plus grosses tailles, cela introduit une dépendance supplémentaire en *R* pour le champ électrique de part les développements à l'ordre supérieur en R/λ. L'intensité devrait donc varier en V^2. Comme le montre la figure 15, on pourrait se convaincre que la dépendance en taille augmente avec la taille, mais il faut rester prudent étant donnée la dispersion des points. Les mêmes expériences effectuées pour les particules d'argent conduisent au contraire à une dépendance en V^2 quelque soit la taille des particules ($R \geq 10$ nm). On pourrait alors argumenter que les effets retard interviennent plus tôt dans les particules d'argent que dans les particules d'or, comme nous l'enseigne la théorie de Mie en optique linéaire, mais cet argument va à l'encontre de l'observation d'une forte émission dipolaire pour les petites particules d'argent. Il faut aussi mentionner que, dans le cas des particules d'argent, la résonance plasmon est proche de la fréquence harmonique dans l'approximation quasistatique

et qu'elle se décale rapidement vers le rouge lorsque la taille de la particule augmente (autour de 450 nm pour des particules de 80nm de diamètre dans l'eau). Ainsi, le signal devrait être plus exalté pour les petites particules que pour les grosses, ce qui aurait pour effet de diminuer et non d'augmenter la dépendance en taille de l'intensité HRS. Ainsi, à l'issue de ces études, si la nature des multipôles mis en jeu à l'émission des photons harmoniques est bien établie, l'origine en termes de source de surface ou de volume reste assez largement ouverte.

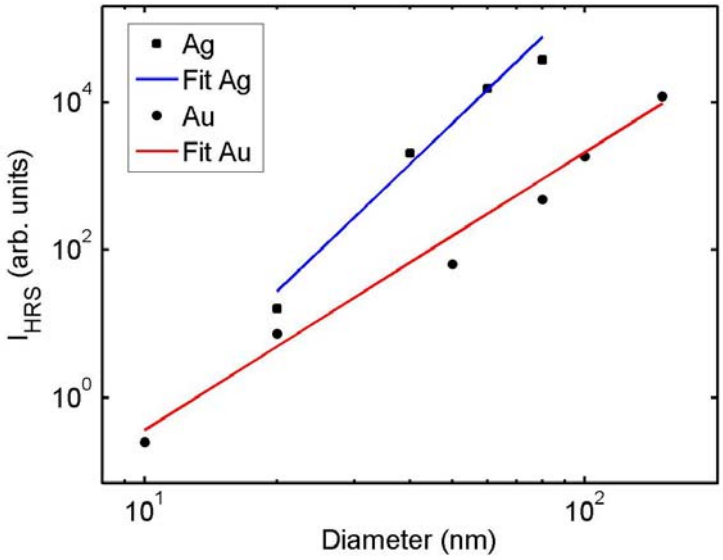

Figure 15: *Evolution de l'intensité HRS analysée verticalement en fonction de la taille des particules dans le cas de l'or et de l'argent.*

Multipolar Contributions of the Second Harmonic Generation from Silver and Gold Nanoparticles

I. Russier-Antoine,* E. Benichou, G. Bachelier, C. Jonin, and P. F. Brevet

Laboratoire de Spectrométrie Ionique et Moléculaire, UMR CNRS 5579, Université Claude Bernard Lyon 1, Bâtiment Alfred Kastler, 43 Boulevard du 11 Novembre 1918, 69622 Villeurbanne cedex, France

Received: November 13, 2006; In Final Form: May 4, 2007

Hyper Rayleigh scattering is used to investigate the second harmonic light collected from a liquid suspension of silver metallic particles, the diameter of which ranges from 20 nm up to 80 nm. From the dependence of the quadratic hyperpolarizability as a function of the particle size, it is inferred that retardation effects of the electromagnetic fields play a major role in the frequency conversion process. The hyper Rayleigh scattering intensity was also recorded as a function of the angle of polarization of the incident fundamental wave. For the particles with a diameter of 20 nm, the harmonic response is dominated by the dipolar contribution arising from the deviation of the particle shape from that of a perfect sphere. It is therefore concluded that the origin of the nonlinear polarization for the smaller silver particle sizes arises from the surface similarly to the case of the gold metallic particles. For larger diameter particles, retardation effects in the interaction of the electromagnetic fields with the particles cannot be neglected any longer, and the response deviates from the pure dipolar response, exhibiting a strong quadrupolar contribution. The weighting parameter ζ^V is used, equaling unity for a pure quadrupolar contribution and vanishing for a pure dipolar response, in order to quantify the relative magnitude of these two dipolar and quadrupolar contributions. The size dependence of this parameter obtained for the silver particles is compared to the dependence previously reported for gold metallic particles.

I Introduction

Over the past decade, the interest in small metal particles, especially gold and silver metallic particles, has dramatically increased, mostly because of their unique optical and electronic properties. These properties are dominated by the collective excitation of the conduction band electrons known as the surface plasmon resonance (SPR).[1] These particles can be used as the building blocks of more elaborate structures where the arrangement of the particles is crucial for the use of these architectures in future devices. These properties are often investigated by optical methods, principally linear optical methods, but more recently, nonlinear optical methods have been successively used. This is due to the large enhancements expected for the electromagnetic fields through the SPR.[2] For particles dispersed in a liquid solution, a method of choice is hyper Rayleigh scattering (HRS), namely, the scattering of the incoherent light produced by the conversion of two photons at a fundamental frequency into one photon at the harmonic frequency.[3,4] SPR enhancement can be obtained at the fundamental or the harmonic frequency yielding more versatility, although SPR enhancement at the fundamental frequency is usually avoided in order to preserve the sample solution from degradation. As a result, large magnitudes for the hyperpolarizability tensor of silver and gold nanoparticles have been reported.[5−8] However, for perfectly spherical metallic nanoparticles that are small compared with the wavelength of light, in the electric dipole approximation, no HRS signal intensity should be collected owing to the centrosymmetry of both the material crystal structure and the shape of the particle.[9−13] This paradox has been solved for metallic gold particles. Indeed, it has been demonstrated that the frequency conversion process finds its origin at the surface of the particles when the shape of the particles is not perfectly spherical. As a consequence, the total HRS response is of electric dipole nature for small particles; however, for larger particles, retardation effects in the electromagnetic fields must be considered, and a non negligible quadrupolar contribution is observed.[12,14,15] It has been demonstrated that a similar origin for the HRS process occurs for silver particles. Furthermore, the influence of the fundamental wavelength used in these experiments on the weight of the electric dipolar and quadrupolar contributions to the HRS signal intensity has also been discussed.[16] It is however of interest to perform a more refined comparison between gold particles and silver particles in order to discuss in greater details the role and the appearance of the retardation effects of the electromagnetic fields in the second harmonic generation (SHG) process. In aqueous suspensions, the SPR is located at about 520 nm for gold metallic particles with diameters in the range of a few tens of nanometers, and therefore, for a harmonic wavelength of 400 nm, the SPR enhancement is weaker than for silver metallic particles, the SPR location of which is located at about 420 nm for similar sizes. On the opposite side, the HRS response for gold metallic particles should be dominated by an interband transitions resonance enhancement. Hence, it is of interest to investigate thoroughly the size effects in silver particles as well and compare the data to the case of the gold metallic particles. This present work therefore relates to the angle-resolved SHG measurements performed previously on molecules adsorbed at the surface of colloidal particles.[17,18]

In the present work, the value of the hyperpolarizability tensor magnitude is reported for aqueous suspensions of silver metallic

* Corresponding author. Phone: +33 472 431 914. Fax: +33 472 445 871. E-mail: russier@lasim.univ-lyon1.fr.

10.1021/jp0675025 CCC: $37.00
Published on Web 06/09/2007

particles, the diameter of which ranges from 20 up to 80 nm in a first section. It is demonstrated that although the origin of the second harmonic generation arises from the surface of the particles, the size dependence of the SH intensity exhibits a scaling with the volume of the particles. Then, in a second section, the theoretical framework to describe the multipolar contributions of the SHG process is discussed. In a last section, the case of large diameter particles is presented, and the results are recast in the general context of the electric dipole and quadrupole contributions to the HRS intensity. Finally, the results obtained here for silver particles are compared to those previously obtained for gold ones.

II Experimental Section

The light source of these HRS experiments was a mode-locked Ti:sapphire laser delivering at fundamental wavelengths of 780 nm pulses with a duration of about 170 fs at a repetition rate of 76 MHz. After passing through a low-pass filter to remove any unwanted harmonic light generated prior to the cell, the fundamental beam of about 700 mW was focused by a microscope objective into a 1 × 1 cm spectrophotometric cell containing the aqueous solutions of the metallic particles. The HRS light was collected at an angle of 90° from the incident direction by a lens with a 5 cm long focal length and a 5 cm diameter. The second harmonic light was separated from its linear counterpart by a high-pass filter, and a monochromator was positioned on the second harmonic wavelength. The HRS light was then detected with a cooled photomultiplier tube, and the pulses were counted with a photon counter. The fundamental beam was chopped at about 97 Hz to enable the gated photon counting mode allowing automatic subtraction of the noise level. The fundamental input beam was linearly polarized, and the input angle of polarization γ was selected with a rotating half-wave plate. The configuration of the experimental setup was such that the fundamental beam was propagating in the Z direction with the electric field polarized in the $\{X,Y\}$ plane with the polarization angle γ. The harmonic light was collected along the Y direction, at right angle from the fundamental beam propagation direction. In all experiments reported, the polarization state of the harmonic light was selected along the X axis, namely, the harmonic light was vertically polarized.

The silver nanoparticles were purchased from British Biocell International (United Kingdom, diameters of 20, 40, 60, and 80 nm) and used as received.

III Results and Discussion

A. Hyperpolarizability Magnitudes. The initial experiments consisted of the determination of the absolute hyperpolarizability tensor magnitudes of the silver metallic particles as a function of their diameter. The latter diameter ranged between 20 and 80 nm. This experiment entails the dilution of the initial concentrated solution since the HRS intensity is given by:[3,4]

$$I_{\mathrm{HRS}} = G\langle N_S\beta_S{}^2 + N\beta^2\rangle I^2 \qquad (1)$$

where I is the fundamental intensity, N_S and N and β_S and β are the number densities and the hyperpolarizabilities of a solvent molecule and a silver particle, respectively. The HRS intensity was always corrected for self-absorption in the cell from the focal point to the exit cell wall. G is a general factor embedding all geometrical factors as well as absolute constants. Finally, the brackets stand for an orientational average owing to the isotropy of the liquid phase. The measurement of the HRS intensity in the absence of particles provides an internal reference for the determination of the absolute values of the first quadratic hyperpolarizabilities since N_S and β_S are known. For water, the value of $\beta_S = 0.56 \times 10^{-30}$ esu (electrostatic unit) was used.[6]

TABLE 1: Absolute Magnitude of the First Hyperpolarizability Tensor for Gold ($\beta_{Au}/10^{-25}$ esu) and Silver ($\beta_{Ag}/10^{-25}$ esu) Metallic Particles for Several Diameters at the Harmonic Wavelength of 400 and 390 nm, Respectively[a]

diameter/nm	$\beta_{Au}/10^{-25}$ esu	$\beta_{Ag}/10^{-25}$ esu
10	0.5	
20	2.7	4
40		45
50	8	
60		124
80	22	194
100	43	
150	109	

[a] Data for gold are taken from ref 14. All hyperpolarizabilities present errors of about 10%. 10^{-50} C^3 × m^3 × J^{-2} = 2.694×10^{-30} esu.

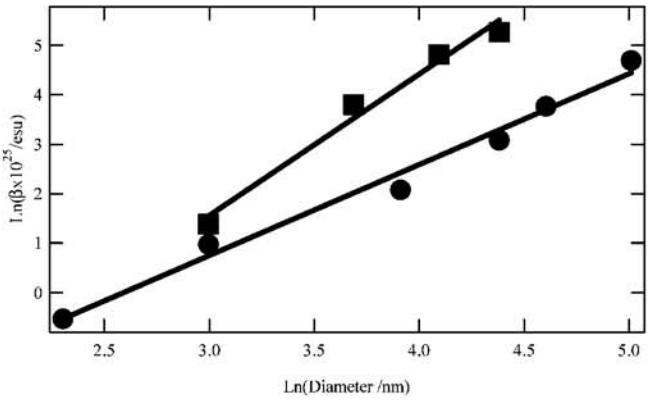

Figure 1. Log−log plot of the hyperpolarizability magnitude against the particle diameter for silver and gold particles at the harmonic wavelength of 390 and 400 nm, respectively. All data are taken from Table 1.

The quadratic hyperpolarizability tensor magnitudes are reported in Table 1. The values obtained for gold metallic particles are given for comparison at the fundamental wavelength of 800 nm instead of 780 nm for the silver particles. Rather large magnitudes are observed for the silver particles as compared with the gold ones. The SPR enhancement for the silver particles is indeed rather strong owing to the harmonic wavelength used in these experiments which is in close vicinity with the SPR wavelength. The hyperpolarizability magnitudes reported for the silver particles are in excellent agreement with previously reported data.[5,12] To determine the origin of the response at the harmonic frequency and in particular to distinguish between a volume and a surface origin, the log−log plot corresponding to the data of Table 1 is given in Figure 1. For gold metallic particles, a value of 1.9 ± 0.2 was found for the slope, indicating that the origin of the phenomenon was arising from the surface of the particles. On Figure 1, a slope of 2.9 ± 0.3 is found for the silver metallic particles. This result is markedly different from that of the gold particles and indicates a scaling of the HRS intensity with the volume of the particles. As it has been pointed out in the past, the slope of the log−log plot of the hyperpolarizability magnitude against the diameter of the particle is 2 for a surface origin and 3 for a volume origin of the conversion process. In the former case, the hyperpolarizability magnitude will indeed scale with the area of the particle surface, whereas in the latter case it will scale with its volume. At this stage, it is therefore questionable whether the origin of

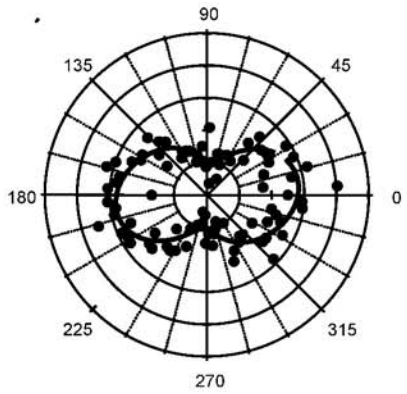

Figure 2. Polar plot of the HRS intensity as a function of the incoming fundamental beam polarization angle: (filled circles) experimental points and (solid) fit to the experimental data points using eq 2 for an aqueous suspensions of 20 nm diameter silver particles for a harmonic wavelength of 390 nm vertically polarized.

the SH response from silver metallic particles is similar to that of the gold metallic particles or not.

To investigate further this question, in Figure 2 is displayed a polar plot of the HRS intensity as a function of the angle of polarization of the linearly polarized fundamental beam for 20 nm diameter silver particles. For vertically polarized harmonic light collected at 390 nm, two lobes are clearly observed as expected for the local pure electric dipole response from noncentrosymmetrical particles.[13] Along with the experimental points is displayed the curve adjusted with the following expression of the HRS intensity:

$$I_{\mathrm{HRS}}^{\Gamma} = a^{\Gamma} \cos^4 \gamma + b^{\Gamma} \cos^2 \gamma \sin^2 \gamma + c^{\Gamma} \sin^4 \gamma \qquad (2)$$

where the different parameters a^{Γ}, b^{Γ}, and c^{Γ}, can be related to the initial parameters of eq 1 once the solvent contribution has been removed. For the output harmonic light vertically polarized, namely, for $\Gamma = 0$ also denoted as $\Gamma = V$, the coefficients must obey the equality $b^V = a^V + c^V$ if the origin is a purely electric dipole.[14] For the 20 nm diameter particles, one gets $a^V = 0.68 \pm 0.03$ and $c^V = 0.26 \pm 0.03$ with the normalizing parameter $b^V = 1$ in close agreement with a purely electric dipole response under experimental uncertainties. The observation of two lobes in Figure 2 clearly indicates that the response is largely dominated by the electric dipole response and thus that the origin of the second harmonic process stems from the surface of the particle. This result is therefore in line with the conclusion reached for the case of the gold nanoparticles. It has been previously observed that, for 40 nm diameter silver particles, this equality was however broken.[16] This feature is a clear indication that, although the origin of the nonlinearity stems from the surface, the electric quadrupole contribution arising from the finite size of the particles cannot be neglected at diameters as small as 40 nm for silver particles.

B. Electric Dipole and Quadrupole Contributions. In order to investigate further this problem of the multipolar response of the HRS intensity for gold and silver particles, the problem of the origin of the conversion phenomenon of two photons at the fundamental frequency into one photon at the harmonic frequency is investigated. Several theoretical and experimental works have been devoted to this question for particles.[5−7,9,10] At the microscopic scale, the breaking of the centrosymmetry required for the harmonic generation process is located at the surface of the particle. Hence, it is customary to introduce a corresponding nonlinear polarization contribution localized at the surface of the particle. Next, it is also customary to introduce for metallic surfaces contributions arising from the bulk material even if some of them are only effective at the surface. Finally, owing to the description of rather large particles with diameters in the range of up to more than 100 nm, the approximation where the electromagnetic fields are spatially constant over the volume of the particle is not suitable anymore. Higher orders of the electromagnetic fields spatial expansion must be incorporated into the description. As a result, the total nonlinear polarization consists of different contributions in line with the models originally derived for planar metallic surfaces.[19−21] The HRS intensity therefore also consists of several contributions. The first one dominates at very small diameters and is usually called purely local. This is the electric dipole approximation which may vanish if the small metallic particle is perfectly centrosymmetrical. This would be the case if the particles are perfectly spherical. This contribution noted here as $\vec{a}_{\mathrm{eff}}$ is actually identical to the one observed for any noncentrosymmetrical point-like objects such as efficient rod-like push−pull molecules[22] and may be represented through the scheme $E_1 + E_1 \rightarrow E_1$, where E_1 stands for the spatially invariant contribution of the electric field. The pattern of the HRS intensity as a function of the angle of polarization of the incoming fundamental field is well-known in this case. It is characteristic of its electric dipole nature and present two lobes oriented along the 0°−180° axis. The second contribution is 1 order of magnitude smaller and scales with the ratio of the particle diameter a and the fundamental wavelength λ, namely, $x = a/\lambda$. This contribution must be introduced when the diameter of the particles is no longer negligible before the wavelength whatever the exact shape of the particle. This contribution has been discussed for perfectly spherical particles as well as its pattern as a function of the angle of polarization of the incoming fundamental field.[13,23] This pattern is that of four lobes oriented on the 45°, 135°, 225°, and 315° axes when the vertically polarized harmonic output is considered and is that of a circle when the horizontally polarized harmonic output is measured. It is itself the sum of two contributions. The first one noted $\vec{p}_{\mathrm{eff}}$ arises from the retardation effect at the fundamental frequency and is often described as the nonlocal excitation of the surface nonlinearity. It may be represented through the scheme $E_1 + E_2 \rightarrow E_1$ where E_2 stands for the first correction to the electric field with respect to its spatial variation. The second one, noted $\vec{Q}_{\mathrm{eff}}(\hat{n})$, arises from the retardation at the harmonic frequency and is usually described as the nonlocal radiation at the harmonic frequency. It may be described through the scheme $E_1 + E_1 \rightarrow E_2$.

Hence, in a rather general manner, the total HRS field amplitude may be decomposed as:

$$\vec{E}^{(\Omega)}(\vec{r}) = \frac{\Omega^2 [n^{(\Omega)}]^2}{c^2} \frac{e^{iKr}}{r} [\hat{n} \times (\vec{a}_{\mathrm{eff}} + x\{\vec{p}_{\mathrm{eff}} + \vec{Q}_{\mathrm{eff}}(\hat{n})\})] \times \hat{n} \qquad (3)$$

In eq 3, the direction of collection of the harmonic light is $\hat{n} = \vec{r}/r$, the harmonic frequency is $\Omega = 2\omega$, and the optical index of the surrounding medium at the harmonic frequency is $n^{(\Omega)}$. Also, the harmonic wave vector is such that $K = 2n^{(\Omega)}\Omega/c$. Hence, $\vec{a}_{\mathrm{eff}}$ is a locally excited dipole contribution whereas $\vec{p}_{\mathrm{eff}}$ is a nonlocally excited dipole contribution and $\vec{Q}_{\mathrm{eff}}(\hat{n})$ is an electric quadrupole contribution. Finally, the role of the polarization must be emphasized. The pure electric dipole term $\vec{a}_{\mathrm{eff}}$ may have contributions in both the vertical and the horizontal

component of the harmonic amplitude $\vec{E}^{(\Omega)}(\vec{r})$. This is not the case for the two other terms. It has been shown that $\vec{p}_{\text{eff}}$ only contributes to the horizontal component of the harmonic amplitude owing to its orientation along the direction of propagation of the fundamental beam, whereas $\vec{Q}_{\text{eff}}(\hat{n})$ only contributes to the vertical component of the harmonic amplitude if $\hat{n} = \vec{r}/r$, the direction of collection of the harmonic light, is at a right angle from the fundamental beam incident direction.[13,23] Hence, in experiments where only the vertical component of the harmonic amplitude is measured, only the $\vec{a}_{\text{eff}}$ and $\vec{Q}_{\text{eff}}(\hat{n})$ contributions will be observed.

In the case of gold metallic particles, it has been determined that the local electric dipole contribution to the HRS signal intensity dominates over the electric quadrupole contribution for small diameter particles.[14] Indeed, the electric dipole contribution arises from the breaking of the centrosymmetry of the particle owing to an imperfect spherical shape. At large diameters, however, the electric quadrupole contributions $\vec{Q}_{\text{eff}}(\hat{n})$ dominate though. In the present case of the silver metallic particles, already at rather small diameters, the electric quadrupole contribution $\vec{Q}_{\text{eff}}(\hat{n})$ does dominate over the electric dipole contribution $\vec{a}_{\text{eff}}$. Indeed, the local electric dipole contribution scales with the area of the particle surface, whereas the electric quadrupole contribution scale with the volume of the particles. The measured slope of 2.9 ± 0.3 therefore indicates that the electric quadrupole contribution dominates for silver particles at the excitation wavelength of 780 nm. A slope of 2 should therefore be recovered at diameters smaller than 40 nm just like a slope of 3 improves the fitting procedure at large diameters for the gold particles. Nevertheless, one may still wonder whether silver metallic particles are closer to the perfect spherical shape than gold metallic particles or if retardation effects dominate already for smaller sizes in the case of silver particles. A first argument supporting the latter hypothesis rather than the former one is found in the comparison of their synthesis. Both particles are synthesized through the salt reduction method, and it would be surprising that for silver this procedure would lead to particles closer to the perfect spherical shape than it would for gold. Another possibility is the proximity of the harmonic wavelength with the SPR wavelength in the case of silver particles. Resonance enhancements are known to alter the weight of the different contributions depending on the excitation wavelength. This question has been discussed concerning the wavelength dependence of the polarization resolved HRS measurements performed on 40 nm diameter silver metallic particles.[16,24] The observation of a clear electric dipole pattern unambiguously confirmed that the origin was stemming from the breaking of the centrosymmetry of the particles and that in this respect the silver particles behave like the gold particles. Such a surface origin is in agreement with the previously reported results for a hemispherical boss, another noncentrosymmetrical geometry.[25,26]

C. Retardation Contribution at Large Sizes. In order to get a broader view of the problem at hand, Figure 3a−c reports the polar plots of the HRS intensity vertically polarized as a function of the angle of polarization of the fundamental incoming beam for different sizes. The two-lobe pattern disappears with the increasing particle diameter to leave a clear four-lobe pattern. This four-lobe pattern is not regular as demonstrated by the size inequality between the lobes. In particular, the lobes at 45° and 225° are larger than the ones collected at 135° and 315°. As a result, eq 2 is no longer valid.

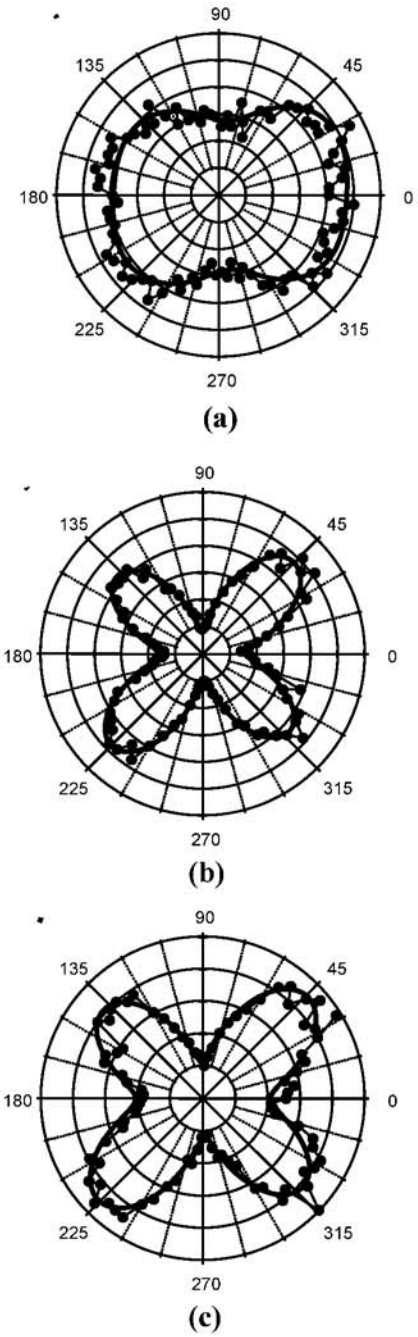

Figure 3. Polar plot of the HRS intensity as a function of the incoming fundamental beam polarization angle: (filled circles) experimental points and (solid) fit to the experimental data points using eq 4 for aqueous suspensions of (a) 40 nm, (b) 60 nm, and (c) 80 nm diameter silver particles for a harmonic wavelength of 390 nm vertically polarized.

The equality between the coefficients $b^V = a^V + c^V$ is no longer preserved, and two new coefficients must be introduced:

$$I_{\text{HRS}}^{\Gamma} = a^{\Gamma}\cos^4\gamma + b^{\Gamma}\cos^2\gamma\sin^2\gamma + c^{\Gamma}\sin^4\gamma + d^{\Gamma}\cos^3\gamma\sin\gamma + e^{\Gamma}\cos\gamma\sin^3\gamma \quad (4)$$

The presence of these two new parameters d^{Γ} and e^{Γ} only arise for the larger particle diameters and therefore should be related to retardation effects. They are required in order to adjust for the experimental observation of the size inequality of the lobes. Their origin is not clear yet, but their magnitude nevertheless remains weak in front of the other parameters. Since the breaking of the equality $b^V = a^V + c^V$ is explained by the

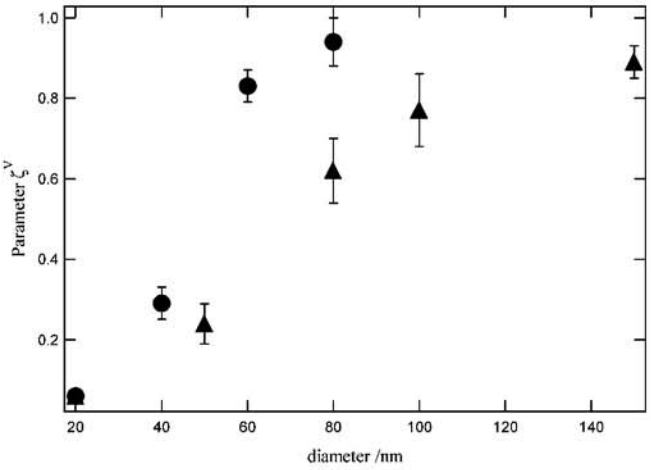

Figure 4. Plot of the ζ^V parameter as a function of the diameter of the (circle) silver metallic particles at 390 nm and (triangle) gold metallic particles at 400 nm as a function of the diameter.

increase of the electric quadrupole contribution, a quantitative approach may be given using the weighting parameter ζ^V defined by:

$$\zeta^V = \left| \frac{b^V - (a^V + c^V)}{b^V} \right| \tag{5}$$

Figure 4 reports the value obtained at 390 nm for the silver particles and that obtained at 400 nm for the gold particles. All of the data points obtained for the silver particles are above the ones obtained for the gold particles. This clearly underlines that although the origin of the response for both metallic particles is identical, the electric quadrupole contribution appears at smaller diameters for silver particles. Hence, since this contribution scales with the volume of the particles, the log−log plot of the hyperpolarizability tensor magnitude as a function of the diameter exhibits a slope of 2.9 ± 0.3 in agreement with this conclusion. Finally, it has to be added that introducing the retardation effect at large sizes of the particles accounts rather well for all of the experimental data provided so far. It is thus still opened whether a volume contribution of the nonlinear polarization arising from field gradients should be incorporated as well, in line with a recent theoretical approach developed.[26]

Conclusion

In conclusion, this study confirms that the first hyperpolarizability of the small gold and silver metallic nanoparticles used in these studies is of electric dipole origin and arises from a deviation of the shape of the nanoparticles from that of a perfect sphere. Within a general framework including both the electric dipole and the electric quadrupole contributions, the size dependence of the absolute values of the hyperpolarizability tensor magnitude with the volume of the particle and the polarization resolved HRS intensity plots are correctly described at all diameters. For silver metallic particles and a harmonic wavelength of 390 nm, both the electric dipole and the electric quadrupole surface plasmon resonance enhancements occur yielding a behavior different from the one observed for the gold metallic particles. The weighting parameter ζ^V used to quantify the different behavior of the gold and the silver particles is therefore very sensitive to the particle material.

References and Notes

(1) Kreibig, U.; Vollmer, *Optical Properties of Small Particles*; Wiley: New York.
(2) Antoine, R.; Brevet, P. F.; Girault, H. H.; Bethell, D.; Schiffrin, D. J. *Chem. Commun.* **1997**, 1901.
(3) Clays, K.; Persoons, A. *Phys. Rev. Lett.* **1991**, *66*, 2980.
(4) Clays, K.; Persoons, A. *Rev. Sci. Instrum.* **1992**, *63*, 3285.
(5) Clays, K.; Hendrickx, E.; Triest, M.; Persoons, A. *J. Mol. Liq.* **1995**, *67*, 133.
(6) Vance, F. W.; Lemon, B. I.; Hupp, J. T. *J. Phys. Chem. B* **1998**, *102*, 10091.
(7) Galletto, P.; Brevet, P. F.; Girault, H. H.; Antoine, R.; Broyer, M. *Chem. Commun.* **1999**, 581.
(8) Johnson, R. C.; Li, J.; Hupp, J. T.; Schatz, G. C. *Chem. Phys. Lett.* **2002**, *356*, 534.
(9) Agarwal, G. S.; Jha, S. S. *Solid State Commun.* **1982**, *41*, 499.
(10) Oestling, D.; Stampfli, P.; Bennemann, K. H. *Z. Phys. D: At., Mol. Clusters* **1993**, *28*, 169.
(11) Brudny, V.; Mendoza, B. S.; Mochan, W. L. *Phys. Rev. B* **2000**, *62*, 11152.
(12) Hao, E. C.; Schatz, G. C.; Johnson, R. C.; Hupp, J. T. *J. Chem. Phys.* **2002**, *117*, 5963.
(13) Dadap, J. I.; Shan, J.; Eisenthal, K. B.; Heinz, T. F. *Phys. Rev. Lett.* **1999**, *83*, 4045.
(14) Nappa, J.; Revillod, G.; Russier-Antoine, I.; Benichou, E.; Jonin, C.; Brevet, P. F. *Phys. Rev. B* **2005**, *71*, 165407.
(15) Shan, J.; Dadap, J. I.; Stiopkin, I.; Reider, G. A.; Heinz, T. F. *Phys. Rev. A* **2006**, *73*, 023819.
(16) Nappa, J.; Russier-Antoine, I.; Benichou, E.; Jonin, C.; Brevet, P. F. *Chem. Phys. Lett.* **2005**, *415*, 246.
(17) Yang, N.; Angerer, W. E.; Yodh, A. G. *Phys. Rev. Lett.* **2001**, *87*, 103902.
(18) Jen, S. H.; Dai, H. L. *J. Phys. Chem. B* **2006**, *110*, 23000.
(19) Brown, F.; Parks, R. E.; Sleeper, A. M. *Phys. Rev. Lett.* **1965**, *14*, 1029.
(20) Jha, S. S. *Phys. Rev. Lett.* **1965**, *15*, 412.
(21) Brown, F.; Mastuoka, M. *Phys. Rev.* **1969**, *185*, 985.
(22) Brasselet, S.; Zyss, J. *J. Opt. Soc. Am. B* **1998**, *15*, 257.
(23) Nappa, J.; Revillod, G.; Abid, J. P.; Russier-Antoine, I.; Jonin, Ch.; Benichou, E.; Girault, H. H.; Brevet, P. F. *Faraday Discuss.* **2004**, *125*, 145.
(24) Russier-Antoine, I.; Jonin, C.; Nappa, J.; Benichou, E.; Brevet, P. F. *J. Chem. Phys.* **2004**, *120*, 10748.
(25) Chen, C. K.; Heinz, T. F.; Ricard, D.; Shen, Y. R. *Phys. Rev. B* **1983**, *27*, 1965.
(26) Dadap, J. I.; Shan, J.; Heinz, T. F. *J. Opt. Soc. Am. B* **2004**, *21*, 1328.

2.2- Développement des simulations par éléments finis

A la lumière des résultats expérimentaux et des difficultés dans leur analyse un constat s'imposait. Il fallait pouvoir rendre compte à la fois de la non-sphéricité des particules, des effets retards sur les champs électromagnétiques ainsi que des différentes sources non-linéaires: les courants locaux de surface et non-locaux de volume. Une méthode numérique était donc indispensable. Le fait de devoir intégrer des sources dans le volume du matériau excluait par principe les approches de type Boundary Element Method. Deux techniques numériques discrétisant le volume du matériau paraissaient particulièrement attractives: les différences finies (Finite Difference Time Domain) et les éléments finis (Finite Element Method). Cependant, dans nombre de travaux que j'ai pu voir en conférence ou dans la littérature, le champ électrique au voisinage des interfaces métal-matrice semblait être mal défini en FDTD, faisant apparaître une sorte de "halo" au voisinage de la surface. Ce problème de condition aux limites a peut-être été résolu depuis mais il était rédhibitoire dans le cadre des simulations que je souhaitais développer, dans la mesure où les courants non-linéaires de surface sont directement proportionnels au carré du champ évalué juste à l'extérieur de la particule. Ensuite, la FDTD se positionnant dans l'espace temporel, il faut en principe connaître l'évolution temporelle des grandeurs telles que la constante diélectrique $\varepsilon(\vec{r},t)$ et non leur expression dans l'espace des fréquences $\varepsilon(\vec{r},\omega)$. Si ce problème peut être résolu aisément dans le cas d'une forme simple de $\varepsilon(\vec{r},\omega)$, il me semblait plus que difficile de pouvoir faire de même en optique non-linéaire, pour la simple raison que personne ne connaît actuellement la dépendance fréquentielle des différentes susceptibilités non-linéaire $\chi_{s,\perp\perp\perp}$, $\chi_{s,///\perp}$ et γ_{bulk}, et encore moins leur évolution temporelle... C'est ainsi que mon choix s'est porté sur les simulations par éléments finis, bien que cette technique était nouvelle au sein du laboratoire et qu'elle n'avait été développée nulle part ailleurs pour l'optique non-linéaire dans les nanoparticules métalliques. Le pari était de taille mais les retombées potentielles conséquentes. Ainsi, après avoir fourbi mes armes (et essuyé quelques plâtres) sur l'optique linéaire, comme discuté dans la partie "plasmonique", je devais donc m'attacher à ce qui a été ma plus grosse contribution théorique depuis mon arrivée au sein du LASIM: les simulations par éléments finis de la génération de second harmonique.

Les premiers travaux ont naturellement porté sur le système le plus simple qui soit à savoir la sphère parfaite. Même si je n'avais pas de calculs analytiques pouvant se comparer quantitativement aux simulations numériques, contrairement au cas de l'optique linéaire, ce

système modèle avait pour vertu de me permettre de vérifier toutes les propriétés de symétrie que devaient satisfaire les simulations. Cependant, le seul moyen de ne pas travailler en aveugle (n'oublions pas que les simulations numérique ont un petit côté boite noire) était de coller le plus près de l'expérience. Je me suis ainsi intéressé très tôt à des particules non-sphériques telles que celle présentée dans la figure 16. L'idée était de dilater uniquement la partie supérieure dans une direction afin d'obtenir une particule non-centrosymétrique: un œuf. La particule ayant une symétrie plus basse que la sphère, les diagrammes de rayonnement à la fréquence harmonique sont assez fortement déformés et dépendent de l'orientation de la particule. Mais, une fois moyennées sur différentes orientations, les représentations polaires obtenues dans la figure 16 retrouvent un caractère parfaitement symétrique. Notons que les simulations étant très gourmandes en temps de calculs, le moyennage n'a été effectué que pour une rotation de la particule autour de l'axe z. La déformation choisie n'étant pas vraiment réaliste, le but était simplement de montrer les implications de la non-sphéricité des particules et non de rendre compte quantitativement des résultats expérimentaux.

Le point important ici est donc que les courbes obtenues sont symétriques après moyennage sur l'orientation de la particule (la symétrie sphérique est partiellement retrouvée). L'absence de symétrie dans certaines courbes expérimentales ne trouvait donc pas son origine dans la déformation des particules. Ce résultat étant le même quelque soit le courant non-linéaire choisi (surfacique ou volumique), l'hypothèse de la contribution d'un autre mécanisme que celui de surface généralement invoqué était écartée. Il restait donc la question de l'alignement du dispositif expérimental. Pour y répondre, j'ai simulé deux types de désalignements: un désalignement "vertical" (le faisceau incident plonge ou remonte après l'objectif de microscope) et un désalignement "horizontal" (le faisceau est dévié vers la gauche ou la droite, de sorte que le signal harmonique n'est plus collecté à 90 degrés). Les déformations obtenues sur les courbes en V et en H se sont révélées être en bon accord avec celles vues parfois expérimentalement. Plus intéressant encore, cette étude a montré que si l'effet d'un désalignement est relativement faible dans le cas d'une réponse dipolaire associés à une petite particule (ou à une molécule comme le DiA par exemple), plus la particule métallique est grosse et plus la symétrie de la courbe est affectée par le moindre défaut d'alignement. Une attention toute particulière doit donc être portée dans le cas d'une réponse multipolaire provenant des effets retards. Cela constitue d'ailleurs à présent un critère test de l'alignement du dispositif expérimental.

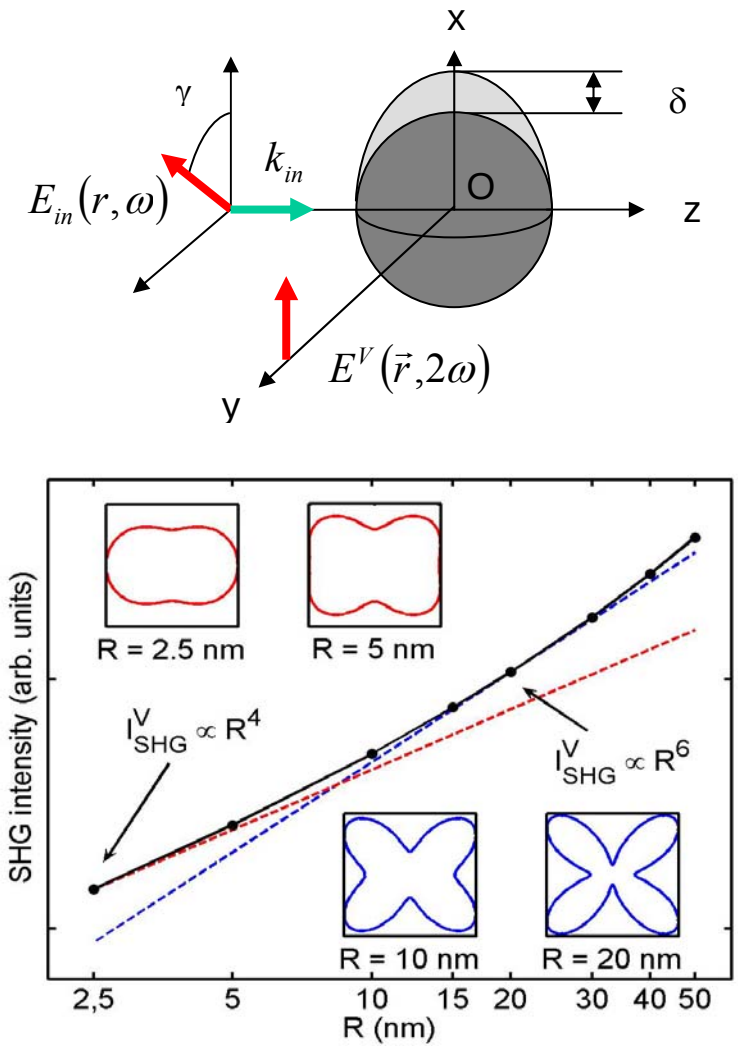

Figure 16: *Simulation par éléments finis de la réponse HRS polarisée verticalement dans le cas d'une particule déformée selon le schéma (ovoïde). La réponse est moyennée sur l'orientation de la particule. La dépendance du signal HRS en fonction de la polarisation incidente est donnée dans les inserts pour des rayons de 2.5 nm, 5 nm, 10 nm et 20 nm. La courbe représente l'évolution de l'intensité diffusée en fonction de la taille de la particule avec deux comportements limites (pointillés) correspondant à une dépendance en fonction du carré de la surface et du volume.*

Comme le montre la figure 16, les simulations ont permis de rendre compte des principaux résultats expérimentaux obtenus jusqu'alors dans le cas de particules d'or. Pour les petites tailles, la diffusion Hyper Rayleigh est dominée par la déformation de la particule, induisant une réponse dipolaire et une intensité évoluant comme le carré de la surface des particules. Au contraire, pour les grandes tailles, les effets retards prennent le dessus et la réponse de la particule se rapproche de celle d'une particule sphérique, à savoir qu'elle présente quatre lobes bien marqués et une intensité proportionnelle au carré du volume de la particule. Le fait que l'intensité ne s'annule pas pour des polarisations horizontales et

verticales du champ électrique fondamental est une signature de la non-sphéricité de la particule. Ainsi, si l'on cherche à comprendre l'origine de la réponse non-linéaire dans les métaux nobles, il faut choisir des particules de grande taille pour pouvoir s'affranchir autant que possible de l'effet de déformation. Notons que dans ces simulations, la transition dipôle-quadripôle se fait autour de 20 nm de diamètre, ce qui est très inférieur à la valeur observée expérimentalement. Ceci vient de la déformation très particulière que j'ai choisie et qui ne rend pas compte de la forme réelle des particules. Dans la pratique, il faudra prendre des particules de diamètre supérieur à la centaine de nanomètres pour que les effets de déformations deviennent faibles.

L'un des grands enseignements qu'ont également apportés ces premières simulations est que, contrairement à toute intuition et à ce qui a été largement écrit dans la littérature, la dépendance en taille (S^2 ou V^2) ne dit rien sur l'origine surfacique ou volumique de la réponse! Ceci mérite donc bien quelques explications. Ce résultat m'est tout d'abord apparu en reproduisant les simulations présentés dans la figure 16 pour les trois contributions: $\chi_{s,\perp\perp\perp}$, $\chi_{s,//\perp}$ et γ_{bulk}. Le résultat est sans appel: quelque soit le terme utilisé, la dépendance en taille de l'intensité HRS est la même. La seule légère différence observée est la taille pour laquelle la transition dipôle-quadripôle a lieu. Pour expliquer qualitativement l'origine de ce phénomène, il faut revenir à l'expression des polarisations non-linéaires que je rappelle ici par commodité:

$$\vec{P}_{surf,\perp}(\vec{r},2\omega) = \chi_{s,\perp\perp\perp}\vec{E}_{\perp}(\vec{r},\omega)\vec{E}_{\perp}(\vec{r},\omega)$$

$$\vec{P}_{surf,//}(\vec{r},2\omega) = \chi_{s,//\perp}\vec{E}_{//}(\vec{r},\omega)\vec{E}_{\perp}(\vec{r},\omega)$$

$$\vec{P}_{bulk}(\vec{r},2\omega) = \gamma_{bulk}\vec{\nabla}\left[\vec{E}(\vec{r},\omega)^2\right] + \delta_{bulk}\left[\vec{E}(\vec{r},\omega).\vec{\nabla}\right]\vec{E}(\vec{r},\omega)$$

Il y a ainsi une différence fondamentale entre les contributions locales de surface et non-locale de volume: l'apparition d'un gradient. Bien que la polarisation volumique ait à être intégrée sur le volume de la particule (d'où la proportionnalité attendue à *V*), le gradient introduit une dépendance supplémentaire en 1/r comme on peut aisément s'en convaincre au vu de l'expression des composantes transverses du gradient en coordonnées sphériques:

$$\frac{1}{r}\frac{\partial}{\partial\theta} \text{ et } \frac{1}{r\sin\theta}\frac{\partial}{\partial\varphi}.$$

C'est donc bien le caractère non-local de la contribution de volume qui lui conduit à la même dépendance en taille qu'une contribution locale de surface (le cas aurait été bien différent dans un milieu non-centrosymétrique où la contribution locale de volume domine). La conséquence

directe est que rien ne peut être déduit de la dépendance en taille (S^2 ou V^2) de l'intensité quant à l'origine surfacique ou volumique de la génération de second harmonique dans les métaux nobles. De ce constat s'en est suivi une longue "traversée du désert" afin de trouver un moyen de différentier les trois contributions $\chi_{s,\perp\perp\perp}$, $\chi_{s,//\perp}$ et γ_{bulk}. J'ai ainsi exploré de nombreuses pistes: effets de l'indice de réfraction de la matrice, de la forme des particules, etc., en vain. Jusqu'à ce que...

Multipolar second-harmonic generation in noble metal nanoparticles

Guillaume Bachelier, Isabelle Russier-Antoine, Emmanuel Benichou, Christian Jonin, and Pierre-François Brevet

Laboratoire de Spectrométrie Ionique et Moléculaire, Université Claude Bernard Lyon 1—CNRS UMR 5579, 43 Boulevard du 11 novembre 1918, 69622 Villeurbanne Cedex, France
**Corresponding author: guillaume.bachelier@lasim.univ-lyon1.fr*

Received November 15, 2007; revised February 26, 2008; accepted March 24, 2008; posted April 7, 2008 (Doc. ID 89723); published May 20, 2008

Second-harmonic generation from noble metal nanoparticles with a noncentrosymmetrical shape is theoretically investigated by using finite element method simulations. The relative weight of the dipolar and quadrupolar responses is investigated in terms of both light polarization and size dependence of the harmonic scattered intensity. It is shown that, even for small deformations as compared with purely spherical particles, the dipolar response dominates and scales as the nanoparticle surface area squared. The difference between gold and silver metal nanoparticles is also addressed. © 2008 Optical Society of America

OCIS codes: 190.2620, 190.4350, 240.4350, 240.6680.

1. INTRODUCTION

Noble metal nanoparticles have received increasing attention over the past years due to their optical properties governed by surface plasmon polaritons, the collective electronic oscillation coupled to the electromagnetic field, in the visible domain. These optical properties are highly sensitive not only to their environment but also to the particle morphology [1,2]. Recently, the convergence of transmission electron microscopy characterization, single nanoparticle detection, and numerical simulations has triggered an extensive interest in designing various particle shapes such as nanorods, nanocubes, nanorices, or nanostars to adjust the morphology to obtain the desired spectral responses [3–5]. Indeed, one of the main specificities of noble metals is their ability to support electric field localization at the nanometer scale owing to the evanescent character of the surrounding waves. This allows the eventual guiding of light below the diffraction limit [6]. This localization is also responsible for very large field enhancements of first interest in spectroscopic applications such as Raman scattering, and more particularly surface enhanced Raman scattering [7] or nonlinear optical processes such as two-photon luminescence or wave mixing [8]. This localization effect is furthermore strengthened at rough surfaces or random materials with the appearance of hot spots, leading to very large enhancements due to the overlap of fundamental and harmonic eigenmodes [9–11]. However, the spatial distribution of these hot spots being hardly predictable, another approach was proposed to tailor the electric field either by using sharp metal tips for near-field applications [12] or nanolenses composed of self-similar chains of nanoparticles [13].

Among all nonlinear optical phenomena, second harmonic generation (SHG) is the simplest, but like all even-order processes it is also forbidden within the electric dipole approximation in centrosymmetrical bulk materials such as noble metals like gold and silver [14–19]. For nanosized noble metal structures, this selection rule is still valid if one assumes a volume material structure identical to the bulk material one. Hence, in such structures, contributions arising from the breaking of centrosymmetry at the surface must be taken into account, since they may not be negligible anymore. However, if these structures also possess centrosymmetrical shapes, the surface SHG response will again vanish in the electric dipole approximation. Contributions involving quadrupolar surface plasmon polaritons associated with retardation effects either at the excitation or the radiation stage are therefore expected as well as contributions arising from nonlocal nonlinear sources. They are both responsible for a nonvanishing SHG intensity scaling with the square of the particle volume [14–19]. As a matter of fact, several experiments were performed recently on spherical gold nanoparticles showing a clear dipolar response for the smaller sizes together with a SHG intensity scaling with the particle surface area squared [20–22]. These results are at variance with the theoretical expectations for particles with centrosymmetrical shapes. Deviations from such regular shapes therefore had to be introduced to correctly account for the experimental data [21,22]. This approach has been further confirmed in recent results obtained with L-shaped nanoparticles, where the nonlinear optical properties are largely dominated by dipolelike contributions [23,24]. The aim in this work is thus to address the problems of the deviation from centrosymmetrical shapes and the retardation effects in the nonlinear properties of metal nanoparticles to clarify the origin of the observed discrepancies between experimental and theoretical results.

2. MODEL

Quadrupolar SHG is the expected response for spherical, and more generally centrosymmetrical, particles, and its size and light polarization dependence is now well established [14–19]. Deviations from these predictions may be

due to either heterogeneities in the particle volume, namely, a noncentrosymmetrical material structure, or to deviations from the spherical shape. At this point it must be stressed that the deviations could arise either from a genuine morphological deviation from the spherical shape, among other centrosymmetrical shapes like ellipsoids, for instance, or from an inhomogeneous surface adsorption layer, for example. It has to be pointed out, though, that the first case, with an origin arising from volume defects of the material structure, would lead to nonlinear sources distributed randomly in the particle volume and thus to a SHG intensity scaling with the particle volume squared. This is not in agreement with the experimental results [21,22]. For this reason, only the deviation of the particle shape from that of a perfect sphere is considered here.

To obtain a noncentrosymmetrical deformation, the top half-sphere of the particle was rescaled along the x axis (see Fig. 1) in such a way that the deformation can be parameterized with a single parameter, namely, $\delta R/R$, which corresponds to the relative increase of the particle radius along the x axis. This done, an analytical approach is no longer possible, and therefore finite element method (FEM) simulations were performed by using a commercial software (COMSOL Multiphysics). The electric field $\mathbf{E}(\mathbf{r},\omega)$ at the fundamental frequency was computed in the framework of the scattered field formulation by using perfectly matched layers to avoid spurious reflections at the surrounding medium boundaries [25]. The dielectric constants used for the metal particle were taken from [26].

The nonlinear sources of the SH field are usually recast into local and nonlocal responses, the latter involving not only the electric fields but also the electric field gradients. For centrosymmetrical materials, the appropriate nonlinear response is that composed of the surface local term

$$\mathbf{P}_{\mathrm{surf}}(\mathbf{r},2\omega) = \vec{\vec{\chi}}_{\mathrm{surf}}:\mathbf{E}(\mathbf{r},\omega)\mathbf{E}(\mathbf{r},\omega) \tag{1}$$

and the bulk nonlocal terms

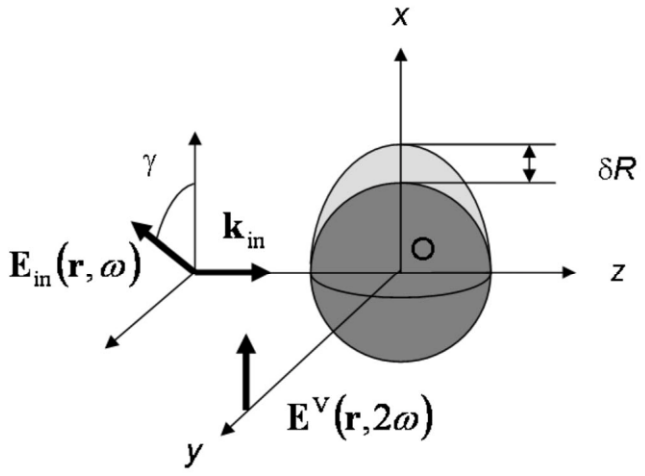

Fig. 1. Schematic of the geometrical configuration used for the simulations: γ is the angle of polarization of the linearly polarized incident beam $\mathbf{E}_{\mathrm{in}}(\mathbf{r},\omega)$ propagating along the z axis (wave vector $\mathbf{k}_{\mathrm{in}}$). δR corresponds to the deformation applied to the upper half-sphere part of the particle. The vertically polarized electric field $\mathbf{E}^{V}(\mathbf{r},2\omega)$ scattered at the harmonic frequency is collected at a right angle in the y axis direction.

$$\mathbf{P}_{\mathrm{bulk}}(\mathbf{r},2\omega) = \alpha\nabla[\mathbf{E}(\mathbf{r},\omega)\cdot\mathbf{E}(\mathbf{r},\omega)] + \beta[\mathbf{E}(\mathbf{r},\omega)\cdot\nabla]\mathbf{E}(\mathbf{r},\omega), \tag{2}$$

where $\mathbf{P}$ is the polarization vector, $\vec{\vec{\chi}}_{\mathrm{surf}}$ the second-order nonlinear susceptibility, and α and β two parameters defining the nonlocal nonlinear response [18,19]. The second bulk nonlocal term may dominate at the particle surface, but it has also been shown that it could be incorporated into the surface response [27]. The nonlinear currents, effectively the true sources of the electric field $\mathbf{E}(\mathbf{r},2\omega)$ at the harmonic frequency, were deduced in a second step from the spatial distribution of the polarization vector $\mathbf{P}$ through the well-known relation $\mathbf{J}(\mathbf{r},2\omega)=\partial\mathbf{P}(\mathbf{r},2\omega)/\partial t$. After the Maxwell equations were solved by using the weak formulation, the far-field component of the electric field at the harmonic frequency $\mathbf{E}(\mathbf{r},2\omega)$ was computed from the near-field component by using the Stratton–Chu formula [25]. This procedure allows us to evaluate a scattered SHG intensity that is, to some extent, comparable with the experimental data.

While solving Maxwell equations, we take into account all multipolar components in the sense of the scattering theory of both the fundamental and harmonic electric fields. However, for the sizes and the spherical shape deviations studied in the present work, the SHG scattered intensity is dominated mainly by the dipolar and quadrupolar terms. The aim in this work is therefore to weight the dipolar and quadrupolar responses driven by retardation and deformation effects. In this respect, the general behavior of all nonlinear sources, both surface and volume, were found to be similar, and thus the discussion will be limited to the surface local term only:

$$P_{\mathrm{surf},\perp}(\mathbf{r},2\omega) = \chi_{\mathrm{surf},\perp\perp\perp}E^{2}_{\mathrm{ex},\perp}(\mathbf{r},\omega), \tag{3}$$

where the nonlinear surface susceptibility tensor is reduced to the single element $\chi_{\mathrm{surf},\perp\perp\perp}$. $P_{\mathrm{surf},\perp}(\mathbf{r},2\omega)$ and $E_{\mathrm{ex},\perp}(\mathbf{r},\omega)$ are the surface nonlinear polarization and the fundamental electric field components perpendicular to the particle surface, respectively. The normal component of the electric field being discontinuous at the particle surface, the nonlinear current $J_{\mathrm{surf},\perp}(\mathbf{r},2\omega) = \partial P_{\mathrm{surf},\perp}(\mathbf{r},2\omega)/\partial t$ was arbitrarily computed by using the external fundamental field.

3. RESULTS AND DISCUSSION

A. Single Particle Response

The geometrical configuration used to compute the light scattered at the harmonic frequency is given in Fig. 1. The linear polarization of the incident electric field propagating along the z axis is defined with the angle γ, and the vertically polarized SHG intensity along the x axis is collected at the right angle in the y axis direction for direct comparison with the experimental setup used in a previous study [21,22]. The scattered harmonic intensity is plotted on a polar plot as a function of the incident polarization angle γ. For a perfectly spherical nanoparticle, typically 5 nm in radius, this plot reveals a typical four-lobe pattern corresponding to a pure quadrupolar response of a centrosymmetrical particle [14–19]. This pattern simply arises from the fact that for $\gamma=0[\pi/2]$, the

yOz plane is a symmetry plane for the nonlinear sources. Therefore, the component of the nonlinear electric field $\mathbf{E}^v(\mathbf{r},2\omega)$ perpendicular to the yOz plane vanishes in this case. When the particle is deformed in a noncentrosymmetrical way following the procedure described above (see Fig. 1), the yOz plane is no longer a symmetry plane, and a dominant dipolelike pattern is observed; see Fig. 2(a). It is interesting to note that the two major lobes are not symmetric with respect to the horizontal axis in Fig. 2, since the $+\gamma$ and $-\gamma$ polarization angles are no longer equivalent. The SHG response is thus not purely dipolar, containing a quadrupolar contribution as well; otherwise it would have been fully symmetrical with only two lobes. To account for the full γ dependence of the vertically polarized SHG intensity $I^V_{\mathrm{SHG}}(\gamma)$, the following expression was therefore used:

$$I^V_{\mathrm{SHG}}(\gamma) = a^V \cos^4(\gamma) + b^V \cos^2(\gamma)\sin^2(\gamma) + c^V \sin^4(\gamma) + d^V \cos^3(\gamma)\sin(\gamma) + e^V \cos(\gamma)\sin^3(\gamma), \quad (4)$$

where a^V, b^V, and c^V are the usual parameters regularly introduced in previous works, whereas d^V and e^V account for the asymmetry of the polar graphs introduced by the angle ϕ [21,22]. These latter parameters are necessary to account for the incomplete orientational averaging procedure over the orientations taken by the particles [28–30]. As shown in Figs. 2(a)–2(c), this expression perfectly accounts for the data points calculated with the FEM simulations.

B. Orientation Averaging Effect

The SHG experiments on metal nanoparticles are usually performed through hyper-Rayleigh scattering in solutions where the particle orientation is random [21,22]. The scattered intensity thus has to be averaged randomly over all particle orientations. To highlight the importance of such an averaging procedure, Figs. 2(a) and 2(c) show the results obtained when the particle is rotated around the z axis by the angles $\phi=\pi/4$ and $\phi=\pi/2$, respectively. For $\phi=\pi/2$, the yOz plane is again a plane of symmetry of the nonlinear sources for an incident polarization angle $\gamma=0[\pi/2]$. In this case, the polar graph recovers the four-equivalent-lobes pattern, as is the case for a perfect sphere. In contrast, the γ dependence of the SHG intensity for $\phi=\pi/4$ is highly distorted owing to the rotation by 45° of the particle x axis. Averaging over all values of the orientation angle ϕ [Fig. 2(d)], the polar graph recovers a fully symmetric pattern, leading to a vanishing value for the parameters d^V and e^V. The observed four-lobe response with nonvanishing intensity at $\gamma=0[\pi/2]$ is characteristic of the coexistence of both a dipolar and a quadrupolar contribution in the SHG response from the particle: the remaining intensity at $\gamma=0[\pi/2]$ is due to the pure dipolar response only.

A realistic comparison to the hyper-Rayleigh scattering experiments would require an averaging procedure over all 3D random orientations but also over the deformations of the particles. This is beyond the scope of the present work and the capacities of the simulations performed in this work. Hence, only the averaging involving a rotation about the z axis of Fig. 1 will be discussed to illustrate the salient features of the orientational effects.

C. Deformation Effect

The relative weight of the dipolar and the quadrupolar contributions strongly depends on the amplitude of the deformation applied to the particle as shown in Fig. 3. The larger the deviation from a perfect spherical shape,

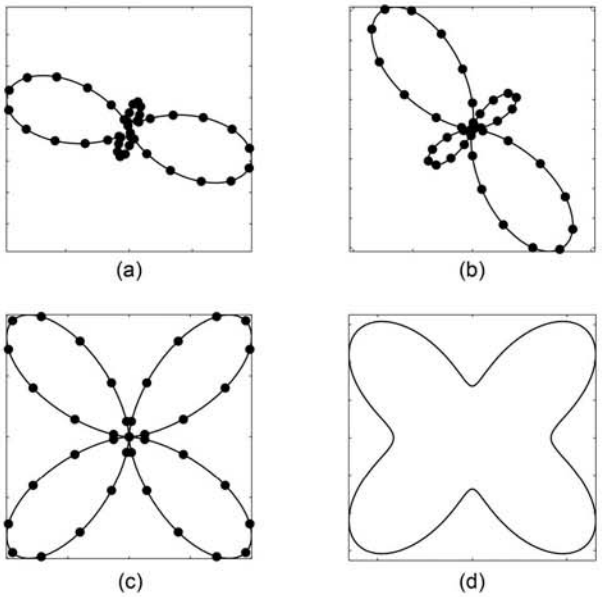

Fig. 2. Normalized polar plots of the vertically polarized SHG intensity as a function of the incident polarization angle γ for different orientation of the particle in the xOy plane determined by the angle ϕ: (a) $\phi=0$, (b) $\phi=\pi/4$, (c) $\phi=\pi/2$, (d) averaged. $\gamma=0$ coincides with the right-hand side of the horizontal axis, and γ increases anticlockwise. The radius of the gold particle is 5 nm, and the deformation is $\delta R/R=15\%$.

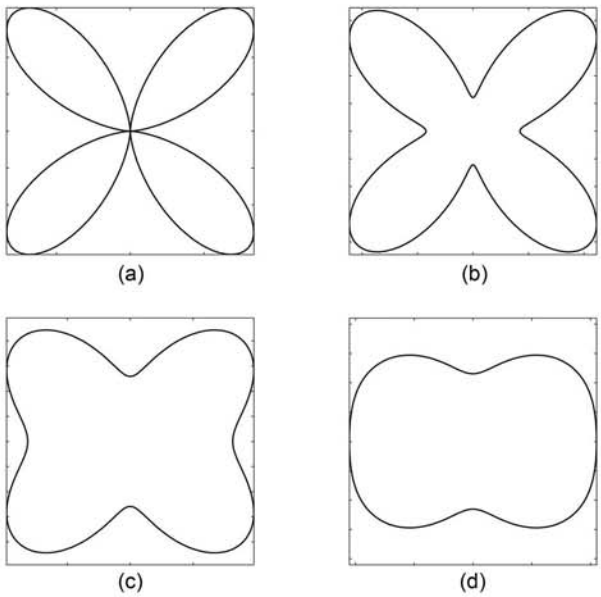

Fig. 3. Normalized polar plots of the vertically polarized SHG intensity as a function of the incident polarization angle γ for different deformations of a 5 nm radius gold particle. $\gamma=0$ coincides with the right-hand side of the horizontal axis, and γ increases anticlockwise. The scattered intensity is averaged over the orientations of the particles in the xOy plane determined by the angle ϕ. (a) $\delta R/R=0\%$, (b) $\delta R/R=10\%$, (c) $\delta R/R=20\%$, (d) $\delta R/R=40\%$.

the higher the dipolar contribution, as expected. To quantify the ratio between the two contributions, the weighting parameter ζ^V is introduced as [21,22,31]

$$\zeta^V = \left| \frac{b^V - (a^V + c^V)}{b^V} \right|. \quad (5)$$

Based on the fact that $a^V = c^V = 0$ for a pure quadrupolar pattern and $a^V + c^V = b^V$ for a pure dipolar one, ζ^V ranges from zero for a pure dipolar response to unity for a pure quadrupolar one. This is shown in Fig. 4 for a gold nanoparticle with a 5 nm radius and an increasing relative deformation $\delta R/R$. Despite the highly symmetrical deformation introduced—in particular this deformation possesses an axial symmetry leading to a rather regular shape—a strong dipolar response can already be achieved for a deformation of $\delta R/R = 30\%$, i.e., for a diameter increase of only 15% along the deformation axis. For more realistic noncentrosymmetrical deformations, including faceting, an even stronger dipolar contribution is expected, explaining why the second-harmonic response of small gold nanoparticles is essentially of dipolar type [21,22].

D. Size Effect

Now focusing on the size dependence of the vertically polarized SHG intensity for a given deformation of the particle, namely, $\delta R/R = 30\%$, a clear transition from a dipolar to a quadrupolar response is observed while the particle size is increased (see Fig. 5), despite the noncentrosymmetrical shape of the particle. This is attributed to the retardation effects taking place for larger nanosized particles, enhancing the quadrupolar contribution with respect to the dipolar one. This transition can be easily followed by using the weighting parameter ζ^V as shown in Fig. 4. The general trend of the ζ^V size dependence is in good agreement with the experimental data reported previously [21,22], although it is not possible to quantitatively reproduce the size at which the transition occurs ($\zeta^V = 0.5$), about 6 nm in radius in the present study in contrast to the 35 nm in radius reported experimentally. This originates from the rather smooth deformation used here for the FEM simulation as compared with the real morphology of the particles experimentally studied. It is thus not surprising that the agreement is only qualitative.

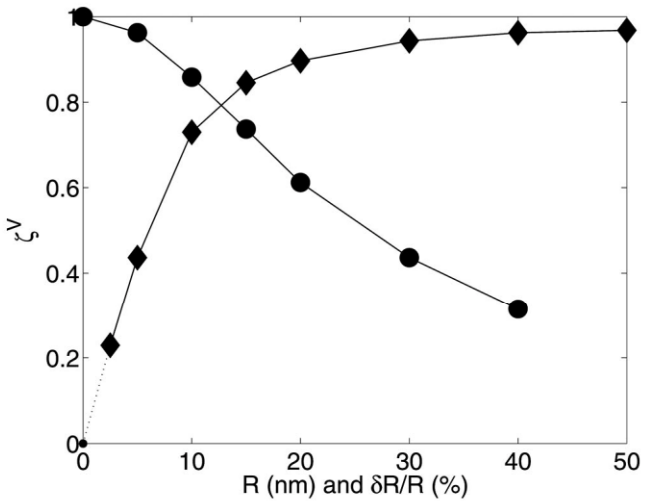

Fig. 4. Plot of the ζ^V parameter for a gold nanoparticle as a function of the relative deformation $\delta R/R$ (circles) for a fixed particle size (5 nm radius) and as a function of the particle size (diamonds) for a fixed deformation ($\delta R/R = 30\%$). The scattered intensity used for the computation of ζ^V is averaged over the orientations of the particles in the xOy plane determined by the angle ϕ. The lines are guides for the eye.

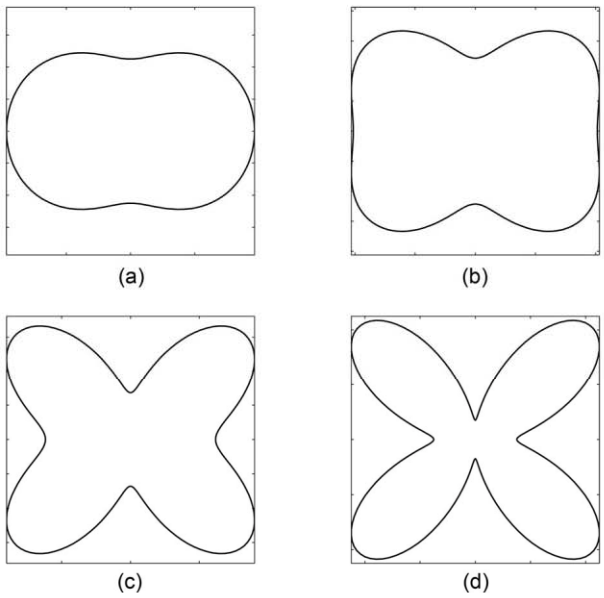

Fig. 5. Normalized polar plots of the vertically polarized SHG intensity as a function of the incident polarization angle γ for different a gold particle sizes with a fixed relative deformation of $\delta R/R = 30\%$. $\gamma = 0$ coincides with the right-hand side of the horizontal axis, and γ increases anticlockwise. The scattered intensity is averaged over the orientations of the particles in the xOy plane determined by the angle ϕ. (a) $R = 2.5$ nm, (b) $R = 5$ nm, (c) $R = 10$ nm, (d) $R = 20$ nm.

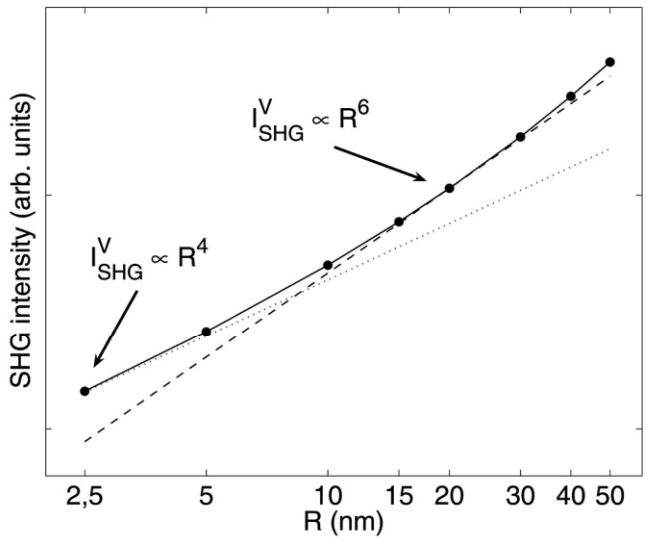

Fig. 6. Size dependence of the vertically polarized SHG intensity for a gold particle with a relative deformation of $\delta R/R = 30\%$. The scattered intensity is averaged over the orientations of the particles in the xOy plane determined by the angle ϕ. The dotted and dashed curves correspond to a surface area squared (R^4) and volume squared (R^6) dependence, respectively (log–log plot).

For a given deformation, the relative weight between the dipolar and the quadrupolar contributions to the SHG intensity is directly governed by the size dependence of these two contributions. As shown in Fig. 6, the SHG intensity is found to be proportional to the particle surface area squared (R^4) when the dipolar response dominates at small radii, whereas it is proportional to the particle volume squared (R^6) when the SHG response is dominated by the quadrupolar response at large radii. The present FEM simulations clearly support the interpretations of the experimental data reported recently [21,22], which deviates from the common belief that the SHG intensity from nanosized quasi-spherical particles always scales as the particle volume squared. It is also interesting to note in Fig. 6 that for the largest particles a deviation from the volume-squared dependence toward higher powers of the particle radius is observed owing to the influence of higher multipoles.

Finally, the case of silver nanoparticles (data not shown here) has been investigated as well. The same general behavior is observed except that the retardation effects arise at smaller particle sizes as compared with gold particles, as is the case for the linear optical properties. As a consequence, the quadrupolar contribution leading to the four-lobe pattern and the particle surface-area-squared dependence of the SHG intensity are observed at smaller sizes, in good qualitative agreement with the experimental observation reported recently [21,22].

4. CONCLUSION

In conclusion, FEM simulations have been performed to investigate the effects of a noncentrosymmetrical deformation on the SHG response from noble metal nanoparticles. It is found that (i) the SHG response from small particles is dominated by the dipolar response even for small deformations; (ii) the dipolar contribution to the SHG response of a quasi-spherical particle is proportional to the surface area squared and not to the volume squared, as is the case for the quadrupolar response; (iii) the light scattered at the harmonic frequency is dominated by the quadrupolar response for large particles even for noncentrosymmetrical particles owing to retardation effects; and (iv) the retardation effects responsible for the quadrupolar SHG contribution are observed at smaller sizes for silver particles than for gold ones, similarly to the linear optical properties. All these results are supported by the experimental results published recently.

REFERENCES

1. C. F. Bohren and D. R. Huffman, *Absorption and Scattering of Light by Small Particles* (Wiley Interscience, 1983).
2. U. Kreibig and M. Vollmer, *Optical Properties of Metal Clusters* (Springer, 1995).
3. T. K. Sau and C. J. Murphy, "Room temperature, high-yield synthesis of multiple shapes of gold nanoparticles in aqueous solution," J. Am. Chem. Soc. **126**, 8648–8649 (2004).
4. R. Jin, J. E. Jureller, H. Y. Kim, and N. F. Scherer, "Correlating second harmonic optical responses of single Ag nanoparticles with morphology," J. Am. Chem. Soc. **127**, 12482–12483 (2005).
5. C. L. Nehl, H. Liao, and J. H. Hafner, "Optical properties of star-shaped gold nanoparticles," Arch. Hist. Exact Sci. **6**, 683–688 (2006).
6. S. I. Bozhevolnyi, V. S. Volkov, E. Devaux, J. -Y. Laluet, and T. W. Ebbesen, "Channel plasmon subwavelength waveguide components including interferometers and ring resonators," Nature **440**, 508–511 (2006).
7. M. Moscovits, "Surface-enhanced spectroscopy," Rev. Mod. Phys. **57**, 783–826 (1985).
8. M. Danckwerts and L. Novotny, "Optical frequency mixing at coupled gold nanoparticles," Phys. Rev. Lett. **98**, 026104 (2007).
9. C. K. Chen, T. F. Heinz, D. Ricard, and Y. R. Shen, "Surface-enhanced 2nd-harmonic generation and Raman-scattering," Phys. Rev. B **27**, 1965–1979 (1983).
10. M. I. Stockman, D. J. Bergman, C. Anceau, S. Brasselet, and J. Zyss, "Enhanced second-harmonic generation by metal surfaces with nanoscale roughness: nanoscale dephasing, depolarization, and correlations," Phys. Rev. Lett. **92**, 057402 (2004).
11. S. I. Bozhevolnyi, J. Beermann, and V. Coello, "Direct observation of localized second-harmonic enhancement in random metal nanostructures," Phys. Rev. Lett. **90**, 197403 (2003).
12. A. Bouhelier, M. Beversluis, A. Hartschuh, and L. Novotny, "Near-field second-harmonic generation induced by local field enhancement," Phys. Rev. Lett. **90**, 013903 (2003).
13. K. R. Li, M. I. Stockman, and D. J. Bergman, "Enhanced second harmonic generation in a self-similar chain of metal nanospheres," Phys. Rev. B **72**, 153401 (2005).
14. G. S. Agarwal and S. S. Jha, "Theory of 2nd harmonic-generation at a metal-surface with surface-plasmon excitation," Solid State Commun. **41**, 499–501 (1982).
15. X. M. Hua and J. I. Gersten, "Theory of 2nd-harmonic generation by small metal spheres," Phys. Rev. B **33**, 3756–3764 (1986).
16. D. Oestling, P. Stampfli, and K. H. Bennemann, "Theory of nonlinear-optical properties of small metallic spheres," Z. Phys. D: At., Mol. Clusters **28**, 169–175 (1993).
17. V. L. Brudny, B. S. Mendoza, and W. L. Mochan, "Second-harmonic generation from spherical particles," Phys. Rev. B **62**, 11152–11162 (2000).
18. J. I. Dadap, J. Shan, K. B. Eisenthal, and T. F. Heinz, "Second-harmonic Rayleigh scattering from a sphere of centrosymmetric material," Phys. Rev. Lett. **83**, 4045–4048 (1999).
19. J. I. Dadap, J. Shan, and T. F. Heinz, "Theory of optical second-harmonic generation from a sphere of centrosymmetric material: small-particle limit," J. Opt. Soc. Am. B **21**, 1328–1347 (2004).
20. E. C. Hao, G. C. Schatz, R. C. Johnson, and J. T. Hupp, "Hyper-Rayleigh scattering from silver nanoparticles," J. Chem. Phys. **117**, 5963–5966 (2002).
21. J. Nappa, G. Revillod, I. Russier-Antoine, E. Benichou, C. Jonin, and P. F. Brevet, "Electric dipole origin of the second harmonic generation of small metallic particles," Phys. Rev. B **71**, 165407 (2005).
22. I. Russier-Antoine, E. Benichou, G. Bachelier, C. Jonin, and P. F. Brevet, "Multipolar contributions of the second harmonic generation from silver and gold nanoparticles," J. Phys. Chem. C **111**, 9044–9048 (2007).
23. B. K. Canfield, S. Kujala, K. Jefimovs, J. Turunen, and M. Kauranen, "Linear and nonlinear optical responses influenced by broken symmetry in an array of gold nanoparticles," Opt. Express **12**, 5418–5423 (2004).
24. S. Kujala, B. K. Canfield, M. Kauranen, Y. Svirko, and J. Turunen, "Multipole interference in the second-harmonic optical radiation from gold nanoparticles," Phys. Rev. Lett. **98**, 167403 (2007).
25. J. Jin, *The Finite Elements Method in Electrodynamics* (Wiley Interscience, 2002).
26. P. B. Johnson and R. W. Christy, "Optical constants of noble metals," Phys. Rev. B **6**, 4370–4379 (1972).
27. P. Guyot-Sionnest and Y. R. Shen, "Bulk contribution in surface second-harmonic generation," Phys. Rev. B **38**, 7985–7989 (1988).
28. S. Brasselet and J. Zyss, "Multipolar molecules and

multipolar fields: probing and controlling the tensorial nature of nonlinear molecular media," J. Opt. Soc. Am. B **15**, 257–288 (1998).
29. S. J. Cyvin, J. E. Rauch, and J. C. Decius, "Theory of hyper-Raman effects (nonlinear inelastic light scattering): selection rules and depolarization ratios for the second-order polarizability," J. Chem. Phys. **43**, 4083–4095 (1965).
30. R. Bersohn, Y.-H. Pao, and H. L. Frisch, "Double-quantum light scattering by molecules," J. Chem. Phys. **45**, 3184–3198 (1966).
31. J. Nappa, I. Russier-Antoine, E. Benichou, C. Jonin, and P. F. Brevet, "Wavelength dependence of the retardation effects in silver nanoparticles followed by polarization resolved hyper Rayleigh scattering," Chem. Phys. Lett. **415**, 246–250 (2005).

2.3- Interférence entre multipôles

Comme je l'ai mentionné précédemment, l'origine de la génération de second harmonique ne peut trouver son dénouement qu'avec des particules de grandes tailles afin de minimiser l'impact de l'écart à la sphéricité des particules étudiées. Qui dit particules de grande taille dit naturellement effets retards et excitation multipolaire. Arrêtons-nous donc quelques instants sur les modes du champ électromagnétiques qui peuvent être excités par une onde plane. En optique linéaire, le résultat est bien connu dans le cadre de la théorie de Mie. Toutes les valeurs du moment cinétique l sont permises au delà de $l = 1$ dans la mesure où l'invariance par translation de l'onde plane est rompue, conduisant à l'excitation de tout le spectre du moment angulaire (excepté $l = 0$). Dans l'onde incidente, seules les composantes $m=\pm 1$, correspondant au spin du photon, sont présentes. Les particules étant sphériques, et donc invariantes par rotation autour du vecteur d'onde incident, cette propriété est transférée au champ diffusé. En optique non-linéaire et plus particulièrement dans la génération de second harmonique, les choses sont quelque peu différentes. Certes tout le spectre du moment angulaire va également être excité, mais les valeurs de m à présent permises vont à présent de $m=-2$ à $m=+2$. C'est là une conséquence directe des règles de composition du moment cinétique et du fait que les sources du champ harmonique diffusé sont proportionnelles au carré du champ à la fréquence fondamentale.

Une étape supplémentaire vers la détermination des modes excités peut être franchie en utilisant les plans de symétrie du problème physique. Dans le cas de l'onde plane, le plan d'incidence (contenant le champ électrique et le vecteur d'onde) est un plan de symétrie des sources. Au contraire, le plan qui lui est perpendiculaire (défini par le champ magnétique et le vecteur d'onde) est un plan d'antisymétrie. C'est d'ailleurs ce qui donne naissance à la réponse dipolaire de la matière. Les sources non-linéaires étant proportionnelles au carré du champ à la fréquence fondamentale, les plans d'anti-symmétrie pour le champ fondamental deviennent des plans de symétrie pour l'onde harmonique. Ainsi, $\left(\vec{E},\vec{k}\right)$ et $\left(\vec{B},\vec{k}\right)$ sont tous deux des plans de symétrie du champ harmonique diffusé. Une conséquence directe est que seules les valeurs $m=0, \pm 2$ sont permises.

La dernière étape est un peu plus technique mais peut également se discuter en n'utilisant que des arguments de symétrie (je vous épargnerai donc l'expression des champs). Les modes associés à des valeurs paires de l admettent un autre plan de symétrie: le plan $\left(O,\vec{E},\vec{B}\right)$ passant par l'origine. Le champ électrique harmonique est donc contenu dans ce

plan. Une conséquence importante est que les modes pairs (quadripôles, etc) ne peuvent être observés expérimentalement que pour une détection verticale V. Notons que la valeur m=0 leur est interdite à cause des plans de symétrie $\left(\vec{E},\vec{k}\right)$ et $\left(\vec{B},\vec{k}\right)$. Dans le cas des modes impairs, c'est l'inverse: le plan $\left(O,\vec{E},\vec{B}\right)$ est un plan d'antisymétrie de sorte qu'ils ne sont visibles (hors brisure de symétrie) que pour une détection horizontale. Pour résumer et en considérant une symétrie sphérique parfaite des particules:

- en V, seuls les modes avec l pair et m= ±2 sont observés,
- en H, seuls les modes associés à l impair et m=0, ±2 sont permis.

Deux conclusions importantes découlent de l'analyse précédente. Tout d'abord, le choix d'une configuration expérimentale collectant le signal harmonique à 90 degrés permet de découpler les modes pairs et impairs. Dans le cas d'une collection en V, tous les modes présentent la même réponse en polarisation (quatre lobes associés à m=±2). Il n'y a donc aucune information supplémentaire à attendre de ce côté là. En revanche, en collection H, les modes peuvent présenter soit une réponse invariante en fonction de la polarisation (m=0), soit une réponse donnant quatre lobes (m=±2). Les simulations prédisaient donc en configuration H l'apparition de phénomènes d'interférences qui, comme nous le verront plus tard, constitue la porte d'entrée vers la détermination de l'origine de la génération de second harmonique.

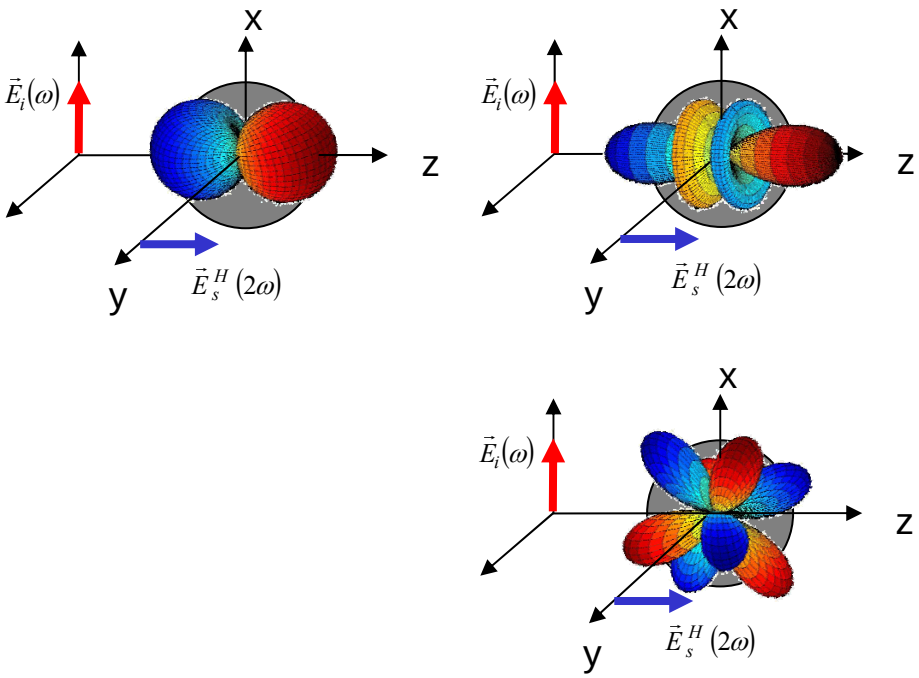

Figure 17: *Schéma présentant les modes plasmons observé en HRS collectée perpendiculairement au faisceau incident et pour une polarisation horizontale (parallèle au faisceau incident). A gauche le mode dipolaire (l=1, m=0) et à droite les modes octupolaires (l=3, m=0) et (l=3, m=2).*

De nombreuses mesures en collection horizontale avaient été réalisées au sein de l'équipe, notamment par Isabelle Russier-Antoine, sur des particules de toutes tailles et composée aussi bien d'or que d'argent. Elles n'avaient cependant pas trouvé d'explication cohérente pour leur évolution en fonction de la taille et n'avaient donc pratiquement jamais été discutées, si ce n'est pour les plus petites particules. Dans ce dernier cas, l'intensité est indépendante de la polarisation incidente de part l'excitation d'un dipôle orienté selon le vecteur d'onde et donc invariant par rotation du champ incident (voir figure 17). Le moment était donc venu de revisiter ces expériences, avec comme contrainte d'apporter le plus grand soin possible à l'alignement tant nous avions vu, au travers des simulations, son influence dans le cas des particules de grandes tailles. Cette étude a été réalisée dans le cadre de la thèse de Jérémy Butet, que j'ai co-encadré jusqu'au début de cette année avec Pierre-François Brevet, mais a largement bénéficié de tout le travail réalisé en amont par Isabelle Russier-Antoine. Comme attendu, la réponse en polarisation est constante pour des particules d'or allant jusqu'à 50 nm de diamètre (dipôle non-linéaire orienté selon z) mais présente une déformation de plus en plus prononcée au fur et à mesure que la taille de la particule augmente (voir figure 18).

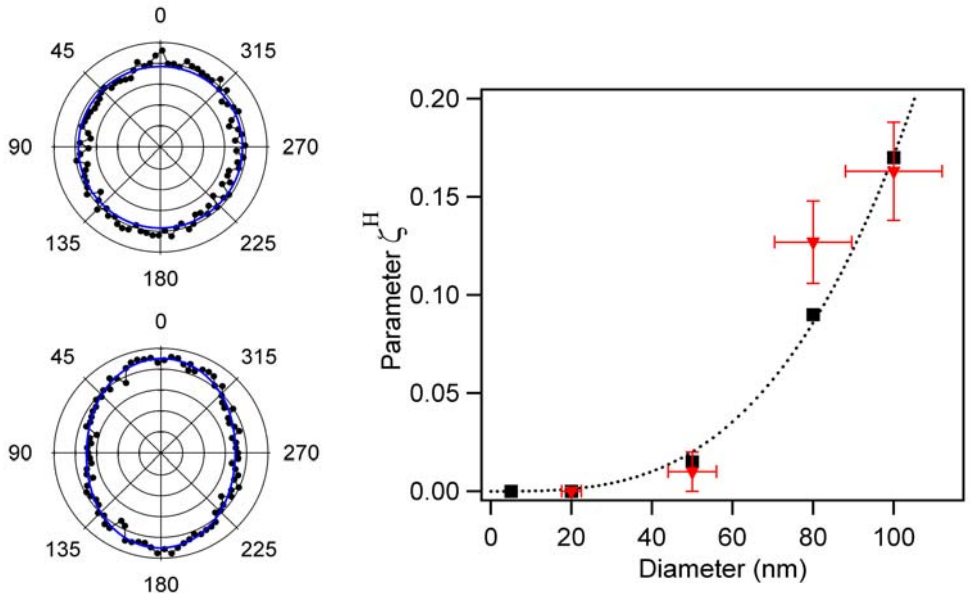

Figure 18: *Intensité HRS collectée perpendiculairement au faisceau incident en fonction de la polarisation du champ (0 correspond à un champ perpendiculaire au plan de diffusion, c'est-à-dire une polarisation verticale). Le signal est analysé horizontalement pour une particule d'or de diamètre 50 nm (diagramme polaire du haut) et 100 nm (bas) et une longueur d'excitation de 780 nm. La figure de droite présente l'évolution du paramètre* $\zeta^H = (I_{max} - I_{min})/(I_{max} + I_{min})$ *en fonction de la taille des particules. En rouge sont présentés les mesures expérimentales et en noir les simulations par éléments finis pour un courant non-linéaire perpendiculaire à la surface de la particule.*

L'interprétation va être grandement facilitée par la discussion précédente: les modes impairs associés à m=0 (dipôle et octupole), qui donneraient une intensité constante, et ceux associés à m=±2 (octupole) donnant des maxima pour une polarisation incidente horizontale ou verticale (notez la rotation de 45 degrés par rapport aux quadripôles observés en V) étants excités de manière cohérente, ils vont interférer entre eux. Le maximum d'intensité correspond donc à des interférences constructives et les minima à des interférences destructives. La mesure de la réponse HRS en fonction de la polarisation incidente a ainsi permis, pour la première fois, de sonder l'ensemble du profil d'interférence entre les modes dipolaires et octupolaires, sélectionnés par la configuration expérimentale adoptée.

Comme le montre la figure 18, les résultats expérimentaux obtenus par Jérémy sont en excellent accord avec les simulations que j'ai réalisées par éléments finis. Il est à noter que dans le cas présent, seule la contribution de surface de type $\chi_{s,\perp\perp\perp}$ est prise en compte dans les simulations. Cet accord tant qualitatif que quantitatif n'est cependant pas une preuve que cette contribution soit dominante, comme il a souvent été écrit dans la littérature, puisqu'une combinaison linéaire des différentes sources pourrait parfaitement convenir. Au contraire même. Comme je le dis souvent, c'est lorsque la théorie commence à fitter avec l'expérience que l'on peut se mettre en danger et raconter des bêtises... Mais nous touchons bientôt au but.

Pour conclure cette partie, je souhaiterais mentionner les tous derniers travaux que nous avons entrepris avec Jérémy sur les particules d'argent cette fois. L'idée est que, puisque les modes pairs et impairs sont découplés de part la géométrie expérimentale choisie, il doit être possible de sonder sélectivement les résonances plasmons dipolaires et octupolaires d'une part, et quadripolaire de l'autre. Pour cela, nous allons tirer profit du fait que les résonances plasmons dans les particules d'argent prennent naissance autour de 400nm, la longueur d'onde harmonique typique, et qu'il est possible de les décaler vers le rouge en utilisant les effets retards, beaucoup plus forts dans les particules d'argent que dans les particules d'or (les résonances ne sont pas "engluées" dans les interbandes). Ainsi, pour des particules de 130 nm de diamètre, les simulations ont montré qu'il était possible de sonder la résonance plasmon quadripolaire en détection V et de suivre l'évolution du contraste d'interférences entre les plasmons dipolaires et octupolaires en détection H dans la gamme de longueur d'onde accessible expérimentalement. Les premiers résultats expérimentaux en ce sens sont pour le moins encourageants...

Interference between Selected Dipoles and Octupoles in the Optical Second-Harmonic Generation from Spherical Gold Nanoparticles

J. Butet, G. Bachelier,* I. Russier-Antoine, C. Jonin, E. Benichou, and P.-F. Brevet

Laboratoire de Spectrométrie Ionique et Moléculaire (LASIM), Université Claude Bernard Lyon 1 - CNRS (UMR 5579), Bâtiment A. Kastler, 43 Boulevard du 11 novembre 1918, 69622 Villleurbanne, France

(Received 21 April 2010; published 10 August 2010)

Optical second-harmonic generation from gold nanoparticles is investigated both experimentally and theoretically. The contribution of octupoles is reported for the first time in the second-harmonic emission pattern, by using an harmonic polarization in the scattering plane. The experimental results presented here for particle sizes up to 100 nm are in excellent agreement with finite element method simulations involving the normal surface term only in the nonlinear polarization source. In addition, analytical calculations based on nonlinear Mie scattering theory clearly evidence the constructive and destructive interferences occurring between the dipolar and octupolar responses selected with this polarization configuration.

DOI: 10.1103/PhysRevLett.105.077401 PACS numbers: 78.67.Bf, 42.25.Hz, 42.65.Ky, 73.20.Mf

Noble-metal nanoparticles play a singular role in nanosciences and nanotechnology owing to the well-known surface plasmon polaritons [1] leading to both field localization and enhancement. These two key features have opened extensive applications in surface-enhanced spectroscopies [2] and light guiding and coupling in plasmonic devices and nanoantennas [3,4]. Nowadays, almost any particle shape (spheres, rods, cubes, decahedra) can be obtained owing to the progress in the synthesis of shape-controlled nanocrystals [5]. This allows tailoring the desired spectral response but also the desired particle symmetry, leading to specific near-field distributions of the electromagnetic field. Owing to all these properties, noble-metal nanoparticles have triggered a new and exponentially increasing interest in linear and, more recently, nonlinear optics such as the second-harmonic generation (SHG) phenomenon for almost a decade. The specificity of the second-order nonlinear process is that it is forbidden in the dipolar approximation in centrosymmetric materials, as is the case for noble metals [6]. Hence, the nonlinear response is dominated by the contribution of the metal surface, where the centrosymmetry is broken, and of the bulk owing to field gradients [7]. Metal films and L-shaped structures prepared by lithography were recently investigated by the group of Kauranen [8] evidencing interferences between the two kinds of contributions.

Systematic experimental investigations have also been performed on colloidal solutions allowing the analysis in a homogeneous environment of the intrinsic properties of the metal particles [9–14]. More precisely, the size dependence of the nonlinear efficiency, the effects of the surface plasmon resonances, the composition (gold, silver, or copper), and the homogeneity of the internal structure (alloys or core-shell structures) have been addressed. The SH scattering properties of spherical nanoparticles were found to be dominated by the dipolar and quadrupolar responses (where the multipoles are those of the Mie theory) as evidenced by polarization-resolved measurements. The dipolar response is, in principle, forbidden by symmetry arguments in the specific experimental configuration [15]. Its observation was attributed to the deviation of the exact shape of the particle from the perfect spherical shape [9] and recently confirmed by finite elements methods (FEM) simulations [16], accounting for both polarization and size dependences. An almost pure quadrupolar response has been reported very recently at the single particle level [17].

In this Letter, we investigate further, experimentally and theoretically, the SHG response from approximately spherical gold nanoparticles with hyper-Rayleigh scattering where the SH light is collected at a right angle from the fundamental beam. We report for the first time the observation of an octupolar response in the harmonic field component parallel to the scattering plane for particles as small as 70 nm in diameter. The experimental data are compared to both FEM [16] and analytical [18] simulations, giving a clear picture of the interference phenomenon occurring between the polarization-selected dipolar response, already reported in a few works only [9,19], and this new octupolar contribution. The role of the retardation effects in the interference contrast is, in particular, quantitatively addressed.

We used a mode-locked Ti:sapphire laser tuned to 780 nm and delivering pulses of about 180 fs at a repetition rate of 76 MHz. The average output power was about 800 mW at the laser exit. The polarization angle of the input beam γ is selected with a rotating half-wave plate, $\gamma = 0$ or π corresponding to a vertically polarized incident wave. A red filter was placed in front of it to remove any residual light at the harmonic frequency generated in the wave plate. The fundamental beam is focused into a quartz cell with a microscope objective (16, numerical aperture 0.32). The collection is performed perpendicular to the

incident beam with a 25 mm focal length lens with a numerical aperture of 0.5. The SH photons, the polarization of which is selected by an analyzer, are collected by a cooled photomultiplier after spectral selection performed by a blue filter and a monochromator. A mechanical chopper on the fundamental beam allows the rejecting of undesirable photons coming from the environment. This experimental setup has recently been used to performed hyper-Rayleigh scattering from metallic nanoparticles with very low concentrations, ultimately where a single nanoparticle is located in the focal volume of the beam [20]. The gold nanoparticle aqueous solutions were purchased and used as received (BBI international).

Horizontally analyzed second-harmonic measurements (electric field in the scattering plane) have been reported in the past for small spherical [9] and flat triangular [19] metallic nanoparticles only. The corresponding SH intensity was found to be independent of the incident polarization angle as expected for the excitation of an electric dipole at the harmonic frequency arising either from the noncentrosymmetry of the particles randomly distributed into the liquid aqueous phase [16] or from the spatial variation of the fundamental electric field over the nanoparticles [15]. In the latter case, in particular, this dipole is aligned with the fundamental beam propagation axis, and its amplitude is independent of the input polarization angle for spherical particles. It therefore leads to a constant SH intensity. Figure 1 shows horizontally analyzed SH measurements as a function of the input polarization for 50 and 100 nm gold nanoparticles. As expected, the results obtained for the 50 nm diameter gold nanoparticles are independent of the input polarization in agreement with the dipolar emission properties discussed above [9,15,16]. In contrast, the horizontally analyzed SH intensity for 100 nm gold nanoparticles reaches a maximum value for vertically polarized input electric fields ($\gamma = 0$ or π). This additional contribution increases in amplitude as the particle size increases. It is therefore likely related to retardation effects.

Additional measurements were performed for 20 and 80 nm nanoparticles evidencing a smooth evolution of the polar graphs as a function of the particle size (data not shown). All SH emission patterns were perfectly fitted with the following equation:

$$I^H_{HRS} = a^H \cos^4\gamma + b^H \cos^2\gamma \sin^2\gamma + c^H \sin^4\gamma, \quad (1)$$

where the parameters a^H, b^H, and c^H are real coefficients. For horizontally analyzed SHG with constant amplitude, the γ dependence in Eq. (1) vanishes owing to the relation $2a^H = 2c^H = b^H$ [21]. For nonconstant SH emission patterns, this equality no longer holds. Since the deformed polar plots exhibit maxima at $\gamma = 0$ or π, as shown in Fig. 1, the parameter a^H becomes larger than c^H. Hence, the deviation from a pure dipolar response corresponding to a constant horizontally analyzed SH intensity can be quantified by the single parameter $\zeta^H = (a^H - c^H)/(a^H + c^H)$. Its dependence on the diameter of the gold nanoparticle is shown in Fig. 2. As expected, this ratio vanishes for gold particles smaller than 50 nm as their response is dominated by a pure dipolar contribution. It, however, increases with the particle size up to 0.16 for 100 nm diameter gold nanoparticles. As shown in Fig. 2, the deviation from a pure dipolar SH response starts to be effective (larger than the experimental uncertainty) for nanoparticles as small as 70 nm.

To characterize this new contribution to the SHG response in large noble-metal nanoparticles, FEM simulations were performed as reported in Ref. [16]. Briefly, the

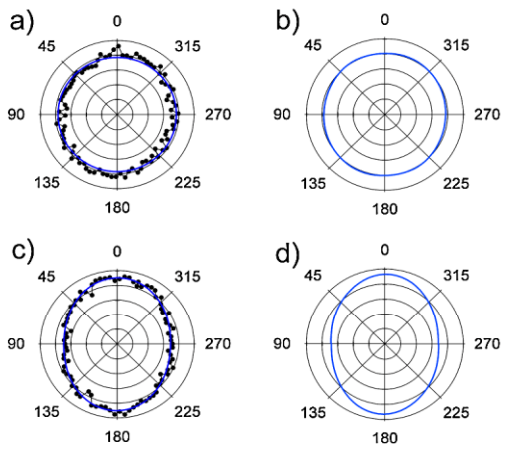

FIG. 1 (color online). Horizontally analyzed SH intensity as a function of the input polarization for 50 (a),(b) and 100 nm (c),(d) gold nanoparticles. The experimental data are shown with filled circles (a),(c) and fitted by using Eq. (1) (plain curves). The corresponding FEM simulations are shown in the right-hand panel (b),(d).

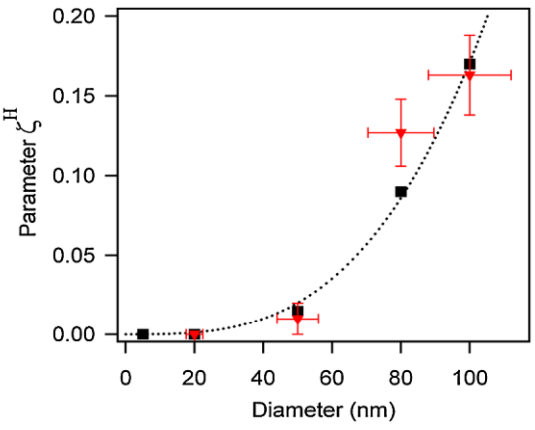

FIG. 2 (color online). Parameter ζ^H as a function of the gold nanoparticle diameter as experimentally measured (red triangles) and calculated by using FEM simulations (black squares). The dotted line is a fit of the simulated data with the equation Ad^p, where d is the nanoparticle diameter. The vertical and horizontal error bars are obtained from the fitting procedure and the size dispersion, respectively.

field distribution at the fundamental frequency excited by the incident beam is determined first; see Figs. 3(a) and 3(b). It is then used to calculate the nonlinear sources associated with the surface quadratic susceptibility tensor component $\chi^{(2)}_{s,nnn}$. Maxwell's equations are solved in a second step by using the weak formulation in order to obtain the near-field distribution of the fields at the harmonic frequency; see Figs. 3(c) and 3(d). As shown in Figs. 3(a) and 3(b), the retardation effects at the fundamental wavelength are very weak for both 50 and 100 nm nanoparticles, the linear optical properties being largely dominated by the dipolar response. In contrast, the near-field distribution of the SH electric field strongly differs for 50 and 100 nm gold nanoparticles. It clearly shows that retardation effects at the emission step are prominent for the larger particles [see Fig. 3(d)] as evidenced by the asymmetry of the near-field map and the distortion of the multipolar lobes. The far-field scattered intensity, which can be compared to the experimental data, is calculated from the near-field distribution of the SH field by using the Stratton-Chu formula [16]. As shown in Fig. 1, the deviation from a constant horizontally polarized SH intensity is very well reproduced by the FEM simulation for both the orientation and the amplitude of the deformation. The experimental results presented here can therefore be accounted for with FEM simulations including the normal quadratic susceptibility surface term only. Additional FEM simulations, not shown here, were performed with deformed particles [16]. As a matter of fact, a constant intensity was also obtained as a function of the input polarization for weakly deformed particles. This latter simulation confirms that the deformation of the SH emission patterns experimentally observed cannot be explained by the deviation of the nanoparticles shape from that of a perfect sphere.

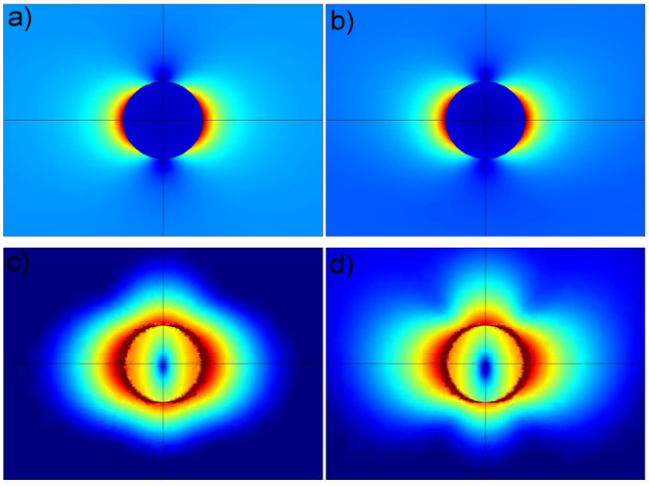

FIG. 3 (color online). Calculated near-field distribution for the fundamental (a),(b) and harmonic (c),(d) electric fields for 50 (a),(c) and 100 nm (b),(d) gold nanoparticles. The image plane is given by the incident electric field, aligned with the dipolar lobes (a),(c), and the corresponding wave vector. The harmonic fields are shown in a logarithmic scale.

The parameter ζ^H determined from the FEM simulations is reported in Fig. 2, pointing out that calculated SH responses and experimental measurements are in excellent agreement. A fitting procedure with the function Ad^p, where d is the nanoparticle diameter and A and p are the parameters, leads to a variation of the parameter ζ with the third power of the nanoparticle diameter ($p = 3.01 \pm 0.02$). From the size dependence of this additional contribution, one cannot directly infer the nature of the additional multipole involved. One way to answer this question would have been to project the harmonic near field obtained with the FEM simulations on the different multipolar surface plasmon modes. Instead, we follow an analytical approach in order to establish a link with previous theoretical works.

Following the notation introduced by Dadap and coworkers [15], the more efficient mechanism leading to a dipolar SH emission for a perfect sphere is $E1 + E2 \rightarrow E1$, where the two terms on the left of the arrow refer to the nature of the interaction with the fundamental wave and the third term describes that of the SH emission. Explicitly, this notation corresponds to a dipolar emission ($E1$) coming from the combination of an electric dipole ($E1$) and an electric quadrupole ($E2$) excitation. The $E1 + E1 \rightarrow E1$ mechanism is forbidden for centrosymmetric objects, since this channel violates parity conservation. In addition to the well-known $E1 + E1 \rightarrow E2$ channel, there is a third possibility involving electric dipoles ($E1$) and quadrupoles ($E2$) and satisfying the conservation of the angular momentum. This mechanism, corresponding to a $E1 + E2 \rightarrow E3$ contribution, was not previously taken into account in the small-particle limit [15] but has to be considered where larger particles are involved. This octupolar term ($E3$) appears as a good candidate to account for the observed deformation of the SH intensity pattern and is related to retardation effects.

In order to establish the role of each multipole in the SH response and confirm the octupolar origin of the additional contribution in the nonconstant SH intensity pattern, analytical calculations were performed by using the nonlinear Mie scattering model developed by Pavlyukh and Hübner [18]. After determining the multipole expansion for the fundamental field inside the sphere, the SH surface sources were computed by using Clebsch-Gordan algebra. The appropriate formulation for the boundary conditions applied to the harmonic field is still under discussion [22]. Nevertheless, the symmetry of the excited multipoles is well accounted for by the present calculation and leads to a clear and simple interpretation of the experimental data.

By using surface nonlinear sources given by $\chi^{(2)}_{s,nnn}$, very simple selection rules are obtained. The vertically E^V_l and horizontally E^H_l polarized harmonic fields are nonzero for angular momenta l even and odd, respectively, as discussed

by Dadap *et al.* [15]. Hence, in our experimental configuration and for the surface nonlinear source $\chi^{(2)}_{s,nnn}$, odd and even plasmon modes are decoupled and can be independently selected in vertically or horizontally analyzed measurements. This would not be the case in other configurations such as that used in Ref. [23] due to the presence of the substrate and the scattering angle. The following expressions for the far-field SH electric field can be deduced from Ref. [18]:

$$E_1^H = \alpha, \tag{2}$$

$$E_3^H = \kappa + \eta\cos(2\gamma), \tag{3}$$

where α, κ, and η are three functions of the nanoparticle diameter and the gold dielectric constants at the fundamental and the harmonic frequencies. Obviously, the equality $2a^H = 2c^H = b^H$ is now broken with the introduction of the term E_3^H, which is the only one depending on the incident polarization angle. The deviation from a pure dipolar SH response leading to a variation of the horizontally analyzed SH intensity with the input polarization angle is therefore due to the electric octupolar term as anticipated above. The constant term $\alpha + \kappa$ arises from both the dipolar and the octupolar fields, and therefore it cannot be separated into its two components. However, the ratio between the oscillating and the constant parts, namely, the ratio $\eta/(\alpha + \kappa)$, is found to be 8% for 100 nm gold particles, evidence of an already significant contribution of the octupole contribution to the scattered SH intensity for this particle size.

The dipolar and the octupolar modes both contribute to the horizontally polarized SH electric field. Therefore, they do interfere in the far-field region. The deformation of the polar plot shown in Fig. 1 can hence be analyzed in terms of constructive interferences for the maxima of the SH intensity at the angles $\gamma = 0$ and π and destructive interferences at the angles $\gamma = \pi/2$ and $3\pi/2$. Rotating the polarization of the fundamental electric field allows exploring the entire interference patterns. In this context, the parameter ζ^H finds a natural interpretation if recast in the following form:

$$\zeta^H = \frac{I^H_{\max} - I^H_{\min}}{I^H_{\max} + I^H_{\min}}. \tag{4}$$

Clearly, ζ^H translates the interference contrast between the dipolar and the octupolar plasmon modes selected in our specific experimental configuration. As the particle size increases, the amplitude of the octupolar contribution increases owing to the retardation effects, leading to a growing interference contrast with the dipolar contribution.

In summary, octupolar SHG from spherical gold nanoparticles is reported for the first time. This contribution starts to be effective for nanoparticles as small as 70 nm in diameter. Owing to the setup geometry we used where the fundamental input and the scattered output directions are at a right angle, even and odd multipolar contributions to the total SH response can be independently selected by using orthogonal analyzers. The octupolar contribution is revealed in the horizontally analyzed SH intensity configuration through to its interference with the dipolar one. The interference contrast is controlled by the input polarization and shown to increase with the particle volume. All experimental observations are in excellent agreement with FEM simulations. The pioneering combination of FEM simulations and analytical models provides furthermore a clear understanding of the characteristics of the SH emission from noble-metal nanoparticles.

*Corresponding author.
guillaume.bachelier@lasim.univ-lyon1.fr

[1] A. V. Zayats, I. I. Smolyaninov, and A. A. Maradudin, Phys. Rep. **408**, 131 (2005).
[2] K. Kneipp *et al.*, Phys. Rev. Lett. **78**, 1667 (1997).
[3] P. Muhlschlegel, H. J. Eisler, O. J. F. Martin, B. Hecht, and D. W. Pohl, Science **308**, 1607 (2005).
[4] J. C. Weeber, A. Dereux, C. Girard, J. R. Krenn, and J. P. Goudonnet, Phys. Rev. B **60**, 9061 (1999).
[5] Y. Xia, Y. J. Xiong, B. Lim, and S. E. Skrabalak, Angew. Chem., Int. Ed. **48**, 60 (2009).
[6] R. W. Boyd, *Nonlinear Optics* (Academic, New York, 1992).
[7] S. S. Jha, Phys. Rev. **140**, A2020 (1965).
[8] S. Kujala, B. K. Canfield, M. Kauranen, Y. Svirko, and J. Turunen, Phys. Rev. Lett. **98**, 167403 (2007).
[9] J. Nappa *et al.*, Phys. Rev. B **71**, 165407 (2005).
[10] I. Russier-Antoine, E. Benichou, G. Bachelier, C. Jonin, and P. F. Brevet, J. Phys. Chem. C **111**, 9044 (2007).
[11] I. Russier-Antoine *et al.*, Phys. Rev. B **78**, 035436 (2008).
[12] E. C. Hao, G. C. Schatz, R. C. Jonhson, and J. T. Hupp, J. Chem. Phys. **117**, 5963 (2002).
[13] R. C. Johnson, J. Li, J. T. Hupp, and G. C. Schatz, Chem. Phys. Lett. **356**, 534 (2002).
[14] M. Chandra and P. K. Das, Chem. Phys. **358**, 203 (2009).
[15] J. I. Dadap, J. Shan, K. B. Eisenthal, and T. F. Heinz, Phys. Rev. Lett. **83**, 4045 (1999); J. I. Dadap, J. Shan, and T. F. Heinz, J. Opt. Soc. Am. B **21**, 1328 (2004).
[16] G. Bachelier, I. Russier-Antoine, E. Benichou, C. Jonin, and P. F. Brevet, J. Opt. Soc. Am. B **25**, 955 (2008).
[17] J. Butet *et al.*, Nano Lett. **10**, 1717 (2010).
[18] Y. Pavlyukh and W. Hübner, Phys. Rev. B **70**, 245434 (2004).
[19] A. K. Singh *et al.*, Chem. Phys. Lett. **481**, 94 (2009).
[20] J. Duboisset *et al.*, J. Phys. Chem. C **113**, 13 477 (2009).
[21] S. Brasselet and J. Zyss, J. Opt. Soc. Am. B **15**, 257 (1998).
[22] A. G. F. de Beer and S. Roke, Phys. Rev. B **79**, 155420 (2009).
[23] M. D. McMahon, R. Lopez, R. F. Haglund, Jr., E. A. Ray, and P. H. Bunton, Phys. Rev. B **73**, 041401(R) (2006).

2.4- Détermination quantitative des contributions de surface et de volume

Voici donc après cinq années d'un travail assidu, la clé du problème auquel je m'étais attelé: comprendre l'origine de la génération de second harmonique dans les nanoparticules métalliques. Incontestablement, il s'agit là, avec l'étude de la diffusion Raman dans les particules métalliques au cours de ma thèse, de l'un des plus beaux travail scientifique qu'il m'ait été donné de réaliser à ce jour, alliant théorie et expérience, un gros développement technique avec les simulations par éléments finis et enfin l'observation d'un nouveau phénomène d'interférence entre multipôles. Pour atteindre mon objectif, il me fallait trouver une signature qui me permettrait de différentier les différents mécanismes. Cette signature allait m'être apportée par les interférences entre multipôles. Comme le montre la figure 19 pour des particules d'or excitées à 800 nm, les effets d'interférences sont pratiquement invisibles pour des rayons inférieurs à 40 nm et ce quelque soit la source du courant non linéaire. Ce n'est qu'à partir d'un rayon de 40 nm que les contributions de surfaces commencent à osciller significativement. Il faut cependant atteindre des rayons de 75 nm pour que la réponse non-locale de volume présente à son tour des interférences constructives et destructives en fonction de la polarisation incidente. Nous avons donc utilisé les plus grosses particules que nous avions à notre disposition, à savoir des particules d'or de 150 nm de diamètre.

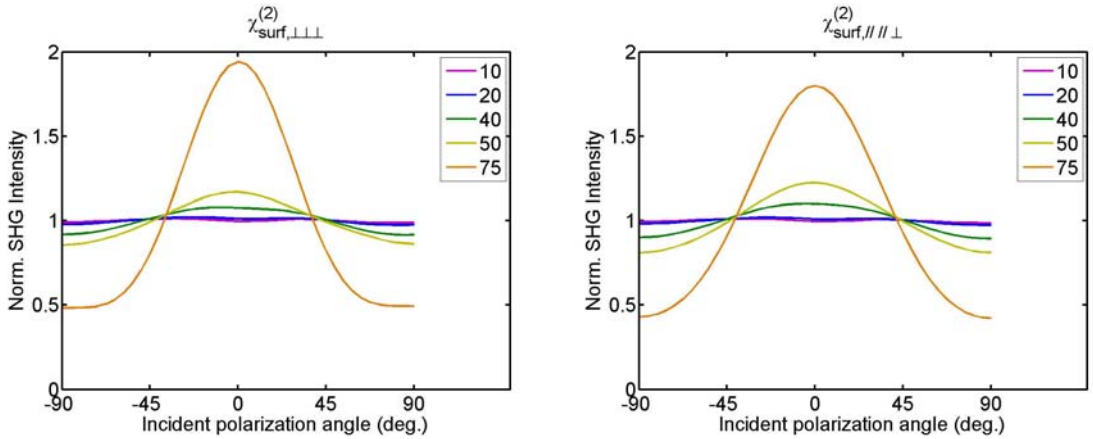

Figure 19a: *Intensité HRS normalisée diffusée par des particules d'or dont le rayon est indiqué en légende et excitées à 800 nm. Le signal est collecté perpendiculairement au faisceau incident et analysée pour une polarisation dans le plan de diffusion. Les courants locaux surfaciques utilisés pour les simulations sont indiquées dans le titre des graphiques.*

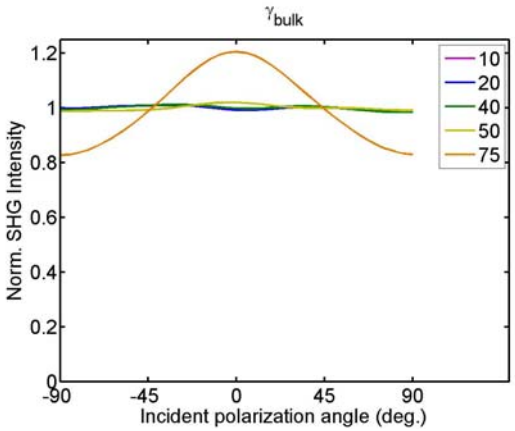

Figure 19b: *Même chose que précédemment mais calculé pour les courants volumiques non-locaux.*

Le point important ici est que, suivant l'origine de la réponse, la modulation de l'intensité par les effets d'interférences n'est pas aussi importante. En particulier, la réponse non-locale de volume présente une forte composante continue et une oscillation de faible amplitude. Au contraire, les réponses surfaciques sont associées à une très forte variation de l'intensité avec des maximas pratiquement quatre fois plus intenses que les minimas. En revanche, les deux sources surfaciques conduisent à des réponses très semblables qu'il ne sera donc pas possible de discriminer à partir de ces seules courbes. L'idée a donc été d'utiliser simultanément les mesures réalisées avec une analyse horizontale (dans le plan de diffusion) et verticale (perpendiculaire au plan de diffusion). Comme nous l'avons vu précédemment, les modes du champ électromagnétique excités dans ces deux configurations ne sont pas les même et bien que l'on ne puisse voir que des réponses à quatre lobes pour une détection verticale (et donc aucun effet d'interférence), la mesure de l'intensité maximale va être déterminante: le rapport des intensités mesurées en V et en H dépend très fortement de l'origine de la réponse, ce qui va permettre de les discriminer.

Comme nous l'avons discuté au début de ce chapitre, les susceptibilités $\chi_{s,\perp\perp\perp}$, $\chi_{s,////\perp}$ et γ_{bulk} associées aux différents courants non-linéaires sont souvent exprimées en fonctions des paramètres *a*, *b* et *d* introduits par Rüdnick et Stern. Dans le cadre du modèle hydrodynamique, ces paramètres valent $a = 1$, $b = -1$ et $d = 1$. D'autres modèles, introduisant un terme d'amortissement dans le modèle hydrodynamique (voir Corvi *et. al.*) ou prenant en compte explicitement la distribution de la densité électronique sur des échelles comparables à la longueur de Fermi (voir la référence de Liebsch), ont montré que le paramètre *a* présente un caractère résonant. Il fallait donc dans un premier temps tester la validité de tels modèles.

Pour cela, Jérémy Butet a réalisé l'ajustement simultané des courbes expérimentales V et H à l'aide des champs que j'ai simulés pour une particule sphérique unique:

$$I_{SHG} = G\left|a\vec{E}_{surf,\perp}(\vec{r},2\omega)+b\vec{E}_{surf,//}(\vec{r},2\omega)+d\vec{E}_{bilk}(\vec{r},2\omega)\right|^2 .$$

$\vec{E}_{surf,\perp}(\vec{r},2\omega)$, $\vec{E}_{surf,//}(\vec{r},2\omega)$ et $\vec{E}_{bilk}(\vec{r},2\omega)$ sont les champs correspondant aux trois contributions $\chi_{s,\perp\perp\perp}$, $\chi_{s,////\perp}$ et γ_{bulk} et les paramètres de Rüdnick et Stern *a*, *b* et *d* sont utilisés ici comme variables d'ajustement (*G* est une constante de normalisation).

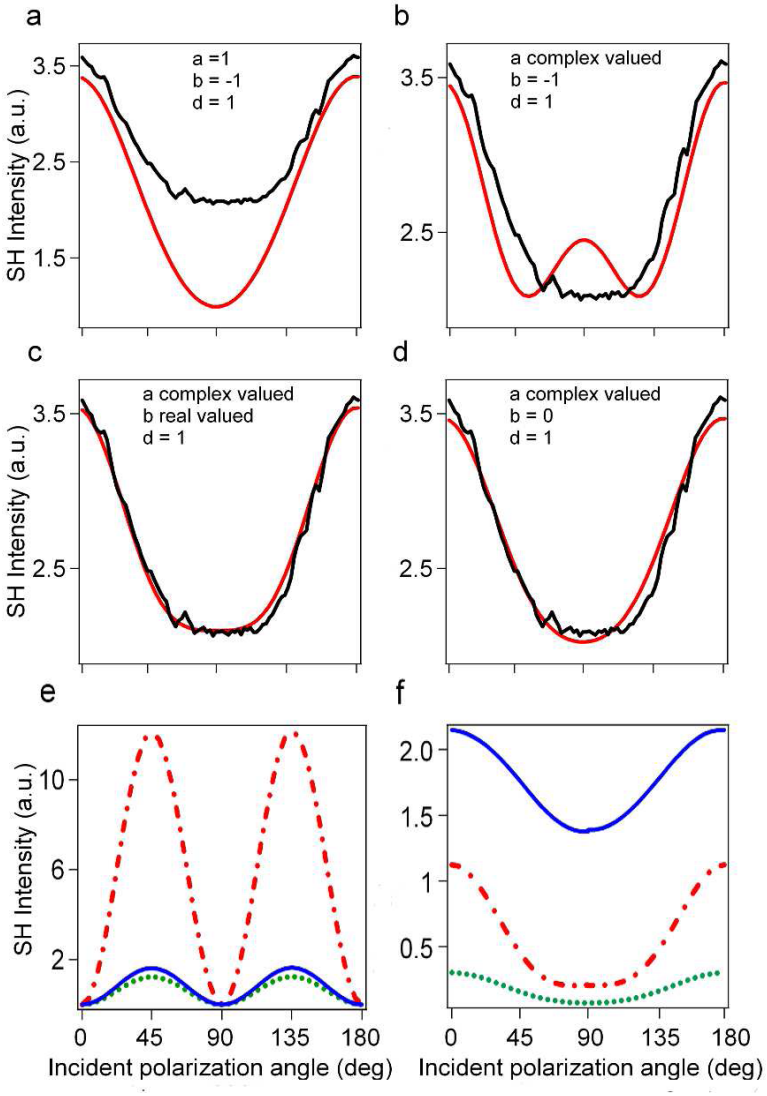

Figure 20: *Ajustements des intensités HRS expérimentales (seule la polarisation horizontale est montrée) en utilisant les champs calculés par éléments finis et en appliquant des contraintes sur les paramètres de Rüdnick et Stern indiquées sur chaque graphe (a-d). Les contributions du courant surfacique normal (traits-pointillés), tangentiel (pointillés) et du courant de volume (trait plein) pour une polarisation de détection perpendiculaire (e) et parallèle (f) au plan de diffusion et les paramètres indiqués dans le panel c.*

Comme le montre la figure 20a, le modèle hydrodynamique simple (sans ajout d'un terme d'amortissement) ne permet pas de reproduire l'intensité HRS diffusée par les particules d'or. En particulier, l'intensité obtenue pour une polarisation incidente horizontale (γ=90°) est largement sous-estimée par rapport aux résultats expérimentaux. La prise en compte du caractère résonant du courant non-linéaire normal à la surface, par l'intermédiaire d'un paramètre *a* complexe et dont l'amplitude n'est pas fixée, ne fournit cependant pas un ajustement de meilleure qualité (cf. figure 20b). Ainsi, le premier enseignement que l'on peut tirer de cette étude est que les modèles actuels visant à décrire les propriétés optiques non-linéaires des métaux nobles ne semblent pas suffisants. Ce désaccord tant qualitatif que quantitatif pourrait s'expliquer par le fait qu'aucun de ces modèles n'inclut les transitions interbandes, qui, pourtant, jouent un rôle déterminant dans les propriétés optiques linéaires autour de la longueur d'onde harmonique (400 nm). On pourrait également invoquer la présence de surfactants pour stabiliser les particules, modifiant au voisinage de la surface la densité électronique, ou encore l'existence d'états électroniques de surface comme cela a été largement débattu par le passé. Une multitude de pistes pourraient ainsi être explorées mais dépassent largement le cadre de ce qui était réalisable.

Nous pouvons néanmoins tenter d'aller un peu plus loin en autorisant également pour le paramètre *b* (associé aux courants tangentiels de surface) de prendre une valeur quelconque. On se heurte cependant à une difficulté liée au nombre de paramètres indépendants que l'on peut extraire des courbes expérimentales. En effets, nous ne disposons que de trois ingrédients permettant de fixer les coefficients *a*, *b* et *d*: la différence d'intensité entre les courbes V et H, l'amplitude de modulation des courbes H dues aux effets d'interférences et l'apparition d'un méplat au niveau de la réponse en polarisation pour un angle de 90° (polarisation incidente horizontale). Ainsi, si l'on fixe le paramètre *d* à 1 (ce qui est possible grâce à la constante de normalisation *G*) et qu'on autorise une valeur complexe pour *a*, il ne reste qu'un seul paramètre ajustable, c'est-à-dire qu'il n'est possible de déterminer que la partie réelle ou que la partie imaginaire de *b*. Nous avons ainsi obtenu deux jeux de paramètres permettant d'ajuster parfaitement les courbes expérimentales: *a*=0.5-0.2i, *b*=0.1 et *d*=1 en choisissant *b* réel et *a*=0.5-0.2i, *b*=-0.1i et *d*=1 avec *b* imaginaire pur. Au contraire, si la contribution du courant tangentiel est supprimée (*b*=0), l'ajustement ne parvient pas à reproduire le méplat obtenu pour polarisation incidente horizontale. Ainsi, si la phase du paramètre *b* ne peut être déterminée, il apparaît que la contribution du courant tangentiel est faible mais nécessaire pour rendre compte des résultats expérimentaux. Le résultat final de

l'ajustement des résultats expérimentaux obtenus pour les deux configurations V et H est présenté dans la figure 21, soulignant l'excellent accord entre les simulations et l'expérience.

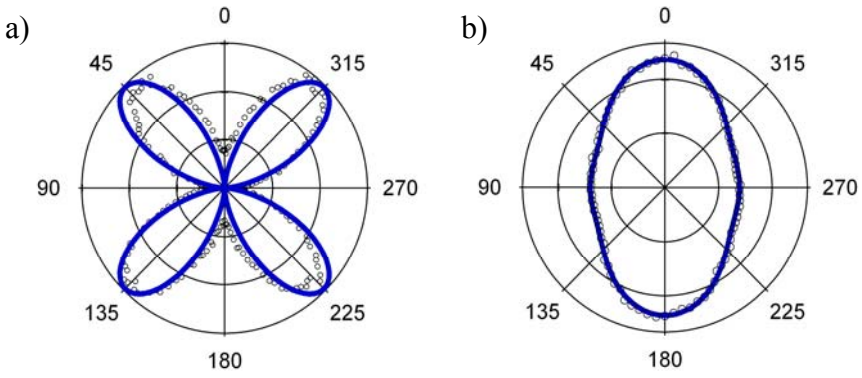

Figure 21: *Les courbes expérimentales (cercles) et simulées (trait plein) sont comparées après ajustement avec les même paramètres de Rüdnick et Stern des résultats expérimentaux obtenus avec une analyse verticale (gauche) et horizontale (droite).*

Le dernier point que je souhaiterais discuter ici concerne la contribution relative des sources de surface et de volume à la génération de second harmonique dans les nanoparticules métalliques. Contrairement à une idée reçue, provenant de la rupture de la centrosymétrie à la surface des particules de métaux nobles, la contribution des courants locaux de surface associés à $\chi_{s,\perp\perp\perp}$ ne domine pas nécessairement la réponse SHG des particules. Au contraire. Comme le montrent les figures 20e et 20f, si le signal non-linéaire est bien produit majoritairement par les courants de surface pour une détection verticale des photons harmoniques, il en va tout autrement pour une détection horizontale, dominée, elle, par les courants volumiques non-locaux. Ainsi, selon la configuration expérimentale, l'un ou l'autre des mécanismes peut-être privilégiés. Il est intéressant de rappeler à ce stade que les courants volumiques non-locaux sont associés à la force de Lorentz et donc intrinsèquement au champ magnétique de l'onde incidente (même si la forme finale que nous utilisons fait intervenir le gradient du champ électrique). Bien que le rapport d'amplitude entre le champ électrique et le champ magnétique soit donné par la vitesse de la lumière, l'effet du champ magnétique sur la trajectoire des électrons, conduisant à la génération de photons harmoniques, est du même ordre de grandeur que celui du champ électrique induit par la rupture de centro-symétrie à la surface des particules. Cette nécessité de prendre en compte les deux types de sources (courants locaux de surface et non-locaux de volume) s'est manifestée très tôt du point de vue des simulations puisque rien ne permettait a priori de privilégier une contribution plutôt que

l'autre (tout ce qui n'est pas interdit est autorisé...). Les résultats présentés dans la figure 20 constituaient ainsi la consécration d'un long travail d'investigation, parfois à contre-courant, qui a aboutit à la première détermination quantitative des contributions de surface et de volume dans les nanoparticules métalliques. Les perspectives de ces travaux sont multiples avec notamment la vérification du caractère résonant des courants locaux de surfaces par l'intermédiaire du paramètre *a*, l'évaluation de la contribution des transitions interbandes, ou encore la vérification que les paramètres obtenus sont transportables à d'autres géométries de particules et qu'ils sont donc bien "universels" et non particules dépendants (pour peu que les mêmes surfactants soient utilisés...).

Origin of optical second-harmonic generation in spherical gold nanoparticles: Local surface and nonlocal bulk contributions

G. Bachelier,* J. Butet, I. Russier-Antoine, C. Jonin, E. Benichou, and P.-F. Brevet
Laboratoire de Spectrométrie Ionique et Moléculaire (LASIM), Université Claude Bernard Lyon 1–CNRS, UMR 5579, Bat. A. Kastler, 43 Bd du 11 novembre 1918, 69622 Villleurbanne, France

(Received 15 June 2010; revised manuscript received 17 September 2010; published 1 December 2010)

The second-harmonic generation of 150 nm spherical gold nanoparticles is investigated both experimentally and theoretically. We demonstrate that the interference effects between dipolar and octupolar plasmons can be used as a fingerprint to discriminate the local surface and nonlocal bulk contributions to the second-harmonic generation. By fitting the experimental data with the electric fields computed with finite-element method simulations, the Rudnick and Stern parameters weighting the relative nonlinear sources efficiencies are evaluated and the validity of the hydrodynamic model and the local density approximation approaches are discussed.

DOI: 10.1103/PhysRevB.82.235403 PACS number(s): 78.67.Bf, 42.25.Hz, 42.65.Ky, 73.20.Mf

I. INTRODUCTION

Nanoscience and nanotechnology have focused a wide interest in the past decades on noble-metal nanostructures in view of the unique optical properties offered by the surface plasmon resonances (SPRs). Their understanding is nowadays reaching one of its ultimate development with the ability to combine numerical simulations, three-dimensional transmission electronic microscopy, optical extinction measurements, or electron loss spectroscopy at the single-particle level.[1–3] In addition, new opportunities in plasmonics and metamaterials have been recently opened with the coupling electric and magnetic dipoles in split-ring resonators or the tailoring of the SPR using Fano interferences.[4,5] Though, one of the main emerging challenges lies in the dynamical, time-resolved control of the SPR. In this context, one appealing route is the use of nonlinear optics driven by femtosecond laser pulses. The understanding of the nonlinear processes at play in plasmonic nanostructures is therefore becoming a very active topic.

The second-harmonic generation (SHG), whereby two photons at the fundamental frequency are converted into a single photon at the harmonic frequency, has quite a long history as it will soon celebrate its 50 years anniversary with the pioneer works of Franken *et al.*[6] The origin of the nonlinear sources has early been established as arising from the breakdown of the centrosymmetry at the metal surface (local response) or from field gradients inside the bulk (nonlocal response). Two theoretical approaches were pursued to account for their relative intensity: the analytic hydrodynamic model introduced by Sipe *et al.*[7] and the density-functional approach proposed by Liebsch.[8] The later was found to be the most accurate description although a complete theoretical framework involving both intraband and interband transitions is still missing. Noble-metal nanoparticles have triggered a renewed interest in SHG. Especially, the size dependence of the nonlinear efficiency, the effects of resonance, composition and chirality of the nanostructures have been addressed.[9–15] Single-particle sensitivity has also been reached in different configurations.[16–18] Analytical models have been developed for simple geometries such as spheres and cylinders.[19–21] If these important works mainly derived the selections rules and therefore the excited and radiating multipolar surface plasmon modes, they did not quantitatively evaluate the relative contributions of surface and bulk sources to the SHG, which therefore remains a largely open question. Few recent works involving numerical simulations have suggested that the bulk currents are indeed a fundamental contribution to the nonlinear response in noble-metal nanostructures.[22]

In this work, we investigate both experimentally and theoretically the nonlinear optical properties of 150 nm spherical gold nanoparticles in solution. We demonstrate that the interference effects between dipolar and octupolar plasmons, which has been addressed recently,[23] can be used as a fingerprint to discriminate the local surface and nonlocal bulk contributions to the second-harmonic generation. In particular, the Rudnick and Stern parameters, weighting their relative efficiencies,[24] are evaluated by fitting the experimental data with the electric fields computed with finite-element method (FEM) simulations.

II. RESULTS AND DISCUSSION

A. Local surface and nonlocal bulk contributions

For isotropic and centrosymmetric materials, the second-order surface susceptibility tensor can be drastically reduced to only three independent components: $\chi_{\perp\perp\perp}$, $\chi_{\perp\parallel\parallel}$, and $\chi_{\parallel\parallel\perp}$, where $\perp$ and $\parallel$ stem for perpendicular and parallel to the surface, respectively. However, from both theoretical and experimental point of view,[25] the $\chi_{\perp\parallel\parallel}$ component only weakly contributes to the SHG of noble metals. Hence, the two dominant surface nonlinear polarizations can be written as

$$P_{surf,\perp}(\mathbf{r},2\omega) = \chi_{\perp\perp\perp} E_{\perp}(\mathbf{r},\omega) E_{\perp}(\mathbf{r},\omega), \tag{1}$$

$$P_{surf,\parallel}(\mathbf{r},2\omega) = \chi_{\parallel\parallel\perp} E_{\parallel}(\mathbf{r},\omega) E_{\perp}(\mathbf{r},\omega), \tag{2}$$

where the electric fields are evaluated inside the metal. These polarization vectors lead to surface currents located just outside the metal[7] and given by $\mathbf{j}_{surf} = \partial \mathbf{P}_{surf} / \partial t$. From general considerations, the nonlocal bulk polarization may also have different contributions. However, in the special case of noble metals probed by a single fundamental field, it reduces to the following expression:[25]

$$\mathbf{P}_{bulk}(\mathbf{r},2\omega) = \gamma_{bulk}\nabla .[\mathbf{E}(\mathbf{r},\omega).\mathbf{E}(\mathbf{r},\omega)], \quad (3)$$

where γ_{bulk} is the bulk susceptibility. The associated bulk current is given by $\mathbf{j}_{bulk}=\partial\mathbf{P}_{bulk}/\partial t$. Hence, the knowledge of $\chi_{\perp\perp\perp}$, $\chi_{\parallel\perp}$, and γ_{bulk} allows in principle to completely determine the nonlinear optical properties of noble-metals nanostructures. Following Sipe *et al.*[7] these parameters can be linked to the adimensional Rudnick and Stern parameters[24] through the relations

$$\chi_{\perp\perp\perp} = -\frac{a}{4}[\epsilon_r(\omega)-1]\frac{e\epsilon_0}{m\omega^2}, \quad (4)$$

$$\chi_{\parallel\perp} = -\frac{b}{2}[\epsilon_r(\omega)-1]\frac{e\epsilon_0}{m\omega^2}, \quad (5)$$

$$\gamma_{bulk} = -\frac{d}{8}[\epsilon_r(\omega)-1]\frac{e\epsilon_0}{m\omega^2}, \quad (6)$$

where e and m are the electron charge and mass and $\epsilon_0\epsilon_r(\omega)$ stems for the dielectric function of the metal at the frequency ω.[26] In the framework of the hydrodynamic model,[7] the Rudnick and Stern parameters have very simple expressions: $a=1$, $b=-1$, and $d=1$. However, if both tangential and bulk currents are well described by macroscopic parameters related to the dielectric functions, the normal current is driven by the local distribution of the electronic density over the Fermi length below the metal surface. Therefore, one has to go beyond the hydrodynamic model in order to properly evaluate the parameter a. In particular, the latter was found to be larger than 1, frequency dependent and complex valued using local density approximation applied to conduction electrons only.[8] It is also important to note that both the hydrodynamic model and the local density approximation approach were designed for planar surfaces and not for spherical particles. However, for particle radii by far larger than the Fermi length, the surface curvature effect can be assumed to be negligible, as well as quantum-size effects.

B. Finite-element method simulations

The nonlinear currents corresponding to Eqs. (1)–(3) were computed for a 150 nm gold nanoparticle assuming $a=1$, $b=-1$, and $d=1$ [see Figs. 1(a)–1(c)]. The fundamental electric field was obtained through FEM using the scattered field formulation and perfectly matched layers in order to avoid any unwanted reflection at the simulation boundaries.[27] In a second step, the near-field distribution of the harmonic field was calculated solving the Maxwell's equations within the weak formulation, allowing to incorporate both surface and bulk sources. As shown in Figs. 1(d)–1(f), the obtained near-field maps around the nanoparticle do not strongly depend on the nonlinear source, except in terms of overall intensity. The latter is directly driven by the parameters a, b, and d but also by the evanescent and therefore localized character of the harmonic field. The knowledge of the far-field SHG intensity is a key ingredient to compare simulations with experimental measurements. It was computed from the near-field distribution of the harmonic field using the Stratton-Shu formula.[27]

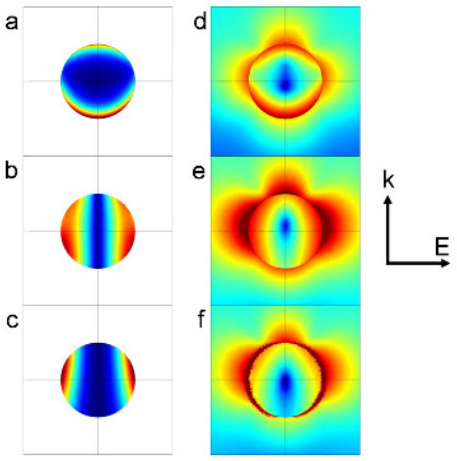

FIG. 1. (Color online) Spatial distribution of the nonlinear currents calculated (a) for the bulk contribution, (b) the tangential, and (c) normal surface currents for a 150 nm gold nanoparticle excited at 800 nm. The near-field map of the corresponding harmonic field amplitudes are given in panels d–f.

Figures 2(a) and 2(b) show the SHG intensities simulated for an excitation beam (wave vector $\mathbf{k}$) along the z axis and a collection at right angle (along the y axis). The fundamental electric field polarization angle with respect to the x axis is noted γ. For $\gamma=0$ the polarization is along the x axis i.e., perpendicular to the scattering plane and $\gamma=90°$ corresponds to a polarization along the y axis, i.e., in the scattering plane. Depending on the selected polarization for the harmonic field, different patterns are observed. For a detection polar-

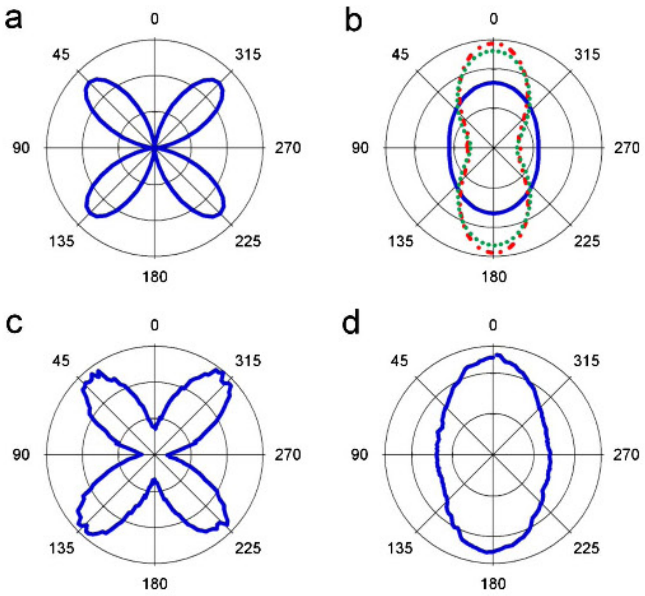

FIG. 2. (Color online) Normalized far-field second-harmonic intensity computed using FEM simulations [(a) and (b)] and measured experimentally [(c) and (d)] as a function of the electric field polarization at the fundamental frequency. The polarization of the harmonic field is perpendicular [(a) and (c)] and parallel [(b) and (d)] to the scattering plane. The normal surface current (dashed-dotted lines), tangential surface current (dotted lines), and bulk currents (full lines) contributions are shown separately.

ization perpendicular to the scattering plane, a four lobe pattern is obtained whatever the origin of the nonlinear sources, arising either from the surface or from the bulk of the nanoparticle [all curves are superposed in Fig. 2(a)]. Invoking spherical harmonics characterized by the angular momenta (l,m) with $-l \leq m \leq l$, the latter property can be explained considering that (i) the $[\mathbf{k}, \mathbf{E}(\mathbf{r},\omega)]$ plane and the plane normal to it are symmetry planes for the harmonic field allowing only even values for m, (ii) the component of the field perpendicular to symmetry planes cancels out imposing $m \neq 0$ for detection polarization perpendicular to the scattering plane, and (iii) the fundamental field contains only $m = \pm 1$ terms leading to polarization vectors in Eqs. (1)–(3) having $|m| \leq 2$. Hence, a quadrupolar pattern associated to $m = \pm 2$ is always observed, whatever the excited multipole given by l. This detection configuration is therefore unlikely to discriminate the different contributions from the polarization measurements.

C. Discrimination between the nonlinear sources

Owing to the surface and bulk origin of the nonlinear currents, it might be tentative to use the size dependence of the SHG intensity to assess the relative contributions of the nonlinear sources. As a matter of fact, it was found experimentally that the SHG intensity scales as the squared surface for small gold nanoparticles whereas a squared volume dependence is observed for larger ones.[9] However, unexpected dipolar patterns, normally forbidden owing to the previous discussion, were revealed for small particles and for detection polarization perpendicular to the scattering plane. This was attributed to the centrosymmetry breaking of the particle shape[9] as later demonstrated with FEM simulations.[28] Indeed, all nonlinear sources lead to the same size dependence of the scattered intensity, regardless of their surface or bulk origin. This was verified with FEM simulations for spherical and deformed particles (data not shown here) but can be directly understood from Eqs. (1)–(3): the gradient appearing in the bulk polarization of centrosymmetric materials [Eq. (3)] introduces in spherical coordinates an additional term scaling as $1/r$ and leading therefore to the same size dependence for the volume and surface polarization induced SH intensities. As a consequence, the size dependence cannot be used to separate bulk and surface contributions in centrosymmetric materials.

Another strategy has therefore to be pursued in order to weight the nonlinear surface and bulk contributions in gold nanoparticles. This is provided by the interference effects between selected dipoles and octupoles we have recently demonstrated[23] for a detection polarization in the scattering plane. In this specific configuration, constructive and destructive interferences are controlled by the incident polarization angle, leading to the varying intensities shown in Fig. 2(b). The key point here is that the interference pattern depends on the nonlinear source (surface or bulk). More precisely, if both surface terms have nearly the same polarization dependence for the SHG intensity, they clearly deviate from the bulk contribution for which the intensity weakly oscillates for a 150 nm gold nanoparticle excited at 800 nm.

D. Quantitative determination of the nonlinear sources efficiencies

The experimental data shown in Fig. 2 were obtained using a mode-locked Ti:sapphire laser tuned to a wavelength of 800 nm and delivering pulses of about 180 fs at a repetition rate of 76 MHz. The pulse energy measured at the laser exit was 10 nJ. The laser beam was focused onto a quartz cell with a microscope objective ($\times 16$, NA=0.32) leading to a beam waist at the fundamental frequency of 5 μm.[16] A low-pass filter was used in order to remove any residual light at the harmonic frequency generated prior to the cell. The SH photons are collected perpendicularly to the incident beam with a 25 mm focal length lens (NA=0.5). The scattered photons at the fundamental frequency are removed by a high-pass filter placed before the monochromator. The polarization angle of the fundamental beam is selected with a rotating half-wave plate and the polarization of the SH photons is selected by an analyzer. The photon detection was performed by a sensitive cooled photomultiplier tube and the fundamental beam was chopped at 130 Hz allowing a gated photon counting regime in order to remove the background light. The colloid solution of gold nanoparticles dispersed in water (1.4 pM) were purchased from BBI International (average diameter of 150 nm with a standard deviation of 8%).

Comparing the calculated and measured signals [see Figs. 2(b) and 2(d)], one can directly conclude that the normal surface current, which is usually considered as dominating the nonlinear response, cannot account by itself for the observed pattern, in contrast with the results obtained in Ref. 23 for particle sizes smaller than 100 nm. Bulk and surface nonlinear sources being excited coherently, the corresponding SHG intensities shown in Fig. 2(b) cannot be summed up directly: the relative phases of the harmonic fields have to be taken into account. More precisely, it has to be noted that these phases depend on the input polarization angle since different multipoles are involved. This key feature allows the discrimination of the two surface contributions, having otherwise nearly the same intensity pattern [see Fig. 2(b)]. The experimental data were therefore fitted by

$$I_{\mathrm{SHG}} = G|a\mathbf{E}_{surf,\perp}(\mathbf{r},2\omega) + b\mathbf{E}_{surf,\parallel}(\mathbf{r},2\omega) + d\mathbf{E}_{bulk}(\mathbf{r},2\omega)|^2 \tag{7}$$

where a, b, and d are the adjustable Rudnick and Stern parameters and G is a normalizing constant. $\mathbf{E}_{surf,\perp}$, $\mathbf{E}_{surf,\parallel}$, and $\mathbf{E}_{bulk}$ are harmonic fields associated with the source terms given by Eqs. (1)–(3) as obtained from the FEM simulations in the far-field region. The intensities recorded for a harmonic polarization in and out of the scattering plane were simultaneously fitted using the same Rudnick and Stern parameters in order to fully account for all experimental data. Owing to the normalizing constant G, their absolute values cannot be extracted by the fitting procedure but the relative amplitude and phase do.

E. Comparison with existing models

Different constraints were applied to the fitting Rudnick and Stern parameters in order to check the validity of exist-

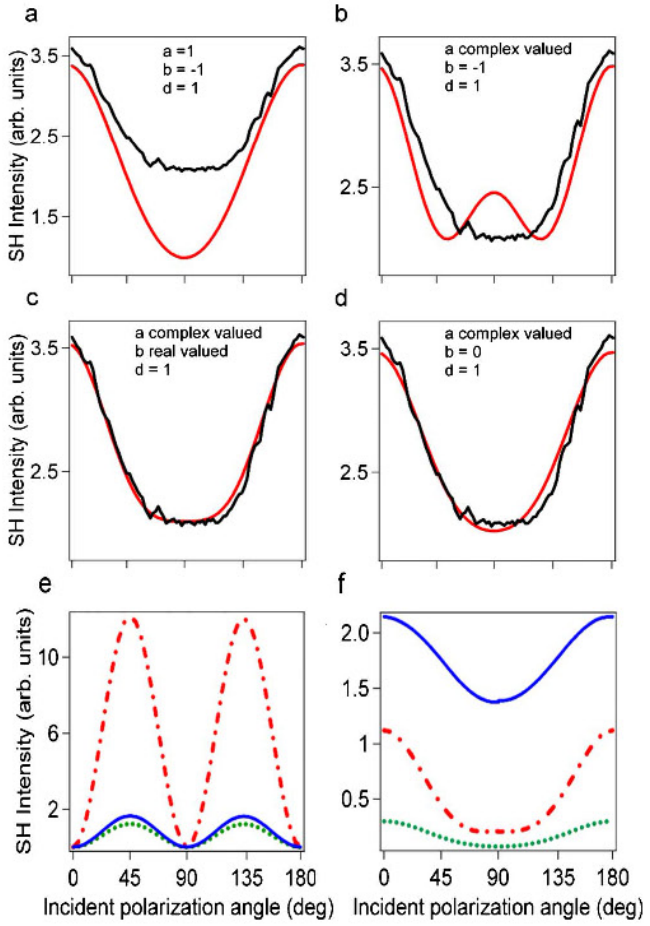

FIG. 3. (Color online) Fits of the experimental data (only the harmonic polarization in the scattering plane is shown) using the complex-valued harmonic fields, as computed with the FEM simulations, and the following restrictions on the Rudnick and Stern parameters: (a) $a=d=-b=1$, (b) a complex valued and $d=-b=1$, (c) a complex valued, b real valued, and $d=1$, and (d) a complex valued, $b=0$ and $d=1$. The scattered intensities corresponding to the normal surface current (dashed-dotted lines), tangential surface current (dotted lines), and bulk currents (full lines) computed separately with the fitted Rudnick and Stern parameters of panel (c) are shown for a harmonic polarization parallel (e) and perpendicular (f) to the scattering plane.

ing models. We first considered the hydrodynamic model[7] where the Rudnick and Stern parameters satisfy $a=d=-b=1$. Clearly, the obtained result cannot account for the experimental data, as shown in Fig. 3(a). More advanced models were early proposed including a damping term to the hydrodynamic model[29] or taking into account the spatial distribution of the electrons over the Fermi length below the surface within local density approximation.[8] All these models suggest that $d=-b=1$ and a is complex valued and exhibit resonant behavior largely exceeding in amplitude the two other parameters. As a matter of fact, it was here again not possible to reproduce the experimental data by the fitting procedure [see Fig. 3(b)]: additional minor peaks appear at 90° and 270°, in contrast with the experimental data. The fact that the damped hydrodynamic model and the local density approximation approaches can not accurately account for the SHG in gold nanoparticles is not surprising since they do not take into account the interband transitions that are resonantly excited at the harmonic wavelength (400 nm). Hence, a complete theoretical investigation of both intraband and interband transitions is required in order to correctly describe the nonlinear optical properties of noble-metal nanoparticles.

In order to go further in the understanding of the bulk and surface contributions in the SHG from gold nanoparticles, the condition $d=-b=1$ was relaxed, allowing the parameter b to take any real values. As shown in Fig. 3(c), a very good agreement between experimental data and FEM simulations is obtained for $d=1$, $b=0.1(1)$, and $a=0.5(6)-i0.2(5)$. If either the volume contribution (d) or the tangential surface contribution (b) is suppressed, a less satisfactory fit is achieved as shown in Fig. 3(d) for $b=0$: it is not possible to reproduce the plateau observed at 90° nor the intensity maximums reached at 0° and 180°, indicating that some physics is missing. Hence all contributions are necessary to account for the scattered SH intensity, even if in the present case the tangential surface contribution is rather weak [see Fig. 3(f)]. Despite the fact that $|a|<|d|$, the normal surface current largely dominates the nonlinear response for a detection polarization perpendicular to the scattering plane [Fig. 3(e)] with an intensity nearly 7.5 larger than the other contributions. In contrast, the SHG intensity collected for harmonic polarization in the scattering plane is dominated by the bulk currents as shown in Fig. 3(f). The ratio between bulk and surface contributions ranges from 2 to 6.5 depending on the fundamental polarization angle. This clearly underlines the importance of the bulk source that can be the dominant contribution in the SHG from gold nanostructures depending on the experimental configuration.[22]

III. CONCLUSION

In conclusion, it is shown that the local surface and nonlocal bulk contributions to the harmonic generation can be discriminated using an interference effect between the selected dipolar and octupolar plasmon modes, in a specific scattering and polarization configuration. By fitting the experimental data by the simulated electric fields, we report the quantitative determination of the nonlinear sources efficiencies in spherical gold nanoparticles. We show that the actual theoretical models, namely, the hydrodynamic model and the density-functional approach, cannot account for the experimental data obtained on 150 nm spherical gold nanoparticles. This is attributed to the interband transitions that are excited resonantly in the present case and not included in these models. Finally, we demonstrate that the relative local surface and nonlocal bulk contributions strongly depend on the experimental configuration.

*guillaume.bachelier@lasim.univ-lyon1.fr

[1] E. M. Perassi, J. C. Hernandez-Garrido, M. S. Moreno, E. R. Encina, E. A. Coronado, and P. A. Midgley, Nano Lett. **10**, 2097 (2010).
[2] J. Nelayah, M. Kociak, O. Stephan, F. J. G. de Abajo, M. Tence, L. Henrard, D. Taverna, I. Pastoriza-Santos, L. M. Liz-Marzan, and C. Colliex, Nat. Phys. **3**, 348 (2007).
[3] O. L. Muskens, G. Bachelier, N. Del Fatti, F. Vallee, A. Brioude, X. C. Jiang, and M. P. Pileni, J. Phys. Chem. C **112**, 8917 (2008).
[4] V. M. Shalaev, Nat. Photonics **1**, 41 (2007).
[5] G. Bachelier, I. Russier-Antoine, E. Benichou, C. Jonin, N. Del Fatti, F. Vallee, and P. F. Brevet, Phys. Rev. Lett. **101**, 197401 (2008).
[6] P. A. Franken, G. Weinreich, C. W. Peters, and A. E. Hill, Phys. Rev. Lett. **7**, 118 (1961).
[7] J. E. Sipe, V. C. Y. So, M. Fukui, and G. I. Stegeman, Phys. Rev. B **21**, 4389 (1980).
[8] A. Liebsch, Phys. Rev. Lett. **61**, 1233 (1988).
[9] I. Russier-Antoine, E. Benichou, G. Bachelier, C. Jonin, and P. F. Brevet, J. Phys. Chem. C **111**, 9044 (2007).
[10] I. Russier-Antoine, G. Bachelier, V. Sabloniere, J. Duboisset, E. Benichou, C. Jonin, F. Bertorelle, and P. F. Brevet, Phys. Rev. B **78**, 035436 (2008).
[11] E. C. Hao, G. C. Schatz, R. C. Johnson, and J. T. Hupp, J. Chem. Phys. **117**, 5963 (2002).
[12] M. Chandra and P. K. Das, Chem. Phys. Lett. **476**, 62 (2009).
[13] S. Kujala, B. K. Canfield, M. Kauranen, Y. Svirko, and J. Turunen, Phys. Rev. Lett. **98**, 167403 (2007).
[14] B. K. Canfield, H. Husu, J. Laukkanen, B. F. Bai, M. Kuittinen, J. Turunen, and M. Kauranen, Nano Lett. **7**, 1251 (2007).
[15] V. K. Valev, N. Smisdom, A. V. Silhanek, B. De Clercq, W. Gillijns, M. Ameloot, V. V. Moshchalkov, and T. Verbiest, Nano Lett. **9**, 3945 (2009).
[16] J. Butet, J. Duboisset, G. Bachelier, I. Russier-Antoine, E. Benichou, C. Jonin, and P. F. Brevet, Nano Lett. **10**, 1717 (2010).
[17] R. C. Jin, J. E. Jureller, H. Y. Kim, and N. F. Scherer, J. Am. Chem. Soc. **127**, 12482 (2005).
[18] B. K. Canfield, H. Husu, J. Kontio, J. Viheriala, T. Rytkonen, T. Niemi, E. Chandler, A. Hrin, J. A. Squier, and M. Kauranen, New J. Phys. **10**, 013001 (2008).
[19] J. I. Dadap, J. Shan, K. B. Eisenthal, and T. F. Heinz, Phys. Rev. Lett. **83**, 4045 (1999).
[20] A. G. F. de Beer and S. Roke, Phys. Rev. B **75**, 245438 (2007).
[21] C. I. Valencia, E. R. Mendez, and B. S. Mendoza, J. Opt. Soc. Am. B **21**, 36 (2004).
[22] Y. Zeng and J. V. Moloney, Opt. Lett. **34**, 2844 (2009).
[23] J. Butet, G. Bachelier, I. Russier-Antoine, C. Jonin, E. Benichou, and P. F. Brevet, Phys. Rev. Lett. **105**, 077401 (2010).
[24] J. Rudnick and E. A. Stern, Phys. Rev. B **4**, 4274 (1971).
[25] F. X. Wang, F. J. Rodriguez, W. M. Albers, R. Ahorinta, J. E. Sipe, and M. Kauranen, Phys. Rev. B **80**, 233402 (2009).
[26] P. B. Johnson and R. W. Christy, Phys. Rev. B **6**, 4370 (1972).
[27] J. Jin, *The Finite-Elements Method in Electrodynamics* (Wiley Interscience, New York, 2002).
[28] G. Bachelier, I. Russier-Antoine, E. Benichou, C. Jonin, and P. F. Brevet, J. Opt. Soc. Am. B **25**, 955 (2008).
[29] M. Corvi and W. L. Schaich, Phys. Rev. B **33**, 3688 (1986).

3- Vers le système modèle : la particule unique en milieu homogène

Les mesures d'ensembles que nous avons réalisées jusque là nous ont permis de faire des avancées significatives sur l'origine des propriétés optiques non-linéaires des particules métalliques. Elles présentent cependant un défaut majeur inhérent à ce type de technique: le moyennage sur une collection d'objets pouvant présenter une distribution de taille, de forme, etc. induisant d'inévitables élargissements hétérogènes. La génération de second harmonique dans les particules métalliques a, de ce point de vue, une position singulière comparée à la diffusion élastique (Mie) par exemple: étant interdite à l'ordre dipolaire dans les milieux centrosymmétriques, elle est particulièrement sensible à toute déformation qui brise la symétrie, modifiant drastiquement le diagramme de rayonnement ou la réponse en polarisation comme nous l'avons vu pour les particules sphériques de petite taille (partie 2.1). L'intérêt d'atteindre la sensibilité de la particule unique est alors évident. La question qui se pose, comme toujours, est de savoir si l'on dispose d'une sensibilité suffisante pour arriver à extraire le signal SHG d'une particule du signal de fond provenant du solvant. D'un côté, la génération de second harmonique dans une particule d'or ou d'argent est un processus très peu efficace comme nous le verrons quantitativement par la suite. Il faut donc un système de détection extrêmement sensible, capable de compter quelques photons par secondes, rendant les expériences délicates notamment à toute source de bruit. D'un autre côté, contrairement au cas des expériences d'extinction en optique linéaire sur une particule unique, on travaille ici à la fréquence harmonique et à 90 degrés du faisceau incident. Pour peu que le solvant ne génère pas trop, nous ne sommes pas dans le cas où il faut extraire un petit signal d'un fond très important, ce qui est une situation plutôt favorable.

Un très joli travail a été réalisé dans ce sens par Julien Duboisset, alors en thèse au LASIM et encadré par Pierre-François Brevet (cf. référence 32 de la liste de publication). L'idée était de diluer progressivement la concentration en particules d'argent de 80 nm de diamètre jusqu'à atteindre le seuil de quelques particules dans le waist du faisceau femtoseconde. Dans ce régime, les fluctuations d'intensité du signal harmonique sont pondérées par la probabilité de trouver N particules dans le waist, probabilité de type poissonienne vu le faible nombre de particules. Il s'en suit que la valeur du signal évolue bien proportionnellement au nombre de particules contenues dans le waist, comme attendu, mais que l'histogramme des coups du photomultiplicateur présente une asymétrie, issue de la

distribution de Poisson, signature du nombre limité de particules. En comparant les résultats expérimentaux et simulés pour différentes concentrations (d'environ 3fM à 100fM), Julien Duboisset est parvenu à extraire la concentration correspondant à une particule en moyenne dans le volume sondé (29 fM) et l'hyperpolarisabilité d'une particule unique (200E-25 esu) en bon accord avec les mesures d'ensemble réalisées à plus grande concentration (170E-25 esu).

Fort de ce très beau résultat, prouvant que dispositif avait atteint la sensibilité de la particule unique, il ne restait plus qu'à figer les particules pour observer au cours du temps une seule et unique particule, plutôt que de moyenner au cours du temps la réponse des particules traversant le volume focal du faisceau femtoseconde (fusse-t-il avec en moyenne une seule particule dans le volume sondé). Nous franchissions ainsi le fossé entre la diffusion Hyper Rayleigh (moyenne incohérente sur plusieurs particule dans l'espace ou dans le temps) et la génération de second harmonique (diffusion cohérente au niveau de la particule unique ou d'un agrégat fixe dans le temps). Deux stratégies s'offraient à nous: soit immobiliser les particules sur un substrat, par spin-coating par exemple en assurant une distance interparticule grande devant le waist, soit "geler" les particules dans une matrice de gélatine ou de polymère avec une distance interparticule grande devant le paramètre confocal, afin d'assurer qu'une seule particule se trouve dans le volume sondé. Cette deuxième solution offrait le très grand avantage de préserver l'environnement homogène et isotrope de la particule unique et donc de se rapprocher du système idéal. D'autre part elle permet de maximiser la collection du signal SHG qui est émis principalement à 90° par rapport au faisceau incident. Elle présente en revanche un inconvénient: il n'est pas possible de faire du TEM sur les particules étudiées et de pouvoir corréler la morphologie et la réponse optique de la particule unique. Ce point n'étant pas déterminant dans une première approche, nous avons opté pour cette configuration.

Ce travail a été largement initié par Julien Duboisset à la fin de sa thèse avec notamment la mise en place des platines de translation pour réaliser les cartographies, le test des différentes gélatines pour minimiser à la fois la génération d'harmonique par la matrice et son absorption. Les toutes premières cartographies ont été réalisées sur des particules d'argent de 80nm de diamètre mais se sont révélées non reproductibles, vraisemblablement à cause de la détérioration des particules sous irradiation femtoseconde. L'origine du signal observé alors était donc pour le moins discutable, mais les premiers résultats étaient néanmoins encourageants... Ce travail s'est poursuivi avec Jérémy Butet tout d'abord "en biseau" au cours de son stage de M2 (co-encadré avec Isabelle Russier-Antoine et Pierre-François Brevet) puis de manière "autonome" au début de sa thèse (co-encadrée avec Pierre-François Brevet). Je passerai les nombreuses tentatives infructueuses, les optimisations multiples pour éviter tout

gradient d'indice dans la gélatine et prévenir l'évaporation de l'eau qu'elle contenait, donnant lieu à des ménisques fort beaux au demeurant mais désastreux du point de vue de l'optique. Je vous épargnerai aussi les tests sur l'intensité du laser pour ne pas dénaturer la gélatine et les x dilutions des solutions mères de particules, réalisées en espérant atteindre un régime où l'intensité montrerait des variations spatiales encourageantes (rappelons que la concentration des particules est mal connue et que ces dernières ne se répartissent probablement pas de manière homogène dans la gélatine!). C'est au moment critique où un certain doute sur la réelle faisabilité de l'expérience et une pointe de fatalisme commençaient à nous gagner que Jérémy a proposé de tester les particules d'or de 150 nm. Ces dernières ont en effet l'avantage d'être plus stables à la lumière et de présenter une efficacité non-linéaire équivalente à celle des particules d'argent utilisées jusque là. Ca n'a peut-être l'air de rien comme cela, mais ayant atteint le cap où toutes les alternatives possibles avaient été explorées, nous approchions dangereusement du point de renoncement où il fallait faire le dernier test ou tout abandonner. La suite lui a donné mille fois raison et à démontré une fois de plus qu'en recherche, comme dans bien d'autres domaines d'ailleurs, il ne faut jamais rien lâcher tant que subsiste une petite lueur d'espoir...

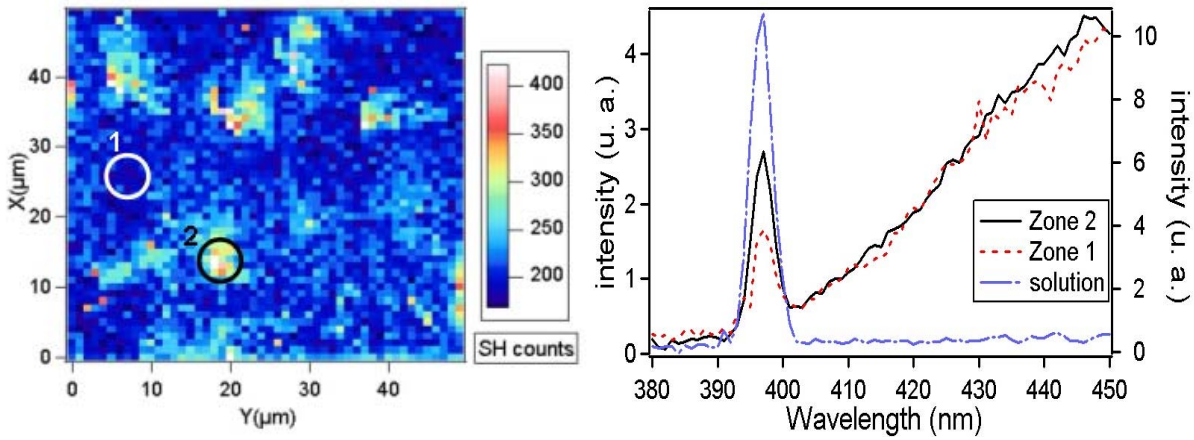

Figure 22: *Cartographie 2D du signal SHG obtenu en translatant perpendiculairement au faisceau incident un échantillon de nanoparticules d'or de 150 nm de diamètre immobilisées en matrice de gélatine. Le signal est collecté à 90° par rapport au faisceau incident, comme dans les expériences d'HRS, à une longueur d'onde de 397 nm. Les spectres présentent l'intensité collectée dans une zone de fort et faible signal de la cartographie (ordonnée de gauche) et sont comparés au signal obtenu pour une solution contenant les mêmes particules (axe de droite).*

La figure 22 présente une cartographie typique du signal SHG obtenu sur des particules d'or de 150 nm de diamètre et isolées en matrice. Si ce résultat a été un grand

succès pour nous, je concède volontiers que le rapport signal sur bruit n'est pas vraiment à notre avantage (notez que le très fort contraste entre le bleu foncé et le bleu clair a plutôt tendance à exagérer le bruit du signal sur la matrice...). Je souhaiterais tout de même souligner ici que cette "simple" cartographie correspond à une acquisition de 10 secondes par pixel, soit près de 7 heures d'acquisition! D'autre part, le signal moyen provenant de la matrice n'excède guère 20 photons par seconde auxquels viennent se superposer au maximum 20 photons par seconde venant des particules, lorsque celles-ci se trouvent au point de focalisation du laser, soulignant une fois de plus la grande sensibilité nécessaire pour faire ce type d'expériences.

La toute première question qui se posait à nous était de savoir comment prouver que les maxima d'intensité étaient (enfin!) bien associés à des particules métalliques et pas à des artéfacts venant d'impuretés ou d'agrégats de molécules de gélatine (la matrice). Pour ce faire, nous avons sélectionné deux zones sur la cartographie, l'une ayant une intensité faible (zone 1) et l'autre présentant un maximum de signal (zone 2). Dans la zone 1, le signal SHG est le même que celui enregistré dans une solution ne contenant que de la gélatine, démontrant ainsi que cette zone est dépourvue de particule métallique et que nous avons bien atteint un régime où les particules sont éloignées à l'échelle du volume sondé par le faisceau focalisé, ce qui était une condition sine qua non pour faire des mesures à l'échelle de la particule unique. Afin d'attribuer sans ambigüité le surplus de signal de la zone 2 à la présence d'une particule métallique, nous avons réalisés des spectres autour de la fréquence harmonique. On observe clairement deux types de contributions: i) une contribution large bande présente dans les zones 1 et 2 au-delà de la fréquence harmonique et qui correspond donc à de la fluorescence biphotonique provenant de la gélatine et ii) une raie plus étroite à la fréquence harmonique provenant de la matrice et de la particule sondée. Dans la mesure où le signal de fluorescence est pratiquement le même dans les zones 1 et 2, nous pouvons exclure la présence d'un agrégat de gélatine qui aurait modifié à la fois le signal harmonique et le signal de fluorescence. D'autre part, le même spectre réalisé sur des particules d'or en solution donne une quasi-absence de fluorescence comparée à la contribution HRS. La réponse non-linéaire de la particule domine donc très largement sa florescence expliquant les différences d'intensité mesurées dans les zones 1 et 2. Les plus sceptiques répliqueront que c'est une indication forte que le maximum d'intensité de la zone 2 pourrait être associé à une particule métallique, mais pour autant pas une preuve puisque d'autres particules pourraient donner la même réponse spectrale que les particules d'or (fort signal SHG et faible fluorescence). Ils n'auraient pas tord...

Pour avancer dans la démonstration, il fallait mesurer l'efficacité non-linéaire de la particule et la comparer à des mesures d'ensemble réalisées sur des particules d'or. Pour cela, nous avons utilisé la gélatine comme "référence interne". Cette dernière a un indice proche de celui de l'eau mais une efficacité non-linéaire 2.5 fois plus élevée. Dès lors, nous avons employé le même formalisme que celui utilisé au sein de l'équipe, mais adapté ici au cas d'une nanoparticule unique en matrice:

$$I_{SHG} = G\beta_{part}^2 I_{part}^2 + G\int 2.5 C_w \left\langle \beta_w^2 \right\rangle I_w^2 dV \,.$$

I_{part} et I_w sont les intensités vues respectivement par la particule et par les molécules constituant la gélatine, le facteur 2.5 traduisant le rapport entre les efficacités non-linéaires de l'eau et de la gélatine (C_w est donc la concentration des molécules d'eau dans de l'eau pure). Dans cette expression, β_{part} et β_w correspondent aux hyperpolarisabilités de la particule et des molécules d'eau respectivement. N'ayant pas introduit jusque là la notion d'hyperpolarisabilité, je précise juste qu'elle est le pendant de la susceptibilité non-linéaire, que nous avons discutée précédemment et qui relient la polarisation surfacique ou volumique aux champs, mais intégrée à l'échelle du diffuseur non-linéaire: $\vec{p} = \vec{\vec{\beta}} : \vec{E}\vec{E}$ où $\vec{p}$ est le moment dipolaire d'une molécule par exemple. Une conséquence est que le mécanisme lui donnant naissance et le caractère local ou non local n'apparaît pas explicitement. Notons que dans cette description la nature multipolaire du champ rayonné à la fréquence harmonique n'est pas prise en compte. En ce sens, l'hyperpolarisabilité β_{part} intervenant dans l'expression de l'intensité devrait plus être considérée comme une "section efficace", traduisant l'efficacité non-linéaire de la particule, que comme une réelle hyperpolarisabilité dans le cas de particules de grande taille (intervention des effets retard). Enfin, le caractère tensoriel de l'hyperpolarisabilité ainsi que toutes les corrélations induites entre les composantes du champ ont été masquées, pour ne pas alourdir les notations et au vue de l'étude qui va être menée. Seul subsiste dans le cas des molécules constituant la gélatine l'effet du moyennage sur toutes les orientations des molécules d'eau traduit par le bra-ket $\left\langle \beta_w^2 \right\rangle$.

Une fois toutes ces précautions prises quant à la signification des termes de l'expression donnant l'intensité mesurée, deux difficultés demeurent pour remonter à la réponse SHG de la particule unique: il faut évaluer le terme $\int I_w^2 dV$, la concentration de l'eau et son hyperpolarisabilité étant connues, et déterminer la position de la particule dans le waist pour obtenir la valeur de l'intensité I_{part} vue par la particule. Pour répondre à la première

interrogation, nous avons utilisé un moyen quelque peu détourné mais finalement assez efficace. N'ayant pas de moyen direct de mesurer la taille du waist, et ne souhaitant pas passer par des logiciels de calcul de faisceau en sortie d'un système optique, j'ai proposé d'utiliser le fait que la réponse d'une particule lors d'un scan est convoluée par la taille du spot laser. Ainsi, la fonction d'auto-corrélation d'une cartographie telle que celle présentée dans la figure 22 est directement liée à la géométrie du faisceau laser. Directement oui, mais il faut tenir compte du fait que les particules sont réparties aléatoirement dans l'espace, et non déposées sur un substrat. Selon la position de la particule par rapport au waist, l'extension spatiale du faisceau et l'intensité vue par la particule ne seront pas les mêmes. Pour faire le lien entre la fonction d'auto-corrélation 2D issues des cartographies et le waist, Jérémy Butet a simulé les fonctions d'auto-corrélations de particules présentant une fluorescence à deux photons (pour présenter la même dépendance en fonction du champ incident que le SHG) et comparé le résultat au waist utilisé comme paramètre dans la simulation. Une simple abaque donnant la largeur de la fonction d'auto-corrélation en fonction du waist nous a ainsi permis de remonter aux spécifications du faisceau utilisé dans le dispositif expérimental (waist w_0=5µm) et donc de calculer le terme $\int I_w^2 dV$.

La deuxième difficulté que j'ai évoquée est associée à connaissance de la position de la particule par rapport au waist. Cette question paraît triviale à première vue puisqu'il suffirait de faire un scan en 3D et de repérer la position donnant un maximum d'intensité, position où la particule serait sur le point de focalisation. Cependant, étant donné la taille du waist, la longueur de Rayleigh correspondante ($l=\pi w_0/\lambda$=140µm) serait trop longue pour réaliser une telle expérience sans désaligner le dispositif expérimental. Nous avons donc préféré enregistrer des cartographies dans différentes portions de l'échantillon et déduire l'hyperpolarisabilité de la particule à partir de la valeur la plus grande de l'intensité mesurés. Nous avons ainsi obtenue une valeur $\beta_{part} = (1.0 \pm 0.15).10^{-23}$ esu en excellent accord avec des mesures d'ensemble réalisées en solution sur les mêmes particules d'or de 150 nm de diamètre et donnant une valeur moyennée sur les orientations des particules $\langle \beta_{part} \rangle = (1.1 \pm 0.1).10^{-23}$ esu. Ce résultat a été une grande victoire pour nous. Pour autant, un doute pouvait encore subsister sur le fait que la particule de la zone 2 soit bien une particule d'or unique et non un agrégat contenant plusieurs particules. Dans la mesure où nous travaillons en "aveugle" (pas d'image TEM pour comparer), il fallait donc trouver une autre preuve: le simple fait de ne pas avoir observé d'intensité correspondant à N particules n'étant pas une preuve en soit mais juste une forte présomption...

Comme nous l'avons vu précédemment avec les simulations numériques, la génération de second harmonique est un processus extrêmement sensible à la symétrie, en particulier en termes de réponse en fonction de la polarisation incidente. Ainsi, dans l'hypothèse de la formation d'un agrégat, la réponse en polarisation devrait-être fortement chahutée. L'idée était donc de vérifier si nous obtenions bien une réponse quadripolaire (ou plus exactement associée à m=±2), en détectant le signal toujours à 90° du faisceau incident et avec une analyse verticale. Le résultat est présenté dans la figure 23b.

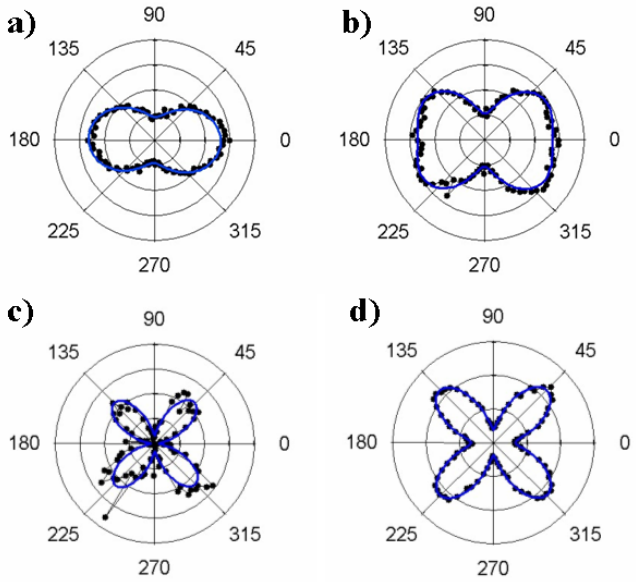

Figure 23: *Intensité SHG collectée pour une polarisation de détection perpendiculaire au plan de diffusion en fonction de la polarisation incidente (le zéro correspond à un champ perpendiculaire au plan de diffusion). Le signal est collecté dans la zone 1 (a) et la zone 2 (b) donnant par soustraction le graphe polaire (c) que l'on peut comparer au graphe (d) réalisé sur des particules en solution (mesure d'ensemble).*

De toute évidence, nous étions loin des quatre lobes attendus. Il faut cependant prendre en compte le fait que la réponse mesurée dans la zone 2 provient de la particule mais aussi de la matrice environnante, qui contribue dans tout le volume sondé, volume bien supérieur à la taille de la particule. Nous avons donc comparé ce signal à celui enregistré sur la zone 1 ne contenant que de la gélatine. Comme attendu, une contribution purement dipolaire a été obtenue de part l'orientation aléatoire des molécules dans la gélatine. Ce dernier point est en fait capital et a constitué la clé de l'énigme: grâce à l'orientation aléatoire des molécules de la gélatine, leur réponse est incohérente (cf. HRS) et n'interfère donc pas avec la réponse de la particule unique! Il suffisait donc de soustraire les réponses des zones 1 et 2 pour obtenir la réponse en polarisation de la particule. Le résultat est sans appel (cf.

Figure 23c): au bruit près qui vient de l'opération de soustraction, nous obtenons très clairement une réponse à quatre lobes (m=±2) présentant des maximas de même intensité et des minimas nuls. Ces deux derniers points sont particulièrement important dans la mesure où ils sont la signature d'une symétrie quasi-parfaite. Ceci nous permettait donc de rejeter définitivement l'hypothèse d'un agrégat et de pouvoir affirmer que nous venions de réaliser la toute première mesure de génération de second harmonique sur une particule métallique dans un milieu homogène et que le résultat obtenu était en parfait accord avec la théorie.

Cette première mondiale ouvre potentiellement de nombreuses perspectives puisqu'elle fournit un système modèle pour la compréhension des propriétés non-linéaires des particules métalliques (ou autres d'ailleurs). En particulier, comme le montre la figure 23d, elle permet de s'affranchir de l'effet de distribution de formes, responsables dans les mesures d'ensemble de l'apparition d'une intensité non-nulle pour des polarisations incidentes verticales ou horizontales (cf. partie 2.2). Ce type de mesures sur particules uniques présente néanmoins quelques inconvénients. Tout d'abord, il n'est pas possible de corréler les résultats à des images TEM, ce qui s'avère pourtant un outil décisif comme nous l'avons vu dans la partie traitant de la plasmonique (optique linéaire). Ensuite, elles nécessitent l'utilisation d'une intensité assez importante (la centaine de milliwatts) et des temps d'acquisitions conséquents (80s par point de mesure pour les spectres et les réponses en polarisation), ce qui restreint de fait les études à des particules ayant une très bonne stabilité à l'irradiation. Ce n'était manifestement pas le cas pour les particules d'argent par exemple ni pour des nano-bâtonnets d'or. Les campagnes d'expériences menées sur ces derniers par Jérémy Butet n'ont jamais donné de résultats positifs: la résonance dipolaire des bâtonnets se déplaçant dangereusement vers le rouge, l'explication la plus probable est la dénaturation des particules. Pour ces raisons et pour bien d'autres, il apparaît donc nécessaire de développer conjointement de nouveaux moyens d'investigations.

NANO LETTERS

pubs.acs.org/NanoLett

Optical Second Harmonic Generation of Single Metallic Nanoparticles Embedded in a Homogeneous Medium

Jérémy Butet, Julien Duboisset, Guillaume Bachelier,* Isabelle Russier-Antoine, Emmanuel Benichou, Christian Jonin, and Pierre-François Brevet

Laboratoire de Spectrométrie Ionique et Moléculaire, Université Claude Bernard Lyon 1 - CNRS, UMR 5579, 43 Boulevard du 11 Novembre 1918, 69622 Villleurbanne, France

ABSTRACT We report the optical second harmonic generation from individual 150 nm diameter gold nanoparticles dispersed in gelatin. The quadratic hyperpolarizability of the particles is determined and the input polarization dependence of the second harmonic intensity obtained. These results are found in excellent agreement with ensemble measurements and finite element simulations. These results open up new perspectives for the investigation of the nonlinear optical properties of noble metal nanoparticles.

KEYWORDS Single nanoparticle, gold, plasmonics, nonlinear optics, second harmonic generation, finite element method simulation

The observation of single objects the dimensions of which are much smaller than the wavelength of light has become a great technical challenge in optical sciences. The detection of single molecules has already been achieved with light emission-based techniques like fluorescence or Raman scattering.[1,2] Single metallic particle sensitivity has also been demonstrated in the past and applied to the investigation of the linear optical properties of metallic nanoparticles, and their absorption cross-section in particular, overcoming the heterogeneous broadening inherent to shape and size distributions of real samples.[3] Combined with numerical simulations, the size, shape, and orientation of single nanostructures such as metallic nanorods can be precisely determined although their size is largely below the diffraction limit.[4] Correlating the optical properties with that obtained from transmission electronic microscopy further deepens the understanding of the link between morphology and linear optical properties. This is especially true for coupled particles when the interparticle distance or the radius of curvature of the particle surface approaches the electron spill-out thickness.[5]

Nonlinear optical techniques, and more precisely second harmonic (SH) generation, the phenomenon whereby two photons at the fundamental frequency are converted into one photon at the harmonic frequency, have also been widely used for the investigation of noble metal particles produced by wet chemical synthesis and dispersed in solutions[6−11] or metallic nanostructures produced by e-beam lithography methods on substrates for instance.[12−15] However, only few works have been devoted to single particle analyses.[16−19] This is mainly due to the very weak signals expected for second order nonlinear optical processes like SH generation. These second order processes are indeed forbidden within the electric dipole approximation in centrosymmetric materials such as silver and gold. Furthermore, in small particles with a centrosymmetric shape, where small must be understood as much smaller than the wavelength of light, these second order processes allowed at the particle surface where the centrosymmetry of the material is broken vanish also for the same symmetry reasons. As a result, any deviation from centrosymmetry yields a nonvanishing SH intensity. For small particles, the SH response is thus dominated by the electric dipole contribution arising from the shape centrosymmetry breaking if the material centrosymmetry is assumed preserved.[8,20] In ensemble measurements, the averaging over the size, shape, and orientation distributions prevents one from getting a deeper understanding on the origin of the nonlinear optical properties of metal nanoparticles. With the availability of the required sensitivity,[21] going to the single particle level appears as a promising tool to go beyond ensemble measurements and investigate single metallic particles with a technique sensitive to shape centrosymmetry breaking.

In this letter, we report for the first time experiments where the SH intensity of a single metallic nanoparticle dispersed in a homogeneous medium is achieved. The quadratic hyperpolarizability determined is compared with standard hyper Rayleigh scattering (HRS) measurements on ensemble solutions[8] and with previous experiments where single metallic nanoparticle sensitivity was achieved with HRS measurements with low-concentration solutions.[21] In addition, the homogeneous and isotropic environment of the

* To whom correspondence should be addressed. E-mail: guillaume.bachelier@lasim.univ-lyon1.fr.

Received for review: 01/12/2010
Published on Web: 04/26/2010

DOI: 10.1021/nl1000949 | *Nano Lett.* **2010,** *10,* 1717–1721

nanoparticle used in the present configuration allows a direct comparison with theoretical simulations obtained with finite element method (FEM).[20] In particular, the SH intensity polarization pattern of a single gold metallic nanoparticle is used to further ensure that a single particle is observed and assess the nature of the SH fields in terms of the multipolar plasmon excitations.

The experimental setup was designed as follows. A mode-locked Ti:sapphire laser tuned to a wavelength of 794 nm and delivering pulses of about 180 fs at a repetition rate of 76 MHz was used as the laser source. The average output power was set at about 300 mW right after the laser exit. The fundamental beam was focused into a quartz cell with a microscope objective (×16, NA 0.32) and a red filter was placed in front of it to remove any residual light at the harmonic frequency generated prior to the cell. The cell position with respect to the laser focus was controlled by three micrometer-resolution translation stages (Newport, MFA-CC). The SH intensity collection was performed at right angle with a 25 mm focal length lens with a numerical aperture of 0.5. A blue filter was placed before a monochromator to remove the fundamental light. The detection was made with a cooled photomultiplier tube and the fundamental beam was chopped at 130 Hz to enable a gated photon counting regime allowing the removal of the background photons. The sketch of the setup can be found in ref 22. The aqueous solutions of the gold nanoparticles, the average diameter of which was about 150 nm, were purchased from BBI International and used as received. The gold nanoparticles were dispersed in a gelatin matrix (BLOOM 250, 8%). The gelatin matrix was obtained by raising the temperature of a water−gelatin mixture beyond the critical temperature at about 70 °C for 20 min and then cooled down to 4 °C for 12 h in the quartz cell with the particles. Gelatin is transparent at the wavelengths of excitation at 794 nm and SH emission at 397 nm and possesses a weak SH efficiency as required in order not to dwarf the SH signals from the gold nanoparticles.

The sample scans were carried out perpendicularly to the incident fundamental beam direction in order to obtained two-dimensional (2D) maps of the SH intensity versus cell position; see Figure 1. The heterogeneous spatial distribution of the SH intensity reveals areas with low (Zone 1) and high (Zone 2) intensities. The SH intensity from Zone 1 corresponds to the signal recorded for neat gelatin, that is, without particles, indicating that the low-intensity areas are composed exclusively of gelatin. In Zone 2 however, the SH intensity is significantly increased. This is attributed to the presence of the gold metal nanoparticles in this zone. To reject the possibility of other origins like gelatin inhomogeneities, broadband emission spectra of Zones 1 and 2 were recorded; see Figure 2. Two distinct features are observed, a narrow peak at 397 nm corresponding to the SH intensity and the onset of a broadband background with an increasing intensity toward longer wavelengths attributed to the gelatin

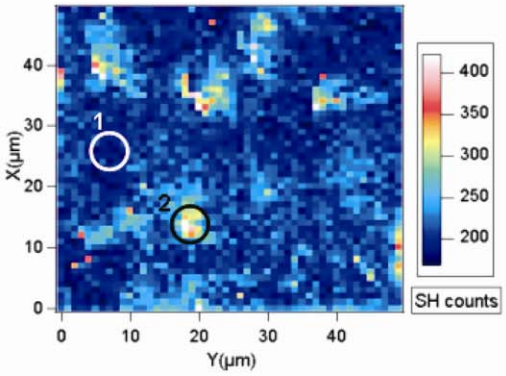

FIGURE 1. Two dimensional map of the SH intensity at 397 nm obtained for 150 nm gold nanoparticles embedded in gelatin by scanning the sample perpendicularly to the beam direction with 10s acquisition time per pixel. The two circles correspond to Zone 1 and Zone 2 as discussed in the text.

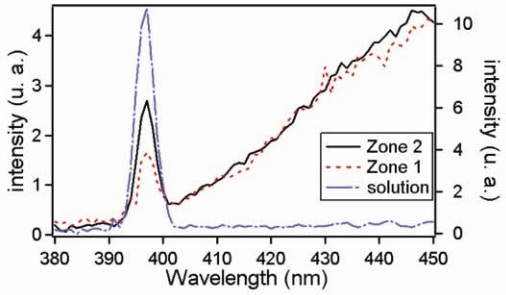

FIGURE 2. Emission spectrum from the zones 1 and 2 shown in Figure 1 for an excitation at 794 nm and 80 s acquisition time for each data point (left axis) and emission spectrum of 150 nm gold nanoparticles in solution (right axis).

multiphoton excited luminescence. This broadband luminescence background is identical in the two Zones 1 and 2 to that obtained from a neat gelatin sample without particles. Gelatin inhomogeneities are therefore not responsible for the large intensity recorded in Zone 2. One therefore concludes that the high intensity areas are related to the presence of the gold metal nanoparticles. This conclusion is further supported by the broadband emission spectrum obtained for an aqueous solution of these gold metallic nanoparticles, where almost no photoluminescence is observed.

The nonlinear efficiency of the gold metallic nanoparticles can be obtained by subtracting the SH intensity of the neat gelatin area, Zone 1, from the high intensity one, Zone 2; see Figure 2. The gelatin matrix can be used as an internal reference to determine the quadratic hyperpolarizability of the 150 nm diameter gold nanoparticles. For this purpose, the SH intensity scattered from a neat water cell and obtained under the same experimental conditions was used as an external reference for the neat gelatin. The refractive index of the gelatin, estimated either form a simple averaged value based on the water/gelatin molar ratio or from the shift of the surface plasmon resonance wavelength of the gold particles dispersed in water with respect to the resonance wavelength of those dispersed in gelatin, was found to be

DOI: 10.1021/nl1000949 | Nano Lett. 2010, 10, 1717–1721

1.36 as compared to 1.33 for pure water. This allows the neglect of any changes in the reflection conditions at the cell surface and any modification of the beam waist size and position in the cell. The SH intensities obtained for neat water and neat gelatin can hence be directly compared. The SH intensity of neat gelatin was found to be 2.5 times larger than that of neat water. The intensity radiated at the harmonic frequency for gelatin in the presence of the metallic particles can therefore be written as

$$I_{SHG} = G \int (2.5 C_w \langle \beta_w^2 \rangle I_\omega^2 + \beta_{part}^2 I_{\omega,part}^2) dV \qquad (1)$$

where C_w and $\beta_w = 0.56 \times 10^{-30}$ esu[23] are the concentration and quadratic hyperpolarizability of water, respectively. β_{part} stands for the quadratic hyperpolarizability of a single gold nanoparticle and $I_{\omega,part}$ for the fundamental intensity of the fundamental beam illuminating the gold nanoparticle. Note that the response of the particles and that of the gelatin background have been summed up incoherently in eq 1. This is allowed owing to the random orientations and positions of the gelatin molecules across the laser beam, leading to an intrinsically incoherent response as observed Hyper Rayleigh Scattering.[24] There is therefore no interference between the particle and the background responses.

There are two major difficulties in eq 1. (i) One has to determine properly the integral $\int I_\omega^2 \, dV$ of the squared fundamental intensity over the focused beam to determine the gelatin internal reference and (ii) one has to know precisely where the gold nanoparticle is located with respect to the fundamental beam waist. These two difficulties must be overcome simultaneously in order to take into account the fact that the gold particle, because of its small size, does not probe to whole cross-section of the fundamental beam but rather only a small portion of it. To address the first difficulty (i), 2D maps were recorded for 300 nm diameter fluorescein-doped latex particles. With the input fundamental beam wavelength fixed at 794 nm, these particles exhibit a strong two photon-excited luminescence leading to the same squared dependence of the fluorescence intensity with the fundamental beam intensity. The spatial autocorrelation of the 2D fluorescence maps were compared with simple calculations taking into account a random distribution of the fluorescent particles and a Gaussian beam with various waist sizes w_0. The best agreement was found for a beam waist of $w_0 \approx 5$ μm. Using this value as an input parameter, the integral $\int I_\omega^2 \, dV$ was easily computed. The second difficulty (ii) is more difficult to handle since the present method cannot determine the exact position of the gold particle along the beam propagation direction. A simple scan of the sample along to the fundamental beam direction could be used to determine that the particle position in this direction. However, the Rayleigh length $l = \pi w_0^2/\lambda = 140$ μm associated with the fundamental Gaussian beam is too long to perform this experiment without misalignment of the focus. Instead, 2D SH maps in different locations in the sample were recorded and from the highest intensity, corresponding to positions of the particle in the or very close to the beam waist, a quadratic hyperpolarizability $\beta_{part} = (1.0 \pm 0.15) \times 10^{-23}$ esu was measured. This value is in excellent agreement with ensemble measurements where a value of $\langle \beta_{part} \rangle = (1.1 \pm 0.1) \times 10^{-23}$ esu was obtained.[8] In the latter case, the brackets stand for the size, shape, and orientational average owing to the ensemble nature of the measurement.

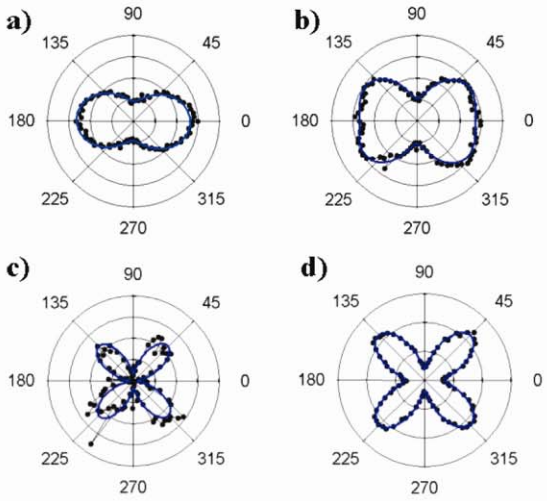

FIGURE 3. Vertically polarized SH intensity from Zone 1 (a) and Zone 2 (b) shown in Figure 1 with 80 s acquisition time for each data point. The corresponding difference is reported in panel c. For comparison, the corresponding ensemble measurement is shown in panel d. All curves are fitted using the expression of the SH intensity given in the text.

In order to obtain a deeper understanding of the nonlinear optical nature of the signals collected at the single nanoparticle level and confirming that a single particle is observed, the SH intensities of the vertically polarized harmonic field from Zones 1 and 2 were measured as a function of the input polarization angle of the fundamental beam. In this case, a zero angle corresponds to the vertical polarization. As shown in Figure 3a, the SH intensity from Zone 1 exhibits a typical two lobes pattern due to the purely dipolar contribution from the gelatin matrix. The orientation and position of the gelatin and water molecules being random, their response adds up incoherently as it is the case in Hyper Rayleigh Scattering.[24] The obtained pattern corresponds therefore to that of an orientation averaged response of single gelatin and water molecules. The same measurement in Zone 2 shows a clear deviation from the pure dipolar response. As for the unpolarized measurements presented above, this additional contribution can be attributed to the gold metallic nanoparticle. Polar plots are usually fitted with the following expression[6-8]

$$I_{SHG}^V = a^V \cos^4 \gamma + b^V \cos^2 \gamma \sin^2 \gamma + c^V \sin^4 \gamma \qquad (2)$$

DOI: 10.1021/nl1000949 | *Nano Lett.* **2010,** *10,* 1717–1721

where the parameters a^V, b^V and c^V are related to the elements of the quadratic hyperpolarizability tensor. Besides, these coefficients obey specific relationships depending on the contribution they describe. For a pure electric dipolar response they are related through $a^V + c^V = b^V$ whereas for a pure electric quadrupole contribution, they are related through $a^V = b^V = 0$.[6] To quantify the ratio between these two dipolar and quadrupolar contributions, an empirical weighting parameter has been introduced in the past as[7]

$$\zeta^V = \left| \frac{b^V - (a^V + c^V)}{b^V} \right| \quad (3)$$

ζ^V ranges from zero for a pure dipolar response to unity for a pure quadrupolar one. As expected, experimentally, ζ^V is equal to 0.019 ± 0.002 in Zone 1 but rises to 0.37 ± 0.03 in Zone 2. The difference between the two polar plots mentioned above is therefore attributed to a quadrupolar contribution associated to the gold metallic nanoparticle presence. The neat signal from the nanoparticle can be obtained by subtracting the neat gelatin signal of Zone 1, see Figure 3a, from that recorded in Zone 2 and displayed in Figure 3c. One clearly recovers an almost pure quadrupolar response since the SH intensities obtained at angles 0 and $\pi/2$ almost completely vanish.[25] Despite the low signal-to-noise ratio of the single particle measurement, there is a clear difference from ensemble measurements. Indeed, as shown in Figure 3d, the ensemble measurements lead to non vanishing intensities at angles 0 and $\pi/2$ of the incident polarization in contrast to the single particle case, see Figure 3c. Furthermore, it has been reported in the past that elongated rodlike gold metallic particles are extremely sensitive to the angle between the particle long axis and the direction of the linear polarization of the exciting field.[26] Hence, the relatively equal SH intensities recorded at angles $\pi/4$, $3\pi/4$, $5\pi/4$, and $7\pi/4$, see Figure 3c, indicate that a single nanoparticle is observed and not a small aggregate of particles, like a dimer or trimer system, which would exhibit unequal SH intensities for these four angles of polarization. In this analysis, we do not consider the configuration where the long axis of a dimer aggregate would be perfectly aligned along the beam direction of propagation because of the extremely unfavorable probability of appearance of this configuration. Moreover, in this singular configuration, the responses of the two particles have to be summed up coherently. Therefore, neglecting further enhancement arising from near-field coupling, a four times larger SHG intensity is expected. Using the hyperpolarizability obtained from ensemble measurements, the spots would reach roughly 1000 SHG counts (200 SHG counts from the gelatin and 4 × 200 SHG counts from the dimer). Such a strong signal has never been observed in the cartographies performed in different locations in the sample and for different particle concentrations. This clearly demonstrates

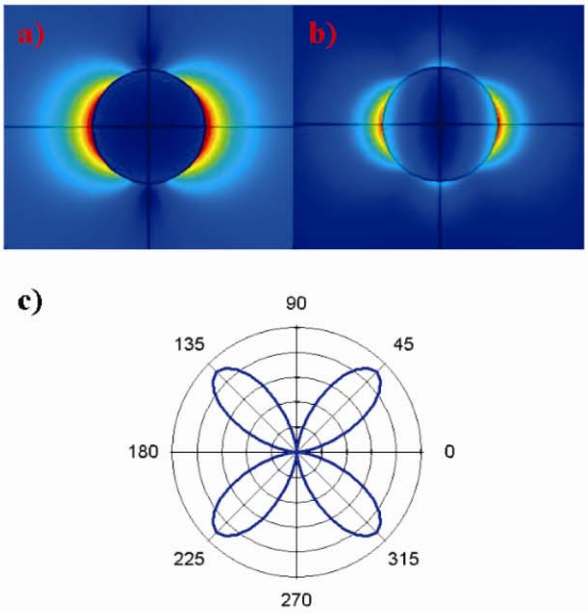

FIGURE 4. Near-field distribution of (a) the fundamental and (b) the harmonic fields for a 150 nm gold nanoparticle excited at a wavelength 794 nm. The corresponding far-field intensity collected at right angle for a vertical polarization is plotted as a function of the input polarization angle (c).

that the hypothesis of aggregates formation can be ruled out in the present experiments.

Finally, FEM simulations were also performed following the lines of that reported in ref 20. In the present simulations, a perfect spherical shape is assumed for the gold nanoparticle. The fundamental input field is first computed allowing for the calculation of the nonlinear sources; see Figure 4a. The harmonic field is then obtained by solving the Maxwell equations with the use of the weak form; see Figure 4b.[20] In a third step, the far-field scattered intensity is computed from the near-field distribution of the harmonic field. The result is shown in Figure 4c for a vertically polarized detection of the SH field. This polar graph is independent of the nonlinear sources assumed for the calculation, whether a surface or a bulk contribution for the nonlinear polarization. The agreement with the single particle experiment is excellent. Hence, it is concluded that the differences observed between single particle and ensemble measurements stem from the averaging procedure over different particle shapes leading to, in the case of strong deviations from the perfect spherical shape, the nonvanishing of the dipolar response owing to the breaking of the centrosymmetry.[20] The almost purely quadrupolar origin shown in Figure 3c provides evidence that the particle investigated has a near spherical shape, that is, the shape symmetry is not much broken. This result underlines the interest for performing single particle measurements as opposed to ensemble ones to allow for a direct comparison between experiments and simulations.

In conclusion, we have observed for the first time the SH intensity signal from a single metallic nanoparticle embed-

DOI: 10.1021/nl1000949 | *Nano Lett.* **2010,** *10,* 1717–1721

ded in a homogeneous medium. This configuration is critical to investigate the intrinsic nonlinear optical properties of nanoparticles without centrosymmetry breaking induced by the surrounding medium like for the configurations where the particles are supported on a substrate for example. The quadratic hyperpolarizability values obtained are in excellent agreement with ensemble measurements. Polarization resolved experiments have also been performed and compared to FEM simulations. The weak differences between single particle and ensemble measurements are attributed to the averaging of the SH response from particles with different size, shape and orientation in ensemble measurements. The achievement of single particle experiments and their direct comparison with FEM calculations open up new perspectives in the investigation of the nonlinear optical properties of metallic nanoparticles.

REFERENCES AND NOTES

(1) Mertz, J.; Xu, C.; Webb, W. W. *Opt. Lett.* **1995**, *20*, 2532.
(2) Kneipp, K.; Wang, Y.; Kneipp, H.; Perelman, L. T.; Itzkan, I.; Dasari, R. R.; Feld, M. S. *Phys. Rev. Lett.* **1997**, *78*, 1667.
(3) Muskens, O. L.; Del Fatti, N.; Vallée, F.; Huntzinger, J. R.; Billaud, P.; Broyer, M. *Appl. Phys. Lett.* **2006**, *88*, 063109–3.
(4) Muskens, O. L.; Bachelier, G.; Del Fatti, N.; Vallée, F.; Brioude, A.; Jiang, X.; Pileni, M. P. *J. Phys. Chem. C* **2008**, *112*, 8917.
(5) Marhaba, S.; Bachelier, G.; Bonnet, C.; Broyer, M.; Cottancin, E.; Grillet, N.; Lermé, J.; Vialle, J.-L.; Pellarin, M. *J. Phys. Chem. C* **2009**, *113*, 4349.
(6) Nappa, J.; Revillod, G.; Russier-Antoine, I.; Benichou, E.; Jonin, C.; Brevet, P. F. *Phys. Rev. B* **2005**, *71*, 165407.
(7) Nappa, J.; Russier-Antoine, I.; Benichou, E.; Jonin, C.; Brevet, P. F. *J. Chem. Phys.* **2006**, *125*, 184712.
(8) Russier-Antoine, I.; Benichou, E.; Bachelier, G.; Jonin, C.; Brevet, P. F. *J. Phys. Chem. C* **2007**, *111*, 9044.
(9) Chandra, M.; Indi, S. S.; Das, P. K. *Chem. Phys. Lett.* **2006**, *422*, 262.
(10) Chandra, M.; Das, P. K. *Chem. Phys. Lett.* **2009**, *476*, 62.
(11) Chandra, M.; Das, P. K. *Chem. Phys.* **2009**, *358*, 203.
(12) Canfield, B. K.; Kujala, S.; Jefimovs, K.; Turunen, J.; Kauranen, M. *Opt. Exp.* **2004**, *12*, 5418.
(13) Canfield, B. K.; Husu, H.; Laukkanen, B.; Bai, F.; Kuittinen, M.; Turunen, J.; Kauranen, M. *Nano Lett.* **2007**, *7*, 1251.
(14) Kujala, S.; Canfield, B. K.; Kauranen, M.; Svirko, Y.; Turunen, J. *Phys. Rev. Lett.* **2007**, *98*, 167403.
(15) Kujala, S.; Canfield, B. K.; Kauranen, M.; Svirko, Y.; Turunen, J. *Opt. Exp.* **2008**, *16*, 17196.
(16) Jin, R.; Jureller, J. E.; Kim, H. Y.; Scherer, N. F. *J. Am. Chem. Soc.* **2005**, *127*, 12482.
(17) Zavelani-Rossi, M.; Celebrano, M.; Biagioni, P.; Polli, D.; Finazzi, M.; Duo, L.; Cerullo, G.; Labardi, M.; Allegrini, M.; Grand, J.; Adam, P. M. *Appl. Phys. Lett.* **2008**, *92*, 093119.
(18) Lippitz, M.; van Dijk, M. A.; Orrit, M. *Nano Lett.* **2005**, *5*, 799.
(19) Canfield, B. K.; Husu, H.; Kontio, J.; Viheriälä, J.; Rytkönen, T.; Niemi, T.; Chandler, E.; Hrin, A.; Squier, J. A.; Kauranen, M. *New J. Phys.* **2008**, *10*, No. 013001.
(20) Bachelier, G.; Russier-Antoine, I.; Benichou, E.; Jonin, C.; Brevet, P. F. *J. Opt. Soc. Am. B* **2008**, *25*, 955.
(21) Duboisset, J.; Russier-Antoine, I.; Benichou, E.; Bachelier, G.; Jonin, C.; Brevet, P. F. *J. Phys. Chem. C* **2009**, *113*, 13477.
(22) Deniset-Besseau, A.; Duboisset, J.; Benichou, E.; Hache, F.; Brevet, P. F.; Schanne-Klein, M. C. *J. Phys. Chem. B* **2009**, *113*, 13437.
(23) Vance, F. W.; Lemon, B. I.; Hupp, J. T. *J. Phys. Chem. B* **1998**, *102*, 10091.
(24) Clays, K.; Persoons, A. *Phys. Rev. Lett.* **1991**, *66*, 2980.
(25) Dadap, J. I.; Shan, J.; Eisenthal, K. B.; Heinz, T. F. *Phys. Rev. Lett.* **1999**, *83*, 4045.
(26) Hubert, C.; Billot, L.; Adam, P.-M.; Bachelot, R.; Royer, P.; Grand, J.; Gindre, D.; Dorkenoo, K. D.; Fort, A. *Appl. Phys. Lett.* **2007**, *90*, 181105.

DOI: 10.1021/nl1000949 | *Nano Lett.* **2010,** *10,* 1717–1721

Three-dimensional mapping of single gold nanoparticles embedded in a homogeneous transparent matrix using optical second-harmonic generation

Jérémy Butet, Guillaume Bachelier*, Julien Duboisset, Franck Bertorelle, Isabelle Russier-Antoine, Christian Jonin, Emmanuel Benichou and Pierre-François Brevet

Laboratoire de Spectrométrie Ionique et Moléculaire (LASIM),
Université Claude Bernard Lyon 1 – CNRS (UMR 5579),
Bat. A. Kastler, 43 Boulevard du 11 novembre 1918, 69662 Villeurbanne, France
**guillaume.bachelier@lasim.univ-lyon1.fr*

Abstract: We report the three-dimensional mapping of 150 nm gold metallic nanoparticles dispersed in a homogeneous transparent polyacrylamide matrix using second-harmonic generation. We demonstrate that the position of single nanoparticles can be well defined using only one incident fundamental beam and the harmonic photon detection performed at right angle. The fundamental laser beam properties are determined using its spatial autocorrelation function and used to prove that single nanoparticles are observed. Polarization resolved measurements are also performed allowing for a clear separation of the second-harmonic response of the single gold metallic nanoparticles from that of aggregates of such nanoparticles.

OCIS codes: (190.2620) Harmonic generation and mixing; (240.6680) Surface plasmons; (160.4236) Nanomaterials.

References and links

1. U. Kreibig, and M. Vollmer, Optical properties of metal cluster, Springer Series in Materials Science (Springer, Berlin, 1995).
2. A. Arbouet, D. Christofilos, N. Del Fatti, F. Vallée, J. R. Huntzinger, L. Arnaud, P. Billaud, and M. Broyer, "Direct measurement of the single-metal-cluster optical absorption," Phys. Rev. Lett. **93**(12), 127401 (2004).
3. S. Marhaba, G. Bachelier, C. Bonnet, M. Broyer, E. Cottancin, N. Grillet, J. Lerme, J.-L. Vialle, and M. Pellarin, "Surface Plasmon Resonance of Single Gold Nanodimers near the Conductive Contact Limit," J. Phys. Chem. C **113**(11), 4349–4356 (2009).
4. D. Boyer, P. Tamarat, A. Maali, B. Lounis, and M. Orrit, "Photothermal imaging of nanometer-sized metal particles among scatterers," Science **297**(5584), 1160–1163 (2002).
5. L. J. Sherry, S. H. Chang, G. C. Schatz, R. P. Van Duyne, B. J. Wiley, and Y. N. Xia, "Localized surface plasmon resonance spectroscopy of single silver nanocubes," Nano Lett. **5**(10), 2034–2038 (2005).
6. E. M. Perassi, J. C. Hernandez-Garrido, M. S. Moreno, E. R. Encina, E. A. Coronado, and P. A. Midgley, "Using highly accurate 3D nanometrology to model the optical properties of highly irregular nanoparticles: a powerful tool for rational design of plasmonic devices," Nano Lett. **10**(6), 2097–2104 (2010).
7. R. W. Boyd, Nonlinear Optics (Academic Press, New York, 1992).
8. B. K. Canfield, H. Husu, J. Laukkanen, B. F. Bai, M. Kuittinen, J. Turunen, and M. Kauranen, "Local field asymmetry drives second-harmonic generation in non-centrosymmetric nanodimers," Nano Lett. **7**(5), 1251–1255 (2007).
9. S. Kujala, B. K. Canfield, M. Kauranen, Y. Svirko, and J. Turunen, "Multipole interference in the second-harmonic optical radiation from gold nanoparticles," Phys. Rev. Lett. **98**(16), 167403 (2007).
10. V. K. Valev, A. V. Silhanek, N. Verellen, W. Gillijns, P. Van Dorpe, O. A. Aktsipetrov, G. A. E. Vandenbosch, V. V. Moshchalkov, and T. Verbiest, "Asymmetric optical second-harmonic generation from chiral G-shaped gold nanostructures," Phys. Rev. Lett. **104**(12), 127401 (2010).
11. J. Nappa, G. Revillod, I. Russier-Antoine, E. Benichou, C. Jonin, and P. F. Brevet, "Electric dipole origin of the second harmonic generation of small metallic particles," Phys. Rev. B **71**(16), 165407 (2005).
12. I. Russier-Antoine, J. Duboisset, G. Bachelier, E. Benichou, C. Jonin, N. Del Fatti, F. Vallee, A. Sanchez-Iglesias, I. Pastoriza-Santos, L. M. Liz-Marzan, and P. F. Brevet, "Symmetry Cancellations in the Quadratic Hyperpolarizability of Non-Centrosymmetric Gold Decahedra," J. Phys. Chem. Lett. **1**(5), 874–880 (2010).

#134427 - $15.00 USD Received 1 Sep 2010; revised 24 Sep 2010; accepted 24 Sep 2010; published 6 Oct 2010

13. G. S. Agarwal, and S. S. Jha, "Theory of 2nd Harmonic-Generation at a metal-surface with surface-plasmon excitation," Solid State Commun. **41**(6), 499–501 (1982).
14. F. W. Vance, B. I. Lemon, and J. T. Hupp, "Enormous hyper-Rayleigh scattering from nanocrystalline gold particle suspensions," J. Phys. Chem. B **102**(50), 10091–10093 (1998).
15. Y. Pu, R. Grange, C. L. Hsieh, and D. Psaltis, "Nonlinear Optical Properties of Core-Shell Nanocavities for Enhanced Second-Harmonic Generation," Phys. Rev. Lett. **104**(20), 207402 (2010).
16. J. Duboisset, I. Russier-Antoine, E. Benichou, G. Bachelier, C. Jonin, and P. F. Brevet, "Single Metallic Nanoparticle Sensitivity with Hyper Rayleigh Scattering," J. Phys. Chem. C **113**(31), 13477–13481 (2009).
17. J. Butet, J. Duboisset, G. Bachelier, I. Russier-Antoine, E. Benichou, C. Jonin, and P.-F. Brevet, "Optical second harmonic generation of single metallic nanoparticles embedded in a homogeneous medium," Nano Lett. **10**(5), 1717–1721 (2010).
18. R. C. Jin, J. E. Jureller, H. Y. Kim, and N. F. Scherer, "Correlating second harmonic optical responses of single Ag nanoparticles with morphology," J. Am. Chem. Soc. **127**(36), 12482–12483 (2005).
19. M. Lippitz, M. A. van Dijk, and M. Orrit, "Third-harmonic generation from single gold nanoparticles," Nano Lett. **5**(4), 799–802 (2005).
20. J. I. Dadap, J. Shan, K. B. Eisenthal, and T. F. Heinz, "Second-harmonic Rayleigh scattering from a sphere of centrosymmetric material," Phys. Rev. Lett. **83**(20), 4045–4048 (1999).
21. J. I. Dadap, J. Shan, and T. F. Heinz, "Theory of optical second-harmonic generation from a sphere of centrosymmetric material: small-particle limit," J. Opt. Soc. Am. B **21**(7), 1328 (2004).
22. V. L. Brudny, B. S. Mendoza, and W. L. Mochan, "Second-harmonic generation from spherical particles," Phys. Rev. B **62**(16), 11152–11162 (2000).
23. W. L. Mochán, J. A. Maytorena, B. S. Mendoza, and V. L. Brudny, "Second-harmonic generation in arrays of spherical particles," Phys. Rev. B **68**(8), 085318 (2003).
24. J. P. Dewitz, W. Hübner, and K. H. Bennemann, Z. Phys. **37**, 75–84 (1996).
25. J. I. Dadap, "Optical second-harmonic scattering from cylindrical particles," Phys. Rev. B **78**(20), 205322 (2008).
26. A. G. F. de Beer, and S. Roke, "Sum frequency generation scattering from the interface of an isotropic particle: Geometrical and chiral effects," Phys. Rev. B **75**(24), 245438 (2007).
27. A. G. F. de Beer, and S. Roke, "Nonlinear Mie theory for second-harmonic and sum-frequency scattering," Phys. Rev. B **79**(15), 155420 (2009).
28. G. Bachelier, I. Russier-Antoine, E. Benichou, C. Jonin, and P. F. Brevet, "Multipolar second-harmonic generation in noble metal nanoparticles," J. Opt. Soc. Am. B **25**(6), 955 (2008).
29. Y. Zeng, W. Hoyer, J. J. Liu, S. W. Koch, and J. V. Moloney, "Classical theory for second-harmonic generation from metallic nanoparticles," Phys. Rev. B **79**(23), 235109 (2009).
30. J. Butet, G. Bachelier, I. Russier-Antoine, C. Jonin, E. Benichou, and P. F. Brevet, "Interference between Selected Dipoles and Octupoles in the Optical Second-Harmonic Generation from Spherical Gold Nanoparticles," Phys. Rev. Lett. **105**(7), 077401 (2010).
31. G. Bachelier, J. Butet, I. Russier-Antoine, C. Jonin, E. Benichou and P. F. Brevet, submitted.
32. X. H. Huang, I. H. El-Sayed, W. Qian, and M. A. El-Sayed, "Cancer cell imaging and photothermal therapy in the near-infrared region by using gold nanorods," J. Am. Chem. Soc. **128**(6), 2115–2120 (2006).
33. N. J. Durr, T. Larson, D. K. Smith, B. A. Korgel, K. Sokolov, and A. Ben-Yakar, "Two-photon luminescence imaging of cancer cells using molecularly targeted gold nanorods," Nano Lett. **7**(4), 941–945 (2007).
34. J. I. Dadap, H. B. de Aguiar, and S. Roke, "Nonlinear light scattering from clusters and single particles," J. Chem. Phys. **130**(21), 214710 (2009).
35. L. Novotny, and B. Hecht, Principles of nano-optics, (Cambridge university Press, New York, 2006).
36. I. Russier-Antoine, E. Benichou, G. Bachelier, C. Jonin, and P. F. Brevet, "Multipolar contributions of the second harmonic generation from silver and gold nanoparticles," J. Phys. Chem. C **111**(26), 9044–9048 (2007).
37. P. Galletto, P. F. Brevet, H. H. Girault, R. Antoine, and M. Broyer, "Enhancement of the second harmonic response by asorbates on gold colloids: the effect of aggregation," J. Phys. Chem. B **103**(41), 8706–8710 (1999).
38. E. C. Hao, G. C. Schatz, R. C. Johnson, and J. T. Hupp, "Hyper-Rayleigh scattering from silver nanoparticles," J. Chem. Phys. **117**(13), 5963 (2002).
39. M. Finazzi, P. Biagioni, M. Celebrano, and L. Duo, "Selection rules for second-harmonic generation in nanoparticles," Phys. Rev. B **76**(12), 125414 (2007).
40. A. Benedetti, M. Centini, C. Sibilia, and M. Bertolotti, "Engineering the second harmonic generation pattern from coupled gold nanowires," J. Opt. Soc. Am. B **27**(3), 408 (2010).

1. Introduction

The optical properties of metallic nanoparticles are dominated by the Surface Plasmon resonances arising from the collective oscillation of the conduction electrons [1]. The size and shape effects on the linear optical properties of metallic nano-objects are now widely understood. A deeper understanding has nevertheless been possible through the use of experimental set-ups allowing single nanoparticle measurements, preventing the averaging procedure over the morphology and orientation distributions [2–5]. These experimental set-ups include dark field spectroscopy, photothermal emission and spatial modulation techniques, the advantage of the latter being the determination of the absolute extinction

#134427 - $15.00 USD Received 1 Sep 2010; revised 24 Sep 2010; accepted 24 Sep 2010; published 6 Oct 2010

cross-section. Nowadays, the ability to combine numerical simulations and 3D transmission electronic microscopy at the single particle level offers an ultimate development to characterize the linear optical properties of these particles [6].

The nonlinear optical properties of metallic nanoparticles have also been widely studied in the past decades. Second-harmonic generation (SHG), in particular, is an optical process very sensitive to the nanoparticles shape because it is forbidden in centrosymmetric media within the frame of the electric dipole approximation [7]. Kauranen's group and more recently Valev and associates have investigated the SHG from gold metallic nanoparticles with various non-centrosymmetric shapes produced by nanolithography. They especially discussed the local field effects and the multipole contributions to the nonlinear optical response [8–10]. Nanoparticles dispersed in solution were also studied by Hyper Rayleigh Scattering (HRS). The role played by the breaking of the centrosymmetry induced by the non perfect spherical shape of the nanoparticles was clearly demonstrated [11] as well as the symmetry cancellations occurring in the quadratic hyperpolarizability of non centrosymmetric gold decahedra [12]. The SHG intensity from metallic nanoparticles is furthermore enhanced by the surface plasmon resonances leading to much higher hyperpolarizability magnitudes than the one reported for the best available molecular chromophores [13, 14]. The SHG efficiency can be increased further with core-shell nanocavities filled with a non centrosymmetric crystalline core [15]. We have recently demonstrated that HRS is sensitive enough to reach the single nanoparticle detection level [16] opening the way to the first measurements of the second-harmonic generation of a single 150 nm gold nanoparticle embedded in a gelatin matrix [17]. The main advantage of this configuration where the centrosymmetry of the surrounding medium is preserved around the nanoparticle studied is to allow the direct comparison with theoretical works, something which is no longer easily feasible in the case of nanoparticles deposited on a substrate [18]. One can note that single gold nanoparticles can also be detected by Third Harmonic Generation enhanced by the Plasmon resonance [19].

Theoretical works have been devoted to the SHG response from a small perfect sphere, the diameter of which is much smaller than the wavelength of light, when the SH emission is due to retardation effects [20, 21] or to the presence of an inhomogeneous incident electric field [22, 23]. A nonlinear Mie theory has early been developed [24] (note that the set of boundary conditions have been corrected in ref. 25) and recently updated to describe sum-frequency scattering in the case of non-collinear incident beams [26, 27]. Finite Element Method (FEM) simulations [28] and classical electrodynamics where the quasi-free electrons inside the metal are approximated as a classical Coulomb-interacting electron gas [29] were also reported with the purpose of taking into account the SHG response from metallic nano-objects with non-spherical shapes. Comparison between FEM simulations and experimental results has in particular enabled us to determine the role played by the local and non-local effects in the SHG response from gold metallic nanoparticles using interferences between the selected dipolar and octupolar plasmons [17, 30, 31].

From a practical point of view, metallic nanoparticles are widely used in biological applications since they constitute both nano-sources of light and nano-sources of heat. Indeed, the optical and thermal properties of metallic nanoparticles are used for cancer cell imaging and therapy. The photo-thermal cancer therapy requires however that the position of the nanoparticles used as labels is well determined in the cancer cells [32]. This can be carried out with nonlinear spectroscopic processes such as two-photon fluorescence [33]. Then, the high absorption cross section of the nanoparticles can be used to locally heat up and kill the targeted cells. We have shown that the nonlinear optical process SHG allows the determination of single nanoparticles position in a transparent and homogeneous matrix [17]. These results are promising for the use of the nonlinear optical properties in biological applications.

In this work, we study spherical gold nanoparticles the diameter of which is 150 nm dispersed in a transparent polyacrylamide (PAA) matrix. We show that the position of single nanoparticles could be well determined in the three directions of space by collecting at right angle their SHG signal driven by only one laser beam. Aggregation between the nanoparticles

#134427 - $15.00 USD Received 1 Sep 2010; revised 24 Sep 2010; accepted 24 Sep 2010; published 6 Oct 2010

can occur during the sample preparation and their presence can be a serious impediment in single particle measurements. The clear separation of the responses of a single nanoparticle and an aggregate is shown to be readily accessible in polarization resolved SH measurements. The SH response from a single nanoparticle is shown to be quadrupolar as expected in this experimental configuration whereas the response from the aggregate is more complicated. The present report therefore shows that SHG is sensitive enough to symmetry to distinguish at the single particle level these two kinds of nano-objects.

2. Experimental set-up and sample preparation

A mode-locked Ti:sapphire laser tuned to a wavelength of 804 nm and delivering pulses of about 180 fs at a repetition rate of 76 MHz was used as the laser source. The pulse energy measured at the laser exit was 10 nJ. The laser beam was focused into a quartz cell with a microscope objective (X16, NA 0.32) and a low-pass filter was used to remove any residual light at the harmonic frequency generated prior to the cell. The SH photons were collected perpendicularly to the incident beam with a 25 mm focal length lens with a numerical aperture of 0.5. The scattered fundamental photons were removed by a high-pass filter placed before the monochromator. The polarization angle γ of the fundamental beam was selected with a rotating half-wave plate ($\gamma = 0$ for a vertically polarized field) and the polarization of the SH photons was selected by an analyzer for the polarization resolved measurements. The photon detection was performed by a sensitive cooled photomultiplier tube and the fundamental beam was chopped at 130 Hz to allow a gated photon counting regime removing the background photons.

The polymer matrix was prepared using a water solution (milliQ grade) of 10% acrylamide and bisacrylamide (ratio 98:2). After dispersion of the gold nanoparticles (150 nm, BBInternational), polymerisation occured in 30 minutes by adding ammonium peroxodisulfate ($(NH_4)_2S_2O_8$) and TEMED (1,2-Bis(dimethylamino)ethane). The refractive index of the matrix is close to that of pure water (taking into account 10% of PAA with a refractive index of 1.52 compared to 1.33 for water), leading to a broad dipolar plasmon resonance at around 650 nm, ie far from both the fundamental and the harmonic wavelengths. There is therefore no resonance effect in the present experiments.

3. Experimental results and discussion

The sample scans were carried out perpendicularly to the incident fundamental beam direction in order to obtained two-dimensional (2D) maps of the SH intensity versus cell position with 14 seconds acquisition time per pixels, following the experimental protocol described in ref 17, see Fig. 1. The heterogeneous spatial distribution of the SH intensity reveals areas with low and high intensities. The background SH intensity corresponds to the signal recorded for the polymer matrix without particles and the low SH intensity areas correspond therefore to areas composed exclusively of the polymer matrix. This SH intensity produced by the PAA matrix is weaker than the one emitted by the gelatin matrix used in our previous single nanoparticles measurements [17] and allowed a higher signal-to-noise ratio. More precisely, the SHG signal from the matrix has been reduced down to 1.2 times that of water, in which the particles are dispersed. We have therefore almost reached the best contrast particle/matrix that can be obtained.

The high SH intensity zones in Fig. 1 are attributed to the presence of the gold metallic nanoparticles [17]. In order to demonstrate the 3D imaging capability, successive 2D maps were recorded for different positions of the cell along the direction propagation of the incident beam with a distance of 8 μm from one map to the other (only four are shown here). The positions of the SH intensity maxima are well correlated between the different maps pointing out that the particles lateral positions are very well known. However, the amplitudes of these maxima evolve from one map to the other owing to the displacement of the nanoparticles along the laser beam. For example, one can note that four maxima appear on the right of the first map. Their amplitude increases as the sample is moved along the beam direction. This

#134427 - $15.00 USD Received 1 Sep 2010; revised 24 Sep 2010; accepted 24 Sep 2010; published 6 Oct 2010

behaviour can be understood as follows: the nanoparticles are dispersed in the three dimensions in the sample. The nanoparticles are therefore moved in and out of the laser beam waist as the cell is moved along the incident beam.

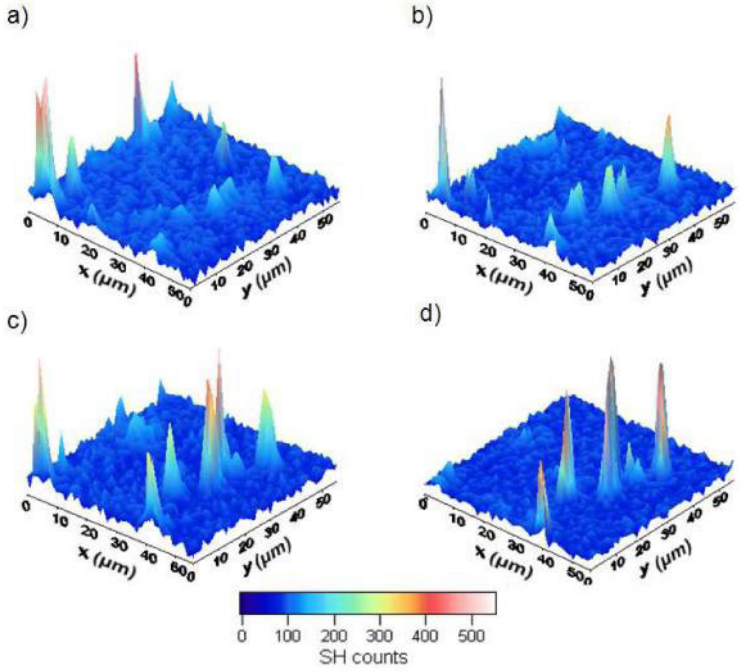

Fig. 1. 2D maps of the SH intensity at 402 nm obtained for 150 nm gold nanoparticles embedded in PAA polymer matrix by scanning the sample perpendicularly to the beam direction. The cell is moved along the incident beam direction with a distance of 8 μm from one map to the next one. The acquisition time is 14s per pixels.

The nonlinear efficiency of a given metallic nanoparticles can be obtained by subtracting the SH intensity from the maxima corresponding to a nanoparticle that of the background signal emitted by the polymer matrix, about 5 photons/s [17]. The PAA polymer matrix can then be used as an internal reference to determine the quadratic hyperpolarizability of the 150 nm diameter gold nanoparticles. Preliminary experiment have demonstrated that the SH intensity recorded for the pure polymer matrix is identical to the one recorded for water in the same experimental configuration. The intensity radiated at the harmonic frequency for the matrix in the presence of the metallic particles can therefore be written as [17]:

$$I_{SHG} = G\left[\int 1.2\, C_w \left\langle \beta_w^2 \right\rangle I_w^2 dV + \beta_{part}^2 I_{part}^2\right], \qquad (1)$$

where C_w and $\beta_w = 0.56\times 10^{-30}$ esu [14] are the concentration and the quadratic hyperpolarizability of water, respectively and the factor 1.2 stems for the relative efficiency of water and PAA matrix. G is a geometrical factor. In Eq. (1), we consider that the molecules are randomly oriented in a mesoscopic volume dV leading to an expression very similar to that used for hyper Rayleigh scattering. Note that a more detailed description taking into account all the components of the quadratic hyperpolarizability tensor might be found in Ref. 34. The quadratic hyperpolarizability of a single gold nanoparticle is given by β_{part} and I_{part} stems for the intensity of the fundamental beam illuminating the gold nanoparticles. In this case, the particle being fixed and isolated, there is no averaging over the particle orientations.

In Eq. (1), the spatial distribution of the square of the fundamental intensity has to be determined over the laser beam section. We use the PAA matrix as an internal reference for

#134427 - $15.00 USD Received 1 Sep 2010; revised 24 Sep 2010; accepted 24 Sep 2010; published 6 Oct 2010

the determination of quadratic hyperpolarizability of the nanoparticles in the mapped area. For this purpose, the spatial autocorrelation map of Fig. 1(d) for which the amplitudes of the picks are maximum was calculated in order to determine the experimental conditions and is displayed in Fig. 2.

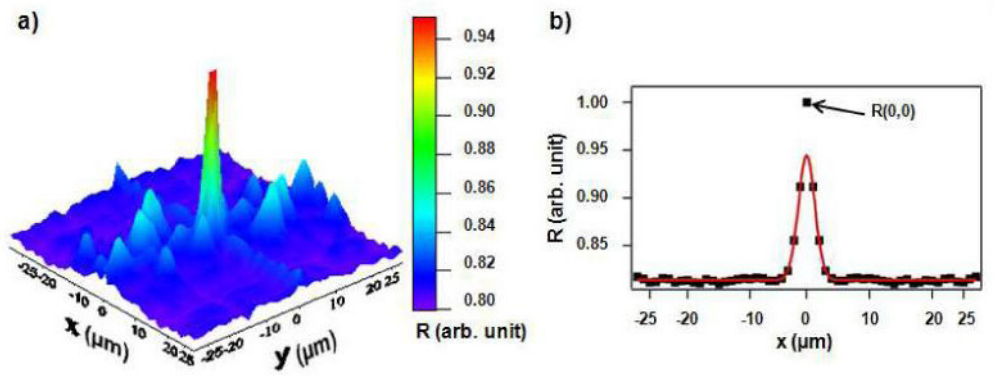

Fig. 2. (a) Spatial autocorrelation for the map of Fig. 1(d) with the origin at (0,0) not shown, see text. (b) The autocorrelation profile for Y=0 and its fit where the noise is rejected, point R(0,0)

The spatial autocorrelation for a real-valued function of two variables is given by:

$$R(\xi,\eta) = \iint I(x-\xi, y-\eta) I(x,y) dx dy \qquad (2)$$

where $R(\xi,\eta)$ is the autocorrelation function and $I(x,y)$ stands for the collected SH intensity at the cell position (x,y), as shown in Fig. 1. The integration is performed over the whole map. The spatial autocorrelation map exhibits three specific length scales. First, the correlation of the noise itself with a length equal to one pixel contributes only to the origin $R(0,0)$. Hence, the high value of $R(0,0)$ is due to the noise affecting the data during the acquisition runs and will not be further taken into account in the following analysis. The second characteristic length is related to the lateral dimensions of the laser beam. Indeed, the nanoparticles studied the diameter of which is 150 nm are much smaller than the waist of the fundamental laser beam. This implies that the number of pixels on the map corresponding to one nanoparticle is determined by the dimension of the laser beam in the sample and by the position of the nanoparticle in the beam. This contribution explains the maximum obtained at the centre $R(0,0)$ even though the noise contribution has been rejected. This maximum has a gaussian profile with a standard deviation equal to 3.53 µm as determined by fitting procedure. This corresponds to the lateral resolution in the 3D imaging. This value is therefore related to the transverse dimension of the laser beam but is not the waist size of the fundamental beam. Indeed, SHG is a second order nonlinear process and the SH intensity is proportional to the fundamental intensity squared since two fundamental photons are necessary to create a single second-harmonic photon. In the present case, the SH intensity emitted by a nanoparticle is proportional to the squared local incident intensity at its position. In order to determine the waist size, the spatial autocorrelation of the 2D gold nanoparticles maps were compared with simple numeric calculations taking into account a random distribution of the nanoparticles and a gaussian beam with various waist sizes w_0. The best agreement was found for a beam waist of about $w_0 \approx 4$ µm. The determination of the beam waist enables to compute the spatial distribution of both the intensity and the intensity squared, see Fig. 3. It is obvious that the intensity squared decreases faster than the intensity itself. The volume probed by a two photons excited process is therefore much smaller than the

#134427 - $15.00 USD Received 1 Sep 2010; revised 24 Sep 2010; accepted 24 Sep 2010; published 6 Oct 2010

one probed by a one photon excited process such as fluorescence for instance. This property is well known in microscopy and largely applied by imaging techniques in order to increase the spatial resolution [35]. The evolution of the four maxima on the maps is in agreement with the spatial distribution of the fundamental intensity squared and its decrease along the incident beam propagation direction. The resolution of the 3D imaging along the incident beam propagation direction is therefore about 40 µm. This rather large value could be largely reduced by the use of a stronger focusing objective (larger numerical aperture). Finally, the last contribution length scale in Fig. 2 is due to the distribution of the gold nanoparticles in the probed area. The small maxima are related to the position of the gold nanoparticles which are randomly distributed in the sample.

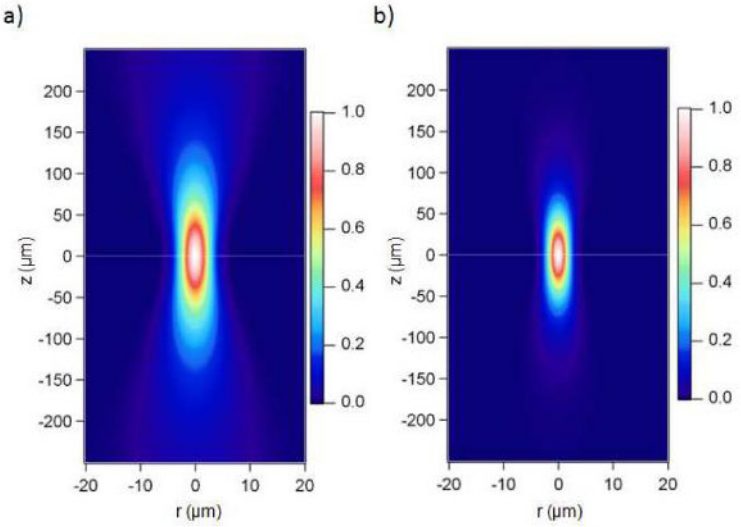

Fig. 3. Normalized spatial distribution of both a) intensity and b) intensity squared as a function of the axial distance Z from the beam waist and the radial distance from the beam axis R for a beam waist of 4 µm.

Knowing the spatial distribution of the intensity squared, one is able to determinate the quadratic hyperpolarizability of the nanoparticles with the use of the Eq. (1). The background signal emitted by the matrix is due to the incoherent summation of the molecules forming the polymer matrix weighted by the local intensity squared integrated over the focussed beam crossection. The SH intensity emitted by a given nanoparticle therefore evolves on the different 2D SH maps and is maximum when the nanoparticle is in or very close to the beam waist. It is ensured that the nanoparticle is located within the beam focus when the SH intensity increases or decreases as the cell is moved along the laser beam. This is obviously the case for the nanoparticles on Fig. 1 d) where a maximum intensity of 450 counts is obtained. The broadband emission spectra for the matrix and a single nanoparticle were also recorded with a longer acquisition time than the one used per pixel for the different maps in order to improve the signal-to-noise ratio and to limit the uncertainty on the hyperpolarizability measured, see Fig. 4. These spectra provide evidence for a collected signal intensity dominated by SHG response from the nanoparticles and not a photoluminescence background.

The quadratic hyperpolarizability for the single nanoparticle studied was found to be equal to $\beta_{part} = (1.19 \pm 0.15) \times 10^{-23}$ esu. This value is in excellent agreement with ensemble measurements in solution where a value of $\langle \beta_{part} \rangle = (1.1 \pm 0.1) \times 10^{-23}$ esu was obtained [36]. Here, the brackets stand for the size, shape and orientational average owing to the ensemble nature of the measurement. The value is also very similar to the one obtained for single

#134427 - $15.00 USD Received 1 Sep 2010; revised 24 Sep 2010; accepted 24 Sep 2010; published 6 Oct 2010

nanoparticles in a gelatine matrix [17], namely $\beta_{part} = (1.0 \pm 0.15) \times 10^{-23}$ esu, providing that i) the high intensity areas in Fig. 1 are associated with single particles and ii) the measure of the quadratic hyperpolarizability is almost not affected by the nature of the surrounding medium.

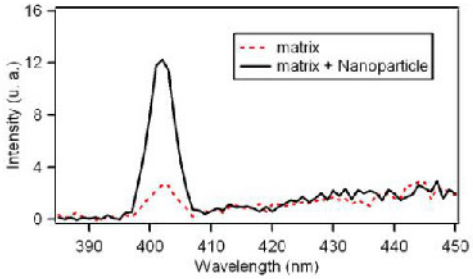

Fig. 4. Emission spectrum from the matrix and from a single nanoparticle embedded in the matrix for an excitation at 804 nm and 60 s acquisition time for each data point.

As described in the experimental section, the nanoparticles were synthesized in solution and then dispersed in the PAA polymer matrix. This process does not prevent the nanoparticles aggregation and it is therefore expected that aggregates can also be locally observed. Figure 5 shows a broad maximum, the amplitude of which is much higher than the one expected for a single nanoparticle. The latter maximum is therefore probably associated to the presence of an aggregate in the area scanned and may correspond to several nanoparticles instead of a single one [37]. The amplitude of the four small maxima corresponds to 35 counts per second as expected for single gold nanoparticles. The two arrows show the aggregate (Agg) and the single nanoparticle (SP) studied below. The number of pixels corresponding to the aggregate Agg is larger than the one observed for single nanoparticles providing further evidence that its dimension is not negligible compared to the waist of the beam.

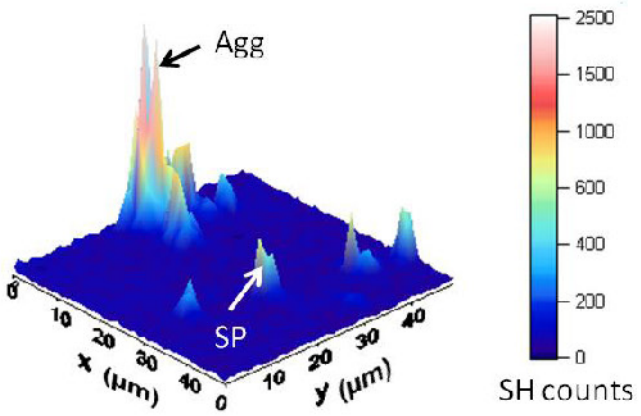

Fig. 5. 2D map of the SH intensity at 402 nm obtained for a 150 nm gold nanoparticles embedded in PAA polymer matrix by scanning the sample perpendicularly to the beam direction. The two arrows show the aggregate (Agg) and the single gold nanoparticle (SP) discussed in the text.

In order to demonstrate the presence of aggregation, the SH intensity for the vertically polarized harmonic field as a function of the fundamental polarization angle from the aggregate (Agg) and from the single nanoparticle (SP) was measured, see Fig. 6. The SH intensity from the neat PAA polymer matrix was also recorded for comparison. The

#134427 - $15.00 USD Received 1 Sep 2010; revised 24 Sep 2010; accepted 24 Sep 2010; published 6 Oct 2010

polarization resolved SH intensity plot from the single nanoparticle reaches maximum intensity values for 45°, 135°, 225° and 315° as expected. Indeed, the leading emission term in the SHG response from a spherical 150 nm diameter nanoparticle is a quadrupole as demonstrated by theoretical analyses [20, 21, 28], ensemble [38] and single nanoparticle measurements [17]. The SH intensity is however not equal to zero for a vertically and horizontally polarized input beam and the four lobes are not exactly equal owing to the imperfect spherical shape of the nanoparticle under study [28], in contrast to the single nanoparticle reported in ref 17. In the case of the aggregate, the SH intensity is drastically larger for a vertically polarized incident electric field (0° and 180°) as compared to the other fundamental polarization states. This behaviour is related to the irregular shape of the aggregate leading to a specific electric field distribution inside and near the aggregate, dramatically modifying the nonlinear optical properties of the aggregate, in particular the SH scattered intensity and the polarization selection rules by symmetry breaking and near field interaction/coupling between the particles forming the aggregate [8, 34, 39, 40]. Furthermore, the pattern of the aggregate is very different from the one obtained for small but imperfectly spherical gold nanoparticles which has two lobes oriented at 0° and 180° characterizing a pure electric dipole emission [11, 28]. The SH intensity recorded as a function of the input polarization therefore allows the complete discrimination between single metallic nanoparticles with a shape close to the perfect sphere and aggregates of nanoparticles.

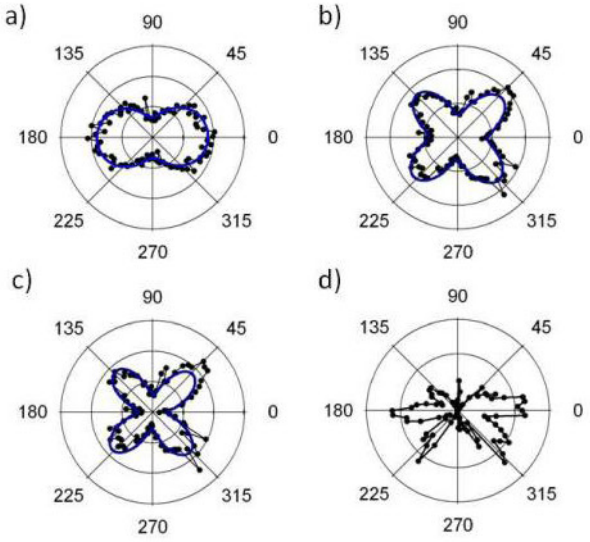

Fig. 6. Vertically polarized SH intensity as a function of the fundamental polarization angle from the matrix (a) and the matrix with a single nanoparticle (b) with 90s acquisition time for each data point. The corresponding difference is reported in panel (c). (d) Vertically polarized SH intensity for the aggregate after subtraction of the matrix contribution.

4. Conclusion

In summary, we have studied single gold metallic nanoparticles embedded in a homogeneous and transparent polyacrylamide (PAA) matrix having a low quadratic nonlinear optical efficiency allowing a high signal-to noise ratio despite the weak signal expected for single nanoparticles. The nanoparticles positions are accurately determined using only their SH signal excited by a single fundamental incident beam. The spatial autocorrelation function of the 2D maps obtained by scans perpendicular to the incident beam allows us to determine the waist of the beam which is equal to $w_0 \approx 4$ μm. This spatial autocorrelation procedure enables us to measure the quadratic hyperpolarizability of single gold metallic nanoparticles which are in good agreement with the value obtained by ensemble and previous single particle measurements. These results provide evidence that indeed single gold nanoparticles

#134427 - $15.00 USD Received 1 Sep 2010; revised 24 Sep 2010; accepted 24 Sep 2010; published 6 Oct 2010

are studied. Finally, the SH intensity from a single gold nanoparticle and from an aggregate is recorded as a function of the polarization angle of the fundamental beam. These results demonstrate that single nanoparticles and aggregates of nanoparticles can be clearly discriminated by polarization resolved SHG measurements.

#134427 - $15.00 USD Received 1 Sep 2010; revised 24 Sep 2010; accepted 24 Sep 2010; published 6 Oct 2010

La plasmonique non-linéaire en champ proche optique

L'une des particularités de ma démarche scientifique est le caractère pionnier des thématiques ou techniques développées dans mes laboratoires d'accueil, avec comme dénominateur commun l'étude des propriétés optiques de nanoparticules de métaux nobles. La plasmonique constitue ainsi le coeur et le fil conducteur de mon activité de recherche depuis près d'une décennie. L'heure étant au bilan, avant de me tourner résolument vers l'avenir, je souhaiterais retracer ici les grandes étapes qui ont jalonné mon parcours dans ce domaine en pleine effervescence:

- L'étude de la diffusion Raman dans les particules de métaux nobles a été le point de départ au cours de ma thèse. J'ai ainsi développé les premières simulations analytiques (et les seules encore à l'heure actuelle) afin de calculer les probabilités de transitions et comparer les spectres simulés aux expériences. Ce travail a conduit à la détermination de l'origine de la diffusion Raman dans les nanoparticules grâce à l'introduction d'un nouveau mécanisme de couplage, qui s'est avéré être la contribution dominante. Bien que cette étude constitue l'un des plus beaux travaux qu'il m'ait été donné de réaliser, j'ai choisi de ne pas développer cet aspect dans ce manuscrit: d'une part, ce travail a été largement initié au cours de ma thèse (qui commence à déjà dater...) même s'il s'est poursuivi notamment avec Alain Mermet du LPCML; d'autre part, je souhaitais suivre un certain fil conducteur et ne pas rallonger encore davantage le document. Une copie de l'article "fondateur" est cependant fournie à la fin de cette partie.
- Le développement de simulations numériques a constitué un tournant important de mon travail théorique à mon arrivée au LASIM. De part la richesse des formes accessibles de nos jours par voie chimique ou physique, une telle approche apparaissait indispensable. Elle a notamment contribué aux premières études quantitatives des effets de forme ou d'interaction comme celles réalisées sur des nano-bâtonnets uniques ou des dimères de particules d'or en collaboration avec les équipes FemtoNanoOptics (N. Del Fatti et F. Vallée) et Agrégats et Nanostructures (M.

Pellarin). Elle s'est poursuivie par la mise en évidence d'un nouveau régime de couplage dans les dimères hétérogènes, faisant apparaître des "profils Fano" contrôlant la forme des résonances plasmoniques.

- L'extension des simulations par éléments finis à la génération de second harmonique est sans aucun doute la contribution théorique majeure de mon travail depuis mon arrivée dans l'équipe de Pierre-François Brevet, dans la mesure où il n'y avait pas d'équivalent ailleurs. Ce travail pionnier a notamment permis d'expliquer le rôle de la rupture de centrosymétrie sur les propriétés optiques de nanoparticules d'or et d'argent observées expérimentalement mais surtout de déterminer l'origine de la réponse non-linéaire dans les particules métalliques avec la toute première mesure des contributions des courants de surface et de volume dans des nanoparticules sphériques. Ce travail de longue haleine s'est concrétisé grâce à la première mise en évidence d'interférences entre les modes dipolaires et octupolaires.
- Enfin, le développement d'une technique capable de mesurer la génération de second harmonique d'une particule unique en matrice a finalement été couronnées de succès. Ce travail, comme le précédent, doit beaucoup à la forte implication de Jérémy Butet que j'ai co-encadré avec Pierre-François Brevet. Au-delà de la "prouesse technique", ce travail a montré le parfait accord entre simulations et expériences dans le cas de particules uniques et mis en exergue la très forte sensibilité de la génération de second harmonique à une légère dissymétrie des particules et à la formation d'agrégats.

Comme le retrace le cheminement précédent, l'autre spécificité de ma démarche scientifique est le va-et-vient permanent entre théorie et expérience, ce à quoi j'attache énormément d'importance. Ainsi, selon les cas, l'approche théorique a permis de rendre compte et d'expliquer les résultats expérimentaux obtenus (diffusion Raman, spectres d'extinction de particules uniques) ou au contraire a suggéré en amont les expériences à réaliser (profils Fano, origine de la réponse non-linéaire). Si la présentation succincte qui vient d'être faite pourrait laisser penser que le cœur de mon travail est théorique, il n'en est rien! Au-delà la SHG à l'échelle d'une particule unique, dans laquelle j'ai été fortement impliqué via le co-encadrement de Jérémy Butet, j'ai largement contribué à la construction de nombreux montages expérimentaux, au premier rang desquels je citerais le dispositif de spectrométrie, d'interférométrie et d'imagerie femtoseconde mise en place pendant mon stage post-doctoral. Il reste à ce jour la plus belle réalisation expérimentale que j'ai pu mener de A à Z, depuis la réalisation des plans, avec plus d'une centaine d'éléments optiques, jusqu'à

l'exploitation des résultats, ayant finalement conduit à de nombreuses publications bien au-delà de mon court séjour madrilène. Ce dispositif d'imagerie pompe-sonde multi-échelle (de la centaine de femtosecondes à la microseconde et plus si besoin!), utilisant notamment une Streak Camera, permettait également de réaliser de l'interférométrie spectrale en combinant dans un spectromètre des pulses jumeaux produits par un interféromètre de Michelson. L'idée de cette fonctionnalité était particulièrement séduisante. Tout comme des fentes d'Young donnent dans l'espace des vecteurs d'ondes un phénomène bien connu d'interférence, deux impulsions temporelles donnent un système de franges dans l'espace des fréquences. Il suffisait donc de faire interférer dans l'espace des fréquences (d'où l'utilisation du spectromètre) deux impulsions générées par le Michelson. Pour peu qu'un faisceau de pompe vienne perturber le système entre les deux pulses de sonde, les franges se décalaient donnant ainsi accès à la phase des modifications induites par le pulse de pompe.

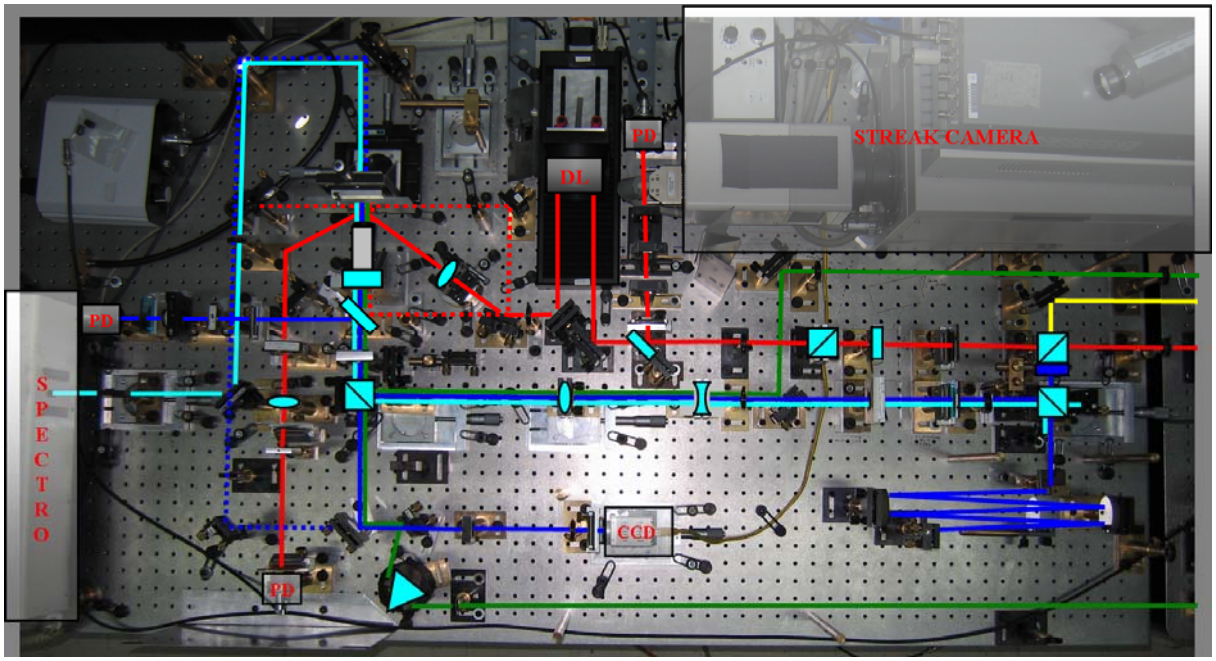

Je me suis par la suite fortement investi dans la construction d'un amplificateur femtoseconde (taux de répétition au kHz), projet porté par Christian Jonin. J'ai notamment dessiné les plans du dispositif actuel afin d'optimiser autant que possible l'encombrement de l'installation et réalisé un premier alignement des différents éléments d'optique, étape ayant permis de faire laser la cavité (en bleu clair sur le schéma), d'injecter le faisceau venant du Mira après passage dans un étireur à 8 passages (en rouge) et d'éjecter les pulses de la cavité via une cellule Pockels avant compression (partie orange). L'optimisation du système au

niveau de l'injection, le choix de la position du cristal Ti:Sa ou encore de la longueur d'onde optimale de fonctionnement sont actuellement achevées par Estelle Salmon et Christian Jonin.

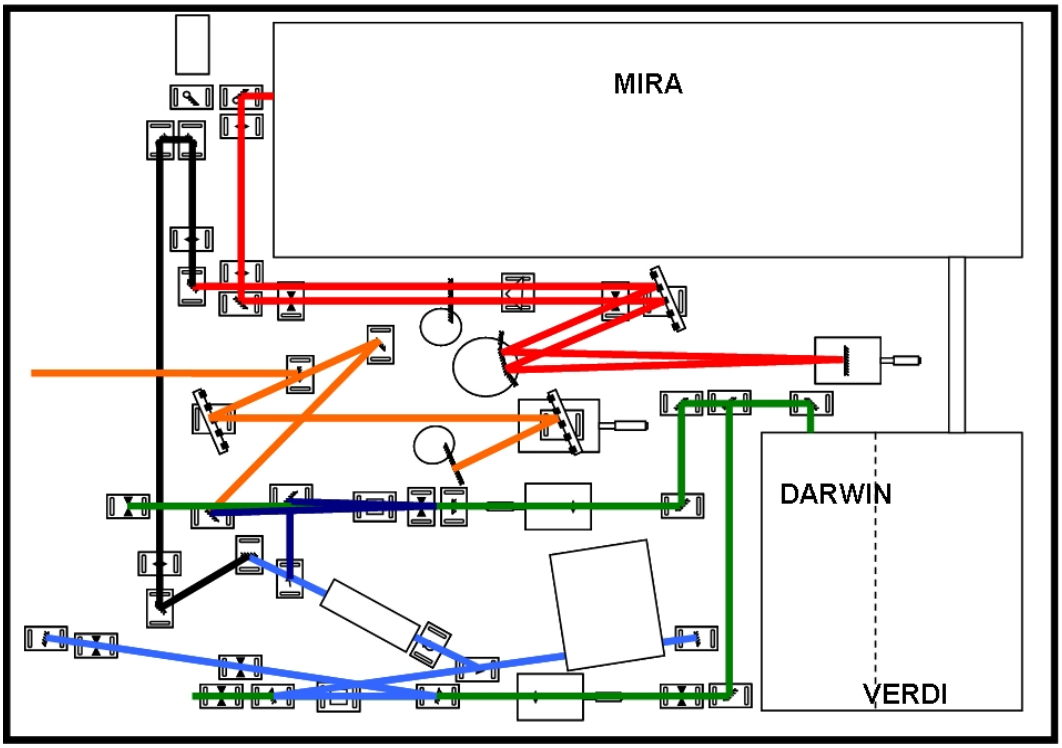

Enfin, et en relation directe avec le titre de cette dernière partie, j'ai entrouvert la porte du monde des microscopies en champ proche optique (SNOM). Ces techniques ont pour but d'aller sonder les photons localisés au voisinage des nanostructures dans la partie évanescente des ondes, présentant des vecteurs d'ondes trop grands pour pouvoir se propager en espace libre. Au-delà de la présence même de la sonde locale, qui a pour potentiel effet collatéral de perturber le système étudié, l'une des difficultés rencontrées avec ces techniques vient de la nécessité de discriminer la réponse provenant de l'objet étudié par rapport à celle de tout le reste de l'échantillon éclairé. De nombreuses solutions ont été proposées comme l'utilisation de sondes métallisées pour localiser la lumière servant à illuminer l'échantillon ou encore l'utilisation de sondes actives présentant un émetteur idéalement unique en bout de pointe et générant in-situ les photons nécessaires à l'investigation. Dans ce cadre, nous avons démontré avec Pietro Gucciardi qu'il était possible de supprimer totalement le signal provenant de la zone "non-utile" de l'échantillon et ce en jouant simplement sur l'amplitude d'oscillation de la sonde et sur quelques propriétés mathématiques des fonctions de Bessel... Ce fut aussi l'occasion pour moi de proposer une technique interférentielle, utilisant une démodulation poly-harmonique, pour mesurer l'amplitude d'oscillation de la sonde d'un SNOM. Fait

remarquable à l'époque (du moins de mon point de vue de néophyte), nous étions parvenus à mesurer une amplitude de 0.50±0.02 nm! La précision obtenue m'avait laissé quelque peu rêveur.

Mon activité champ proche s'est poursuivie plus récemment dans le cadre du centre NanOpTec, en collaboration avec Brigitte Prével du LPMCN, avec le développement d'un SNOM pouvant fonctionner sous différents modes classiques: excitation ou collection par la sonde. J'ai ainsi réalisé le montage optique permettant de basculer aisément entre ces deux configurations ainsi qu'entre les sources (laser ou lampe blanche) et consacré un certain nombre d'heures à l'optimisation de ce qui constitue le nerf de la guerre en SNOM: l'étirage des fibres. Cette dernière activité a maintenant été reprise par Christophe Moulin, recruté au centre NanOpTec comme Ingénieur d'Etude. Preuve du bon fonctionnement du dispositif, nous étions parvenu à mesurer la réponse optique d'une particule d'or de 100 nm de diamètre révélant des profils Fano caractéristiques, dus cette fois à l'interférence entre la lumière directement collectée par la sonde et celle diffusée par la particule d'or. Si ce fait fut marquant pour nous, il n'avait malheureusement rien d'original puisqu'il avait déjà été observé dans la littérature, quelques années auparavant. Il constituait cependant un pas décisif en vue de ce qui sera le coeur de mon projet de recherche pour les années à venir et le point de convergence de toutes les compétences que j'ai acquises au cours de près de dix ans de recherche active: la plasmonique non-linéaire en champ proche optique.

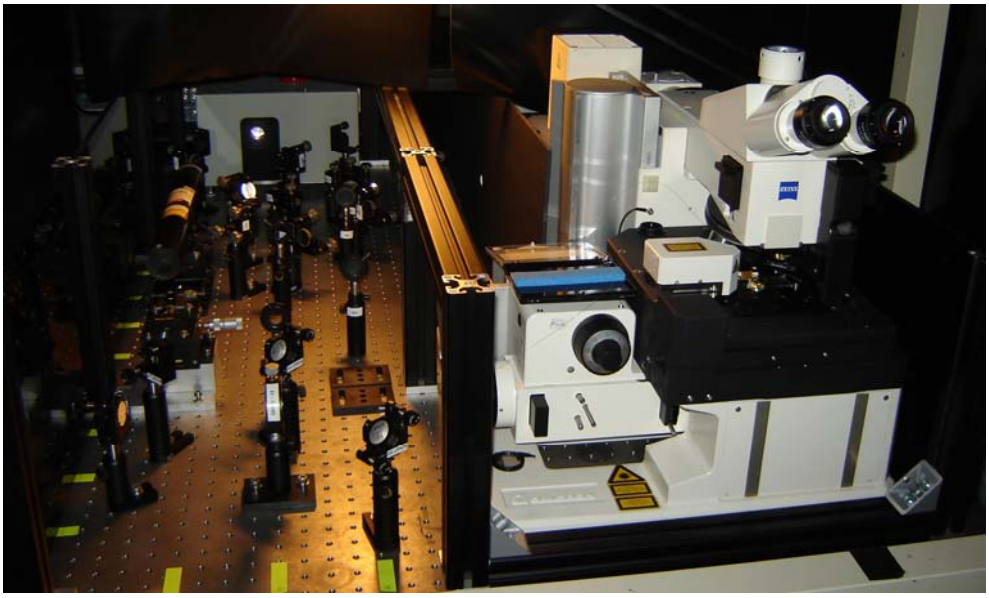

Mais pourquoi donc vouloir faire de la plasmonique non-linéaire en champ proche optique? Le but de mon projet est d'atteindre un niveau d'expertise unique en nano-plasmonique non-linéaire en couplant des techniques de champ proche / champ lointain / simulation par éléments finis à l'échelle de la particule unique. Cette approche constituera clairement une rupture importante avec l'état de l'art actuel. Il y a en effet une multitude d'aspects qui n'ont pas encore été explorés. En particulier, ce projet a pour objectifs :

- de confirmer, par une étude en champ proche, l'origine de la génération de second harmonique dans les nanoparticules de métaux nobles: comme le montre la figure ci-contre, la distribution spatiale du champ au voisinage de nanoparticules dépend très fortement de la nature de la source non-linéaire (courant surfacique local ou courant volumique non-local), et pourrait donc permettre de discriminer les différentes contributions.

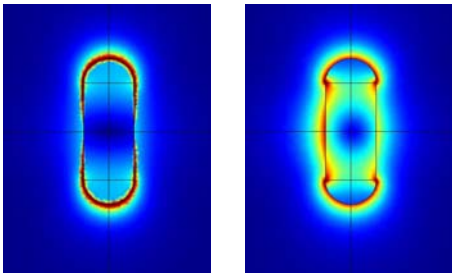

surface bulk

- d'étendre cette étude à la génération de troisième harmonique (THG): contrairement au SHG, qui est un processus normalement interdit dans les milieux centrosymétriques comme l'or et l'argent, ce processus faisant intervenir trois photons est autorisé dans l'approximation dipolaire, apportant ainsi une information complémentaire sur les effets d'exaltation et de symétrie des champs sur les propriétés non-linéaires,
- d'analyser la corrélation spatiale entre les champs linéaires et non-linéaires en utilisant des particules de formes variées comme des bâtonnets, des prismes des cubes etc... Le but est de faire le lien entre la localisation du champ à la fréquence fondamentale, qui est un effet maintenant bien connu en plasmonique, et la production de photons harmoniques,
- de comprendre le lien entre la formation de hot-spots (exaltation du champ électrique) dans le gap entre particules en interaction et les propriétés non-linéaires. Des résultats "inattendus" ont été obtenus numériquement avec des nano-antennes en interaction et doivent être testés expérimentalement pour avoir un plus large impact. Ce travail fait notamment l'objet d'une collaboration avec Bert Hecht, qui est l'un des leaders mondiaux en nano-plasmonique.

La réalisation de ce projet nécessite toute fois trois développements techniques déterminants:

- l'extension des simulations par éléments finis à la génération de troisième harmonique,
- la production de nanoobjets plasmoniques en utilisant trois approches: top-down (lithographie E-beam), bottom-up (la sonde SNOM est utilisée pour positionner les particules avec une résolution nanométrique) et mixte (une particule est greffée sur la sonde pour contrôler dynamiquement sa distance avec une particule déposée sur un substrat),
- l'introduction d'une sonde à champ proche dans un dispositif de particule unique en SHG pour réaliser des mesures en champ proche optique non-linéaire.

Pour lever ces trois verrous techniques, j'ai décidé de rejoindre les équipes de Serge Huant (Microscopies en champ proche) et de Benoît Boulanger (Matériaux, optique non-linéaire et plasmonique) reconnues internationalement pour leurs expertises dans ces domaines. Leurs compétences faciliteront ainsi très largement, si ce n'est garantiront, le succès de mon projet scientifique. Il permettra d'autre part de créer une nouvelle thématique de recherche, la nano plasmonique non-linéaire en champ proche optique, à l'interface entre deux départements de l'institut Néel: "NANOsciences" et "Matière condensée, matériaux et fonctions". Pour soutenir mon arrivée à l'Université Joseph Fourier, nous avons déposé à l'Institut Néel une ANR jeune chercheur dont je serai le coordinateur, avec pour objectif:

- de former une "équipe ANR jeune" compacte constituée essentiellement de jeunes chercheurs en très forte interaction mais bénéficiant de l'expertise et du savoir faire local.
- de construire entièrement, depuis la table optique jusqu'au système de détection, un tout nouveau dispositif expérimental, sans équivalent au monde actuellement,
- d'exprimer mon autonomie et mes idées avec un fort soutient en terme de moyens scientifiques (expertises des deux équipes), humains (chargés de recherche, personnels techniques et étudiant en thèse), matériels (mise à disposition de locaux) et financiers (financement ANR si accepté).

Au-delà de la réalisation des objectifs de mon projet de recherche, cette ANR sera le point de départ de nombreuses aventures scientifiques tant l'adéquation et la complémentarité entre mes compétences et les activités de recherche des deux équipes d'accueil est importante. Certaines se profilent déjà à l'horizon, mais ça, c'est une autre histoire...

Surface plasmon mediated Raman scattering in metal nanoparticles

G. Bachelier and A. Mlayah
Laboratoire de Physique des Solides, UMR 5477, IRSAMC, Université P. Sabatier, 118 Route de Narbonne, 31062 Toulouse Cedex 4, France

(Received 10 December 2003; revised manuscript received 24 February 2004; published 26 May 2004)

The Raman scattering due to confined acoustic vibrations in metal particles is studied theoretically. Various coupling mechanisms between the surface plasmon–polaritons and the confined vibrations are investigated. Their relative contribution to the light scattering is discussed. We found that two mechanisms play an important role: (i) modulation of the interband dielectric susceptibility via deformation potential due to pure radial vibrations and (ii) modulation of the surface polarization charges by quadripolar vibrations. The dependence of the Raman spectra on the nanoparticles size and size distribution and on the excitation energy is studied in connection with the nature of the excited plasmon-polariton states. We found a good agreement between calculated line shapes and relatives intensities of the Raman bands and the experimental spectra reported in the literature.

DOI: 10.1103/PhysRevB.69.205408 PACS number(s): 78.30.Er, 63.22.+m, 73.22.Lp, 78.67.Bf

I. INTRODUCTION

Surface-enhanced Raman scattering[1] has been attracting much interest recently due to the discovery of single-molecule sensitivity.[2,3] The key role of randomly distributed[4] or fractal-like aggregates[5] in the disorder induced localization of the surface plasmons is now well established. In their earlier work,[6] Gersten *et al.* showed that resonance of the incident light with the plasmons of a rough metal surface leads to strong light scattering by confined acoustic vibrations. For an isolated spherical particle, the phonon density of states is discrete and the confined vibrations are expressed in term of vector spherical harmonics labeled (n,l,m). They can be obtained from Lamb's theory[7] applied to nanosized particles (i.e., with a radius much larger than the interatomic distance). Many published experimental works showed that the confined quadripolar vibrations $(n=1,l=2)$ strongly come out in the Raman spectra of Au, Ag, and Cu nanoparticles for resonant excitation with the surface plasmon absorption band.[6,8,9] In contrast, the pure radial vibrations $(l=0)$ are not easily observable and were revealed only recently[10,11] in the Raman spectra of metal particles with a narrow size distribution. On the other hand, time-resolved reflectivity measurements showed periodic intensity oscillations due to pure radial vibrations $(n=1,l=0)$ only.[12] Up to now it is not clear why the quadripolar vibrations should dominate in Raman scattering and pure radial vibrations in time-resolved reflectivity. A complete understanding of the optical properties of a vibrating metal particle still lacks. In their earlier work, Gersten *et al.*[13] proposed a model for Raman scattering from size and shape distributed metal particles. They considered coupling between the dipolar surface plasmons and the quadripolar vibrations due to modulation of the electron charge density (i.e., of the bulk plasmon frequency). Pure radial vibrations were not expected to produce a significant modulation which is apparently in agreement with the experimental observations. Nevertheless, no calculations of the relative contribution of quadripolar and radial vibrations have been reported up to now. In addition, comparison with other possible coupling mechanisms is needed in order to identify the origin of the Raman scattering.

Moreover, Montagna and Dusi[14] proposed a model for the Raman scattering by confined acoustic vibrations of small dielectric spheres. The light scattering was described using the dipole-induced-dipole and bond polarizability models which are suitable for nonresonant scattering in dielectric materials, but cannot apply to resonant light scattering in metals.

In this work, we investigate and compare different coupling mechanisms between the confined vibrations and the surface plasmons of metal particles. They can be classified into surface and volume mechanisms. The surface mechanisms involve changes of the particle surface, whereas the volume mechanisms are due to modulation of the material properties. The Raman scattering efficiency is derived and discussed for each of them. Calculations are presented for silver nanoparticles but apply to gold and copper as well. The dependence of the scattering efficiency on average size and size distribution is discussed in connection with the resonantly excited surface plasmons. The effects of the surrounding medium are not investigated here. They are expected to shift the plasmon resonances and the vibration frequencies.[15] However, they should not affect the conclusions of the present work with respect to the plasmon-vibration coupling and related Raman scattering.

II. MODEL

A. Surface plasmon–polariton states

We use the dielectric confinement model to account for the optical properties of the metal particles.[16] The electromagnetic fields inside and outside the particle are computed from Maxwell equations (i.e., including retardation effects) and using the usual surface boundary conditions: continuity of the normal component of the magnetic field and of the tangential component of the electric field. Contributions of both intraband and interband transitions were taken into account in the frequency-dependent dielectric response of the metal particle. We use the size dependent dielectric susceptibility given by

$$\chi(\omega,R) = -\frac{\omega_p^2}{\omega^2 + i\omega\gamma(\omega,R)} + \chi^{ib}(\omega), \tag{1}$$

where ω_p is the bare plasmon frequency of bulk silver and $\gamma(\omega,R) = \gamma_o + gs(\omega)v_F/R$ the effective Drude damping which accounts for the electron scattering by the nanoparticle surface;[17] v_F is the Fermi velocity and R the nanoparticle radius. $gs(\omega)$ is obtained from a quantum treatment of the electron-surface interaction. $\chi^{ib}(\omega)$ is the interband dielectric function due to electronic transitions from the $4d$ valence band to the $5s$ conduction band.[18] As shown by Hovel *et al.*,[19] $\chi^{ib}(\omega)$ does not change with particle size for $R > 1$ nm. Then $\chi^{ib}(\omega)$ was taken from the data reported for bulk silver in Ref. 20.

Solutions of Maxwell equations are obtained at all frequencies (continuous density of states). Hence, the electromagnetic field and polarization vectors are labeled $\mathbf{E}_{\omega,L,M}$ and $\mathbf{P}_{\omega,L,M}$, respectively; ω being the eigenfrequency and (L,M) the usual integer numbers associated with the spherical harmonic functions. The amplitude of the electromagnetic field inside the metal particle reaches a maximum for discrete frequencies ω_L known as the surface plasmon–polariton (SPP) resonances or as Mie's resonances.[21] For spherical particles, ω_L is $(2L+1)$-fold degenerate.

The lifetime of the SPP states is strongly reduced due to Landau damping (i.e., to decay into electron hole pairs). From Fermi's golden rule one obtains the decay rate[22]

$$\Gamma_{\omega,L}(R) = \Gamma_i + 2\pi \sum_{e,e'} |\langle e'|H_{\omega,L}|e\rangle|^2 \delta(\hbar\omega + \epsilon_e - \epsilon_{e'}), \tag{2}$$

where e and e' are individual electronic states and $H_{\omega,L}$ their interaction Hamiltonian with the SPP states ω,L. Γ_i is given by the bulk material properties. As discussed by Hovel *et al.*,[19] Γ_i turns to be the Drude damping γ_0 [Eq. (1)] in the case of free-electron metals. Using Eq. (2) one recovers the well-known $1/R$ dependence.[22] Moreover, $\Gamma_{\omega,L}(R)$ increases as the squared amplitude of the inner electric field associated with the SPP state (ω,L,M). Hence, for nanoparticles one expects overdamping of the SPP resonant states with $L > 1$ due to their fast decay into electron-hole pairs.[24]

B. Raman scattering

For the calculation of the Raman spectra, we assume a three-step scattering process[23] in which a SPP state (ω,L,M) is excited by the incoming photon and decays into another SPP state (ω',L',M'), via emission or absorption of confined (n,l,m) vibration; finally a scattered photon is emitted. For the Stokes process, the Raman scattering amplitude is given by

$$-2i\pi\delta(\hbar\omega_s + \hbar\omega_{n,l} - \hbar\omega_i) \times \langle n_s + 1, n_{\omega',L',M'}|H_{ph\text{-}SPP}|n_s, n_{\omega',L',M'} + 1\rangle \times \langle n_{\omega,L,M}, n_{\omega',L',M'} + 1, n_{n,l,m} + 1|H_{vib\text{-}SPP}|n_{\omega,L,M} + 1, n_{\omega',L',M'}, n_{n,l,m}\rangle \times \frac{\langle n_i - 1, n_{\omega,L,M} + 1|H_{ph\text{-}SPP}|n_i, n_{\omega,L,M}\rangle}{(\hbar\omega_s - \hbar\omega' + i\Gamma_{\omega',L'})(\hbar\omega + i\Gamma_{\omega,L} - \hbar\omega_i)}, \tag{3}$$

where n_i, n_s, $n_{\omega,L,M}$, and $n_{n,l,m}$ are, respectively, occupation numbers of incoming and outgoing photons, surface plasmon–polaritons (ω,L,M), and confined vibrations (n,l,m). $\Gamma_{\omega,L}$ is given by Eq. (2). $H_{ph\text{-}SPP}$ and $H_{vib\text{-}SPP}$ correspond to the photon-SPP and confined vibration-SPP interaction Hamiltonians.

We assume dipolar interaction between the SPP states and the incoming or outgoing photons. Because spherical symmetry is preserved at the absorption or emission steps of the confined vibrations, conservation of the angular momentum should be fulfilled. This implies the following selection rules:

$$|L - L'| \leq l \leq L + L', \tag{4a}$$

$$L + L' + l \quad \text{even}, \tag{4b}$$

$$M' - M = \pm m. \tag{4c}$$

On the other hand, there is no restriction on the values of L and L' since the spherical symmetry is broken at the photon absorption and emission steps (interaction between plane waves and spherical harmonics). However, in the particular case of nanoparticles we consider only dipolar SPP states (i.e., $L = L' = 1$) as discussed above. Thus, according to selection rules (4a) and (4b), only pure radial ($l = 0$) and quadripolar ($l = 2$) vibrations could be observed by Raman scattering from spherical and noninteracting nanoparticles. This has been already pointed out by Duval[25] using group symmetry arguments. In the three-step light scattering process, it is the symmetry of the intermediate SPP state which determines the symmetry of the Raman active modes. Further considerations on the interaction between dipolar SPP states and vibrations can lead to additional selection rules or at least determine the relative contribution of the quadripolar and the pure radial vibrations.

We now consider dipolar interaction between SPP states. Without particle vibrations, this interaction does not exist since the SPP form a set of orthogonal eigenstates. As the metal particle vibrates, so will the SPP polarization vector and then transitions between SPP states will take place.

Then the interaction matrix elements between confined (n,l,m) vibrations and those dipolar SPP states read

$$H_{vib\text{-}SPP} = -\int_{particle} \mathbf{E}_{\omega',L',M'} \cdot \delta_{n,l,m} \mathbf{P}_{\omega,L,M} dV, \tag{5}$$

where $\delta_{n,l,m}\mathbf{P}_{\omega,L,M}$ is the polarization modulation of the SSP state (ω,L,M) induced by the confined vibrations (n,l,m). $\mathbf{E}_{\omega',L',M'}$ is the electric field associated with the final (ω',L',M') SPP state. For nanoparticles, only dipolar SPP states $(L=L'=1)$ play an important role. The integral in Eq. (5) runs over the particle volume only because there is no polarization outside the metal particle (i.e., in vacuum). In order to calculate the Raman spectra one has to specify $\delta_{n,l,m}\mathbf{P}_{\omega,L,M}$.

C. Volume mechanisms

Let us start with the coupling between confined vibrations and SPP states due to what we named volume mechanisms. By volume mechanisms we mean modulation of the dielectric response independently from the surface motion. This concerns modulation of the bulk metal dielectric response due to changes of the material electronic properties. For instance, deformation potential (DP) interaction[26] between the lattice vibrations and the confined electronic states leads to modulation of the metal dielectric susceptibility (and hence of the SPP's polarization vectors).[27] In principle, both intraband and interband terms of the dielectric response can be modulated via DP interaction. However, because the single particle intraband excitations fall in the infrared range, the effect of their interaction with lattice vibrations on the collective intraband response is negligible in the visible range.[27] In other words, the bare plasmon frequency ω_p is not affected by lattice vibrations. On the contrary, electronic interband excitations fall in the UV range and lead to a strong screening effect of the bare plasmon. As a matter of fact, for bulk silver the bare plasmon energy is about 9 eV whereas the plasmon absorption band is observed around 3 eV. We have calculated the change of the interband dielectric susceptibility of silver due to DP interaction of the interband excitations with lattice vibrations. Since the interband susceptibility is independent of the particle size, quantum confinement effects on electronic states were neglected. In order to compute the overall change of $\chi^{ib}(\omega)$ one has to sum the contributions of transitions involving initial and final states from the whole Brillouin zone, the value of the DP energy depending on the considered states. We assume an average value $D^{e\text{-}ph}=-1.55$ eV intermediate between the values obtained for zone center (Γ point) and for zone edge (L point) states.[28] Hence, the modulation $\delta_{n,l,m}\mathbf{P}_{\omega,L,M}$ of the SPP polarization reads

$$\delta_{n,l,m}\mathbf{P}_{\omega,L,M}=\varepsilon_0\chi^{inter}(\omega)\left(\frac{D^{e\text{-}ph}}{\hbar\omega-\hbar\Omega^{ib}}\nabla\cdot\mathbf{D}_{n,l,m}\right)\mathbf{E}_{\omega,L,M}. \tag{6}$$

In this equation, confinement effects of the lattice vibrations appear in the divergence of the displacement field $\nabla\cdot\mathbf{D}_{n,l,m}$. It is worthwhile to mention that Eq. (6) is valid for bulk as well. The only difference with the nanoparticles is the displacement field $\mathbf{D}_{n,l,m}$ which introduces the confinement of the lattice vibrations. In other words the value of $D^{e\text{-}ph}$ itself is independent of the nanoparticle surface (or radius). In that sense the DP coupling mechanism can be classified as a volume mechanism.

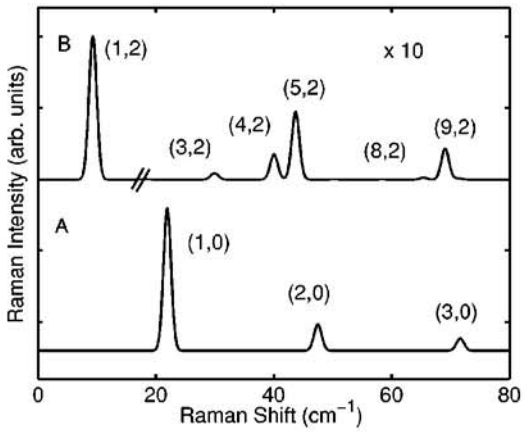

FIG. 1. Normalized Raman spectra of silver nanoparticles calculated with $R=2.5$ nm for resonant excitation with SPP state at 2.5 eV. Spectra correspond to the coupling via (A) deformation potential and (B) surface modulation mechanisms. The frequency range 16–80 cm^{-1} is shown with 10× magnification in spectrum (B). The linewidths result from convolution by a Lorentzian function.

By making Eq. (6) into Eq. (5), and using the three-step light scattering process [Eq. (3)], we are able to calculate the Raman spectra due to DP coupling between confined vibrations and SPP states. As shown in Fig. 1, the Raman scattering (spectrum A) is dominated by the pure radial vibrations ($l=0$). The first three frequencies were found at 21.9 cm^{-1}, 47.5 cm^{-1}, and 71.6 cm^{-1} for $R=2.5$ nm. The intensity ratios between harmonics in spectrum A of Fig. 1 do not depend on the excitation energy since the electromagnetic field distribution inside the nanoparticle is uniform whatever the energy of the dipolar SPP state is. Quadripolar vibrations ($l=2$) are not forbidden since they satisfy selection rules (4a) and (4b). However, their Raman efficiency is here several orders of magnitude smaller than that of the pure radial vibrations.[29] Vallée *et al.* suggested that modulation of the interband susceptibility due to the confined vibrations could be responsible for the oscillation observed in the time-resolved reflectivity of metal nanoparticles.[12] From the oscillations period they identified pure radial vibrations ($n=1,l=0$). Quadripolar vibrations were not revealed. Portales *et al.*[10] suggested that the same modulation is at the origin of the Raman scattering by pure radial vibrations ($l=0$). This is in agreement with our calculations. Indeed, for the DP mechanism, we found that modulation of the interband susceptibility by quadripolar vibrations ($n=1,l=2$) is one order of magnitude smaller than the one due to pure radial vibrations ($n=1,l=0$). This arises from the weak displacement field gradient associated with quadripolar vibrations. Moreover, it is clear that the DP mechanism cannot explain the intense lower frequency peak observed in the Raman spectra and ascribed to the fundamental quadripolar vibrations ($n=1,l=2$).[9–11,13]

D. Surface mechanisms

The surface coupling mechanisms involve changes of the particle radius or shape. First, Gersten *et al.*[13] proposed a

modulation of the bare plasmon frequency ω_p due to electron density oscillations with the particle volume. In fact, one can see in Eq. (1) that the size dependence of the intraband dielectric susceptibility arises from the Drude damping parameter only. For a silver particle with 3 nm radius excited at 3 eV (i.e., close to the dipolar SPP resonance) one obtains $gs(\omega,R)v_F/R=220$ meV.[17] This term is more than one order of magnitude smaller than the excitation energy. So, in terms of relative changes, the effects of particle vibrations on Drude damping, and consequently on the intraband dielectric response, are very weak.[27] Second, in the frame of the dielectric confinement model, the energies of SPP resonances are determined by the electromagnetic boundary conditions at the nanoparticle surface. Strictly speaking, they should be sensitive to oscillations of the particle radius. The dependence of the resonant SPP eigenfrequency on the particle size arises from the retardation effects which are negligible for nanosized particles (particle radius very small in comparison with the visible optical wavelengths). Hence, this coupling mechanism is also very weak. It is worthwhile to mention that all surface coupling mechanisms discussed above involve only pure radial vibrations ($l=0$) because they are associated with changes of the particle volume. Therefore, they cannot explain the lower-frequency Raman peak assigned to quadripolar vibrations. Moreover, compared to the DP coupling mechanism, the surface mechanisms discussed above are several order of magnitudes less efficient.

The change of the particle shape can also lead to a modulation of the SPP polarization vectors. Indeed, the polarization vectors of the SPP states are associated with a distribution of polarization charges at the nanoparticle surface given by $\mathbf{P}_{\omega,L,M}\cdot\mathbf{n}$, $\mathbf{n}$ being the normal to the surface. Therefore, when the particle oscillates, in the (n,l,m) vibration mode, its orientation varies by $(\delta_{n,l,m}\mathbf{n})$; so the polarization charges are redistributed with respect to the static situation according to $\delta_{n,l,m}\sigma_{\omega,L,M}=\mathbf{P}_{\omega,L,M}.\delta_{n,l,m}\mathbf{n}$. This is what we call surface orientation (SO) coupling mechanism. In order to evaluate the modulation $\delta_{n,l,m}\mathbf{P}_{\omega,L,M}$ of the SPP polarization, we expand $\delta_{n,l,m}\sigma_{\omega,L,M}$ on the basis of the surface polarization charges $\sigma_{\omega,L',M'}$ of the motionless particle,

$$\delta_{n,l,m}\sigma_{\omega,L,M}=\sum_{L',M'}\frac{\int\sigma_{\omega,L',M'}\delta_{n,l,m}\sigma_{\omega,L,M}.dS}{\int\sigma^2_{\omega,L',M'}.dS}\sigma_{\omega,L',M'}. \tag{7}$$

By making $\sigma_{\omega,L',M'}=\mathbf{P}_{\omega,L',M'}\cdot\mathbf{n}$ in Eq. (7) one can rewrite $\delta_{n,l,m}\sigma_{\omega,L,M}$ as $\delta_{n,l,m}\mathbf{P}_{\omega,L,M}\cdot\mathbf{n}$ with

$$\delta_{n,l,m}\mathbf{P}_{\omega,L,M}=\varepsilon_0\chi(\omega)\sum_{L',M'}\frac{\int\sigma_{\omega,L',M'}\delta_{n,l,m}\sigma_{\omega,L,M}.dS}{\int\sigma^2_{\omega,L',M'}.dS}\times\mathbf{E}_{\omega,L',M'}. \tag{8}$$

In the SO coupling mechanism, only quadripolar spheroidal vibrations contribute to Raman scattering. Pure transverse and pure radial vibrations are not active because such modes do not change the shape of the particle surface. Moreover, this mechanism is sensitive to the displacement field at the particle surface only. Therefore, the intensity ratio between harmonics [spectrum B of Fig. 1] strongly differ from the one calculated for DP coupling [spectrum A]. The first three quadripolar vibrations were found at 9.3 cm^{-1}, 18.1 cm^{-1}, and 30 cm^{-1} for 2.5 nm particle radius. The most intense contribution from the harmonics is due to the quadripolar $(n=5,l=2)$ modes. The corresponding Raman peak [spectrum B] is 20 times weaker than that of the fundamental vibrations $(n=1,l=2)$. This explains why only the fundamental quadripolar vibration modes were observed experimentally for nanoparticles ensembles with large size dispersion.[6,8,9]

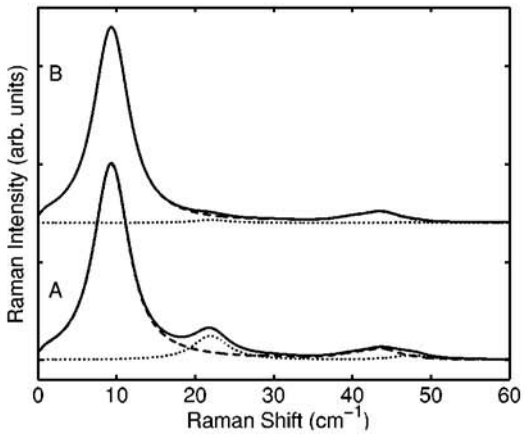

FIG. 2. Normalized Raman spectra of silver nanoparticles calculated with $R=2.5$ nm for resonant excitation with SPP states at (A) 2.5 eV and (B) 2 eV. The contributions of the deformation potentials and surface orientation mechanisms are shown by dotted and dashed lines, respectively. The total scattered intensity is shown as bold lines. The linewidths result from the convolution by a Lorentzian function (finite experimental resolution) and from the size-dependent vibrational lifetime.

III. RESULTS AND DISCUSSION

A. Origin of the Raman bands

Calculation of the Raman scattering efficiencies allows to estimate the contributions of different coupling mechanisms and hence identify the origin of the low-frequency Raman bands. The spectra calculated, assuming both DP and SO coupling mechanisms, are shown in Fig. 2 for an isolated spherical particle with 2.5 nm radius. Calculations were performed for resonant excitation of the SPP states at 2 eV and 2.5 eV, close to the dipolar SPP resonance observed in Ref. 11. We use a size-dependent homogeneous broadening of the confined vibrations given by[12] $\Gamma_{n,l}(R)=2\pi c_l/(\tau_{n,l}R)$, c_l being the longitudinal sound velocity. $\tau_{n,l}$ is a measure of how fast the vibrational excitations fade away.[30] We found that $\tau_{n,l}\approx 10$ for all modes give a reasonable agreement between the calculated and measured spectra reported in the literature.[10,11] In comparison with Fig. 1, only three bands

appear in the simulated spectra (A) of Fig. 2. The intense lower-frequency peak is due to scattering by the fundamental quadripolar vibrations ($n=1,l=2$) coupled to the dipolar SPP states via SO mechanism. The weaker band, around 22 cm^{-1}, is associated with the fundamental radial mode ($n=1,l=0$). Its coupling to the dipolar SPP states occurs via DP mechanism. The higher-frequency band around 45 cm^{-1} has contributions from quadripolar ($n=4$ and 5, $l=2$) and pure radial ($n=2,l=0$) harmonics. The agreement with the measured Raman spectra reported in Ref. 11 is remarkable. In particular, the relative intensities of the Raman bands are well reproduced.

We would like to emphasize that the calculated intensities are directly determined by Eqs. (6) and (8). Only two physical quantities could be viewed as adjustable parameters: the averaged deformation potential $D^{e\text{-}ph}$ and the parameter $\tau_{n,l}$ related to the vibration lifetime, which acts as an homogeneous broadening of the Raman lines. We used the same value of $\tau_{n,l}$ for all vibration modes. Hence, the relative intensities of the calculated bands do not depend on $\tau_{n,l}$. The best agreement with the results of Ref. 11 was obtained for $\tau_{n,l}=10$. This value is three times larger than that obtained by Del Fatti *et al.*[12] for particles embedded in glass matrix. This indicates a weaker coupling between the confined vibrations and the surrounding medium as expected for the particles studied in Ref. 11 which were coated with thiol chains. The value $\tau_{n,l}=10$ is in good agreement with the one obtained by Voisin *et al.*[31] on silver particles in colloidal suspension. Concerning the averaged deformation potential, we did not try to adjust $D^{e\text{-}ph}$. Strictly speaking, its value should be calculated from the electronic properties of the overall Brillouin zone as discussed above. Since the electronic states at the Fermi level involve mainly the zone center and the (L-point) zone edge, we used an average potential extracted from Ref. 28. This value is, of course, material dependent and can also be modified by quantum confinement effects not taken into account.

An important issue of our simulations is that all Raman bands[10,11] do not originate from the same scattering mechanism and can be accounted for without invoking any ellipsoidal distortion of the particle shape, although this may play an important role, as already suggested by Portales *et al.*[10] The dependence of the Raman scattering on incident and scattered photon polarizations can be used to ascertain the origin of the observed bands: since the scattering due to pure radial vibrations is totally polarized, the band around 22 cm^{-1} should disappear in crossed polarizations, whereas the band around 45 cm^{-1} is expected to shift toward lower frequencies due to extinction of the vibration harmonic ($n=2,l=0$). Obviously, these predicted selection rules should be reconsidered in the case of interacting particles or nonspherical particles.

It is interesting to notice that the DP mechanism involves modulation of the dielectric susceptibility and hence pure radial vibrations can be detected in the oscillatory part of the time-resolved reflectivity. In the SO mechanism, it is the SPP polarization vector and not the dielectric susceptibility which is modulated by the particle vibrations. The modulation $\delta_{n,l,m}\mathbf{P}_{\omega,L,M}$ given by Eq. (8) arises from the redistribution of the surface polarization charges. Hence, the reflectivity is not modulated and quadripolar vibrations could not be observed in time-resolved reflectivity measurements.[12]

The different nature of the DP and SO coupling mechanisms leads to different behaviors of the Raman scattering efficiency with respect to excitation energy. Indeed, according to Eq. (6) the DP mechanism involves modulation of the interband susceptibility, only. For the SO mechanism, the modulation of the SPP polarization vectors is proportional to the overall dielectric susceptibility [Eq. (8)]. Therefore, the relative contribution of both mechanisms is expected to change with excitation energy, as shown in Fig. 2. At low excitation energy (spectrum B), the interband susceptibility is rather small with respect to the overall dielectric susceptibility. Then, mainly quadripolar vibrations do contribute to the low-frequency Raman spectra. On the contrary, for excitation close to the SPP resonance (spectrum A), the Raman scattering due to pure radial modes ($l=0$) comes out since the interband susceptibility has a larger contribution. Unlike silver, for which interband transitions fall in the UV domain, gold has a strong interband susceptibility in the visible range. So one expects that Raman scattering by pure radial modes ($l=0$) is more easily observed for gold nanoparticles than for silver. This has been already verified experimentally by Portales *et al.*[10]

B. Effects of size distribution

The spatial distribution of the electric field and polarization associated with the SPP states strongly depends on the particle size, but also on the considered state. The SPP states are intermediate states for the Raman scattering process. Therefore, the dependence of the low-frequency Raman bands on the particle size is not only due to the well-known $1/R$ frequency variation of the confined vibration modes. It also reflects the change of the interaction matrix elements, i.e., absolute Raman intensities, line shapes, and frequencies.

For excitation close to the dipolar SPP resonance ($\omega_{ex} \approx \omega_{L=1}$), the intensity of Rayleigh scattering was found to be proportional to V^2 (V being the particle volume).[32] For Raman scattering, the additional interaction step between confined vibrations and SPP states must be taken into account. We found that the vibration-SPP coupling strength varies as $1/R^4$ for both DP and SO mechanisms. The Raman efficiency is thus proportional to $V^2/R^4=R^2$ as already pointed out by Duval *et al.*[9] for crystallized particles. Hence, the frequencies of the Raman bands do not coincide with the vibration frequencies calculated for the average size of the nanoparticles. This is shown in Fig. 3 for the lowest-frequency band, associated with confined quadripolar vibrations. For small size dispersion (less than 10%), the shift is one order of magnitude smaller than typical spectrometer resolution (about 2 cm^{-1}). In contrast, with 40% size dispersion, the contribution of large particles dominates, leading so to a noticeable down shift of the Raman bands.

As shown in Fig. 3, the sensitivity of the Raman scattering to size dispersion of the nanoparticles depends on the excitation energy. Indeed, for nanoparticles excited well below the dipolar SPP resonance ($\omega_{ex} < \omega_{L=1}$), the down shift

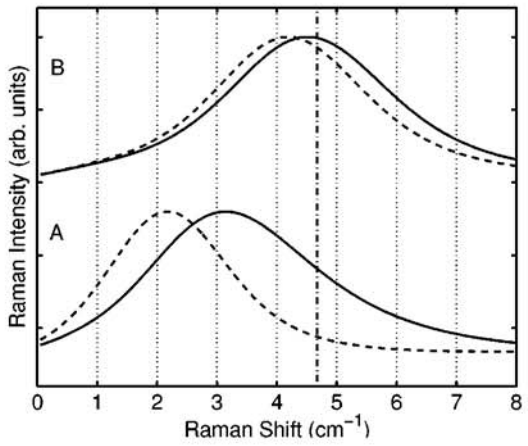

FIG. 3. Normalized Raman spectra of silver nanoparticles calculated with an average radius $R=5$ nm for excitation energy at 3 eV (bold lines) and 2 eV (dashed lines). The simulations were performed with 10% (A) and 40% (B) size dispersion and assuming a size dependent vibration lifetime. The vertical dashed-doted line corresponds to the frequency of the fundamental quadripolar mode calculated for $R=5$ nm.

of the Raman bands with size dispersion is very pronounced. A close inspection of the interaction matrix elements reveals that this very sharp dependence arises from the nature of the intermediate SPP states: for $\omega_{ex}<\omega_{L=1}$ the excited SPP states have electric fields weakly confined inside the metal particle and are therefore rather independent of the particle radius. Then, the interaction matrix elements for the photons-SPP and vibrations-SPP interactions increase as the particle volume. Hence, the Raman scattering efficiency was found to be proportional to V^6/R^4. This sharp dependence is responsible for the different shifts obtained for the resonant and nonresonant situations shown in Fig. 3. For $\omega_{ex}>\omega_{L=1}$, the situation is similar (weak confinement effect of the electric fields associated with SPP). However, the resonant contribution of interband transitions to the Raman scattering should be taken into account. In that case one has to consider electron-hole pairs as possible intermediate states of the scattering process. This is beyond the scope of the present work.

The intensities shown in Fig. 3 were normalized using appropriate scaling factors. In fact, for excitation away from the SPP resonance (at 2 eV) we found that the scattering amplitude is much weaker than that calculated for excitation close to resonance (3 eV). This is partly due to the weakening of the electric-field amplitude [in the interaction matrix elements of Eq. (3)] inside the metal particle. The out of resonance/in resonance intensity ratio depends also on the SPP damping [see Eq. (3)]. We used the plasmon damping given by Eq. (2) in our calculations.[22] Since the Landau damping is proportional to the scarred amplitude of the inner field, it is expected to be very small for nonresonant SPP states. Hence for these states only remains the contribution Γ_i extracted from the bulk material properties. We used $\Gamma_i=0.14$ eV given in Ref. 20.

Since the SO and DP coupling mechanisms have the same dependence on the particle size, one expects the same frequency shift with excitation energy of the Raman bands associated with quadripolar and pure radial vibrations. However, as shown in Fig. 2 (spectrum B), emission of pure radial vibrations is weak for excitation below the dipolar SPP resonance. This means that nonresonant SPP states contribute only little to the Raman scattering by pure radial vibrations. For this reason, we found only a small frequency shift with excitation energy for the Raman bands due to pure radial vibrations. This is in agreement with the experimental data reported by Portales *et al.*[10]

IV. CONCLUSION

We have performed calculations of the Raman scattering efficiency of silver nanoparticles excited close to resonance with the dipolar surface plasmon–polariton resonance. We assumed a three-step scattering process and studied the interaction between confined acoustic vibrations and surface plasmon–polariton states. Several coupling mechanisms were considered. Our main findings can be summarized as follows.

(i) The origin of the lower-frequency intense peak, observed in the Raman spectra of metal particles and ascribed to the fundamental mode of the confined quadripolar vibrations, has been identified: it is due to modulation of the dipolar SPP polarization by the change in the surface orientation as the nanoparticle oscillates. This mechanism involves quadripolar vibrations only. Pure radial vibrations are not active since the surface orientation is unaffected by such modes.

(ii) The higher-frequency bands recently revealed in the Raman spectra of metal particles with narrow size distribution are due to combinations of fundamental and overtones of pure radial and quadripolar vibrations. Scattering by pure radial vibrations is due to modulation of the interband susceptibility and SPP polarization vectors via deformation potential mechanism. The calculated Raman line shapes and intensity ratios are in good agreement with the experimental data published in the literature.

(iii) While in Raman scattering both SO and DP mechanisms manifest, only DP mechanism is relevant for time-resolved reflectivity. That is why only pure radial vibrations can be observed as periodic oscillations of the time-resolved reflectivity. The detailed analysis of the Raman scattering requires identification of the intermediate resonant states and their various coupling mechanisms to the vibrations. Our calculations were performed for the simplest case of spherical and isolated particles surrounded by vacuum. Nevertheless, they shed light on the origin of the low-frequency Raman scattering in metal nanoparticles. The effects of interaction between nanoparticles, nonspherical shapes, and surrounding medium should affect the frequencies, line shapes, and selection rules of the Raman bands.

[1] M. Moscovits, Rev. Mod. Phys. **57**, 783 (1985).
[2] K. Kneipp, Y. Wang, H. Kneipp, L.T. Perelman, I. Itzkan, R.R. Dasari, and M.S. Feld, Phys. Rev. Lett. **78**, 1667 (1997).
[3] H. Xu, E.J. Bjerneld, M. Kall, and L. Borjesson, Phys. Rev. Lett. **83**, 4357 (1999).
[4] K. Arya, Z.B. Su, and J.L. Birman, Phys. Rev. Lett. **54**, 1559 (1985).
[5] M.I. Stockman, V.M. Shalaev, M. Moskovits, R. Botet, and T.F. George, Phys. Rev. B **46**, 2821 (1992).
[6] D.A. Weitz, T.J. Gramila, A.Z. Genack, and J.I. Gersten, Phys. Rev. Lett. **45**, 355 (1980).
[7] A. E. H. Love, *A Treatrise on the Mathematical Theory of Elasticity* (Dover, New York, 1944).
[8] M. Fujii, T. Nagareda, S. Hayashi, and K. Yamamoto, Phys. Rev. B **44**, 6243 (1991).
[9] B. Palpant, H. Portales, L. Saviot, J. Lerme, B. Prevel, M. Pellarin, E. Duval, A. Perez, and M. Broyer, Phys. Rev. B **60**, 17 107 (1999); E. Duval, H. Portales, L. Saviot, M. Fujii, K. Sumitomo, and S. Hayashi, *ibid.* **63**, 075405 (2001).
[10] H. Portales, L. Saviot, E. Duval, M. Fujii, S. Hayashi, N. Del Fatti, and F. Vallee, J. Chem. Phys. **115**, 3444 (2001).
[11] A. Courty, I. Lisiecki, and M.P. Pileni, J. Chem. Phys. **116**, 8074 (2002).
[12] N. Del Fatti, C. Voisin, F. Chevy, F. Vallée, and C. Flytzanis, J. Chem. Phys. **110**, 11 484 (1999).
[13] J.I. Gersten, D.A. Weitz, T.J. Gramila, and A.Z. Genack, Phys. Rev. B **22**, 4562 (1980).
[14] M. Montagna and R. Dusi, Phys. Rev. B **52**, 10 080 (1995).
[15] N.N. Ovsyuk and V.N. Novikov, Phys. Rev. B **53**, 3113 (1996).
[16] K. Arya and R. Zeyher, in *Ligth Scattering in Solids IV*, edited by M. Cardona and G. Gntherodt (Springer-Verlag, Berlin, 1984).
[17] F. Hache, D. Richard, and C. Flytzanis, J. Opt. Soc. Am. B **3**, 1647 (1986).
[18] J. Lindhard, K. Dan. Vidensk. Selsk. Mat.-Fys. Medd. **28**, 8 (1954).
[19] H. Hovel, S. Fritz, A. Hilger, U. Kreibig, and M. Vollmer, Phys. Rev. B **48**, 18 178 (1993).
[20] P.B. Johnson and R.W. Christy, Phys. Rev. B **6**, 4370 (1972).
[21] G. Mie, Ann. Phys. (Leipzig) **25**, 377 (1908).
[22] R.A. Molina, D. Weinmann, and R.A. Jalabert, Phys. Rev. B **65**, 155427 (2002).
[23] P.Y. Yu and M. Cardona, *Fundamentals of Semiconductors* (Springer-Verlag, Berlin, 1999).
[24] The electromagnetic field amplitude associated with the resonant SPP states ω_L is proportional to the Bessel function $\eta_L(k_{ex,L}R)$ where $k_{ex,L}$ is the wave vector outside the nanoparticle, i.e., to $(\lambda_{ex,L}/R)^L$ for nanometer-sized particles ($\lambda_{ex,L} \gg R$).
[25] E. Duval, Phys. Rev. B **46**, 5795 (1992).
[26] J. Bardeen and W. Shockley, Phys. Rev. **80**, 72 (1950).
[27] N. Del Fatti, C. Voisin, M. Achermann, S. Tzortzakis, D. Christofilos, and F. Vallee, Phys. Rev. B **61**, 16 956 (2000).
[28] H. Tups, A. Otto, and K. Syassen, Phys. Rev. B **29**, 5458 (1984).
[29] For excitation of the resonant SPP states, the Raman intensity ratio between the quadripolar and the radial vibrational modes is proportional to $(k_{in,L}R)$ (Ref. 4), where $k_{in,L}$ is the wave vector inside the nanoparticle. Then, for $k_{in,L}R \ll 1$, the contribution of the quadripolar vibrational modes ($l=2$) to the Raman scattering is very weak.
[30] This is the only place where the effect of the surrounding medium was taken into account.
[31] C. Voisin, Ph.D. thesis, Paris XI Orsay University, 2001.
[32] A.J. Cox, A.J. DeWeerd, and J. Linden, Am. J. Phys. **70**, 620 (2002).

Time- and space-resolved dynamics of melting, ablation, and solidification phenomena induced by femtosecond laser pulses in germanium

Jörn Bonse,* Guillaume Bachelier,† Jan Siegel, and Javier Solis‡
Laser Processing Group, Instituto de Optica, C.S.I.C., Serrano 121, E-28006 Madrid, Spain
(Received 17 February 2006; revised manuscript received 30 May 2006; published 6 October 2006)

Femtosecond time-resolved microscopy has been used to analyze the structural transformation dynamics (melting, ablation, and solidification phenomena) induced by intense 130 fs laser pulses in single-crystalline (100)-germanium wafers on a time scale from ~100 fs up to 10 ns. Complementary information on longer time scales (350 ps–1.4 μs) has been obtained by means of simultaneous streak camera and photodiode measurements of the sample surface reflectivity. In the ablative regime, transient surface reflectivity patterns are observed by fs microscopy on a ps to ns time scale as a consequence of the complex spatial density structure of the ablating material. Complementing point-probing streak camera measurements allow one to characterize the temporal evolution in real time up to 40 ns after the fs-laser pulse excitation. Fs microscopy reveals additional reflectivity patterns for fluences below the ablation threshold of the germanium. It is shown that these patterns are originating from the selective removal of the native oxide layer at the wafer surface within a certain fluence range. After solidification, and in contrast to other semiconductors, surface amorphization has not been observed in (100)-germanium upon femtosecond laser pulse irradiation in the studied fluence range.

DOI: 10.1103/PhysRevB.74.134106 PACS number(s): 79.20.Ds, 78.47.+p, 64.70.−p

I. INTRODUCTION

Germanium (Ge) is a group IV semiconductor with a high carrier mobility that has been widely used in solid-state electronics. Due to its small bandgap energy, Ge can be optically excited with infrared and near infrared radiation which makes it useful for detection and modulation applications.[1] Indirect interband transitions between the valence and the conduction band require a minimum photon energy of 0.66 eV, whereas at least 0.80 eV are needed for a direct transition.[2]

Several studies have been devoted to the interaction of laser radiation with this semiconductor for laser energy densities (fluences) below the damage threshold.[3–5] Close to and above this threshold there have been a number of studies investigating the dynamics of phase transitions such as melting, ablation, or rapid resolidification phenomena in the picosecond to microsecond temporal scale.[4,6–10] Up to now, very few studies are available regarding the dynamics of ultrafast phase transitions in germanium induced by femtosecond laser pulses.[11–13]

In this paper we report a detailed study of the melting, ablation, and resolidification dynamics of single-crystalline germanium (c-Ge) under femtosecond laser pulse irradiation using time- and space-resolved reflectivity measurements. Femtosecond time-resolved microscopy has already been used in investigations of laser-induced phase transitions in other semiconductors such as carbon (C),[14] silicon (Si),[15,16] or the III-V compound material gallium arsenide (GaAs).[13,17,18] In this *pump and probe technique* each laser exposure provides a single data point on a time axis. By means of performing multiple measurements the time evolution of the signal can be reconstructed. Due to practical limitations in the use of optical delay lines, this technique has been typically used for delays up to a few nanoseconds, whereas typical solidification processes (crystallization/amorphization) can occur on much longer time scales. In contrast to the pump and probe approach which is usually referred to as a time-resolved technique, so-called *real-time measurements* can provide the complete time evolution of the signal at a single sample location using a single laser pulse exposure.[19] As a consequence, this approach is very robust to sample inhomogeneities and laser pulse fluctuations. The detectors used are either fast photodiodes or streak cameras, depending on the desired time window and temporal resolution.

Our study, combining both approaches and covering a time span from ~100 fs up to a few μs, provides detailed insights into the dynamics of melting and ablation as well as the subsequent resolidification phenomena, using both a fs-time-resolved microscopy and complementary real-time streak camera and photodiode measurements. Taking benefit from the imaging capabilities of our setup, a phenomenon of transient surface wave patterns due to the selective removal of the native oxide layer is reported for the melting regime of femtosecond laser pulse irradiated germanium when a certain fluence threshold is exceeded.

II. EXPERIMENTAL METHODS

The data reported here were obtained on polished (100) crystalline Ge wafers (p-doped, 0.02 Ω cm). Before irradiation, successive ultrasonic bath cleaning in different organic solvents (trichloroethylene, acetone, and ethanol) was performed. No attempt was made to remove the native oxide layer of 3 ± 0.3 nm thickness (determined by variable angle spectral ellipsometry).

The laser used for irradiation was a chirped pulse regenerative amplification Ti:sapphire laser system (Spectra Physics, Spitfire) providing linearly polarized pulses of ~130 fs duration at a center wavelength of 800 nm. Since at this wavelength the photon energy of 1.55 eV is sufficient to in-

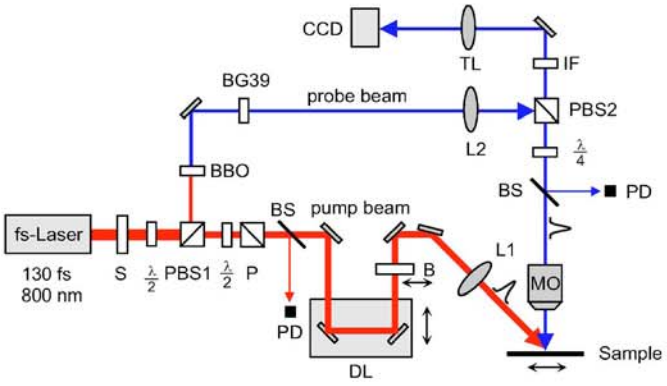

FIG. 1. (Color online) Scheme of the experimental fs-TRM setup. Abbreviations: B—beam stop; BBO—nonlinear crystal; BG39—bandpass filter; BS—beam splitter; CCD—camera; DL—delay line; IF—interference filter; $\frac{\lambda}{2}$—halfwave-plate; $\frac{\lambda}{4}$—quarterwave-plate; L—lens; MO—microscope objective; P—Glan laser polarizer; PBS—polarizing beam splitter; PD—photodiode; S—electromechanical shutter; TL—tube lens.

duce a direct band transition, this mechanism is expected to be dominant in the vicinity of the Γ point of the band structure. The resulting optical penetration depth $1/\alpha$ at low intensities is approximately 200 nm (Ref. 20). The irradiation of the sample was performed in air at atmospheric pressure. Each surface region was irradiated only once in order to induce structural modifications.

A. Fs-time-resolved microscopy (fs-TRM)

The temporal evolution of the surface reflectivity upon irradiation of the sample was measured using a *fs-time-resolved microscopy* (fs-TRM) setup that provides the capability of imaging the laser-excited surface for variable time delays (up to 10 ns) between the surface exciting pump and the illuminating probe pulses.

The fs-TRM experiment was based on a noncollinear geometry[16] with different wavelengths for the pump (800 nm) and probe (400 nm) pulses (see Fig. 1). An electromechanical shutter (S) allowed a single laser pulse to be selected from a continuous pulse-train (100 Hz pulse repetition rate) provided by the regenerative amplifier system. The selected laser pulse was then divided into pump and probe pulses using a combination of a halfwave-plate $(\frac{\lambda}{2})$ and a polarizing beam splitter cube (PBS1) for adjusting the energy ratio between them.

Another combination of a halfwave-plate $(\frac{\lambda}{2})$ and a Glan laser polarizer (P) was used in the pump beam for variable energy attenuation. After passing through an optical delay line (DL), the pump pulse was focused by a lens (L1) at an angle of incidence of 54° onto the sample surface, being *s* polarized with respect to the plane of incidence. At the surface, the elliptical Gaussian spot showed a diameter ($1/e^2$ decrease) of $2w_{0,x} \sim 100$ μ and $2w_{0,y} \sim 60$ μm along its long and short axis, respectively.

The low intensity probe beam (previously split off from the PBS1), was frequency doubled by means of a nonlinear crystal (BBO). The residual 800 nm radiation was eliminated by an IR-cutting bandpass filter (Schott, BG39). The probe beam was then focused by a lens (L2) to the back-focal plane of a long-working distance microscope objective (MO: Mitutoyo, M-Plan-NIR, 20×, NA=0.4) after reflection in a polarizing beam splitter cube (PBS2). A quarterwave-plate $(\frac{\lambda}{4})$ was used to convert the linear polarization state into a circular one. The MO finally recollimates this beam such that it can be used for normal incidence illumination of the sample area which is excited by the 800 nm pump beam.

The probing 400 nm radiation reflected at the sample surface was then reconverted to a linear polarization state of orthogonal orientation by passing a second time through the same $\frac{\lambda}{4}$ plate. The probe beam, capable thus to pass through PBS2, was used directly to image the laser-excited surface region by means of the MO and an additional tube lens (TL, $f=200$ mm) onto a CCD-camera (PCO, Pixelfly HiRes, image acquisition time 100 μs), which was computer controlled and synchronized with the laser system. In order to separate the imaging radiation from scattered light of the pump beam or light originating from optical plasma emissions during the ablation process, a narrow band interference filter (IF) with a center wavelength of 400 nm and a bandwidth of 10 nm was additionally placed in the imaging path.

The reflectivity measurements were performed with a probe beam fluence well below the melting threshold, whereas the fluence in the pump beam was sufficient to induce phase transitions such as melting or ablation. The pump pulse energies were measured by means of a photodiode (PD) calibrated against a pyroelectric detector at the sample site.

At each sample position, two measurements had been used to determine the laser-induced reflectivity change at the chosen delay time τ. The first measurement [with the pump pulse blocked by the beam stop (B)] was used to obtain a reflectivity image $R_0(x,y)$ of the sample surface at the measurement position before exposure of the pump pulse, whereas the second allowed the recording of the surface reflectivity image $R(\tau,x,y)$ upon pump pulse excitation. The normalized reflectivity change $\frac{\Delta R}{R}(\tau,x,y)=\frac{R(\tau,x,y)-R_0(x,y)}{R_0(x,y)}$ has then been calculated by subtracting both images and by normalizing by the reflectivity in the undisturbed surface. In this way, the image normalization procedure allows one to take into consideration the spatial profile of the illumination probe beam as well as variations in the surface reflectivity due to contaminants, small surface imperfections, etc.

Apart from the two images of the nonirradiated surface and the transient image at the chosen delay time, an additional image has been acquired at the same sample site several seconds after the irradiation with the pump pulse in order to reveal the permanent surface modifications. In the following, those final images are indicated by the symbol "∞".

The estimated uncertainty in $\Delta R/R$ at this probing wavelength is ~0.05. The temporal resolution of the fs-TRM setup has been determined to be approximately 400 fs.

B. Real-time reflectivity measurements (RTR)

In order to analyze the surface reflectivity changes over longer time scales from the ps- to the μs-range, a comple-

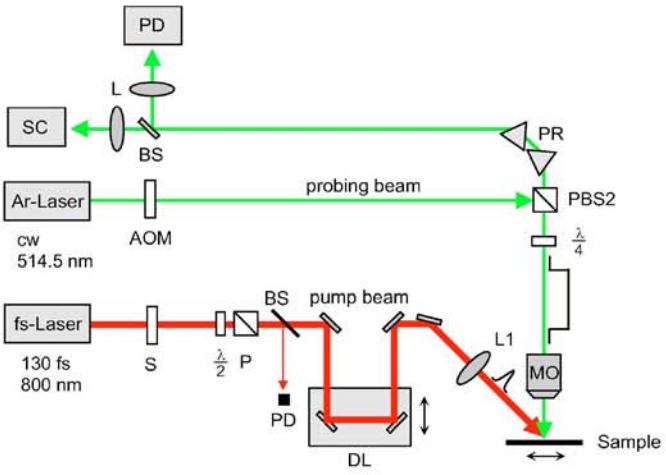

FIG. 2. (Color online) Scheme of the experimental RTR setup. Abbreviations: AOM—acousto-optical modulator; BS—beam splitter; DL—delay line; $\frac{\lambda}{2}$—halfwave-plate; $\frac{\lambda}{4}$—quarterwave-plate; L—lens; MO—microscope objective; P—Glan laser polarizer; PBS—polarizing beam splitter; PD—photodiode; PR—prism pair; S—electromechanical shutter; SC—streak camera.

mentary approach has been used (Fig. 2). It is essentially based on the fs-TRM setup and can be used with small modifications to perform *real-time reflectivity measurements* (RTR) by means of a streak camera (Hamamatsu Model C5680, equipped with a single-sweep unit Model M5676; time resolution of 350 ps in a time window 50 ns) and a fast photodiode coupled to an oscilloscope (time resolution of a few ns).

In that approach, the 400 nm fs-probe beam was substituted by a continuous wave (cw), single mode and single-frequency probing Ar^+-laser beam (514.5 nm), modulated by means of an acousto-optical modulator (AOM) to produce a single rectangular pulse of 2 μs duration. This probe pulse was synchronized with the fs-laser pulse. In order to perform a point-probing measurement in the center of the fs-pumped area, the lens (L2) in the probe beam path, focusing to the back-focal plane of the MO, was removed generating a focused Gaussian beam with a diameter of $2w_0 \sim 0.9$ μm at the sample surface. Hence, a pump-to-probe spot size ratio of ~ 110 was used experimentally. The back-reflected probing signal was recollimated by the MO and analyzed simultaneously by means of the streak camera (SC) and the photodiode (PD). For that purpose, a spectral separation of the monochromatic probing Ar^+ laser beam and other radiation contributions, such as light of the fs-pump beam scattered from the surface upon irradiation or possible subsequent optical plasma emissions, was performed using a prism pair (PR) just after PBS2. As in the case of fs-TRM, the normalized surface reflectivity change $\Delta R/R$ has been calculated using the reflectivity value of the undisturbed surface. The uncertainty in $\Delta R/R$ are ~ 0.04 and ~ 0.03 for the streak camera and the photodiode measurements, respectively. Additional details regarding the temporal characteristics of the probing laser beam and the photodetection systems (PD, SC) can be found in Ref. 19.

III. RESULTS AND DISCUSSION

A. Fs-laser-induced ablation

1. fs-TRM

A series of fs-TRM images obtained on a germanium surface is shown in Fig. 3 for an excitation peak fluence in the ablative regime ($\Phi_0 = 3.10 \pm 0.08$ J/cm^2), well above the ab-

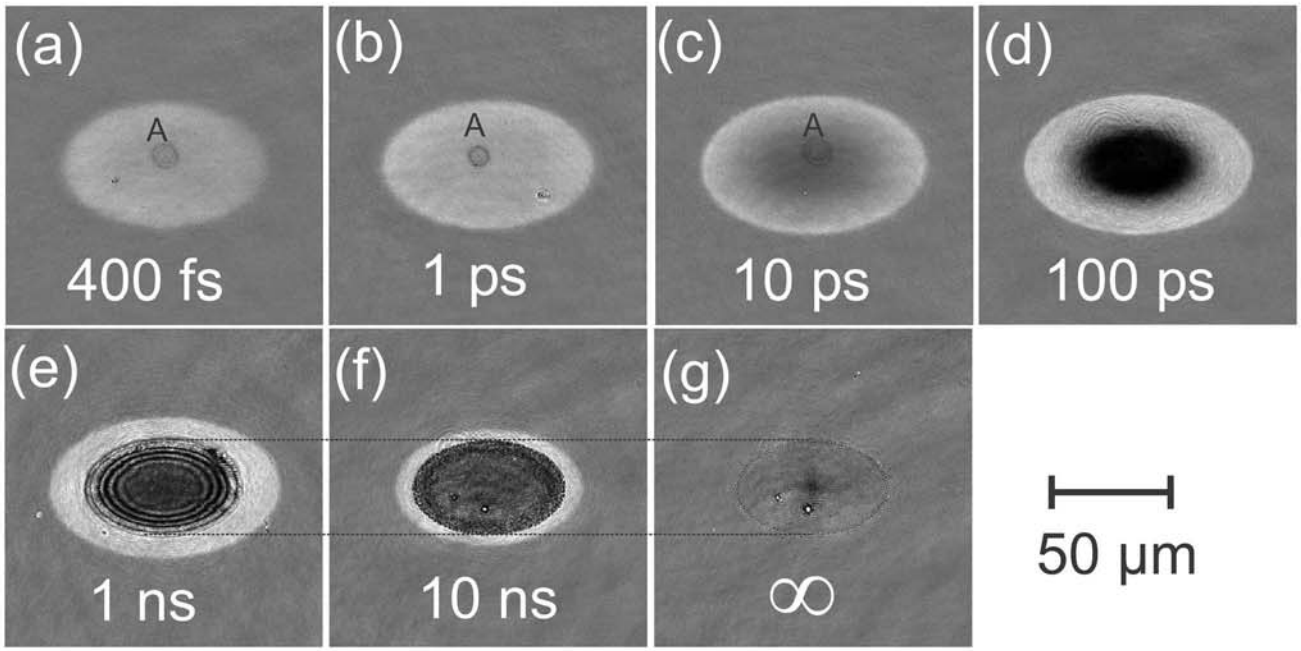

FIG. 3. Images of a germanium surface at different times after the exposure to the pump pulse (pump fluence 3.10 ± 0.08 J/cm^2, ablative regime). A denotes an imaging artifact which is not related to a modification of the sample surface. The image sequence is encoded in a linear gray scale with an optimized contrast.

lation threshold fluence (Φ_{abl}=1.32 J/cm^2). The series covers the entire period from shortly after the end of laser energy deposition up to the appearance of the final surface structure. The number in each frame indicates the delay time between the pump and the probe pulse. Because of the large angle of 54° between the pump beam and the imaging probe beam, the laser excited area has an elliptical shape. Note that the small dark feature (indicated by "A") in Figs. 3(a)–3(c) is an imaging artifact, arising from an optical reflection in the setup in conjunction with the image normalization procedure. It is not related to any transient physical process at the sample surface.

At early times, immediately after the arrival of the pump pulse to the surface (400 fs delay), an increase of the surface reflectivity in the center of the irradiated spot can be seen [Fig. 3(a)]. This is due to the strong electronic excitation resulting in the formation of an electron-hole plasma, which can destabilize the lattice structure on a subpicosecond time scale when a critical electron density between 10^{21} and 10^{22} cm^{-3} in the conduction band is exceeded.[21] This ultrafast phase transition is usually referred to as *nonthermal melting* and has already been reported in germanium[11,12] and also in other semiconductors.[17,22–24]

Already after 1 ps, the reflectivity of the entire irradiated region has increased to almost the same reflectivity value as for the center of the image for 400 fs delay time, giving rise to the appearance of a bright elliptical area with a sharp defined edge [Fig. 3(b)]. It is associated with the formation of an optically thick layer of liquid metallic germanium (ℓ-Ge) on the surface. Note that the optical penetration depth of the 400 nm probe radiation in ℓ-Ge is only 7–8 nm.[25]

On a time scale of tens of picoseconds, the reflectivity of almost the entire spot is lowered [Fig. 3(c)], which might arise from the optical properties of a superheated liquid.[17,26]

After some tens to hundreds of picoseconds, an even darker appearing zone of strongly decreased reflectivity can be seen in the central region of the spot [Fig. 3(d), 100 ps delay]. It is indicative of the onset of ablation. At later times a characteristic pattern of rings develops from this dark central feature [Fig. 3(e), 1 ns delay]. Additional images taken for delay times between 100 ps and 1 ns (not shown here) reveal that these fringes are moving from the center towards the outer regions of the spot for increasing delays while increasing their number and decreasing their radial spacings. The nature of these rings has been already associated with an optical interference effect (dynamically moving Newton fringes).[16,27] The corresponding interference fringes are visible during the formation and spatial movement of a complex material density profile as a consequence of the formation of a so-called *rarefaction wave* (and its subsequent reflection, when material is passing through the liquid-gas coexistence regime[28]) after fs irradiation of semiconductors and metals. The resulting density profile consists, at the air side of the expanding material, of a thin ablating layer with nearly solid state material density and a thickness smaller than the optical penetration depth in this optically excited ablating layer.[28,29] The partial reflections at this dynamically moving layer and the reflection at the remaining surface underneath then allows interference effects to occur transiently.

After 10 ns delay, fringes cannot be observed anymore in the fs-TRM images [Fig. 3(f)]. Their disappearance can arise, for instance, from the gradual flattening of the initially sharp density profile of the ablating layer.[13] Another possible reason for this behavior is that the distance of the interface of the expanding ablated material to the surface has reached a value larger than half the coherence length of the fs-probe beam radiation (≈15–20 μm), thus making interference impossible. The RTR streak camera measurements presented in Sec. III A 2 will provide more detailed insights into the ablation dynamics on the ns time scale and will give additional clues regarding the origin of the disappearance of the fringes.

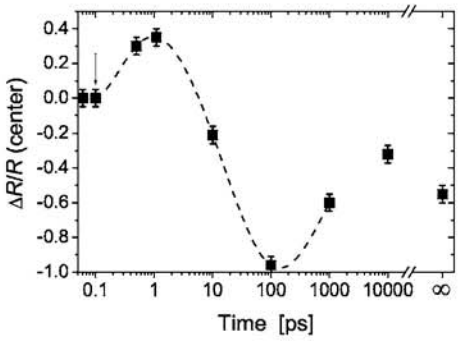

FIG. 4. Normalized surface reflectivity change $\Delta R/R$ as a function of time as measured in center of the irradiated regions shown in Fig. 3. Note the logarithmic time axis. The true zero delay is marked by an arrow. The final reflectivity change ($\Delta t=\infty$) is marked on the right-hand horizontal axis. The line is to guide the eye.

Instead of the fringes, an irregularly shaded central region of reduced reflectivity can be seen then which is surrounded by an annulus of high reflectivity [Fig. 3(f)]. The latter indicates that the material is still molten in that area. Note that the outer diameter of the molten ring has already reduced its size when compared to earlier times [Figs. 3(b)–3(e)]. This indicates that the resolidification, which has started from the outer and deeper lying regions of the melt pool, becomes visible at the surface already after some nanoseconds. The outer edge of the dark central region coincides with the borders of a crater observable in the final surface morphology, as indicated by two horizontal lines [Fig. 3(g)]. However, the reduced reflectivity in the center of Fig. 3(f) when compared to the final image (g) clearly evidences that after 10 ns the probe beam radiation is still interacting with ablating material.

To quantitatively follow the time evolution of the reflectivity, we have plotted in Fig. 4 the normalized surface reflectivity change $\Delta R/R$ as a function of the delay time, as evaluated in the center of the spots shown in Fig. 3. This representation is the equivalent to a point-probing conventional fs-pump-probe experiment and provides complementary information to RTR measurements but on much shorter time scales.

All discussed stages of nonthermal melting, ablation, and a partial recovery of the reflectivity can be seen in Fig. 4. The initial reflectivity increase on the subpicosecond to picosecond scale reaches values of $\Delta R/R \sim 0.35$. The onset of ablation after tens of ps then reduces the normalized reflectivity change to values approaching −1.0 after 100 ps, which means that the probe beam radiation is completely absorbed in the excited surface region. After 1 nanosecond, a partial

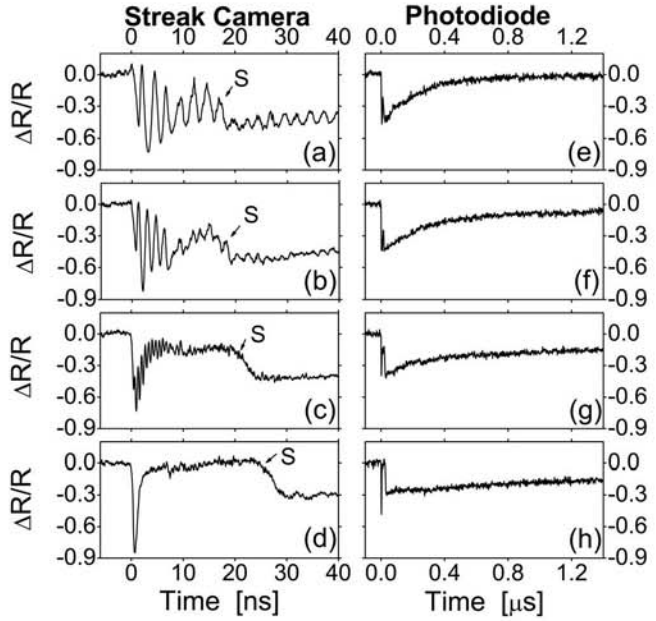

FIG. 5. Normalized surface reflectivity change as a function of time as measured with streak camera (a)–(d) and with a photodiode (e)–(h) at four different fluence levels [(a)+(e): 1.35 J/cm^2, (b)+(f): 1.53 J/cm^2, (c)+(g): 1.68 J/cm^2, (d)+(h): 2.67 J/cm^2].

reflectivity recovery is seen, finally leading to a permanent normalized reflectivity change of −0.55. Note that the complete reflectivity dynamics especially on time scales longer than 1 ns is not resolved in our fs-TRM experiments here, which underlines the benefit of complementary point-probing RTR measurements covering those longer time scales.

2. Ps- and ns-RTR

The ablation process has been studied on longer time scales (ns-μs) using the RTR setup. Figure 5 shows the temporal evolution of the normalized surface reflectivity change as probed simultaneously by the streak camera [(a)–(d)] and the photodiode [(e)–(h)] in the center of the irradiated region upon irradiation at four different pump peak fluence levels up to two times the ablation threshold fluence. At a fluence $\Phi_0 = 1.35$ J/cm^2, slightly above the ablation threshold [Fig. 5(a)], the normalized reflectivity change shows rapid oscillations that last for more than 40 nanoseconds. They are associated with the outward moving dense shell of ablated material, which has already been observed in the fs-TRM (Fig. 3). This is a direct observation of the outward moving dense shell of ablating material for time scales up to 40 nanoseconds as well as in real time for a single laser pulse.

As seen in Figs. 5(a)–5(c), the period of the reflectivity oscillation Δt strongly depends on the laser fluence. For a fluence level of 1.35 J/cm^2 [Fig. 5(a)] an average oscillation period of 2.6 ns is found, whereas at a higher level of 1.68 J/cm^2 it lasts only 0.7 ns [Fig. 5(c)]. The shortest oscillation period of 0.5 ns was observed at 2.08 J/cm^2 (data not shown here). These quantitatively measured values for Δt provide a way for the estimation of the speed of the outward moving dense shell of material.[49] For that we assume that it consists of a layer with constant density and thickness which initially propagates away from the remaining surface at constant velocity $v = \Delta x/\Delta t$,[30] thus leaving behind a gas-filled or bubblelike space with a real part of the refractive index close to 1 (conditions already used and discussed in more detail in Refs. 18 and 28). The assumption of a constant velocity is justified by the experimental results shown in Fig. 5: The period of the reflectivity oscillations is constant [e.g., in Fig. 5(a)], indicating that the speed of the shell of ablating material is constant at least during the first tens of nanoseconds. Then, for adjacent temporal reflectivity maxima or minima, an interference condition $2 \times \mathrm{Re}(n) \times \Delta x = 1 \times \lambda$ should hold for the probing wavelength $\lambda = 514.5$ nm. Hence, the average velocity can be calculated via $v = \lambda/[2\,\mathrm{Re}(n) \times \Delta t] \approx \lambda/(2\Delta t)$. This simple relation provides values between 100 m/s (1.35 J/cm^2) and 515 m/s (2.08 J/cm^2).

In contrast to the fs-TRM measurements, a continuous wave argon laser is used here to probe the reflectivity dynamics of the surface. Hence, the coherence length of the laser beam plays no role in the disappearance of the fringes, as it may in the case of fs microscopy. The RTR technique allows one then to evaluate the "lifetime" of the ablating layer, i.e., the time during which the density profile is sufficiently sharp in the propagation direction and homogeneous in the perpendicular direction to allow interference effects to be observed. As shown in Figs. 5(a)–5(d), this lifetime strongly decreases with increasing fluences from more than 40 ns for 1.35 J/cm^2 down to 5 ns for 2.08 J/cm^2 (data not shown here). For fluence levels exceeding 2.67 J/cm^2 [Fig. 5(d)] the oscillations are not visible anymore. This can be explained by the temporal period of the reflectivity oscillations which becomes at high fluences too small to be resolved by the streak camera (350 ps time resolution under the present conditions).

The RTR measurements finally allow one to determine the distance covered by the ablated layer before the oscillations disappear in the streak camera transients. If m is the number of oscillations observed experimentally, this distance is simply given by $d = m \times \lambda/[2\,\mathrm{Re}(n)] \approx m \times \lambda/2$. This distance decreases for increasing fluences, ranging from more than 4 μm for 1.35 J/cm^2 to $\sim$2 μm for 2.08 J/cm^2 [Fig. 5(a): $m > 16$ (1.35 J/cm^2), Fig. 5(b): $m < 16$ (1.53 J/cm^2), Fig. 5(c): $m < 13$ (1.68 J/cm^2), not shown: $m < 9$ (2.08 J/cm^2)]. In all cases, $2 \times d$ is smaller than the coherence length of the laser pulses used in the fs-TRM measurements (30–40 μm). Assuming that the observed monotonous decrease of d with laser fluence continues for higher fluences, d should be even smaller in the measurements reported in Fig. 3 for a peak fluence level of 3.10 J/cm^2. The disappearance of the spatial fringes in fs-TRM for high fluences and long delays [10 ns, Fig. 3(f)] can thus be attributed to the modification of the density profile of the ablating layer only (decreasing sharpness of the interfaces, as first proposed in Ref. 13) rather than to the short coherence length of the fs probe pulse.

Along with the shortening of the oscillation period and duration, also the movement of a shoulder (marked with an "S" in streak camera transients) towards longer times can be observed in the entire series [Figs. 5(a)–5(d)]. This shoulder

arises from the solidification of the liquid layer left on the surface underneath the ablating materials having a higher reflectivity than the solid (see also Sec. III B 2): Since the ablating layer leading to the interference effects is not optically thick, the reflectivity dynamics of the molten layer underneath will contribute to the reflectivity signal. Once this layer undergoes solidification (after some tens of ns) the reflectivity drops significantly which leads to the appearance of the shoulder S (compare to the results presented in Fig. 11). Hence, in this regime of fluences slightly above the ablation threshold, the streak camera is capable of monitoring both the interference effects due to ablating material as well as the solidification dynamics of the material underneath.

The corresponding surface reflectivity transients as measured simultaneously with the photodiode for times up to 1.4 μs after the arrival of the pump pulse are shown in Figs. 5(e)–5(h). The rapid reflectivity oscillations as seen in the streak camera transients are not resolved by the photodiode detection system. All transients show a similar behavior and are dominated by an initial drop of the reflectivity followed by slow recovery of the reflectivity on the time scale of a few microseconds. This reflectivity recovery cannot solely be associated with the change of the optical properties of the hot germanium after the resolidification upon cooling down to room temperature, since in *c*-Ge and for our conditions such a process would lead to a reflectivity drop of less than 10%.[9] Hence, we rather relate it to the shielding of the probe beam due to thermally induced ablation products arising from thermal evaporation, or the formation of clusters and large particles, which all would absorb and scatter the probe beam radiation. Along with the amplitude of the drop in the reflectivity, this scenario is supported by the characteristic time scale in the nanosecond to microsecond range which has been also observed for the fs-laser pulse ablation of metals.[31] Note that the final reflectivity change at the end of the measurement interval (after 1.4 μs) is gradually decreasing from ≈ 0 to ≈ -0.15, even if a steady state reflectivity value might not have been reached at the highest fluences. This gradual decrease is consistent with the formation of a crater in the surface (always observed in the images of the permanent surface modification), which decreases the reflectivity due to its surface roughness and increasing depth.

B. Fs-laser-induced melting and resolidification

1. fs-TRM

The evolution of the surface reflectivity has been studied by means of fs-TRM also in the fluence regime between the melting and the ablation thresholds. Figure 6 shows an image sequence for four different peak fluences at a fixed delay of 1 ns. As can be seen, no reflectivity decrease develops in the bright center of the irradiated region [compare to Fig. 3(e)]. None of the images shows features being consistent with the ablation of Ge in the corresponding fluence interval, suggesting that no ablation of germanium occurs here. Also the final state of the surface does not indicate the formation of an ablation crater on the surface (images not shown).

Surprisingly, one can clearly observe a similar pattern of fringes (like in the regime of ablation) once a certain fluence threshold (~ 0.55 J/cm^2) is exceeded [compare Fig. 6(a) and Figs. 6(b)–6(d)]. These fringes are spatially confined to a central area of the spots which is smaller than the entire molten region for all delay times studied.

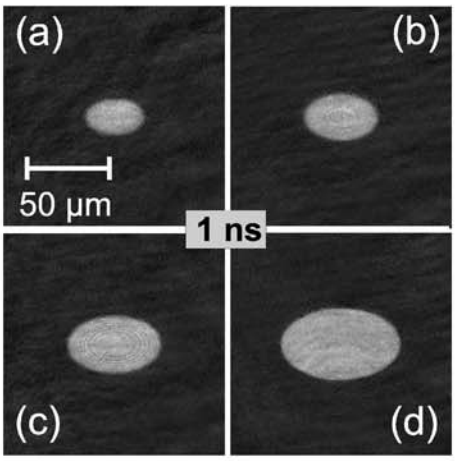

FIG. 6. Images of a germanium surface at 1 ns delay after the exposure to pump pulse of four different fluences in the melting regime (a): 0.51, (b): 0.59, (c): 0.75, and (d): 1.12 J/cm^2 below the ablation threshold (1.32 J/cm^2). The image sequence is encoded in a linear gray scale with an optimized contrast.

In Fig. 7, a direct comparison of representative horizontal reflectivity change profiles is shown. The oscillations in the melting regime show a much smaller degree of reflectivity modulation [$\Delta R/R_{fr}$(melting) $\in [0.50 \cdots 0.85]$, see Fig. 7(a)] than the previously described fringes in the ablative regime of germanium [$\Delta R/R_{fr}$(ablation) $\in [-1.0 \cdots 1.0]$, see Fig. 7(b)]. This underlines that different processes have to be involved in their formation.

Figure 8 shows a more detailed analysis of the temporal and the spatial reflectivity dynamics in laser-induced melt spots as induced by laser pulses with pump peak fluences of 0.83 ± 0.03 J/cm^2.

For early times (400 fs delay), a small bright central area without sharp boundary can be seen in Fig. 8(a). Its size increases until the following 10 ps [Figs. 8(b), 1 ps and 8(c), 10 ps] until a bright spot of ≈ 60 μm horizontal diameter with sharp boundaries can be seen after 100 ps [Fig. 8(d)],

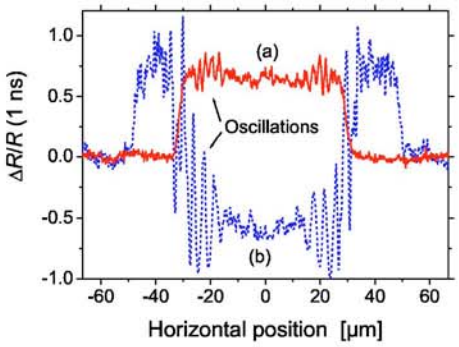

FIG. 7. (Color online) Horizontal profiles of $\Delta R/R$ after 1 ns delay for two different laser fluence values of (a) 0.83 J/cm^2 [melting, compare Fig. 8(f)] and (b) 3.10 J/cm^2 [ablation, compare Fig. 3(e)].

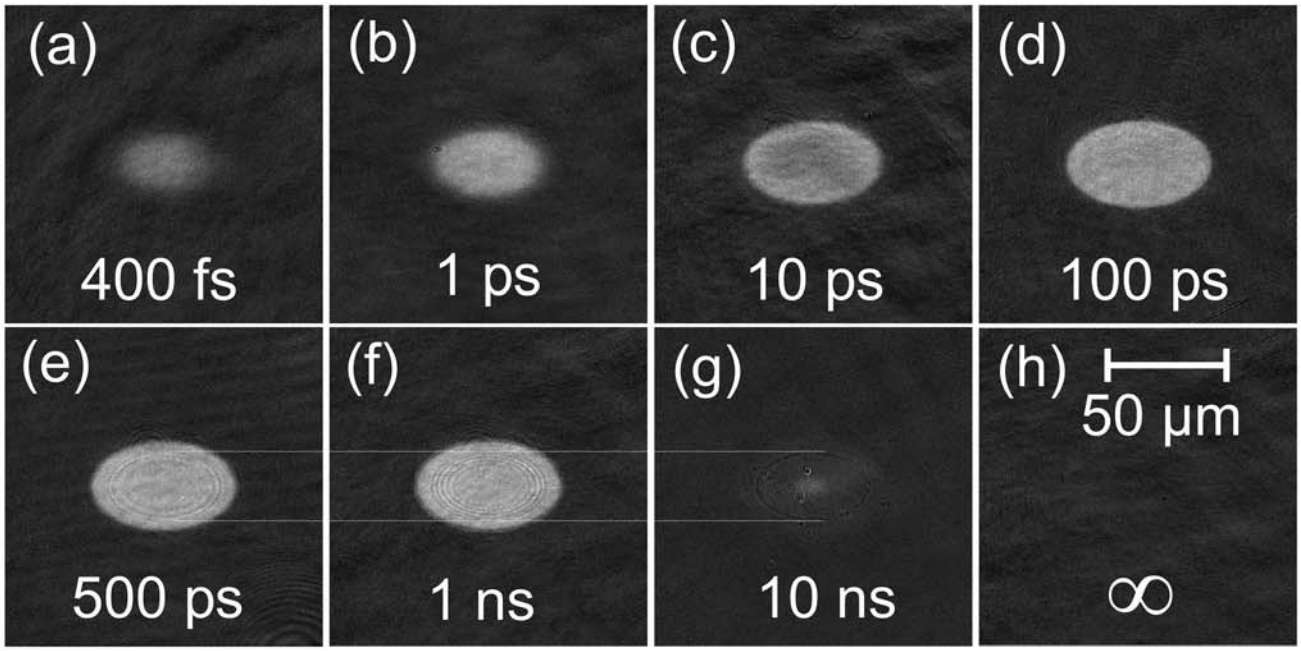

FIG. 8. Images of a germanium surface at different times after the exposure to the pump pulse (pump fluence 0.83 ± 0.03 J/cm^2, melting regime). The image sequence is encoded in a linear gray scale with an optimized contrast.

indicating the formation of a surface layer of molten germanium.

An additional fringe pattern then starts to develop at the surface of the melt pool. As in the case of the fringe pattern observed in the ablative regime, the melt fringes are formed in the center of the spot after ≈200 ps before moving toward the outer edge of the melt pool during the following nanosecond [Figs. 8(e) and 8(f)]. After 10 ns, the surface is nearly completely resolidified and only a very small pool of molten material can be seen in the center [Fig. 8(g)]. Additionally, there is a single fine dark elliptical contour line visible which circumvents the region where the melt fringes have been observed at earlier times. Note that the latter phenomenon is of transient nature only and is not visible anymore in the image of the permanent surface modification [Fig. 8(h)].

Interestingly, the surface reflectivity of the already solidified area is still slightly increased [see Fig. 8(g), $\Delta R/R \sim 0.02-0.05$]. This increase can be attributed to the change of the optical properties of hot crystalline germanium since at the probe wavelength of 400 nm, the surface reflectivity of c-Ge increases by a few percent for rising temperatures close to the melting temperatures [e.g., $\Delta R/R(c\text{-Ge}, 400\ \text{nm}, 1125\ \text{K}) \sim 0.02-0.03$].[32]

In order to reveal the physical origin of the transient fringes in the melt regime, the phase velocity $v_p = \omega/k = \sqrt{\frac{\sigma k}{\rho_l}} \tanh(hk)$ and the group velocity $v_g := d\omega/dk$ of a surface capillary wave[33] have been estimated for a melt pool thickness of $h = 350$ nm.[50] Taking the thermophysical constants of liquid germanium (liquid mass density $\rho_l = 5.5 \times 10^3$ kg/m^3, surface tension $\sigma = 600 \times 10^3$ N/m)[34] and an experimentally observed fringe spacing of $\Lambda = 2\pi/k = 2.42$ μm, values of $v_p = 14.3$ m/s and $v_g = 25.8$ m/s are found.[51] Both values are by three orders of magnitude smaller than the speed of the fringes moving outwards to the edge of the spot (25 km/s).[52]

The striking similarity in the temporal development (100 ps–few ns) and in the spatial period of the fringes (few micrometers) suggests that the low-contrast fringes in the melting regime are generated by the selective ablation of the native oxide layer which is covering the Ge sample surface. This effect of surface oxide removal upon fs-laser pulse irradiation at fluence levels between the melting and the ablation threshold has already been observed for silicon in *ex situ* optical and atomic force microscopic studies,[35] whereas here we provide direct evidence for such a process by an optical *in situ* technique. A selective oxide removal has also been reported for ns-laser pulse irradiation of germanium wafers with fluences below their ablation threshold at 193 nm wavelength where the oxide is slightly absorbent.[8] Furthermore, the hypothesis of oxide removal is fully consistent with our experimental observations, i.e., (i) the existence of a threshold behavior for the appearance of the fringes, (ii) the spatial confinement of the fringes to a region smaller than the extent of melting, and (iii) the thermophysical properties of Ge and the covering oxide layer. We will discuss these issues in more details in the following:

Ad (i) and (ii): For a fixed delay of 1 ns, we have analyzed the outer horizontal diameters of the molten region as well as those of the fringe pattern as a function of the peak laser fluence Φ_0 (Fig. 9). In both cases, a functional dependence of $D^2 = 2w_0^2 \ln(\Phi_0/\Phi_{th})$ is found ($w_0 = 50$ μm: Gaussian $1/e^2$-beam radius). This dependence is exactly the one predicted for any threshold (Φ_{th}) dependent process induced by a spatially Gaussian pulse. Moreover, back-extrapolating $D^2 \to 0$ allows a quantitative determination of both thresholds. A value of $\Phi_{th,fr} = 0.55$ J/cm^2 has been found for the onset of the appearance of the fringes, whereas for melting we have found the smaller value of $\Phi_m = 0.39$ J/cm^2. Since the threshold for fringes is higher than the melting threshold, this explains also why the fringes are confined to an area smaller than the molten region.

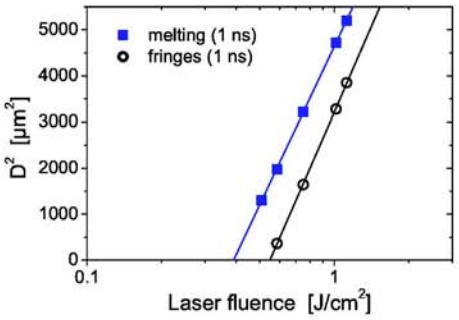

FIG. 9. (Color online) Square of the transient horizontal diameters D^2 at a pump-probe delay of 1 ns as a function of the incident laser fluence Φ_0 for fluence below the ablation threshold of *c*-Ge. The full squares show the data for the molten region, whereas the open circles represent the data for the transient fringe pattern. The solid line indicate least-squares-fits for irradiation with a spatially Gaussian laser beam.

Ad (iii): The hypothesis is further supported by the thermophysical data of germanium and its native oxide. Amorphous germanium dioxide (a-GeO_2) melts at higher temperatures than germanium [$T_m(a\text{-}GeO_2)=1347$ K $> T_m(c\text{-Ge})=1210$ K][30] but it evaporates at a temperature $\approx 500°$ lower than germanium does [$T_b(a\text{-}GeO_2)=2625$ K $< T_b(c\text{-Ge})=3104$ K].[30] Since the laser-induced temperature rise is monotonously increasing related to the local laser fluence, a thermally induced oxide removal will occur in the melting regime of germanium at fluences lower than the ablation threshold.

It should be noted here that for thermally grown oxide films (50–1200 nm thickness) on silicon, a blistering and delamination of the oxide films has been observed very recently by post-irradiation atomic force and optical microscopy following NIR fs-laser pulse irradiation.[36] This also suggests that in our case of a thin native oxide layer on germanium its removal should start at the semiconductor/oxide interface.

In Fig. 10 both the horizontal diameter of the molten region and the normalized surface reflectivity change in the center of the irradiated area are plotted as a function of the delay time between the pump and the probe pulse.

The horizontal diameter of the molten surface region increases during the first 10 ps until a saturation value of 60 μm is reached [Fig. 10(a)]. This might be indicative of a thermal melting process. Between 1 ns and 10 ns the diameter starts to decrease again upon solidification of the melt pool which is completed for times between 10 and 100 ns.

In contrast, the normalized surface reflectivity change increases within the first picosecond to the experimentally measured level of the liquid [$\Delta R/R(\text{exp}) \sim 0.65$] at 400 nm probe wavelength [Fig. 10(a)]. For times between 1 ps and approximately 100 ps, a transient reflectivity decrease up to 25% can be seen. Since this change is too large to be explained only by the changes of the optical properties of a superheated liquid [as it has been observed in other semiconductors like silicon[26] and GaAs (Ref. 17)], the onset of ablation of the oxide layer may additionally contribute to it. After 100 ps delay time, the liquid reflectivity value is recovered again. No permanent surface reflectivity change has been observed after the resolidification [$\Delta R/R(\infty)=0$].

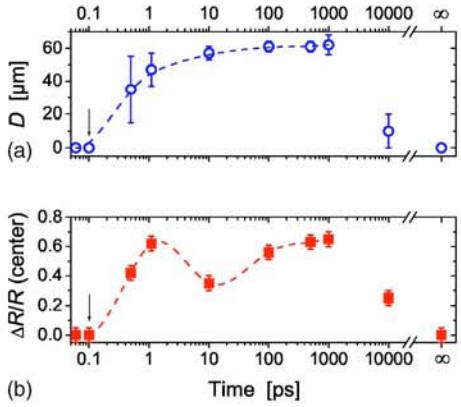

FIG. 10. (Color online) Horizontal diameter D of the molten region (a) and normalized surface reflectivity change $\Delta R/R$ in center (b) as a function of time as measured for the irradiated regions shown in Fig. 8. Note the logarithmic time axis. The true zero delay is marked by an arrow. The final reflectivity change ($\Delta t=\infty$) is marked on the right-hand horizontal axis. The lines are to guide the eye.

2. *Ps- and ns-RTR*

As in the ablative regime, the fs-laser induced melting has been studied on longer timescales (ns-μs) using the RTR-setup. Figure 11 shows the temporal evolution of the normalized surface reflectivity change as probed simultaneously by the streak camera [(a)–(c)] and the photodiode [(d)–(f)] in

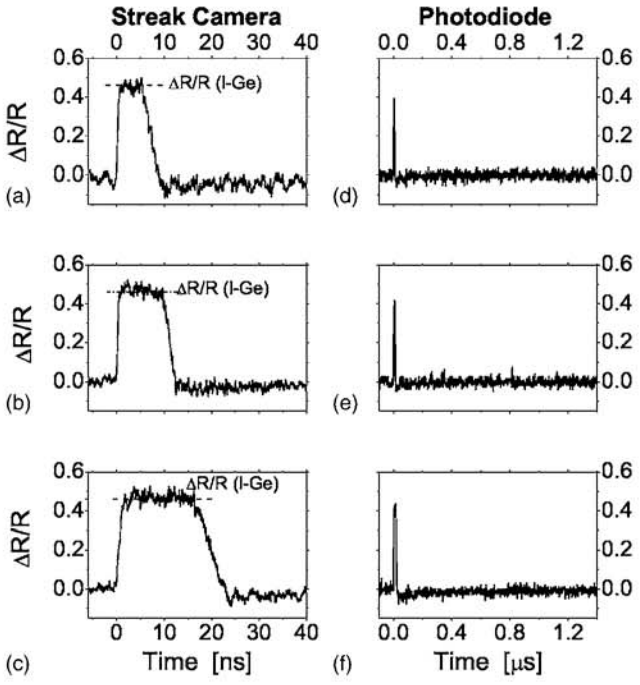

FIG. 11. Normalized surface reflectivity change as a function of time as measured with a streak camera (a)–(c) and with a photodiode (d)–(f) at three different fluence levels [(a)+(d): 0.75 J/cm^2, (b)+(e): 0.84 J/cm^2, (c)+(f): 1.32 J/cm^2].

TABLE I. Optical constants (complex refractive index $n+ik$) used for the thin film optical calculations.

Phase	Wavelength λ [nm]	Refractive index $(n+ik)$ n	k	Opt. penetration depth $\lambda/(4\pi k)$ [nm]	Ref.
c-Ge	400	4.14	2.21	14.4	20
	514.5	4.61	2.45	16.7	20
ℓ-Ge	400	1.81	4.25	7.5	25
	514.5	2.51	5.12	8.0	25
a-Ge	400	3.48	2.89	11.0	42
	514.5	4.30	2.30	17.8	42
a-GeO_2	400	1.64	0.00	∞	43
	514.5	1.61	0.00	∞	43

the center of the irradiated region upon irradiation at three different pump peak fluences in the melting regime.

In all streak camera transients [Figs. 11(a)–11(c)], a similar behavior can be seen, i.e., a rapid reflectivity increase to a reflectivity plateau with a saturated level of $(\Delta R/R)_{max} \approx 0.46$. This is indicative of the formation of a molten layer at the surface with a thickness greater than the optical penetration depth of the probing 514.5 nm radiation (8 nm, see Table I). The experimentally observed plateau values between 0.45 and 0.48 in the normalized reflectivity change perfectly agree with the value of 0.46 obtained by thin film optical simulations for an optically thick layer of molten germanium, which is covered by a native oxide layer (see Sec. III B 3), as indicated by dashed horizontal lines (Fig. 11). The plateau lasts only for up to a few tens of nanoseconds (fluence dependent). After the plateau, the reflectivity change decreases again to a final level around $\Delta R/R(40\ \text{ns}) \sim -0.04$. Depending on the fluence, this occurs within 3 ns [Fig. 11(b)] and 8 ns [Fig. 11(c)]. Analyzing the temporal onset of resolidification in the melting regime shows that the melt-duration scales approximately linearly with the laser fluence (data not shown here). Along with the high thermal conductivity of the crystalline material [0.6 $W/(cm \cdot K)^2$] this is indicative of an interfacial resolidification process, which will be analyzed in detail in Sec. III B 3.

Since the complementary photodiode transients [Figs. 11(d)–11(f)] do not fully resolve the reflectivity plateau, their maximum values $(\Delta R/R)_{max}$ are systematically below that measured by the streak camera. It is interesting to note in this context that immediately after solidification the reflectivity level is slightly lower than the initial one [especially in Figs. 11(c) and 11(f)]. This can be explained by the temperature dependence of the optical properties of c-Ge.[9] However, it can be seen at longer times that the reflectivity recovers its initial value, i.e., $\Delta R/R(1.4\ \mu s)=0$.

Note that the fluence for the reflectivity transient shown in Figs. 11(b) and 11(e) [0.84 J/cm^2] is comparable to the one of the image series depicted in Fig. 8 [0.83 J/cm^2]. Consistently, in both figures the resolidification of the liquid layer can be seen to occur after ≈ 10 ns. However, due to the small modulation depth of the reflectivity oscillations when compared to the signal-to-noise ratio, the fringes in the melting regime cannot be resolved in our RTR measurements, as opposed to the ablative regime in which this was possible (Fig. 5).

3. Calculations of the reflectivity changes

Additional insights into the processes occurring in the melting regime can be obtained from thin film optical calculations, especially by modeling the surface reflectivity change upon melting and resolidification, which might induce the formation of an amorphous top layer. For bulk semiconductors it was found that the resolidification of a laser-induced melt layer occurs interfacially from the solid/liquid interface and the solidifying material turns to an amorphous state when a critical speed in the order of 1–25 m/s is exceeded for the velocity of the resolidification front.[37–40] At such velocities, there is not enough time for the nucleation of a crystalline phase, which leads to the formation of the amorphous material.

The evolution of the reflectivity in such a scenario has been modeled by considering a thin film of molten or amorphous material with variable thickness on top of a crystalline substrate. Additionally, it is assumed that the surface exposed to air is covered by a transparent native layer of amorphous germanium dioxide (a-GeO_2). The optical model used takes into consideration the fully coherent superposition of Fresnel reflections at all interfaces [air/oxide, oxide/liquid(amorphous) and liquid(amorphous)/solid] for the given probe wavelengths (400 nm or 514.5 nm), both at normal incidence.[35,41] For direct comparison, also the case of an oxide-free surface has been considered. The optical constants $n+ik$ for the different material phases (c-Ge, a-Ge, ℓ-Ge, and a-GeO_2) used for the thin film optical calculations are summarized in Table I.

In our calculations, the presence of few nanometers thick transparent oxide layer on the surface causes the reflectivities to be lowered by a few percent. For example, the reflectivity of bulk single-crystalline germanium at both probe wavelengths are $R(c\text{-Ge}, 400\ \text{nm})=0.47$ and $R(c\text{-Ge}, 514.5\ \text{nm})=0.51$, whereas the values for native oxide covered bulk material are $R(a\text{-}GeO_2(3.0\ \text{nm})/c\text{-Ge}, 400\ \text{nm})=0.46$ and $R(a\text{-}GeO_2(3.0\ \text{nm})/c\text{-Ge}, 514.5\ \text{nm})=0.50$, respectively.

Since the native oxide layer is already present on the nonirradiated wafer surface, the latter values have been used to evaluate all normalized reflectivity changes in our thin film optical calculations. Then, the removal of the native oxide layer causes an increase of the normalized surface reflectivity change—in contrast to heating effects, which are lowering the reflectivity by up to 10% (see above). However, these calculations indicate that the differences in the reflectivity between an oxide-covered and an oxide-free wafer surface are too small to be detected directly by our optical probing setups. Nevertheless, following our hypothesis of oxide removal, its direct experimental detection seems to be possible when additional interference phenomena are involved as it is the case in Fig. 8, giving rise to the fringe pattern.

(*a*) *Melt-layer:* The results of these surface reflectivity calculations at both probe wavelengths are shown in Fig. 12, where the normalized surface reflectivity change $\Delta R/R$ is evaluated for different thicknesses d_l of a liquid layer of Ge

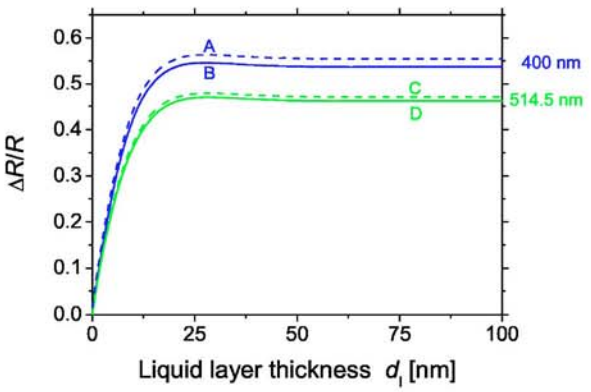

FIG. 12. (Color online) Normalized surface reflectivity change obtained by thin film optical calculations (0° angle of incidence) of a layer of liquid Ge with variable thickness d_l on top of a single-crystalline substrate at two different probe laser wavelengths (400 nm and 514.5 nm). For the solid curves, an additional 3 nm thick native oxide layer is considered, whereas the dashed curves represent calculations without the oxide layer. The optical constants used are listed in Table I. For labeling of the curves refer to the text.

on top of the crystalline substrate. The reflectivity change has been calculated for a layer system with a 3.0 nm thick native oxide layer (solid lines) and also without any covering oxide (dashed lines).

In all curves (Fig. 12, curves A–D), a rapid increase of the surface reflectivity with increasing liquid layer thickness can be observed before reaching a saturation level once the liquid layer becomes optically thick. At the probe wavelength of 400 nm (Fig. 12, curves A and B), we do not observe a satisfying agreement between the experimentally determined [compare Figs. 7(a) and 10(b)] and the calculated reflectivity changes for the liquid phase since the average values in $\Delta R/R$ are too high by as much as 15% for the experimental data (compare Table II). The origin is not fully clear at the moment, but the deviation is significantly larger than the experimental error. Some uncertainty in the calculated values might arise from the optical constants used for ℓ-Ge which were extrapolated to this probe wavelength from a least-squares-fit based on a Drude model.[25] At 514.5 nm probe wavelength, both saturation levels of the normalized reflectivity change for the oxide-free liquid (Fig. 12, curve C, $\Delta R/R_{sat}=0.47$) and the oxide-covered liquid (Fig. 12, curve D, $\Delta R/R_{sat}=0.46$) are in excellent agreement with the experimental data shown in Fig. 11 ($\Delta R/R=0.45-0.48$).

Along with the experimental data shown in Fig. 11, the thin film optical calculations allow a quantitative estimation of the velocity of the resolidification front while approaching the surface: it is seen in Fig. 12 (curves C and D) that the normalized reflectivity starts to decrease rapidly below the bulk reflectivity level of the liquid at a thickness of ~20 nm. Accordingly we can use the transients in Fig. 11 to estimate the time taken by the solidification front to travel a distance equivalent to this liquid layer thickness. This time corresponds to the time elapsed between the end of the reflectivity plateau and the time at which the reflectivity reaches the value of hot solid germanium which ranges from 3 to 8 ns. Hence, mean interfacial speeds between 2.5 and 7 m/s are estimated.

TABLE II. Surface reflectivities obtained by thin film optical calculations at different probe wavelengths (400 nm, 514.5 nm) and for normal incident radiation. Additionally, the corresponding normalized reflectivity changes $\Delta R/R=(R-R_c)/R_c$ are listed, where R_c represents the reflectivity of c-Ge covered by a 3.0 nm thick native layer of a-GeO_2. For comparison, the experimentally obtained values are listed. n.e.: no evidence.

Layer system	Wavelength λ [nm]	Reflectivity (Calc.) R	(Calc.) $\Delta R/R$	(Exp.) $\Delta R/R$
a-GeO_2(3.0 nm)/c-Ge	400	0.464	0	0
	514.5	0.503	0	0
c-Ge	400	0.471	+0.02	—
	514.5	0.508	+0.01	—
a-GeO_2(3.0 nm)/ℓ-Ge	400	0.713	+0.54	0.50–0.85
	514.5	0.735	+0.46	0.45–0.48
ℓ-Ge	400	0.721	+0.55	0.50–0.85
	514.5	0.739	+0.47	0.45–0.48
a-GeO_2(3.0 nm)/a-Ge	400	0.511	+0.08	n.e.
	514.5	0.480	−0.05	n.e.
a-Ge	400	0.510	+0.10	n.e.
	514.5	0.485	−0.04	n.e.

(*b*) *Amorphous-layer:* This speed is lower than the critical speed of resolidification in other elemental semiconductors with a diamond structure, such as silicon, where values between 12 and 25 m/s (depending on the crystal orientation) have to be exceeded for inducing amorphization.[37,38]

Unfortunately, and to the best of our knowledge, no experimental data are available for the critical speed of resolidification in germanium. However, Spaepen and Turnbull have estimated the maximum crystallization speed for germanium to be approx. 100 m/s (Refs. 44 and 45).

In order to investigate the possible existence of an amorphus top layer induced by fs-laser pulse irradiation, additional thin film optical calculations have been performed for a thin layer of amorphous material (a-Ge) with variable thickness d_a on the single-crystalline wafer (c-Ge). The results at both probe wavelengths are shown in Fig. 13. In analogy to the case of a thin liquid layer, the normalized surface reflectivity change has been calculated for a layer system with a 3.0 nm thick native oxide layer (solid lines) and also without any covering oxide (dashed lines).

At 400 nm wavelength, both curves A and B show a rapid increase of the surface reflectivity with increasing layer thickness, followed by a damped oscillation before reaching the saturation value, i.e., the "bulk" reflectivity of amorphous germanium. The oscillation is caused by constructive and destructive interference effects due to the partial reflections mainly at the a-GeO_2/ℓ-Ge(a-Ge) and the ℓ-Ge(a-Ge)/c-Ge interfaces. The extinction coefficient k determines how strong the oscillation is damped. For a-Ge films, thicknesses larger than 75 nm are needed to saturate the reflectivity. These saturation values are $\Delta R/R_{sat}=0.10$ for the oxide free (Fig. 13, curve A) and $\Delta R/R_{sat}=0.08$ for the native oxide-covered a-Ge surface (Fig. 13, curve B).

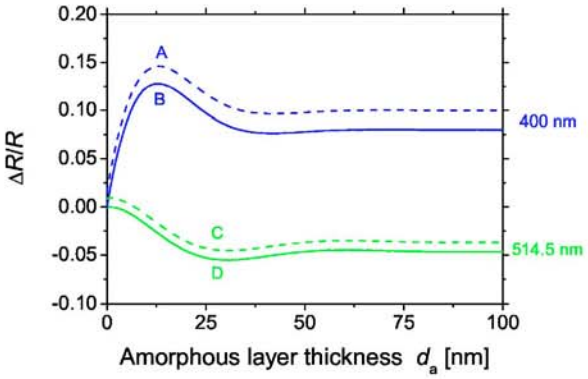

FIG. 13. (Color online) Normalized surface reflectivity change obtained by thin film optical simulations (0° angle of incidence) of a layer of amorphous Ge with variable thickness d_a on top of a single-crystalline substrate at two different probe laser wavelengths (400 nm and 514.5 nm). For the solid curves, an additional 3 nm thick native oxide layer is considered, whereas the dashed curves represent calculations without the oxide layer. The optical constants used are listed in Table I. For labeling of the curves refer to the text.

At 514.5 nm wavelength, the normalized reflectivity change first decreases before reaching a small negative saturation level of some percent (see Fig. 13, curves C and D, and the quantitative values given in Table II).

However, given the absence of any observable permanent change in the surface reflectivity at both probe wavelengths (400 nm and 514.5 nm) after fs-laser pulse irradiation at fluences below the ablation threshold, we conclude that there is no evidence for the formation of a superficial amorphous top layer from the melt. Apparently, and in contrast to the femtosecond laser pulse irradiation of other semiconductors like (111)-silicon[35] or (100)-indium phosphide[40,46] under similar conditions, the regrowth velocity of the liquid-solid interface is sufficiently low to prevent amorphization of the surface. Hence, our values of 2.5 to 7.0 m/s for the interfacial regrowth speed at the end of the solidification process represent a lower limit for the critical resolidification speed in (100)-germanium: despite the fact that the velocity of the liquid/solid interface speeds up at the end of the solidification process driven by the gradually increasing supercooling of the melt,[47] no amorphization has been observed in the present case. Hence, the maximum interface velocity reached here upon the fs-laser pulse induced solidification of germanium has to be smaller than the critical velocity for amorphization to occur.

Two additional aspects have to be mentioned with respect to the different behavior of (100)-Ge upon fs-laser induced irradiation when compared to the other mentioned semiconductors. First, it has been reported by Cullis *et al.* for ns-laser irradiation of various semiconductors (Si, Ge, GaAs, GaP) that the crystal orientation significantly influences the resolidification behavior of the material.[38,48] Crystals with (111) orientation generally exhibit lower recrystallization velocities with consequential enhancement of melt undercooling and a higher amorphous phase nucleation probability when compared to (100)-oriented samples.[48] In other words, (111) crystals amorphize more easily than (100) oriented ones.

Secondly, the recrystallization behavior is directly linked to the heat conduction within the material. Materials with lower thermal diffusivity values reduce the undercooling of the melt (which determines the speed of the solidification front) and therefore slow down the recrystallization rate. Hence, it is less likely that the critical interface speed for crystallization is exceeded in these materials. This trend is also seen in the magnitudes of the thermal diffusivity of c-Si (0.94 cm^2/s),[2] c-InP (0.47 cm^2/s),[2] and c-Ge (0.35 cm^2/s),[2] which consequently reflect the tendency to form an amorphous top layer at the end of the solidification process (for a given crystal orientation).

IV. CONCLUSIONS

In summary, we have studied the temporal dynamics of melting, ablation, and resolidification upon titanium:sapphire femtosecond laser pulse irradiation of single-crystalline germanium. Femtosecond time-resolved microscopic imaging and complementary streak camera and photodiode measurements allowed a complete characterization of the phase change dynamics in a time span covering more than seven orders of magnitude (~100 fs up to 1.4 μs). Our results confirm the few previous studies on ultrafast phase transitions in germanium and provide additional insights due to the joint application of fs-time-resolved and real-time probing techniques: Evidence is presented that the native oxide layer present on germanium wafers can be removed selectively at fluences above the melting but below the ablation threshold of germanium, leading to a transient surface reflectivity pattern in the picosecond to nanosecond range, without a measurable change of the permanent surface reflectivity. In contrast to the femtosecond laser pulse irradiation of other semiconductors, no indication for a laser-induced permanent superficial amorphization was found. From these observation along with the transient solidification behavior of the molten germanium on a time scale of some nanoseconds, a lower limit for the critical speed of the *liquid/solid* interface between 2.5 and 7.0 m/s has been deduced for the fs-laser irradiation of (100) Ge. For single laser pulses with fluences slightly exceeding the ablation threshold, we have been able to observe reflectivity oscillations (caused by the transient Newton-fringe pattern observed in femtosecond microscopy) up to some tens of nanoseconds by means of real-time probing with a streak camera. This extends the maximum duration over which this phenomenon has been monitored via interference phenomena using femtosecond time resolved microscopy by one order of magnitude.

ACKNOWLEDGMENTS

This work has been partially supported by the TEC 2005-00074 project and by the EU in the frame of the TMR project FLASH (MRTN-CT-2003-503641). One author (G.B.) acknowledges the funding in the frame of the same project. Another author (J.B.) acknowledges the funding of the C.S.I.C. through a contract in the frame of the I3P Programme (Ref. I3P-PC2002), co-funded by the European Social Fund. The authors would like to thank R. Serna for performing the ellipsometry measurements.

*Corresponding author, electronic address: bonse@mbi-berlin.de; Present address: Max-Born-Institut für Nichtlineare Optik und Kurzzeitspektroskopie, Max-Born-Strasse 2A, D-12489 Berlin, Germany.

†Present address: Laboratoire de Spectrométrie Ionique et Moléculaire, UMR CNRS 5579, Université Claude Bernard—Lyon I, Bâtiment Alfred Kastler, 43 Boulevard du 11 Novembre 1918, F-69622 Villeurbanne Cedex, France.

‡Electronic address: j.solis@io.cfmac.csic.es

[1] Wikipedia Encyclopedia, http://en.wikipedia.org/wiki/Germanium

[2] A. Dargys and J. Kundrotas, *Handbook on Physical Properties of Ge, Si, GaAs and InP* (Science and Encyclopedia Publishers, Vilnius, 1994).

[3] A. Elci, M. O. Scully, A. L. Smirl, and J. C. Matter, Phys. Rev. B **16**, 191 (1977).

[4] G. E. Jellison, D. H. Lowndes, D. N. Mashburn, and R. F. Wood, Phys. Rev. B **34**, 2407 (1986).

[5] A. Othonos, H. M. van Driel, J. F. Young, and P. J. Kelly, Phys. Rev. B **43**, 6682 (1991).

[6] W. R. Sooy, M. Geller, and D. P. Bortfeld, Appl. Phys. Lett. **5**, 54 (1964).

[7] D. H. Auston, J. A. Golovchenko, A. L. Simons, and T. N. C. Venkatesan, Appl. Phys. Lett. **34**, 777 (1979).

[8] J. Solis, F. Vega, and C. N. Afonso, Appl. Phys. A: Mater. Sci. Process. **62**, 197 (1996).

[9] N. Chaoui, J. Siegel, J. Solis, and C. N. Afonso, J. Appl. Phys. **89**, 3763 (2001).

[10] N. Chaoui, J. Siegel, S. M. Wiggins, and J. Solis, Appl. Phys. Lett. **86**, 221901 (2005).

[11] K. Sokolowski-Tinten, A. Cavalleri, and D. von der Linde, Appl. Phys. A: Mater. Sci. Process. **69**, 577 (1999).

[12] C. W. Siders, A. Cavalleri, K. Sokolowski-Tinten, C. Toth, T. Guo, M. Kammler, M. H. von Hoegen, K. R. Wilson, D. von der Linde, and C. P. J. Barty, Science **286**, 1340 (1999).

[13] B. Rethfeld, V. V. Temnov, K. Sokolowski-Tinten, S. I. Anisimov, and D. von der Linde, Proc. SPIE **4760**, 72 (2002).

[14] K. Sokolowski-Tinten, S. Kudryashov, V. Temnov, J. Bialkowski, M. Boing, D. von der Linde, A. Cavalleri, H. O. Jeschke, M. E. Garcia, and K. H. Bennemann, *Ultrafast Phenomena XII*, Springer Series in Chemical Physics 66 (Springer-Verlag, Heidelberg, 2000).

[15] M. C. Downer, R. L. Fork, and C. V. Shank, J. Opt. Soc. Am. B **2**, 595 (1985).

[16] D. von der Linde and K. Sokolowski-Tinten, Appl. Surf. Sci. **154-155**, 1 (2000).

[17] K. Sokolowski-Tinten, J. Bialkowski, M. Boing, A. Cavalleri, and D. von der Linde, Phys. Rev. B **58**, R11805 (1998).

[18] V. V. Temnov, Ph.D. thesis, University of Duisburg-Essen, Germany, 2004.

[19] J. Solis, J. Siegel, and C. N. Afonso, Rev. Sci. Instrum. **71**, 1595 (2000).

[20] *Handbook of Optical Constants of Solids*, edited by E. D. Palik (Academic Press, Orlando, Florida, 1998).

[21] P. Stampfli and K. H. Bennemann, Phys. Rev. B **42**, 7163 (1990).

[22] C. V. Shank, R. Yen, and C. Hirlimann, Phys. Rev. Lett. **50**, 454 (1983).

[23] I. L. Shumay and U. Höfer, Phys. Rev. B **53**, 15878 (1996).

[24] J. Bonse, S. M. Wiggins, and J. Solis, J. Appl. Phys. **96**, 2628 (2004).

[25] G. E. Jellison and D. H. Lowndes, Appl. Phys. Lett. **51**, 352 (1987).

[26] J. Boneberg, O. Yavas, B. Mierswa, and P. Leiderer, Phys. Status Solidi B **174**, 295 (1992).

[27] K. Sokolowski-Tinten, J. Bialkowski, A. Cavalleri, D. von der Linde, A. Oparin, J. Meyer-ter-Vehn, and S. I. Anisimov, Phys. Rev. Lett. **81**, 224 (1998).

[28] S. I. Anisimov, N. A. Inogamov, A. M. Oparin, B. Rethfeld, T. Yabe, M. Ogawa, and V. E. Fortov, Appl. Phys. A: Mater. Sci. Process. **69**, 617 (1999).

[29] V. V. Zhakhovskii, K. Nishihara, S. I. Anisimov, and N. A. Inogamov, JETP Lett. **71**, 167 (2000).

[30] D. Bäuerle, *Laser Processing and Chemistry*, 3rd ed. (Springer-Verlag, Berlin, 2000).

[31] J. König, S. Nolte, and A. Tünnermann, Opt. Express **13**, 10597 (2005).

[32] D. E. Aspnes and A. A. Studna, Rev. Sci. Instrum. **49**, 291 (1978).

[33] F. Marinozzi, Rev. Sci. Instrum. **71**, 4231 (2000).

[34] S. Nakamura and T. Hibiya, Int. J. Thermophys. **13**, 1061 (1992).

[35] J. Bonse, K.-W. Brzezinka, and A. Meixner, Appl. Surf. Sci. **221**, 215 (2004).

[36] J. P. McDonald, V. R. Mistry, K. E. Ray, S. M. Yalisove, J. A. Nees, and N. R. Moody, Appl. Phys. Lett. **88**, 153121 (2006).

[37] P. H. Bucksbaum and J. Bokor, Phys. Rev. Lett. **53**, 182 (1984).

[38] A. G. Cullis, Rep. Prog. Phys. **48**, 1155 (1985).

[39] R. Cerny, V. Chab, G. Ivlev, E. Gatskevich, and P. Prikryl, Phys. Rev. B **59**, 10685 (1999).

[40] J. Bonse, S. M. Wiggins, and J. Solis, J. Appl. Phys. **96**, 2352 (2004).

[41] F. J. Pedrotti and L. S. Pedrotti, *Introduction to Optics*, 2nd ed. (Prentice Hall, Englewood Cliffs, New Jersey, 1993).

[42] J. C. G. de Sande, C. N. Afonso, J. L. Escudero, R. Serna, F. Catalina, and E. Bernabeu, Appl. Opt. **31**, 6133 (1992).

[43] Y. Z. Hu, J. T. Zettler, S. Chongsavangvirod, Y. Q. Wang, and E. A. Irene, Appl. Phys. Lett. **61**, 1098 (1992).

[44] F. Spaepen and D. Turnbull, *Symposium on Laser-Solid Interactions and Laser Processing*, AIP Conf. Proc. No. 50 (Materials Research Society, Boston, 1978), pp. 73–83.

[45] P. L. Liu, R. Yen, N. Bloembergen, and R. T. Hodgson, Appl. Phys. Lett. **34**, 864 (1979).

[46] J. Bonse, M. Munz, and H. Sturm, IEEE Trans. Nanotechnol. **3**, 358 (2004).

[47] M. von Allmen and A. Blatter, *Laser-Beam Interactions with Materials*, 2nd ed. (Springer-Verlag, Berlin, 1995).

[48] A. G. Cullis, H. C. Webber, and N. G. Chew, Appl. Phys. Lett. **42**, 875 (1983).

[49] It should be noted that this flow velocity u at the vacuum boundary can be derived also in an alternative way. According to Sokolowski-Tinten *et al.* (Ref. 27) it is approximately given by $u \approx c_0 \ln(r_1/r_0)$, where c_0 is the sound velocity and r_0 and r_1 are the solid density and the liquid density near the thermodynamical binodal boundary. Due to the lack of suitable data for Ge, we

will estimate u directly from our experimental data.

[50] This value of $h=350$ nm has been estimated from an energy balance consideration at fluence close to the melting threshold. It represents an upper limit for the real melt layer thickness; for details of the model see J. Bonse, S. M. Wiggins, and J. Solis, Appl. Phys. A: Mater. Sci. Process. **80**, 243 (2005).

[51] Note that both velocities are rather insensitive on the melt layer thickness h: a value of only 50 nm leads to even smaller velocities of $v_p=6$ m/s and $v_g=12$ m/s.

[52] This speed is estimated from the radial distance of 25 μm traveled by the fringe pattern from the center in horizontal direction within 1 ns, e.g., in Fig. 8(f).

Far-field background suppression in tip-modulated apertureless near-field optical microscopy

Pietro Giuseppe Gucciardi[a)]
CNR-Istituto per i Processi Chimico-Fisici, Sezione di Messina, Via La Farina 237, I-98123 Messina, Italy

Guillaume Bachelier
Laboratoire de Spectrométrie Ionique et Moléculaire (LASIM-CNRS UMR 5579), Université Claude Bernard-Lyon I, Bâtiment A. Kastler, 43 Boulevard du 11 Novembre 1918, F-69622 Villeurbanne, France

Maria Allegrini[b)]
Dipartimento di Fisica "E. Fermi," Università di Pisa, and polyLAB-CNR, Largo Bruno Pontecorvo 3, 56127 Pisa, Italy

(Received 13 January 2006; accepted 4 April 2006; published online 29 June 2006)

In apertureless near-field optical microscopy the vertical dithering of the tip, associated with demodulation at higher harmonics ($n>1$), allows us to suppress the far-field background, providing artifact free elastic scattering images. This paper analyzes, both theoretically and experimentally, the physical origin of the background signal at the different harmonics and the mechanisms underlying its rejection for the general case of propagative-field illumination. We show that Fourier components of the background must be expected at every harmonic, evidencing why demodulation at higher harmonics is not an inherently background-free technique, and assessing the experimental conditions in which it becomes like that. In particular, we put forward the fundamental roles of both the harmonic order and the tip oscillation amplitude in the background suppression mechanisms. Furthermore, we outline how the lock-in detection of the signals amplitude can enhance the nonlinear dependence of the background on the tip-sample distance. Such effect provides a more subtle source of topography artifacts since the optical maps become qualitatively uncorrelated from the topographic counterpart, requiring an upgrade of the criteria to assess the absence of artifacts from the optical maps. © *2006 American Institute of Physics*. [DOI: 10.1063/1.2208527]

I. INTRODUCTION

Scanning near-field optical microscopy[1] (SNOM) overcomes the diffraction limit ($\sim\lambda/2$) by scanning a nanometric probe close to the sample surface. The superior resolution of SNOM arises from the exploitation of the evanescent components of the electromagnetic field, the so-called near field, in the probe-sample optical interaction. Due to the evanescent nature of the near fields, the tip must follow the surface at close distance (1–10 nm) during the scanning process [the so-called constant gap operation mode (CGM)]. Aperture-SNOM employs the aperture present at the apex of a tapered, metal coated-optical fiber as a source of evanescent waves.[2] The development of *apertureless*-SNOM (*a*-SNOM) techniques (see Ref. 3, for example) has demonstrated that the use of a sharp tip ending with a nanometer-scale radius of curvature can provide a local enhancement of the field by several orders of magnitude.[4] Optical imaging with spatial resolution in the 1–10 nm range is thus achievable.[5,6] In an ideal elastic scattering SNOM experiment, the radiation reaching the detector should originate only from the nanometric region of the probe-sample optical interaction. In practice, conversely, the total signal is dominated by a large background (BKG) contribution due to stray light scattered by other sources that interfere at the detector. The probe shaft, the optical elements, or portions of the sample "far" from the probe are typical examples of undesirable sources of stray light. The major inconvenience arises from the fact that, since the phase of the stray fields depends on the mutual distance among these sources, the BKG is not a constant plateau, but is sensitive to any position variation of each source. In CGM, in particular, the continuous displacement of the sample, driven by the feedback loop, induces a strong cross talk between the topographical and the optical BKG, whose variations are orders of magnitude more intense than any near-field scattering. Fictitious optical maps are thus obtained, which do not contain information about the optical properties of the sample, but rather representing an optical readout of the topography.[7,8] This is what is called a topography, or *z*-motion artifact.

The most important challenge in *a*-SNOM is, therefore, the extraction of the tiny near-field scattering signal from the huge far-field background. Moreover, due to the fact that the scattering amplitude scales down with the sixth power of the sample's dimensions,[9] such a task becomes more challenging as the structures we want to investigate become smaller. In order to extract the near-field signal from the BKG two steps are required. Firstly, the near-field scattering must be amplified. This is done through heterodyne,[10,11] or homodyne[12–14] interferometric techniques or, when available, by exploiting material-dependent phonon-polariton resonances.[15,16] Sec-

a)Electronic mail: gucciardi@me.cnr.it
b)Present address: National Institute of Standards and Technology, Gaithersburg, Maryland 20899-8424.

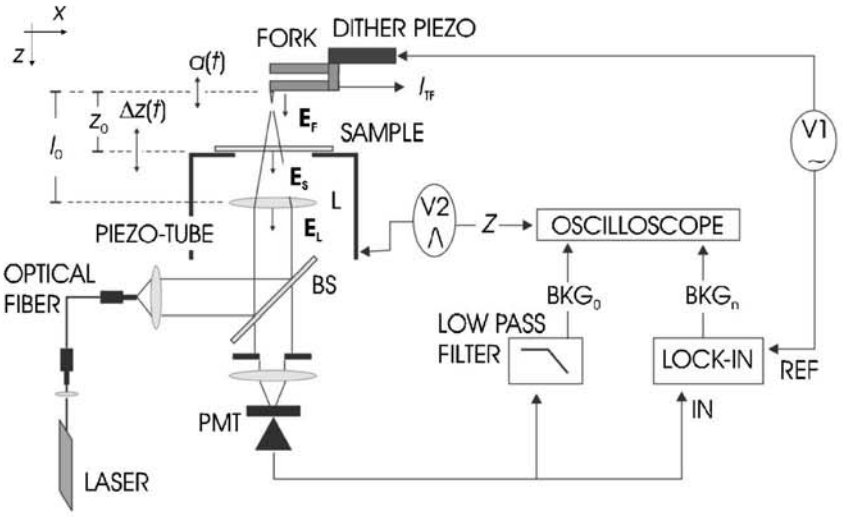

FIG. 1. Sketch of the experimental setup.

ondly, the BKG must be suppressed exploiting the nonlinear part of the tip-sample optical interaction.[9,17] Experimentally, the latter task is accomplished by vertically vibrating the tip at frequency ω and demodulating the optical signal at higher harmonics ($n\omega$, $n>1$).[10,12] This *modus operandi* induces, in fact, a high-pass filtering of the spatial frequencies of the electromagnetic fields.[18–21] The result is that the low-spatial-frequency propagating fields, such as the BKG, are largely suppressed, while the evanescent near-field components are enhanced. Demodulation at higher harmonics is thus considered to be an artifact-free imaging technique.

In this paper we precise under which conditions this statement can be considered true. The paper is organized as follows. In Sec. II we characterize experimentally the BKG signal, in particular its dc, first, and second harmonic components. The results are thus interpreted in a theoretical framework (Sec. III) which allows us to point out the crucial role of the tip oscillation amplitude in the suppression of the BKG at the higher harmonics. Finally, in Sec. IV, we outline how the nonlinear dependence of the BKG can yield fictitious optical images quite different from the topographical counterpart, allowing us to discuss and update the criteria for artifacts identification.

II. EXPERIMENT

Approach curves, in which the optical signal is monitored as a function of the tip-sample distance, represent a powerful instrument to characterize the different far-field and near-field regimes in the tip-sample optical interaction. In particular, they have already allowed us to evidence the occurrence of harmonic components of the far-field BKG at the first[10,22,23] and the second harmonics,[11,24] superimposed to the genuine near-field scattering whose signature shows up at close tip-sample distances (<100 nm). Similar to the dc component, the harmonic components of the BKG (BKG_n, $n=1,2,\ldots$) depend both on the tip's and on the sample's position, representing a source of topography artifacts. Approach curves permit to quantitatively assess the *degree of artifact content* in the optical signal through the ratio $\varepsilon_n = BKG_n/NF_n$ between the oscillation amplitude of the nth-harmonic BKG_n (measured in the far-field region) and the near-field signal enhancement NF_n demodulated at the same harmonic (measured when the tip goes in contact with the sample). In the visible spectrum ($\lambda=633$ nm), first harmonic demodulation leads to values $\varepsilon_1 \sim 1$ for tip oscillation amplitudes ranging from a few nanometers to a few tens of nanometers.[10,11] The consequent optical maps will be very likely affected by severe topography artifacts. Demodulation at the second harmonic demonstrates a stronger BKG rejection power ($\varepsilon_2 < 10^{-1}$).[11,12] Demodulation at the third harmonic guarantees artifact-free imaging[11,12,24] since BKG_3 is always rejected below the noise level ($\varepsilon_3=0$). The situation is better in the IR ($\lambda=10.6$ μm) where the first harmonic demodulation already provides a good BKG suppression power ($\varepsilon_1 \sim 0.2$), even for tip oscillation amplitudes in the 100 nm range.[23,25]

In order to quantitatively assess such results, we have experimentally studied the interferential nature of the far-field BKG with an apparatus working in transmission mode, as shown in Fig. 1. The tip is held in the far field, at a distance Z_0 of several micrometers from a glass coverslip, used as sample, which is scanned in the vertical direction with an excursion Δz of a few microns. The scan allows us to monitor the BKG dependence (both the dc component and all the harmonics) on the tip-sample distance. Our tips are made of gold or silver by means of electrochemical etching techniques[26,27] and are glued orthogonally to one prong of a quartz tuning fork (TF).[28] The assembly is oscillated at resonance ($f_{res}=\omega/2\pi \sim 30$ kHz) by a dither piezo, driven by a function generator (V1) which allows us to change the tip oscillation amplitude a_0. A measure of the effective tip oscillation amplitude is retrieved either interferometrically[29] or by monitoring the piezocurrent I_{TF} delivered by the fork.[30,31] The light is provided by a HeNe laser ($\lambda=632.8$ nm). The beam is coupled to a single mode optical fiber whose output is collimated, reflected by a 50% beam splitter (BS), and finally focused on the tip shaft by means of a lens (L) ($f=8$ mm). The sample is mounted on a piezotube, scanned up and down by means of a linear voltage ramp (V2), never touching the tip. The field backscattered by the tip shaft (E_F) is collected by the same lens and focused on the detector [photomultiplier tube (PMT)]. Due to the high coherence de-

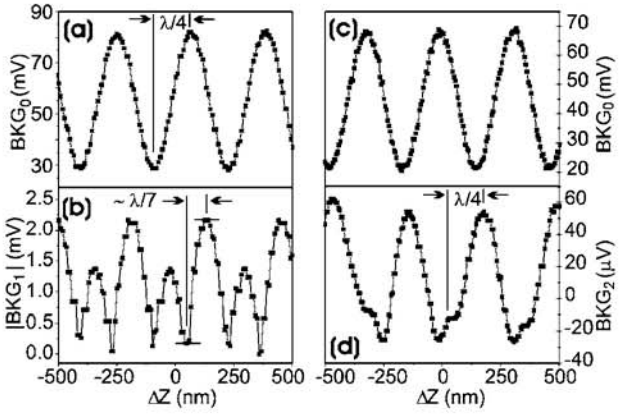

FIG. 2. Plot of the background signals BKG_0 [(a) and (c)], $|BKG_1|$ (b), and BKG_2 (d) vs the sample position.

gree of the light source, E_F will interfere with the back reflection of the sample (E_S), and with part of the light reflected back by the lens (E_L). The total intensity measured by the PMT will thus be

$$\begin{aligned} \mathrm{BKG} &= |E_F + E_S + E_L|^2 \\ &= |E_F|^2 + |E_S|^2 + |E_L|^2 + 2\,\mathrm{Re}(E_F^* E_S) \\ &\quad + 2\,\mathrm{Re}(E_F^* E_L) + 2\,\mathrm{Re}(E_L^* E_S). \end{aligned} \tag{1}$$

As we will see in more detail in the next section, this signal results in a sum of harmonic terms $\mathrm{BKG} = \Sigma_n \mathrm{BKG}_n(a_0, \Delta z)\cos(n\omega t)$, which represent the optical background in a typical *a*-SNOM experiment with propagative-field illumination. In order to measure both the dc part (BKG_0) and the harmonics BKG_n, the PMT output is split in two channels and fed, respectively, to a low-pass filter ($f_{cut}=1.6$ kHz$\ll f_{res}$), and to a lock-in amplifier synchronous with the nth harmonic of the TF oscillation frequency ω. We set the lock-in in amplifier to acquire either the in-phase signal $\mathrm{BKG}_n(a_0,z)$, or its modulus $|\mathrm{BKG}_n(a_0,z)|$. A digital oscilloscope is used to monitor the optical signals, simultaneously with the voltage V2 providing the sample vertical position.

Figures 2(a) and 2(b) show, respectively, the behavior of BKG_0 and of the modulus of BKG_1 ($|BKG_1|$), simultaneously acquired as a function of the sample position, in a scan of 1 μm wide (scan speed of 2 μm/s). In Figs. 2(c) and 2(d) we report two analogous plots for the BKG_0 and the in-phase component of BKG_2, simultaneously acquired. All the signals show an oscillatory dependence on the sample excursion Δz, with periodicity $\lambda/2$, as a result of the interference of the fields scattered by the stray light sources mentioned above. The signals BKG_n are characterized by a modulation amplitude A_n superimposed to a constant offset C_n due, as we will see in the next section, to the backscattering of the lens. Such an offset causes the height asymmetry of the bumps in the $|BKG_1|$ signal [Fig. 2(b)]. The tip oscillation amplitude in this experiment is $a_0=(3.4\pm0.1)$ nm,[29] equivalent to a ratio $a_0/\lambda \approx 5\times10^{-3}$.

To quantitatively assess the BKG rejection power of the demodulation technique at higher harmonics, we can define the quantity $R_n=A_n/A_0$, namely, the nth-harmonic-to-dc

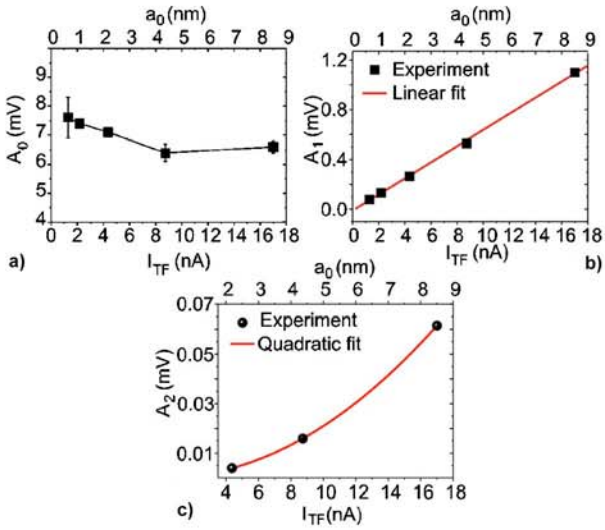

FIG. 3. (Color online) Dependence of the BKG modulation amplitudes $A_{0,1,2}$ [(a)–(c) respectively] on the tuning-fork current (bottom axes) and on the tip oscillation amplitude (top axes). The linear behavior of A_1 is pointed out by a linear fit [(b), red line)]. A power fit ($y=Ax^n$, $n=2.02\pm0.02$) of the second harmonic BKG amplitude [(c), red line)] evidences the quadratic dependence on a_0.

background ratio, representing the fraction between the modulation amplitude of the background demodulated at the nth harmonic with respect to the dc one. The stronger the BKG suppression, the smaller the expected values of R_n. In the experiment of Fig. 2, for example, we find decreasing values of $R_1=6.5\times10^{-2}$ and $R_2=1.2\times10^{-3}$, assessing that the second harmonic demodulation provides a BKG suppression superior of a factor of 50 with respect to the first harmonic demodulation. Even though the BKG_2 is still well above the noise. To study how the BKG_n depends on the tip oscillation amplitude we have monitored the modulation amplitudes $A_{0,1,2}$ varying a_0 in the 0.5–10 nm range. In Figs. 3(a)–3(c) we can note the different behaviors of the three signals. While A_0 is almost constant, the first and the second harmonics increase with a_0, respectively, in a linear and a quadratic fashion [red line in Fig. 3(c)]. In Fig. 4 we plot the corresponding values of R_1 [Fig. 4(a)] and R_2 [Fig. 4(b)]. These graphics allow us to conclude that for tip oscillation amplitudes in the 0.5–10 nm range first harmonic demodulation reduces the BKG by one-two orders of magnitude. For tip oscillation amplitudes between 2 and 10 nm, second harmonic demodulation reduces the BKG down to 10^{-2}–10^{-4}. In our experiment the second harmonic signal is rejected below the noise level for $a_0<1.5$ nm.

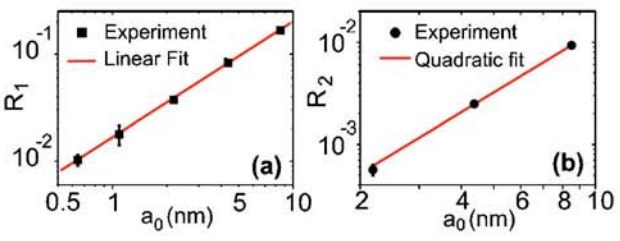

FIG. 4. (Color online) Plot of the nth-harmonic-to-dc-BKG ratio R_n as a function of the tip oscillation amplitude for first (a) and second harmonic (b) demodulations. The red lines reproduce the linear (a) and quadratic (b) fits of the experimental data.

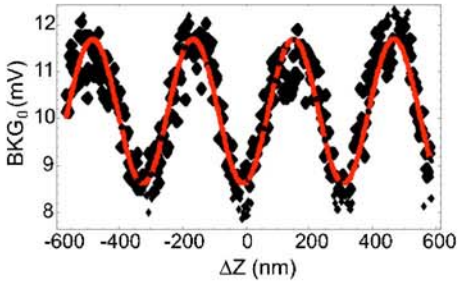

FIG. 5. (Color online) (black symbols) Plot of the dc background observed when removing the tip from the optical path as a function of the sample position. (red line) Sinusoidal fit of the experimental data [$y = A\sin(4\pi/\lambda \cdot \Delta z + \phi)$, $A = (1.5 \pm 0.1)$ mV].

It is also important to evaluate the contribution of the field backscattered by the focusing lens to the total BKG signal. We expect that, since the average tip-lens distance is constant, the contribution of E_L to the harmonic terms BKG_n will be a mere constant offset, i.e., not depending on Δz. Vice versa, the dc term BKG_0, due to the interference between E_L and E_S ($\mathrm{BKG}_0 = |E_S + E_L|^2$), is expected to depend on the sample's position Δz sinusoidally. For these measurements we have retracted the tip by several millimeters and swept the sample vertically. In Fig. 5 (black symbols) we clearly see the interference pattern due to the variation of the lens-sample distance. From a measure of the oscillation amplitude (the red line is from a sinusoidal fit), we assess that the sample-lens interference contribution amounts to a maximum of 10% of the total dc background (BKG_0) measured in the presence of the tip [Fig. 2(a)].

III. THEORETICAL INTERPRETATION

Understanding the physical origin of the background and, in particular, of its harmonic components is of fundamental importance to model and quantitatively evaluate the rejection power of higher harmonics demodulation. The presence of a modulated background field using evanescent wave illumination has been pointed out by Hudlet *et al.*[22] Concerning the illumination with propagative fields, Formanek *et al.*,[25] within the dipole approximation,[9] have shown that the BKG modulated at the first harmonic arises from the interplay of the fields reflected by the sample and the tip shaft. In the following, we will see that such stray fields, interfering with the back reflection of the focusing optics, provide a source of BKG components modulated at every harmonic of the tip vibration frequency. Following the scheme of Fig. 1, let us define a coordinate system in which the z-axis points downward and the zero coincides with the tip position at rest. In this system we call $a(t) = a_0 \cos(\omega t)$ the tip position, l_0 the position of the focusing lens, $z(t) = z_0 + \Delta z(t)$ the sample position, where z_0 is the position at rest, and $\Delta z(t)$ the vertical excursion as a function of the time. As we have observed experimentally, the BKG originates from the interference on the detector of three fields backscattered by the tip shaft $E_F = E_F^0 \exp(-i\Delta\phi_{FL})$, the sample's bottom surface $E_S = E_S^0 \exp(-i\Delta\phi_{SL})$, and the focusing optics $E_L = E_L^0$. Where, given $k = 2\pi/\lambda$, the phases $\Delta\phi_{FL} = 2k[l_0 - a(t)]$ and $\Delta\phi_{SL} = 2k[l_0 - z(t)]$ are related to the optical path differences accumulated by the fields scattered, respectively, by the tip and by the sample, with respect to the one scattered by the lens, in their travel from the laser to the detector. Substituting in Eq. (1), the expression reduces to

$$\begin{aligned}\mathrm{BKG} = {} & C_0 + B_{SL}\cos[\phi_1 - 2k\Delta z(t)] + B_{FL} \\ & \times \cos[\phi_0 - 2ka_0\cos(\omega t)] + B_{FS}\cos[\phi_2 + 2k\Delta z(t) \\ & - 2ka_0\cos(\omega t)],\end{aligned} \tag{2}$$

where the constant parameters $C_0 = |E_F|^2 + |E_S|^2 + |E_L|^2$, $B_{SL} = 2|E_L E_S|$, $B_{FL} = 2|E_L E_F|$, and $B_{FS} = 2|E_F E_S|$ depend on the amount of light backscattered by the single sources. The phases $\phi_0 = 2kl_0$, $\phi_1 = 2k(l_0 - z_0)$, and $\phi_2 = 2kz_0$ depend on the distances of the lens and of the sample at rest from the tip. The latter quantities can be assumed as constants, as well, unless mechanical or thermal drifts take place moving apart the scattering sources. Expanding the cosines in Eq. (2) we find

$$\begin{aligned}\mathrm{BKG} = {} & C_0 + B_{SL}\cos[2k\Delta z(t) - \phi_1] + \{B_{FL}\cos(\phi_0) \\ & + B_{FS}\cos[\phi_2 + 2k\Delta z(t)]\}\cos[2ka_0\cos(\omega t)] \\ & + \{B_{FL}\sin(\phi_0) + B_{FS}\sin[\phi_2 + 2k\Delta z(t)]\} \\ & \times \sin[2ka_0\cos(\omega t)],\end{aligned} \tag{3}$$

from which we evidence the presence of terms having the form $\cos(\alpha\cos\omega t)$ and $\sin(\alpha\cos\omega t)$. The latter expressions can be developed into a series of terms oscillating at the harmonic frequencies $n\omega$, whose amplitudes are given by the nth-order Bessel functions of first kind J_n.[32] This is formally the reason why we must expect a BKG signal at every harmonic order. In particular, the expansion of Eq. (3) yields

$$\begin{aligned}\mathrm{BKG} = {} & C_0 + B_{SL}\cos[2k\Delta z(t) - \phi_1] + \{B_{FL}\cos(\phi_0) \\ & + B_{FS}\cos[\phi_2 + 2k\Delta z(t)]\} \cdot J_0(2ka_0) \\ & + 2\{B_{FL}\cos(\phi_0) + B_{FS}\cos[\phi_2 + 2k\Delta z(t)]\} \\ & \times \sum_{n=1}^{\infty} (-1)^n J_{2n}(2ka_0)\cos[(2n)\omega t] \\ & + 2\{B_{FL}\sin(\phi_0) + B_{FS}\sin[\phi_2 + 2k\Delta z(t)]\} \\ & \times \sum_{n=0}^{\infty} (-1)^n J_{2n+1}(2ka_0)\cos[(2n+1)\omega t],\end{aligned} \tag{4}$$

which is an expression of the form $\mathrm{BKG}_0(a_0, \Delta z) + \Sigma_{n \geq 1}\mathrm{BKG}_n(a_0, \Delta z) \cdot \cos(n\omega t)$, consisting of a dc signal plus a series of harmonics whose amplitudes depend both on the sample position and on the tip vibration amplitude. The amplitude of the dc component is

$$\begin{aligned}\mathrm{BKG}_0(a_0, \Delta z) = {} & C_0 + B_{SL}\cos[2k\Delta z(t) - \phi_1] \\ & + J_0(2ka_0) \cdot \{B_{FL}\cos(\phi_0) \\ & + B_{FS}\cos[\phi_2 + 2k\Delta z(t)]\},\end{aligned} \tag{5}$$

while the amplitudes of the even and of the odd harmonics are, respectively,

$$\mathrm{BKG}_{2n}(a_0,\Delta z) = 2\cdot(-1)^n J_{2n}(2ka_0)\cdot\{B_{FL}\cos(\phi_0) + B_{FS}\cos[\phi_2 + 2k\Delta z(t)]\}, \quad (6)$$

and

$$\mathrm{BKG}_{2n+1}(a_0,\Delta z) = 2\cdot(-1)^n J_{2n+1}(2ka_0)\cdot\{B_{FL}\sin(\phi_0) + B_{FS}\sin[\phi_2 + 2k\Delta z(t)]\}. \quad (7)$$

These expressions represent the transfer functions between the average vertical position of the sample (Z) and the optical far-field background. Let us analyze them in more detail. The dc component is composed of a constant offset $C_0 + J_0(2ka_0)\cdot B_{FL}\cos(\phi_0)$ slightly dependent on a_0 (usually $C_0 \gg B_{FL}$), superimposed to a term

$$B_{SL}\cos[2k\Delta z(t) - \phi_1] + [J_0(2ka_0)B_{FS}]\cdot\cos[\phi_2 + 2k\Delta z(t)], \quad (8)$$

oscillating with the sample position, with period $\Delta z = \lambda/2$. This term arises from the linear superposition of the sample-lens and of the tip-sample interferences, respectively. The two contributions add coherently (amplitude and phase) yielding the total BKG_0 signal experimentally observed in Figs. 2(a) and 2(c). In particular, in absence of the tip [$B_{FS} = 0$ in Eq. (8)], the light scattered by the focusing lens leads to a BKG_0 signal whose modulation amplitude B_{SL} is much smaller than B_{FS}, as reported in Fig. 5. Therefore, since the second term of Eq. (8) is prevalent, we can conclude that the dc background depends on the tip-oscillation amplitude as $\mathrm{BKG}_0 \propto J_0(2ka_0)$. The structure of the BKG at the higher harmonics is similar. The even harmonics [Eq. (6)] are characterized by an offset $2(-1)^n J_{2n}(2ka_0)B_{FL}\cos(\phi_0)$, induced by the backscattering of the lens ($B_{FL} = 2|E_L E_F|$), plus a term $2(-1)^n J_{2n}(2ka_0)B_{FS}\cos[\phi_2 + 2k\Delta z(t)]$ oscillating with the sample vertical position, whose amplitude A_n scales proportionally to $J_n(2ka_0)$. The odd harmonics [Eq. (7)] show the same behavior, but the oscillatory dependence on the sample position is shifted by 90° with respect to the even ones. For small oscillations, $ka_0 << 1$, we can expand the Bessel functions in power series, finding that the background modulation amplitude depends on the tip oscillation amplitude through a polynomial law of the dimensionless quantities $(ka_0)^n \propto (a_0/\lambda)^n$.[29] To the first order in ka_0, R_n is expected to be

$$R_n = \frac{|A_n|}{|A_0|} = \frac{2J_n(2ka_0)}{J_0(2ka_0)} \approx \frac{2}{n!}\left(\frac{2\pi a_0}{\lambda}\right)^n. \quad (9)$$

That is, the background at the nth harmonic scales down as the nth power of the ratio a_0/λ multiplied by a further factor $1/n!$. In particular, the advantage of increasing by 1 the harmonic order, in terms of BKG reduction, is $R_{n+1}/R_n \approx ka_0/(n+1)$. This value must be compared with the near-field signal loss due to the spatial filtering effect[17,18] to assess the best experimental parameters. In Fig. 6 we plot the BKG amplitude at the various harmonics A_n as a function of (a_0/λ) (in the top axis we report the values of a_0 for $\lambda = 633$ nm). In the visible range (e.g., for HeNe illumination), and for a tip oscillation of 20 nm peak to peak ($a_0 = 10$ nm), increasing the harmonic order $n = 1$, 2, and 3 leads to an increased rejection of the background, whose modulation amplitude will be reduced to values of 10^{-1}, 5×10^{-3}, and 2×10^{-4} with respect to the dc amplitude. Decreasing the tip oscillation by one order of magnitude, from 10 to 1 nm (thicker lines in Fig. 6), has different consequences depending on the harmonic order of the BKG. While the dc signal (black line) is almost unaffected, the amplitude of the signal demodulated at the first, second, and third harmonics (red, blue, and green lines) is reduced, respectively, by further one, two, and three orders of magnitude. In the mid IR ($\lambda \sim 10$ μm) the technique is even more powerful, since for $a_0 = 10$ nm [namely, $(a_0/\lambda) \approx 10^{-3}$], first, second, and third harmonic demodulations will reduce the BKG amplitude of factor of 6×10^{-3}, 2×10^{-5}, and 4×10^{-8} with respect to the dc amplitude, respectively. The higher rejection power in the IR part of the electromagnetic spectrum explains why far-field oscillations are clearly visible in the second harmonic approach curves at in the visible ($\lambda = 633$ nm) reported by Hillenbrand and Keilmann[11] and Roy *et al.*,[24] while there is just an outline in the 2ω curve at $\lambda = 10.6$ μm reported by Formanek *et al.*[25]

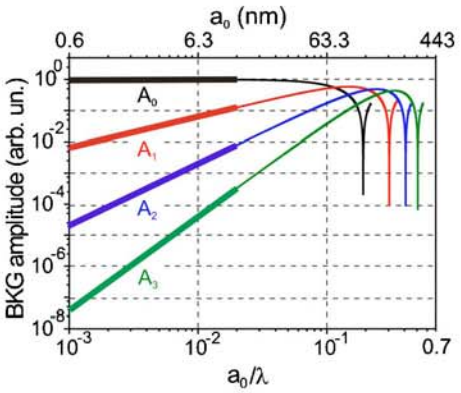

FIG. 6. (Color online) Plot of the background modulation amplitudes at the various harmonics [dc (black), first (red), second (blue), and third (green)] as a function of the ratio (a_0/λ) (bottom axis) and of a_0 assuming $\lambda = 633$ nm (top axis).

Decreasing the oscillation amplitude is, however, not the only way to reduce the BKG. In fact, when we plot the correct expression $|J_n(2ka_0)|$ for the amplitude of the BKG harmonics, as in Fig. 6, it emerges that there are some particular values of the tip oscillation amplitude $\tilde{a}_0$ that strongly reduce the BKG. Such values represent the first zeros of the Bessel functions for which $J_n(2k\tilde{a}_0) = 0$. The corresponding values of the ratios $\tilde{a}_0/\lambda$ for $n = 0, \ldots, 4$ fall in the interval $a_0/\lambda \sim 0.2$–0.7, as reported in Table I. In order to reject the BKG at the nth harmonic we can thus either decrease the oscillation amplitude to smaller and smaller values, or tune the oscillation amplitude a_0 to well defined values $\tilde{a}_0$ which

TABLE I. Theoretical values of the ratios $\tilde{a}_0/\lambda$, corresponding to the zeros of the J_n Bessel functions, that yield complete background suppression at each harmonic n. The values $\Delta a_0/\tilde{a}_0$ indicate the precision needed on $\tilde{a}_0$ to have a BKG rejection better than 10^3 at every harmonic.

Order	$n=0$	$n=1$	$n=2$	$n=3$	$n=4$
$\tilde{a}_0/\lambda$	0.191	0.305	0.409	0.508	0.604
$\Delta a_0/\tilde{a}_0$	0.0016	0.0013	0.0013	0.001	0.001

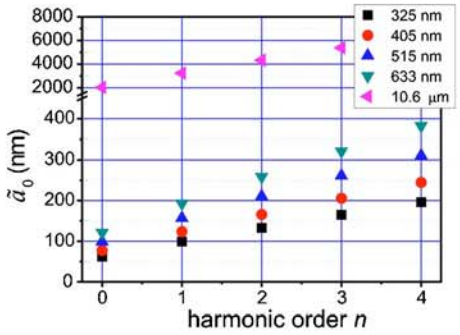

FIG. 7. (Color online) Values of the tip oscillation amplitude $\tilde{a}_0$ corresponding to the first zeros of the nth Bessel functions for various wavelengths λ.

depend on n and λ. The numerical values of $\tilde{a}_0$ for some typical laser wavelengths are shown in Fig. 7. In particular, in the NUV-visible region (black, red, blue, and green symbols in Fig. 7), the spectrum of values of $\tilde{a}_0$ which allow to null the BKG at the first three harmonics falls in the 100–200 nm range. These values are certainly reasonable for experimental configurations employing freestanding tips or atomic force microscopy (AFM) cantilevers,[33,34] but quite unusual for systems based on quartz tuning forks, suited for low oscillation amplitudes. On the contrary, oscillation amplitudes of several microns (pink symbols in Fig. 7) would be required to accomplish such a task in the mid-IR ($\lambda = 10.6\ \mu$m). In order to establish how fine the tuning of a_0 must be, we note that the Bessel functions are almost linear around their first zeros. This implies that the maximum discrepancy interval $\Delta a_0/\tilde{a}_0$ allowed to have a BKG rejection of three orders of magnitude is of the order of 0.1%. More precise calculations for the different harmonics are reported in Table I.[35]

IV. NONLINEAR TOPOGRAPHY ARTIFACTS

In near-field optical microscopy an artifact can generally be defined as information recorded in the optical map which has not an optical origin. In particular, topography artifacts are induced by the vertical motion of the sample that modulates the intensity of the far-field BKG from point to point. Such signal, originating from an interference process, is thus expected to vary on tip-sample distances of the order of the laser wavelength. In particular, if the topography excursions are much smaller than λ, the coupling can be assumed as linear,[7] leading to optical maps very similar to the topographical counterpart, and easily identifiable as affected by artifacts. If the height of the topography structures becomes comparable with the wavelength, or larger, the sinusoidal character of the interference profile will provide optical maps qualitatively different from the topography.[8] From the physical point of view there are almost no differences between topography artifacts in aperture- and apertureless-SNOM. In aperture-SNOM (illumination mode), the far-field emission from the probe interferes with the light reflected by the sample. In apertureless-SNOM it is the light scattered by the tip shaft that interferes with the light reflected by the sample (plus a smaller contribution from the focusing lens which, as we have seen, is negligible). As a consequence, the BKG transfer functions are expected to be analogous. Nevertheless, the different experimental techniques employed to detect the optical signals can yield different results. In aperture-SNOM, the tip is not vertically dithered and the dc component $S \propto A + B\cos[K\Delta z(t) + \phi]$ is the only signal acquired. It consists of an offset A superimposed to a smaller modulation ($B \ll A$). K varies from $k = 2\pi/\lambda$ for grazing collection to $k = 4\pi/\lambda$ for a collection geometry parallel to the tip axis.[8,36,37] In apertureless-SNOM higher harmonics demodulation requires the use of a lock-in amplifier whose output is usually set to provide the modulus of the optical signal, i.e., $S_n \propto |A + B\cos[K\Delta z(t) + \phi]|$. Since the modulation amplitude B is much greater than the offset A ($B \gg A$), the resulting approach curves will be similar to the ones in Fig. 2(b).[10,25] In particular, monitoring the modulus rather than the in-phase component of the optical signal, accentuates its nonlinear dependence on the sample position. The signal, in fact, will vary on length scales which are about halved, passing from the minimum to the maximum on distances of $\sim\lambda/7$ [Fig. 2(b)], rather than $\lambda/4$ [Fig. 2(c)].[38] As a consequence, at least in the visible range, topographic structures as short as 60 nm are already expected to produce optical artifacts nonlinearly related with the topography. To better visualize such phenomenon, starting from Eqs. (5)–(7), we have calculated the approach curves that would be expected for typical experimental conditions: $a_0 = 10$ nm, $\lambda = 633$ nm, 0.5% of light back reflected from the lens, 4% from the sample, and 50% from the tip shaft. In Fig. 8 we show the behavior of the dc background (a) and the modulus of the first three harmonics [(b)–(d), respectively] as a function of the distance between the tip apex and the average sample plane Z. We assume random phases ϕ_0 and ϕ_2 (since they depend on the tip length and on the lens position, these parameters are not really controllable in a experiment). The position $Z = 0$ corresponds to the contact point of the tip with the sample surface. In CGM operation, any topographic feature will cause a drawdown of the sample, and thus an increase of Z. As a consequence, the BKG signal will vary according to the curves in Fig. 8. It must be noted that, in the absence of a clear fingerprint of the near-field optical interaction in the contact region ($Z \sim 0$), the optical signal mea-

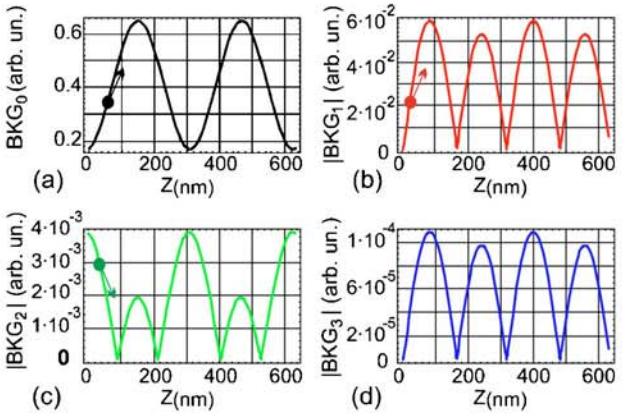

FIG. 8. (Color online) Approach curves predicted for the dc background (a) and the modulus of the first three harmonics [(b)–(d), respectively] base on Eqs. (5)–(7), for $a_0 = 10$ nm and $\lambda = 633$ nm. The colored circles and the arrows indicate how the optical signal changes as a function of an increased sample topography.

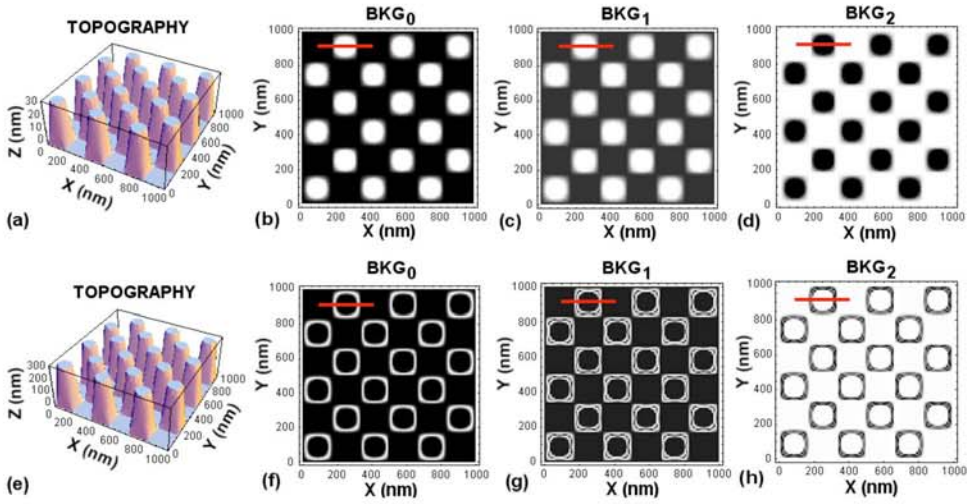

FIG. 9. (Color online) [(b) and (f)] dc, [(c) and (g)] first harmonic, and [(d) and (h)] second harmonic BKG maps simulated for a topography [(a) and (e)] consisting of pillars on a horizontal substrate, having heights of 30 and 300 nm, respectively.

sured will be due entirely to the BKG contribution. And even the presence of such a fingerprint does not guarantee that the optical signal, and the corresponding optical image, will be artifact-free. We must, in fact, assure that the changes of the optical signal are not entirely due to the BKG modulations, but do originate from the near-field scattering of the sample. As a consequence, we should check that at least one of the following conditions is satisfied: (i) the BKG is actually below the noise level, (ii) the excursions of the recorded optical signal are larger than the BKG modulations observed in the far-field region of the approach curves, and (iii) topography structures located at the same absolute position Z produce different optical responses (as in Ref. 11). From Eq. (7) we note that the first and the third harmonic signals have the same functional dependence on Z [Figs. 8(b) and 8(d)]. Therefore, in the presence of artifacts, the corresponding optical maps are expected to be qualitatively alike (the only difference relying on the magnitude of the signal). More generally, we expect the images acquired at the even (or at the odd) harmonics to be all qualitatively identical, independently the specific harmonic order. This would not be the case, indeed, if some near-field contribution was present, due to high-pass filtering effect on the image spatial frequencies.[18]

It is interesting to visualize the fictitious optical maps expected for an experiment like the one mentioned above, assuming the transfer functions plotted in Fig. 8, calculated from Eqs. (5)–(7). In Figs. 9(b)–9(d) we display the images calculated for the dc, the modulus of the first and of the second harmonics, respectively, for a sample consisting of set of truncated cone pillars, having a base diameter of 170 nm and height of 30 nm grown on a flat glass coverslip with plane parallel faces [Fig. 9(a)]. The total sample's scattering is assumed to be due entirely to the back reflection of the bottom coverslip surface, i.e., the scattering of the pillars is assumed negligible. For small topography excursions optical images qualitatively similar to the topography are retrieved, but in the second harmonic map (d) the contrast is reversed. The different behaviors can be understood considering the slope of the approach curves at the contact point ($Z=0$), which is positive for the dc and the first harmonic [Figs. 8(a) and 8(b)], and negative the second harmonic [Fig.

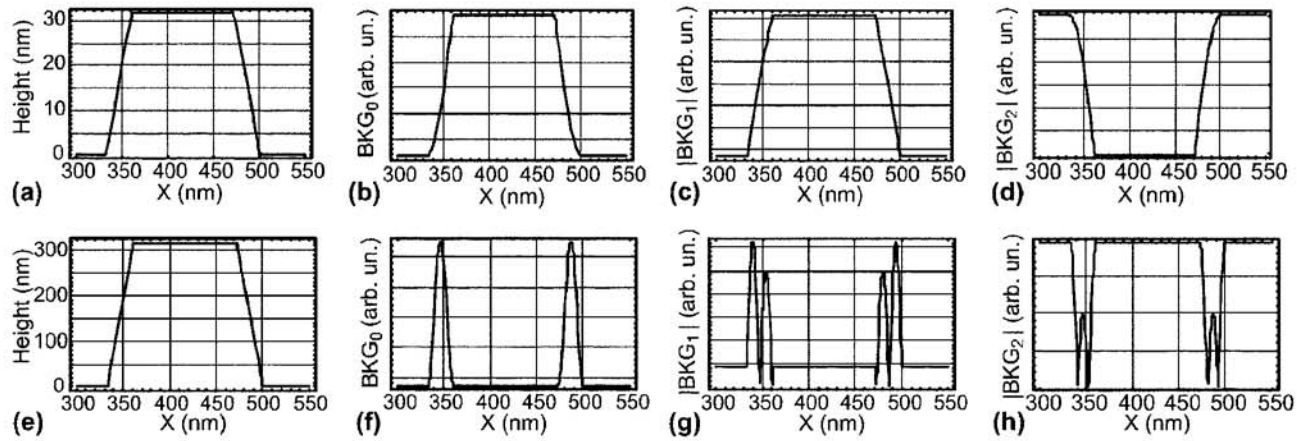

FIG. 10. [(a)–(h)] Line profiles drawn in correspondence of the red lines marked in Fig. 9. The optical profiles reproduce the topography only for the 30 nm high pillars.

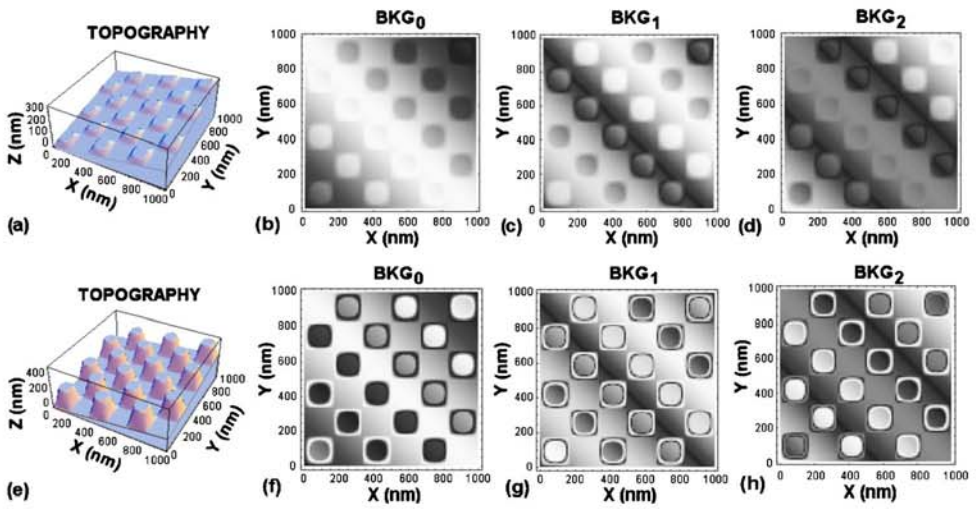

FIG. 11. (Color online) [(b) and (f)] dc, [(c) and (g)] first harmonic, and [(d) and (h)] second harmonic BKG maps simulated a topography [(a) and (e)] consisting of pillars on an wedgelike substrate (inclination 10°), having heights of 30 and 300 nm, respectively.

8(c)]. For structures sensibly higher, as in Fig. 9(e) (300 nm, i.e., $\sim\lambda/2$), the optical maps become different from the topography. Annular structures appear in the dc image [Fig. 9(f)], double rings show up in the $|BKG_1|$ map [Fig. 9(g)], and contrast reversal is observed in the $|BKG_2|$ image [Fig. 9(h)]. The qualitative difference with respect to the previous structures is better highlighted in the line profiles of Fig. 10. For pillar heights of $\sim\lambda/20$ the transfer functions in Figs. 8(a) and 8(c) behave as linear. Therefore, the optical signals in Figs. 10(b) and 10(d) perfectly reproduce the topography profile [Fig. 10(a)], apart from the contrast inversion in the second harmonic. In particular, no lateral shifts are expected between the topography and the optical maps. For pillar heights of $\sim\lambda/2$ [Fig. 10(e)] the nonlinearity of the transfer function yields modulations of the optical signals [Figs. 10(f)–10(h)] difficult to attribute to artifacts *a priori*. The signal enhancement at the structure edges [Figs. 10(g) and 10(h)] could, in fact, be confused with a high-pass spatial frequency filtering,[18] and be attributed to a genuine near-field effect. In particular, the shape and position of such modulations will depend on several experimental parameters such as the harmonic number (experimentally controllable), or the phases ϕ_0, and ϕ_2 (hard to control). This phenomenon appears in a more intriguing way if we suppose that the pillars have grown a coverslip whose faces are not perfectly parallel, i.e., on a wedge. In such case the different local thicknesses of the coverslip will induce a further optical path difference between the light reflected by the bottom sample's surface, and the light reflected by the tip, which will follow the top coverslip surface. As a consequence, a long range sinusoidal modulation is expected in the optical signal, as evidenced in Fig. 11. Here we have simulated the fictitious optical maps (dc, modulus of the first, and of the second harmonics) that would arise for pillars of 30 nm [(b)–(d)] and 300 nm [(f)–(h)] grown onto a coverslip whose top surface is inclined of $\sim 10°$ with respect to the bottom surface, assumed horizontal [Figs. 11(a) and 11(e)]. In particular, we see [Fig. 11(b)] that the pillars can appear either brighter or darker with respect to the neighboring substrate, depending on their spatial position within the map. It can also happen that half of the single pillar looks bright and half dark, as in Fig. 11(d). Moreover, if the pillars height is comparable to the wavelength, they can appear as bright rings with a dark interior or vice versa within the same map, as in Figs. 11(g) and 11(h). A similar situation has already been encountered experimentally for the demodulated first harmonic signal.[3] The presence of artifacts in similar cases can, however, be pointed out noting that an increase of the harmonic order is not expected to suppress the long range modulations. The disappearance of such a feature from the images at higher harmonics can thus be held as a proof of the genuine nature of the optical signal.[3,19]

V. CONCLUSIONS

In conclusion, the far-field background in apertureless-SNOM has been studied both theoretically and experimentally. The occurrence of a signal modulated at frequencies multiple of the tip vibration, evidenced experimentally, has been explained in terms of the interference process taking place between the stray fields scattered by the sample and the tip shaft. The field backscattered by the focusing optics has been observed to take part only in the dc background. The power-law dependence of the background modulations on the harmonic order has been put forward, explaining quantitatively the advantages obtainable in terms of background rejection when increasing the harmonic order. The possibility to reject the background decreasing the tip oscillation amplitude has been quantitatively studied, highlighting at the same time the opportunity to exploit the first zeros of the Bessel functions to accomplish such a task. Finally, we have simulated different optical images induced by topography artifacts in correspondence to structures having different heights, deposited on flat or inclined substrates, pointing out the effect of the nonlinear BKG-topography coupling, and of the substrate inclination on the optical images. This, in particular, has allowed us to state a precise criterion for artefacts identification: in presence of artefacts, the optical maps acquired at the even harmonics are expected to be all qualitatively identical, independently from the harmonic order (the

same states for the odd harmonics). Therefore, any qualitative difference between the optical images acquired at different even (or odd) harmonics, such as the disappearance of the long range modulations induced by the sample's inclination, can be reasonably ascribed to genuine near-field spatial filtering effects.[3,12,19]

ACKNOWLEDGMENTS

A. Mlayah is acknowledged for carefully reading the manuscript and M. Labardi for fruitful discussions. One of the authors (G.B.) acknowledges the CNR-CNRS bilateral project "Diffusione Raman e Brillouin risonante e localizzazione spaziale di stati elettronici" for partial financial support. P.G.G. is grateful to D. Arigò and G. Spinella for their skill ful expertise in the SNOM setup manufacturing.

[1]D. W. Pohl, W. Denk, and M. Lanz, Appl. Phys. Lett. **44**, 651 (1984); A. Lewis, M. Isaacson, A. Harootunian, and A. Murray, Ultramicroscopy **13**, 227 (1984).
[2]E. Betzig, J. K. Trautman, T. D. Harris, J. S. Weiner, and R. L. Kostelak, Science **251**, 1468 (1991).
[3]S. Patanè, P. G. Gucciardi, M. Labardi, and M. Allegrini, Riv. Nuovo Cimento **27**, 1 (2004).
[4]L. Novotny, R. X. Bian, and X.-S. Xie, Phys. Rev. Lett. **79**, 645 (1997).
[5]F. Zenhausern, Y. Martin, and H. K. Wickramasinghe, Science **269**, 1083 (1995).
[6]A. Lahrech, R. Bachelot, P. Gleyzes, and A. C. Boccara, Opt. Lett. **21**, 1315 (1996).
[7]B. Hecht, H. Bielefeldt, Y. Inouye, D. W. Pohl, and L. Novotny, J. Appl. Phys. **81**, 2492 (1997).
[8]P. G. Gucciardi and M. Colocci, Appl. Phys. Lett. **79**, 1543 (2001).
[9]B. Knoll and F. Keilmann, Opt. Commun. **182**, 321 (2000).
[10]R. Hillenbrand and F. Keilmann, Phys. Rev. Lett. **85**, 3029 (2000).
[11]R. Hillenbrand and F. Keilmann, Appl. Phys. Lett. **80**, 25 (2001).
[12]M. Labardi, S. Patanè, and M. Allegrini, Appl. Phys. Lett. **77**, 621 (2000).
[13]T. Taubner, F. Keilmann, and R. Hillenbrand, Nano Lett. **4**, 1669 (2004).
[14]L. Stebunova, B. B. Abramitchev, and G. C. Walker, Rev. Sci. Instrum. **74**, 3670 (2003).
[15]R. Hillenbrand, T. Taubner, and F. Keilmann, Nature (London) **418**, 159 (2002).
[16]N. Ocelic and R. Hillenbrand, Nat. Mater. **3**, 606 (2004).
[17]M. Labardi, S. Patanè, and M. Allegrini, in *Proceedings of the International School of Physics "E. Fermi" Course CXLIV, Varenna, Italy, 2001*, edited by M. Allegrini, N. Garcia, and O. Marti (IOS, Amsterdam, 2001), p. 425.
[18]J. N. Walford *et al.*, J. Appl. Phys. **89**, 5159 (2001).
[19]N. Maghelli, M. Labardi, S. Patanè, F. Irrera, and M. Allegrini, J. Microsc. **202**, 84 (2001).
[20]I. Stefanon, S. Blaize, A. Bruyant, S. Aubert, G. Lerondel, R. Bachelot, and P. Royer, Opt. Express **13**, 5553 (2005).
[21]T. Taubner, F. Keilmann, and R. Hillenbrand, J. Korean Phys. Soc. **47**, S213 (2005).
[22]S. Hudlet *et al.*, Opt. Commun. **230**, 245 (2004).
[23]F. Formanek, Y. De Wilde, and L. Aigouy, J. Appl. Phys. **93**, 9548 (2003).
[24]D. Roy, S. H. Leong, and M. E. Welland, J. Korean Phys. Soc. **47**, S140 (2005).
[25]F. Formanek, Y. De Wilde, and L. Aigouy, Ultramicroscopy **103**, 133 (2005).
[26]B. Ren, G. Picardi, and B. Pettinger, Rev. Sci. Instrum. **75**, 837 (2004).
[27]K. Dickmann, F. Demming, and J. Jersch, Rev. Sci. Instrum. **67**, 845 (1996).
[28]E. Cefalì, S. Patanè, P. G. Gucciardi, M. Labardi, and M. Allegrini, J. Microsc. **210**, 262 (2003).
[29]P. G. Gucciardi, G. Bachelier, A. Mlayah, and M. Allegrini, Rev. Sci. Instrum. **76**, 036105 (2005).
[30]K. Karrai and R. D. Grober, Appl. Phys. Lett. **66**, 1842 (1995).
[31]K. Karrai, in *Le Champ Proche Optique*, edited by D. Courjon and C. Bainier (Springer-Verlag, Paris, 2001).
[32]M. R. Spiegel and J. Liu, *Mathematical Handbook of Formulas and Tables*, 2nd ed. (McGraw-Hill, New York, 1999).
[33]R. Bachelot, P. Gleyzes, and A. C. Boccara, Opt. Lett. **20**, 1924 (1995).
[34]P.-M. Adam, P. Royer, R. Laddada, and J.-L. Bijeon, Ultramicroscopy **71**, 327 (1998).
[35]Here R_n is considered as the ratio between the BKG amplitude A_n and the amplitude of the dc component A_0 calculated in the small oscillations approximation ($ka_0 \ll 1$).
[36]P. G. Gucciardi, M. Labardi, S. Gennai, F. Lazzeri, and M. Allegrini, Rev. Sci. Instrum. **68**, 3088 (1997).
[37]M. Labardi, P. G. Gucciardi, M. Allegrini, and C. Pelosi, Appl. Phys. A: Mater. Sci. Process. **66**, S397 (1998).
[38]The periodicity is exactly halved only if the offset is null.

Rayonnement scientifique

40 articles dans des revues internationales avec comité de lecture dont

2 Phys Rev. Lett.
1 Nano lett.
1 Appl. Phys. Lett.
8 J. Phys. Chem. C
1 J. Phys. Chem. B
1 Opt. Exp.
5 Phys. Rev. B

1 chapitre dans un ouvrage scientifique

P. G. Gucciardi, G. Bachelier, S. J. Stranick, M. Allegrini, Applied Scanning Probe Methods VIII, edited by B. Bhushan, C. Fuchs and S. Kawata, pp. 1-29, Springer-Verlag, New-York, (2008).

1 brevet

G. Revillod, J. Duboisset, I. Russier-Antoine, E. Benichou, G. Bachelier, C. Jonin and P.-F. Brevet, FR 08 52286, déposé le 4 avril 2008.

23 présentations orales depuis 2006 dans des conférences dont

- 2 invitées dans des conférences internationales
- 17 orales dans des conférences internationales
- 4 orales dans des conférences nationales

Collaborations internationales:

- **P. G. Gucciardi**, NanoLab, IPCF, Messina, Italy.
- **B. Hecht**, Nano-Optics and Bio-Photonics Group, Institute of Physics, Universitaet Wuerzburg, Germany.
- **J. Bonse**, Impulslaser Technologien, Lasersicherheit, BAM, Berlin, Germany.
- **J. Gonzalo, C. N. Afonso, J. Siegel and J. Solis**, Laser Processing Group, IO, Madrid, Spain.

Collaborations nationales:

- **A. Bouhelier**, Institut Carnot de Bourgogne, Université de Bourgogne, Dijon.
- **A. Brioude**, Précurseurs moléculaires et matériaux inorganiques, LMI, Lyon.
- **A. Mermet and E. Duval**, Verres, nanostructures et géomatériaux , LPCML, Lyon.
- **B. Prevel**, Agrégats et Nanostructures, LPMCN, Lyon.
- **C. Bonnet, E. Cottancin, J. Lermé and M. Pellarin**, Agrégats et Nanostructures, LASIM, Lyon.
- **F. Vallée and N. Del Fatti**, FemtoNanoOptics, LASIM, Lyon.

Co-encadrement de thèse:

- **J. Butet** 2009-2011 (stage de M2 puis thèse): "Génération de Second Harmonique des Nanostructures Métalliques", 4 articles acceptés [34, 36, 39, 40].

Mise en place d'enseignements directement liés à mon activité de recherche:

- **Cours de plasmonique** au Master Nanoscale Engineering, mise en place novembre 2010.
- **Cours de simulation par éléments finis** ouverts à l'école doctorale, aux Masters et aux enseignants-chercheurs, mise en place janvier 2011 avec David Amans.

Liste des publications:

2010

40- **Origin of the optical second-harmonic generation in spherical gold nanoparticles: local surface and non-local bulk contributions**, G. Bachelier, J. Butet, I. Russier-Antoine, C. Jonin, E. Benichou and P.-F. Brevet, Phys. Rev. B, 82, 235403 (2010).

39- **Three-dimensional mapping of single gold nanoparticles embedded in a homogeneous transparent matrix using optical second-harmonic generation**, J. Butet, G. Bachelier, J. Duboisset, F. Bertorelle, I. Russier-Antoine, C. Jonin, E. Benichou and P.-F. Brevet, Opt. Express, 18, 22314 (2010).

38- **Second Harmonic Generation, a new approach for analyzing the interfacial properties of a short tryptophan-rich peptide**, G. Matar, J. Duboisset, E. Benichou, G. Bachelier, I. Russier-Antoine, Ch. Jonin, D. Ficheux, P.F. Brevet and F. Besson, Chem. Phys. Lett., 500, 161 (2010).

37- **First Hyperpolarizability of the Natural Aromatic Amino Acids Tryptophan, Tyrosine and Phenylalanine and the tripeptide Lysine – Tryptophane - Lysine Determined by Hyper Rayleigh Scattering**, J. Duboisset, G. Matar, I. Russier-Antoine, E. Benichou, G. Bachelier, Ch. Jonin, D. Ficheux, F. Besson, P. F. Brevet, J. Phys. Chem. B 114, 43 (2010).

36- **Interference between selected dipoles and octupoles in the optical Second Harmonic Generation from spherical gold nanoparticles,** J. Butet, G. Bachelier, I. Russier-Antoine, C. Jonin, E. Benichou and P.F. Brevet, Phys. Rev. Lett., 105, 077401 (2010).

35- **Femtosecond laser ablation of indium phosphide in air: dynamical, structural and morphological evolution**, J. Bonse, G. Bachelier, S.M. Wiggins, J. Siegel, J. Solis, J. Krüger, H. Sturm, J. Opt. Adv. Mat., 12, 421 (2010).

34- **Optical Second Harmonic Generation of Single Metallic Nanoparticles Embedded in a Homogeneous Medium**, J. Butet, J. Duboisset, G. Bachelier, I. Russier-Antoine, E. Benichou, C. Jonin, P.-F. Brevet, Nano Lett., 10, 1717 (2010).

33- **Symmetry cancellations in the quadratic hyperpolarizability of non-entrosymmetric gold decahedra**, I. Russier-Antoine, J. Duboisset, G. Bachelier, E. Benichou, C. Jonin, N. Del Fatti, F. Vallée, A. Sánchez-Iglesias, I. Pastoriza-Santos, L.M. Liz-Marzan, P.F. Brevet, J. Phys. Chem. Lett., 1, 874 (2010).

2009

32- **Single Metallic Nanoparticle Sensitivity with Hyper Rayleigh Scattering**, J. Duboisset, I. Russier-Antoine, E. Benichou, G. Bachelier, Ch. Jonin and P. F. Brevet, J. Phys. Chem. C, 113, 13477 (2009).

31- **High-order vibration modes of bimetallic Ag-Au nanoparticles embedded in glass**, S. Adichtchev, S. Sirotkin, G. Bachelier, L. Saviot, S. Etienne, B. Stephanidis, E. Duval and A. Mermet, Phys. Rev. B, 79, 1098 (2009).

30- **"Comment on 'Compression Induced Chirality in Dense Molecular Films at the Air-ater Interface Probed by Second Harmonic Generation'" Reply**, Y. El Harfouch, E. Benichou, I. Russier-Antoine, G. Bachelier, Ch. Jonin, L. Berlouis and P.F. Brevet, J. Phys. Chem. C, 113, 4227 (2009).

29- **Surface plasmon resonance of single gold nanodimers near the conductive contact limit**, M. Pellarin, S. Marhaba, G. Bachelier, C. Bonnet, M. Broyer, E. Cottancin, N. Grillet, J. Lermé and J.-L.Vialle, J. Phys. Chem. C , 113, 4349 (2009).

28- **Combined nanoroughness and electric polarization for the local field enhancement of the Second Harmonic Response from the silver-electrolyte interface**, Y. El Harfouch, E. Benichou, I. Russier-Antoine, G. Bachelier, Ch. Jonin, L. Berlouis and P.F. Brevet, Phys. Rev. B, 79, 113407 (2009).

2008

27- **Fano profiles induced by near-field coupling in heterogeneous dimers of gold and silver nanoparticles**, G. Bachelier, I. Russier-Antoine, E. Benichou, C. Jonin, N. Del Fatti, F. Vallée, P.-F. Brevet, Phys. Rev. Lett. 101, 197401 (2008).

26- **Compression induced chirality in dense molecular films at the air-water interface probed by Second Harmonic Generation**, G. Martin-Gassin, E. Benichou, G. Bachelier, I. Russier-Antoine, C. Jonin, P.-F. Brevet, J. Phys. Chem. C 112, 12958 (2008).

25- **Surface heterogeneity in Au-Ag nanoparticles probed by Hyper-Rayleigh scattering**, I. Russier-Antoine, G. Bachelier, V. Sablonnière, J. Duboisset, E. Benichou, C. Jonin, F. Bertorelle, P.-F. Brevet, Phys. Rev. B 78, 035436 (2008).

24- **Multipolar second harmonic generation in noble metal nanoparticles**, G. Bachelier, I. Russier-Antoine, E. Benichou, C. Jonin, P.-F. Brevet, J. Opt. Soc. Am. B 25, 955 (2008).

23- **Transient reflectivity and transmission changes during plasma formation and ablation in fused silica induced by femtosecond laser pulses**, D. Puerto, W. Gawelda, J. Siegel, J. Bonse, G. Bachelier and J. Solis, Appl. Phys. A 92, 803 (2008).

22- **Quantitative absorption spectroscopy of a single gold nanorod**, O. Muskens, G. Bachelier, N. Del Fatti, F. Vallée, A. Brioude, A. Jiang, M.-P. Pileni, J. Phys. Chem. C 112, 8917 (2008).

21- **Optical response of a single spherical particle in a tightly focused light beam : application to the spatial modulation spectroscopy technique**, J. Lermé, G. Bachelier, P.

Billaud, C. Bonnet, M. Broyer, E. Cottancin, S. Marhaba, and M. Pellarin, J. Opt. Soc. Am. A 25, 493 (2008).

20- **Time- and space-resolved dynamics of ablation and optical breakdown induced by femtosecond laser pulses in indium phosphide**, J. Bonse, G. Bachelier, J. Siegel, J. Solis and H. Sturm, J. Appl. Phys. 103, 054910 (2008).

19- **Multipolar Contributions to the Second Harmonic Response from Mixed DiA-SDS Molecular Aggregates**, G. Revillod, J. Duboisset, I. Russier-Antoine, E. Benichou, G. Bachelier, Ch. Jonin, P.F. Brevet, J. Phys. Chem. C 112, 2716 (2008).

18- **Correlation Reflectance Spectroscopy of Heterogeneous Silver Nanoparticles Films upon Compression at the Air/Water Interface**, G. Martin-Gassin, Y. El Harfouch, E. Benichou, G Bachelier, I Russier-Antoine, Ch. Jonin, S. Roux, O. Tillement, P.F. Brevet, J. Phys. Condens. Matter 20, 055228 (2008).

17- **Correlation between the Extinction Spectrum of a Single Metal Nanoparticle and Its Electron Microscopy Image**, P. Billaud, S. Marhaba, E. Cottancin, L. Arnaud, G. Bachelier, C. Bonnet, N. Del Fatti, J. Lerme, F. Vallee, J.-L. Vialle, M. Broyer, M. Pellarin, J. Phys. Chem. C 112, 978 (2008).

16- **Background-free apertureless near-field optical imaging**, P. G. Gucciardi, G. Bachelier, S. J. Stranick, M. Allegrini, Applied Scanning Probe Methods VIII, edited by B. Bhushan, C. Fuchs and S. Kawata, pp. 1-29, Springer-Verlag, New-York, (2008).

15- **Hyper Rayleigh Scattering of Protein-Mediated Gold Nanoparticles Aggregates**, I. Russier-Antoine, J. Huang, E. Benichou, G. Bachelier, Ch. Jonin, P.F. Brevet, Chem. Phys. Lett. 450, 345 (2008).

2007

14- **Multipolar Contributions of the Second Harmonic Generation from Silver and Gold Nanoparticles,** I. Russier-Antoine, E. Benichou, G. Bachelier, C. Jonin, and P.F. Brevet, J. Phys. Chem. C 111, 9044 (2007).

13- **Size dispersion effects on the low-frequency Raman scattering of quasispherical silver nanoparticles : Experiment and theory,** G. Bachelier, J. Margueritat, A. Mlayah, J. Gonzalo, C. N. Afonso, Phys. Rev. B 76, 235419 (2007).

12- **Plasma formation and structural modification below the visible ablation threshold in fused silica upon femtosecond laser irradiation,** J. Siegel, D. Puerto, W. Gawelda, G. Bachelier, J. Solis, L. Ehrentraut, and J. Bonse, Appl. Phys. Lett. 91, 082902 (2007).

11- **From silver nanolentils to nanocolumns : surface plasmon–polaritons and confined acoustic vibrations,** J. Margueritat, J. Gonzalo, C. N. Afonso, G. Bachelier, A. Mlayah, A. S. Laarakker, D. B. Murray, and L. Saviot, Appl. Phys. A. 89, 369 (2007).

10- **Artifacts identification in apertureless near-field optical microscopy,** P.G. Gucciardi, G. Bachelier, M. Allegrini, J. Ahn, M. Hong, S. Chang, W. Jhe, S. C. Hong, and S. H. Baek, J. of Appl. Phys. 101, 064303 (2007).

2006

9- **Time- and space-resolved dynamics of melting, ablation, and solidification phenomena induced by femtosecond laser pulses in germanium,** J. Bonse, G. Bachelier, J. Siegel et J. Solis, Phys. Rev. B 74, 134106 (2006).

8- **Far-field background suppression in tip-modulated apertureless near-field optical microscopy,** P. Gucciardi, G. Bachelier et M. Allegrini, J. Appl. Phys. 99, 124309 (2006).

2002-2005

7- **Interferometric measurement of the tip oscillation amplitude in apertureless near-field optical microscopy,** P. Gucciardi, G. Bachelier, A. Mlayah et M. Allegrini, Rev. Sci. Instrum. 76, 036105 (2005).

6- **Electron-acoustic phonon interaction in a single quantum dots layer: acoustic mirror and cavity effects,** M. Cazayous, J. Groenen, J.R. Huntzinger, G. Bachelier, A. Zwick, A. Mlayah, E. Bedel-Pereira, F. Negri, H. Carrère, N. Bertru, C. Paranthoen et O. Dehaese, Phys. Rev. B 69, 125323 (2004).

5- **Surface Plasmon mediated Raman Scattering in metal nanoparticles,** G. Bachelier et A. Mlayah, Phys. Rev. B 69, 205408 (2004).

4- **Scattering of fight by sound on a nano-scale**, A. Mlayah, J. Groenen, G. Bachelier, F. Poinsotte, J.R. Huntzinger, M. Cazayous, E. Bedel-Pereira, A. Arnoult, O.G. Schmidt, N. Bertru, C. Paranthoen, O. Dehaese, Conference Information: Conference on Optical Sensing, Strasbourg, 27-29 avril 2004 – Proc. Soc. Photo-Opt. Instr. Eng. (SPIE) 5459, 328 (2004).

3- **Confinement of electronic states in ultimately narrow GaAs/GaP quantum Wells,** A. Mlayah, J.R. Huntzinger, G. Bachelier, R. Carles et A. Zwick, International Conference on Superlattices Nano-structures and Nano-devices, ICSNN, Toulouse, 22 - 26 juillet 2002 - Physica E 17, 204 (2003).

2- **Resonant Raman Scattering in GaAsN: mixing, localization and impurity-band formation,** G. Bachelier, A. Mlayah, M. Cazayous, J. Groenen, A. Zwick H. Carrère, E. BedelPereira, A. Arnoult, A. Rocher et A. Ponchet, Phys. Rev. B 67, 205325 (2003).

1- **Resonant Raman scattering in GaAsN : N-induced Γ-L mixing and localization of electronic states around the E+ level,** G. Bachelier, A. Mlayah, R. Carles, A. Zwick, M. Cazayous, J. Groenen, P. Puech, H.Carrère, A. Arnoult and E. Bedel-Pereira, 26th International Conference on the Physics of Semiconductors, ICPS, Edinburgh, Angleterre, 29 juillet – 2 août 2002 - Proc.